

PROBING EARLY AND LATE INFLATIONS BEYOND
TILTED Λ CDM

by

Zhiqi Huang

A thesis submitted in conformity with the requirements
for the degree of Doctor of Philosophy
Graduate Department of Astronomy & Astrophysics
University of Toronto

Copyright © 2010 by Zhiqi Huang

Abstract

PROBING EARLY AND LATE INFLATIONS BEYOND TILTED Λ CDM

Zhiqi Huang

Doctor of Philosophy

Graduate Department of Astronomy & Astrophysics

University of Toronto

2010

The topic of this thesis is about cosmic inflations, including the early-universe inflation that seeds the initial inhomogeneities of our universe, and the late-time cosmic acceleration triggered by dark energy. The two inflationary epochs have now become part of the standard Λ CDM cosmological model. In the standard paradigm, dark energy is a cosmological constant or vacuum energy, while the early-universe inflation is driven by a slowly rolling scalar field. Currently the minimal Λ CDM model with six parameters agrees well with cosmological observations.

If the greatest achievement of the last twenty golden years of cosmology is the Λ CDM model, the theme of future precision cosmology will be to search for deviations from the minimal Λ CDM paradigm. It is in fact expected that the upcoming breakthroughs of cosmology will be achieved by observing the subdominant anomalies, such as non-Gaussianities in the Cosmic Microwave Background map. The aim of this thesis is then to make theoretical predictions from models beyond Λ CDM, and confront them with cosmological observations. These models include: 1) a new dark energy parametrization based on quintessence models; 2) reconstructing early-universe inflationary trajectories, going beyond the slow-roll assumption; 3) non-Gaussian curvature fluctuations from preheating after the early-universe inflation; 4) infra-red cascading produced by particle production during inflation; 5) preheating after Modular inflation; 6) decaying cold dark matter. We update the cosmological data sets – Cosmic Microwave Background, Type

Ia supernova, weak gravitational lensing, galaxy power spectra, and Lyman- α forest – to the most current catalog, and run Monte Carlo Markov Chain calculations to obtain the likelihood of parameters. We also simulate mock data to forecast future observational constraints.

Dedication

This thesis is dedicated to my wife who has been the great source of motivation and inspiration.

Also I dedicate this thesis to my beloved parents who seed one of the important initial conditions for this thesis.

Finally I dedicate this thesis to my respectful thesis advisors – Professor J. Richard Bond and Professor Lev Kofman.

Acknowledgements

Professor J. Richard Bond and Professor Lev Kofman have been the ideal thesis supervisors. This thesis would not have been possible without their guidance, encouragement, and insightful criticisms. Professor Bond is an expert in almost all fields of cosmology and astrophysics, on both theories and observations. I benefited tremendously from the many stimulating discussions with him. I am greatly indebted to him for teaching me how to think about, visualize and present physics. Professor Kofman is an enthusiastic theorist. I still remember how he helped me, step by step, to learn the cosmological perturbation theory, which later became the most useful tool for my PhD projects. The passing of him in last November, from cancer, was a shocking and sad news for the cosmology community. I believe the completion of this thesis will be the best way to express my gratitude and thanks for his inspiring guidance and supervision.

I would like to thank the PhD committee: Professor Chris Matzner, Professor Ue-Li Pen for their help and advices along the way. I would also like to express my gratitude to Professor Marco Peloso for acting as the external appraiser, and Professor Ray Carlberg for attending my final oral examination.

It is my pleasure to thank my present office mates Nicholas Battaglia, Marzieh Farhang, and Elizabeth Harper-Clark; and my past office mates Pascal Vaudrevange and Lawrence Mudryk for their making the office an enjoyable work place.

I am pleased to thank the collaborators for the successful collaborations: Professor Carlo Contaldi, Professor Andrei Frolov, Professor Dmitri Pogosyan, Dr. Neil Barnaby, Dr. Siew-Phang Ng, Dr. Pascal Vaudrevange, Santiago Amigo, William Cheung. Thanks are also due to the CITA computer facilities, without which many of my numerical works would not have been possible.

Finally I would like to thank the department of astronomy and astrophysics for providing part of the financial support for my PhD study.

Contents

1	Introduction	1
1.1	The Standard Model of Cosmology	1
1.2	Conventions and Notations	5
1.3	Basics of FRW Universe	7
1.4	Dark Energy: Beyond Λ	14
1.5	Early-universe Inflation	16
1.6	Parametric Resonance, Preheating, and Particle Production	27
1.7	Markov Chain Monte Carlo Simulations	31
1.8	Outline of the Thesis	34
2	Parameterizing and Measuring DE Trajectories	36
2.1	Introduction	36
2.1.1	Running Dark Energy and its Equation of State	36
2.1.2	The Semi-Blind Trajectory Approach	38
2.1.3	Physically-motivated Late-inflaton Trajectories	41
2.1.4	Tracking and Thawing Models	43
2.1.5	Parameter Priors for Tracking and Thawing Models	44
2.2	Late-inflation Trajectories and Their Parameterization	45
2.2.1	The Field Equations in Terms of Equations of State	45
2.2.2	A Re-expressed Equation Hierarchy Conducive to Approximation	47

2.2.3	The Parameterized Linear and Quadratic Approximations	49
2.2.4	Asymptotic Properties of $V(\phi)$ & $\sqrt{\varepsilon_{\phi\infty}}$	50
2.2.5	The Two-Parameter $w_\phi(a \varepsilon_s, \varepsilon_{\phi\infty})$ -Trajectories	52
2.2.6	The Three-parameter Formula	54
2.3	Exact DE Paths for Various Potentials Compared with our Approximate Paths	54
2.4	Observational Constraints	57
2.4.1	Current Data Sets Used	57
2.4.2	CosmoMC Results for Current Data	63
2.5	Future Data Forecasts	67
2.5.1	The mock data sets	70
2.5.2	Results of the Forecasts	73
2.6	Discussion and Conclusions	75
2.6.1	Slow-roll Thawing Models, Their One-parameter Approximation and the Burn-in to It	75
2.6.2	A w_0 - w_a Degeneracy for the Slow-roll Thawing Model Prior	78
2.6.3	Transforming w_0 - w_a and ε_s - $\varepsilon_{\phi\infty}$ Contours into w_0 - w_∞ Contours	79
2.6.4	ζ_s , the Potential Curvature and the Difficulty of Reconstructing $V(\phi)$	81
2.6.5	Field Momentum and the Tracking Parameter $\varepsilon_{\phi\infty}$	82
2.6.6	Using Our w_ϕ Parametrization	84
2.7	Appendix: Comparison with Other Parameterizations	85
2.7.1	$\rho_{\text{de}}(z)$ and $H(z)$ reconstruction	87
2.7.2	$V(\phi)$ reconstruction	87
3	Scanning Inflationary Trajectories	89
3.1	Introduction	89
3.2	Updating the Traditional Parametrization	93
3.2.1	Data Sets	93

3.2.2	Constraints on the Conventional Parameters	94
3.3	Statistics of Trajectories	97
3.4	The Bottom-Up Approach: Phenomenological Expansion of \mathcal{P}_S and \mathcal{P}_T .	100
3.4.1	Method	100
3.4.2	Reconstructed Power Spectra	102
3.4.3	Searching for nontrivial features in the power spectra	102
3.5	The Top-down Approach: Scanning the Expansion History	106
3.5.1	Method	106
3.6	Discussion and Conclusions	109
4	Non-Gaussian Curvature Fluctuations from Preheating	112
4.1	Introduction	112
4.2	The Preheating Model	113
4.3	The Comoving Curvature Fluctuations	118
4.4	Analog to Chaotic Billiard Motions	121
4.5	Non-Gaussianity	125
4.6	Discussion	128
5	Infra-red Cascading During Inflation	129
5.1	Introduction	129
5.2	Re-scattering, numerics	134
5.3	Re-scattering, analytics	135
5.4	Discussion of Curvature Fluctuations from IR Cascading	141
5.5	Summary of Theoretical Part	144
5.6	Introduction for the Observational Part	147
5.7	A Simple Parametrization of the Power Spectrum	153
5.8	Data Sets and Analysis	155
5.9	Observational Constraints	157

5.9.1	A Single Burst of Particle Production	157
5.9.2	Multiple Bursts of Particle Production	160
5.10	Particle Physics Models	164
5.10.1	Open String Inflation Models	166
5.10.2	String Monodromy Models	166
5.10.3	A Supersymmetric Model	172
5.11	Conclusions for the Observational Part	172
5.12	APPENDIX A: Analytical Theory of Re-scattering	175
5.12.1	Production of χ -Particles	175
5.12.2	Equations for Re-scattering	177
5.12.3	Renormalization	178
5.12.4	Spectrum of Re-scattered Modes	180
5.13	APPENDIX B: Detailed Computation of P_ϕ	180
5.13.1	Time Integrals	181
5.13.2	Phase Space Integrals	183
6	Preheating after Modular Inflation	185
6.1	Introduction	185
6.2	Kähler Moduli/Roulette Inflation in the Large Volume Compactification	190
6.2.1	Large Volume Compactification	190
6.2.2	Roulette Inflation	194
6.3	Preheating via Self-interactions in the Inflaton Sector	198
6.3.1	Equations for Linear Fluctuations	198
6.3.2	Instability of Kähler Modulus Fluctuations	202
6.3.3	Lattice Simulations of Preheating in Roulette Inflation	207
6.4	Transfer of Energy into the SM Sector: D7 Wrapping the Inflationary 4-Cycle	213
6.4.1	Inflaton Coupling to Photons	214

6.4.2	Photon Preheating	214
6.4.3	Perturbative Decays to Photons	215
6.4.4	Inflaton Coupling to Fermions	218
6.4.5	Reheating Temperature	219
6.5	Transfer of Energy into the SM Sector: D7 Wrapping a Non-Inflationary 4-Cycle	221
6.6	Stringy Reheating via Kähler Moduli Shrinking	224
6.7	Summary and Discussion	226
7	Cosmological Constraints on Decaying Dark Matter	230
7.1	Introduction	230
7.2	Decaying Cold Dark Matter Cosmology	234
7.3	Markov Chain Monte Carlo Results and Discussion	239
7.4	Implications for Particle Physics Models with Decaying Cold Dark Matter	245
7.4.1	Spin-0 Dark Matter	246
7.4.2	Spin-1/2 Dark Matter	250
7.4.3	Spin-1 Dark Matter	256
7.4.4	General Dimensional Considerations	259
7.5	Conclusions and Outlook	260
7.6	Appendix: Compendium of Decay Rates	262
8	Conclusions and Outlook	266
	Bibliography	268

List of Tables

1.1	ABBREVIATIONS	6
1.2	Six-parameter Λ CDM model; The current constraints (68.3% CL) are obtained using CMB + SN + LSS + WL + Ly α . See Chapter 2 for more details about the data sets and how these constraints are derived. The cold dark matter and baryonic matter density are normalized to $\rho_{\text{crit}}/h^2 \approx 11.2$ proton mass per cubic meter. The primordial scalar power spectrum is given by Eq. (1.64) with $k_{\text{pivot}} = 0.002\text{Mpc}^{-1}$ and $n_{\text{run}} = 0$. The primordial tensor spectrum is assumed to be negligible ($r = 0$).	24
1.3	Definition of derived parameters.	24
1.4	Inflation Models	25
2.1	Weak Lensing Data Sets	62
2.2	Cosmic Parameter Constraints: Λ CDM, w_0 -CDM, w_0 - w_a -CDM, ε_s - $\varepsilon_{\phi\infty}$ - ζ_s -CDM	65
2.3	The marginalized 68.3%, 95.4%, and 99.7% CL constraints on ε_s under different prior assumptions.	66
2.4	Fiducial model used in future data forecasts	69
2.5	Planck Instrument Characteristics	70
2.6	21-cm BAO Survey Specifications	72

3.1	The 68.3% CL constraints on cosmological parameters (for r the 68.3%CL and 95.4% CL upperbounds are shown). A Λ CDM model with $n_t = 0$ has been assumed. The scalar power spectrum is expanded at $k_{\text{pivot}} = 0.002\text{Mpc}^{-1}$	95
3.2	The constraints on r using different parametrizations. Here “consistency” stands for the single-field inflation prior (see Section 3.5).	105
5.1	Constraints on the standard (“vanilla”) cosmological parameters for the single-bump model. For comparison we also show the standard Λ CDM constraints using the same data sets. All errors are 95.4% confidence level. (<i>Note we are showing 2-σ constraints here.</i>)	159
5.2	constraints on the standard (“vanilla”) cosmological parameters for the multiple-bump model. All error bars are 95.4% confidence level.	164
7.1	Decay Rate of Spin-0 DM via Different Interaction Terms	263
7.2	Two-Body Decay Rate of Spin-1/2 DM via Generic Interaction Terms	264
7.3	Functions used for the Analysis of Bino Decay	264
7.4	Decay Rate of Spin-1 DM via Different Interaction Terms	265

List of Figures

1.1	CMB temperature auto-correlation angular power spectrum. The solid black data points are Wilkinson Microwave Anisotropy Probe (WMAP) seven-year data [1, 2]. The dotted blue data is from balloon experiment BOOMERANG [3, 4, 5], shown as an example of independent measurements. The solid red line is the theoretical prediction from a best-fit minimal 6-parameter Λ CDM model.	3
1.2	Cosmic abundance varies with time. This is assuming a Λ CDM model with three species of light neutrinos.	10
1.3	The updated Hubble diagram. Here m is the apparent magnitude, and M the absolute magnitude determined by χ^2 fitting, which cancels the dependency of $m - M$ on Hubble constant. See Chapter 2 for more details about the supernova data sets.	13
1.4	When $\epsilon(k) \equiv \epsilon _{k=aH}$ trajectory has complicated structures, the slow-roll solution (1.60) for scalar power spectrum deviate from the full numerical solution, while the slow-roll approximation (1.61) for tensor power spectrum remains a good fit.	22

1.5	The gray contours are the current 68.3% and 95.4% constraints on inflations models. The red contours are constraints using simulated Planck satellite CMB data and EUCLID weak lensing data, for a fiducial $r = 0$ model. See Chapter 2 for the details about the current and forecast data sets.	26
1.6	The real part of the Floquet exponent for the Mathieu equation $\ddot{\chi} + (\lambda - 2q \cos 2t)\chi = 0$. In the white region the solutions are stable. In the colored region the solutions exponentially grow: $\chi \sim e^{\mu t}$	32
2.1	The marginalized 68.3% CL (inner contour) and 95.4% CL (outer contour) constraints on w_0 and w_a for the conventional DETF parametrization $w = w_0 + w_a(1 - a)$, using the current data sets described in § 2.4. The white point is the cosmological constant model. The solid red line is a slow-roll consistency relation, Eq. (2.52) derived in § 2.6.2 (for a fixed $\Omega_{m0} = 0.29$, as inferred by all of the current data). The tilted dashed gray line shows $w_a = -1 - w_0$. Pure quintessence models restrict the parameter space to $1 + w_0 > 0$ and w_a above the line, whereas in the pure phantom regime, $1 + w_0 < -0$ and w_a would have to lie below the line. Allowing for equal a priori probabilities to populate the other regions is quite problematical theoretically, and indeed the most reasonable theory prior would allow only the pure quintessence domain.	39
2.2	Examples of tracking models. The solid red lines and dot-dashed green lines are numerical solutions of w_ϕ with different ϕ_{ini} . Upper panel: $\phi_{\text{ini};\text{red}} = 10^{-7}M_{\text{p}}$, and $\phi_{\text{ini};\text{green}} = 10^{-6}M_{\text{p}}$. Middle panel: $\phi_{\text{ini};\text{red}} = 0.01M_{\text{p}}$, and $\phi_{\text{ini};\text{green}} = 0.03M_{\text{p}}$. Lower panel: $\phi_{\text{ini};\text{red}} = -12.5M_{\text{p}}$, and $\phi_{\text{ini};\text{green}} = -10.5M_{\text{p}}$. The dashed blue lines are $w(a)$ trajectories calculated with the three-parameter $w(a)$ ansatz (2.28). The rapid rise at the beginning is the a^{-6} race of ϵ_ϕ from our start of zero initial momentum towards the attractor. 56	56

2.3	Examples of thawing models. The solid red lines are numerical solutions of w_ϕ . The dashed blue lines are calculated using the three-parameter $w(a)$ formula (2.28). See the text for more details.	58
2.4	An example showing how the ζ_s parameter improves our parametrization in the moderate-roll case. The solid red lines are numerical solutions of w_ϕ . The dashed blue lines are $w(a)$ trajectories calculated with the three-parameter ansatz (2.28). The dotted green lines are two-parameter approximations obtained by forcing $\zeta_s = 0$	59
2.5	An example of phantom model. The solid red lines are numerical solutions of w_ϕ . The dashed blue lines are $w(a)$ trajectories calculated with the three-parameter $w(a)$ formula (2.28).	59
2.6	The marginalized 68.3% CL and 95.4% CL constraints on σ_8 and Ω_{m0} for the Λ CDM model vary with different choices of data sets. For each data set a HST constraint on H_0 and BBN constraint on $\Omega_{b0}h^2$ have been used.	64
2.7	The marginalized 68.3% CL and 95.4% CL constraints on ε_s and Ω_{m0} , using different (combinations) of data sets. This is the key DE plot for late-inflaton models of energy scale, encoded by $1 - \Omega_{m0}$ and potential gradient defining the roll-down rate, $\sqrt{\varepsilon_s}$	66

2.8	The best-fit trajectory (heavy curve) and a sample of trajectories that are within one-sigma (68.3% CL). In the upper panels the current data sets are used, and lower panels the forecast mock data. From left to right the trajectories are the dark energy equation of state, the Hubble parameter rescaled with $H_0^{-1}(1+z)^{3/2}$, the distance moduli with a reference Λ CDM model subtracted, and the growth factor of linear perturbation rescaled with a factor $(1+z)$ (normalized to be unit in the matter dominated regime). The current supernova data is plotted against the reconstructed trajectories of distance moduli. The error bars shown in the upper-left and lower-left panels are one- σ uncertainties of $1+w$ in bands $0 < a \leq 0.25$, $0.25 < a \leq 0.5$, $0.5 < a \leq 0.75$ and $0.75 < a \leq 1$	68
2.9	Marginalized 2D likelihood contours for our three DE parameters derived using ‘‘ALL’’ current observational data. The inner and outer contours are 68.3% CL and 95.4% CL contours. (We actually show $ \varepsilon_{\phi\infty} /\epsilon_m$ since that is the attractor whether one is in the relativistic $\epsilon_m = 2$ or non-relativistic $\epsilon_m = 3/2$ regime.)	69
2.10	Marginalized 2D likelihood contours; Using mock data and assuming thawing prior ($\varepsilon_{\phi\infty} = 0$); The inner and outer contours of each color correspond to 68.3% CL and 95.4% CL, respectively. See the text for more details.	74
2.11	Left panel: the function $F^2(x)$ with $x = a/a_{\text{eq}}$ defined by Eq. (2.26). Right Panel: the derivative dF^2/dx , showing where w_ϕ changes most quickly in thawing models, namely near a_{eq}	77
2.12	The dependence of distance moduli $\mu(z)$ on the slope parameter ε_s for slow-roll thawing models. The prediction of $\mu(z)$ from a reference Λ CDM model with $\Omega_{m0} = 0.29$ is subtracted from each line. The supernova samples are binned into redshift bins with bin width $\Delta z = 0.3$	77

2.13 The upper panel shows the marginalized 68.3% (inner contour) and 95.4% (outer contour) constraints on w_0 and w_∞ for the conventional linear DETF parametrization, recast as $w = w_\infty + (w_0 - w_\infty)a$, using the current data sets described in § 2.4. It is a slightly tilted version of the w_0 - w_a version in Fig. 2.1. The demarcation lines transform to just the two axes, with the upper right quadrant the pure quintessence regime, and the lower right quadrant the pure phantom regime. If the cross-over of partly phantom and partly quintessence are excluded, as they are for our late-inflaton treatment in this chapter, the result looks similar to the lower panel, in which the 2-parameter ε_s - $\varepsilon_{\phi_\infty}$ formula has been recast into $2\varepsilon_0/3$ and $2\varepsilon_\infty/3$, via $\sqrt{\varepsilon_0} = \sqrt{\varepsilon_{\phi_\infty}} + (\sqrt{\varepsilon_s} - \sqrt{2\varepsilon_{\phi_\infty}})F(1/a_{\text{eq}})$. However, as well the prior measure has also been transformed, from our standard uniform $d\varepsilon_s d\varepsilon_{\phi_\infty}$ one to a uniform $d\varepsilon_0 d\varepsilon_{\phi_\infty}$ one. The quadrant exclusions are automatically included in our re-parameterization. 80

2.14 The 68.3% CL (inner contours) and 95.4% (outer contours) CL constraints on ε_s and ζ_s , using forecasted CMB, WL, BAO and SN data. The thawing prior ($\varepsilon_{\phi_\infty} = 0$) has been used to break the degeneracy between ε_s and $\varepsilon_{\phi_\infty}$. The four input fiducial models labeled with red points have $\zeta_s = 0$ and, from bottom to top, $\varepsilon_s = 0, 0.25, 0.5,$ and 0.75 , respectively. Only for large gradients can ζ_s be measured and a reasonable stab at potential reconstruction be made 82

2.15 The dependence of $w_\phi(z)$ on $\varepsilon_{\phi_\infty}$ and ζ_s . We have fixed $\Omega_{m0} = 0.27$ and $\varepsilon_s = 0.5$. The red solid lines correspond to $\zeta_s = 0$, green dashed lines $\zeta_s = -0.5$, and blue dotted lines $\zeta_s = 0.5$. For each fixed ζ_s , the lines from bottom to top correspond to $\varepsilon_{\phi_\infty} = 0, 0.3, 0.6,$ and 0.9 83

3.1	Top panel: the “Starobinsky potential”. The two linear pieces of potential $V(\phi)$ are connected by a quadratic piece with width $0.04M_p$. Bottom panel: the power spectra generated in this inflation model. The solid black line and dashed blue line are numerically calculated \mathcal{P}_S and \mathcal{P}_T , respectively. The dotted green lines are the slow-roll approximations (1.60) and (1.61). The dotted red line at the bottom is the ϵ trajectory.	92
3.2	The marginalized posterior likelihood of cosmological parameters. They are normalized such that the maximum likelihood is 1. A Λ CDM model with $n_t = 0$ has been assumed. The scalar power spectrum is expanded at $k_{\text{pivot}} = 0.002\text{Mpc}^{-1}$. The solid red line in the left panel shows the single-field inflation consistency.	96
3.3	Left panel: the single-field consistency relation (red line) is not tested by the data. Right panel: the degeneracy between n_s and r . A Λ CDM model with $-0.1 < n_t < 0$ and $n_{\text{run}} = 0$ has been assumed. The spectra are expanded at $k_{\text{pivot}} = 0.002\text{Mpc}^{-1}$. The three contours are 68.3% CL, 95.4% CL and 99.7% CL, respectively.	97
3.4	The marginalized 68.3% CL and 95.4% CL constraints on n_s and r using simulated Planck and SPIDER CMB data.	98
3.5	The reconstructed primordial spectra with current data. In the left panel we have used the bottom-up approach with natural cubic spline interpolation. See Section 3.4 for the details of the parametrization. In the right panel the top-down approach with single-field inflation prior is applied. See Section 3.5 for the details about the parametrization. The $1-\sigma$ error bars are uncertainties of the band powers. The band powers are defined as the convolutions of the power spectrum and top-hat window functions in seven uniform bins.	103

3.6	This CMB angular power spectra mapped from reconstructed trajectories (see Figure 3.5). The upper-left and lower-left panels are TT and BB power spectra reconstructed with bottom-up approach, and the upper-right and lower-right panels are using top-down approach. See the text for more details.	104
3.7	The reconstructed primordial spectra with mock data. The fiducial model has $\mathcal{P}_T = 0$ and a power-law \mathcal{P}_S with $n_s = 0.97$. The left panel uses natural cubic spline interpolation on $\ln \mathcal{P}_S$, while the right panel uses Chebyshev interpolation. The $1-\sigma$ error bars are uncertainties of the band powers. The band powers are defined as the convolutions of the power spectrum and top-hat window functions in seven uniform bins.	105
3.8	The reconstructed primordial power spectra, using mock data with a feature in the scalar power spectrum. A fiducial $r = 0$ and $n_s = 0.97$ model has been used, on top of which an IR-cascading bump [6, 7] with amplitude about 10% of the total \mathcal{P}_S and with position $k^* = 0.05\text{Mpc}^{-1}$ is added to the scalar power spectrum, as shown in dot-dashed black color. Monotonic cubic Hermite interpolation is used to interpolate $\ln \mathcal{P}_S$ between 11 knots.	107
3.9	The reconstructed primordial spectra with mock data. The fiducial model that has been used to generate the mock data is the quadratic potential ($V = \frac{1}{2}m^2\phi^2$) model. The left panel shows the reconstructed power spectra using the bottom-up approach described in Section 3.4, with natural cubic spline interpolation method applied. The right panel shows the reconstructed power spectra using the top-down approach scanning $d \ln \epsilon / d \ln k$, as described in Section 3.5. The $1-\sigma$ error bars are uncertainties of the band powers. The band powers are defined as the convolutions of the power spectrum and top-hat window functions in seven uniform bins.	110

4.1 The amplitude of mode functions of χ in the spatial flat gauge at the end of inflation, for the inflation model $V = \frac{\lambda}{4}\phi^4 + \frac{1}{2}g^2\phi^2\chi^2$ with $\lambda = 10^{-13}$ and various values of g^2/λ . The rising tails around $k \sim (aH)_{\text{end}}$ are the vacuum mode functions that have not passed the quantum-decoherence phase. These tails should be renormalized away when calculating the classical r.m.s. of the χ field. 116

4.2 In left panel the solid black line is $\text{Cn}(x; 1/\sqrt{2})$, the dotted red line shows the first ($n = 1$) term on the R.H.S. of Eq. (4.8). In the right panel we show the residuals $\delta f_n(x) \equiv \text{Cn}(x; 1/\sqrt{2}) - f_n(x)$, where $f_n(x)$ is the sum of the first n terms in the R.H.S. of Eq (4.8). The dotted red line, the dashed blue line, and the dot-dashed green line are $\delta f_1(x)$, $\delta f_2(x)$ and $\delta f_3(x)$, respectively. 117

4.3 The Floquet chart for $V = \frac{1}{4}\lambda\phi^4 + \frac{1}{2}g^2\phi^2\chi^2$ preheating model. The white regions give the stable bands where the mode function χ_k does not grow. The coloured regions are the instability bands. Here \tilde{k} is defined as $k/(a\sqrt{\lambda}\phi_{\text{max}})$, where $\phi_{\text{max}} \propto a^{-1}$ is the amplitude of the ϕ oscillation. In the instability bands the growth of mode function χ_k is described by $a\chi_k \sim e^{\tilde{\mu}_k\sqrt{\lambda}\int\phi_{\text{max}}dt}$, where t is the physical time. 119

4.4 The structure of $\delta N(\chi_i)$ on uniform Hubble hypersurfaces probed with $\sim 10^4$ lattice simulations from the end-of-inflation through the end-of-preheating for varying homogeneous χ_i initial conditions, for $g^2/\lambda = 2$. The periods $n\mu_0 T$ in $\ln \chi_i$ are marked by the large green circles, and the higher harmonics (revealed by the Fourier analysis) by smaller green circles. These locate the spikes in $\delta N(\chi_i)$. The effective field $\langle F_{\text{NL}}|\chi_b + \chi_{>h}\rangle$ marginalized over high spatial frequencies with $\sigma_{\text{HF}}=7 \times 10^{-7} M_P$ (vertical line) yields the solid curve. Here χ_b etc. are defined in Section 4.5. A quadratic fit, $f_\chi(\chi_b + \chi_{>h})^2$, is also shown. An issue for *our* Hubble patch is whether the ultra-large scale $\chi_{>h}$ is large enough that the large scale structure fluctuations about it, $\pm\sigma_{b<h}$, encompass smoothed peaks in field space, or not. A typical value for $\sigma_{b<h}$ is $\sim 3 \times 10^{-7} M_P$ 122

4.5 Billiard trajectories of the $k = 0$ modes $\phi(\tau)$ and $\chi(\tau)$ within the $\lambda\phi^4/4 + g^2\chi^2\phi^2/2$ potential well. Upper panel has a “no-spike” initial value $\chi_i = 3.6 \times 10^{-7} M_P$, and the bottom panel has a “spike” $\chi_i = 3.9 \times 10^{-7} M_P$. The solid curves are the (fuzzy) potential walls without the inclusion of mass terms induced by field nonlinearities; the pale green and brighter green border areas include the induced masses at the instances $t = 10.8T$ and asymptotically. Thin and thick parts of the trajectories denote before after $t = 9.7T$, and up to $11.8T$, with the circle on it at $t = 10.8T$. The inserts in the left upper corners of the panels show the first several periods of linear oscillations. 124

4.6 Realizations of the nG map $\langle F_{\text{NL}}|\chi_b \rangle$ on the CMB sky. Top left shows a scale-invariant Gaussian random field realization $\chi_b(d_{\gamma dec}\hat{q})$ in direction \hat{q} on a sphere at the comoving distance to photon decoupling, $d_{\gamma dec}$. Top right shows the action of $\langle F_{\text{NL}}|\chi_b \rangle$ on it, using our Gaussian-line-profile approximation with 2 peaks at $\chi_p = \pm\nu_p\sigma_b$, for $\nu_p = 3.5$. Middle left shows the map convolved with a CMB transfer function, and smoothed on a 1° scale, right with $\nu_p = 4.5$; both show “cold spot” intermittency. . . . 127

5.1 $|\dot{\phi}|/(M_p m)$ plotted against mt for $g^2 = 0.1$ (where $m = V_{,\phi\phi}$ is the effective inflaton mass). Time $t = 0$ corresponds to the moment when $\phi = \phi_0$ and χ -particles are produced copiously. The solid red line is the lattice field theory result taking into account the full dynamics of re-scattering and IR cascading while the dashed blue line is the result of a mean field theory treatment which ignores re-scattering [8]. The dot-dashed black line is the inflationary trajectory in the absence of particle creation. 132

5.2 The power spectrum of inflaton modes induced by re-scattering (normalized to the usual vacuum fluctuations) as a function of $\ln(k/k_*)$, plotted for three representative time steps in the evolution, showing the cascading of power into the IR. For each time step we plot the analytical result (the solid line) and the data points obtained using lattice field theory simulations (diamonds). The time steps correspond to the following values of the scale factor: $a = 1.03, 1.04, 2.20$ (where $a = 1$ at the moment when $\phi = \phi_0$). By this time the amplitude of fluctuations is saturated due to the expansion of the universe. The vertical lines show the range of scales from our lattice simulation. 136

5.3 Physical occupation number n_k as a function of $\ln(k/k_*)$ for $g^2 = 0.1$. The three curves correspond to the same series of time steps used in Fig. 5.2, and demonstrate the growing number of long wavelength inflaton modes which are produced as a result of IR cascading. Because the same χ -particle can undergo many re-scatterings off the background condensate $\phi(t)$, the $\delta\phi$ occupation number is larger than the initial χ particle number (for $g^2 = 0.1$ one can achieve $n_\phi(k) \sim 30$ even though initially $n_\chi(k) \leq 1$). When $g^2 = 0.06$ the IR $\delta\phi$ occupation number exceeds unity within a single e-folding. The yellow envelope line shows the onset of scaling behaviour associated with the scaling turbulent regime. 137

5.4 The dependence of the power spectrum P_ϕ on the coupling g^2 . The three curves correspond to P_ϕ for $g^2 = 0.01, 0.1, 1$, evaluated at a fixed value of the scale factor, $a = 2.20$. We see that even for small values of g^2 the inflaton modes induced by re-scattering constitute a significant fraction of the usual vacuum fluctuations after only a single e-folding. 138

5.5 Probability density function of $\delta\phi$ for $g^2 = 0.1$ at a series of different values of the scale factor, a . The dotted curve shows a Gaussian fit at late time $a = 6.9$ 139

5.6	<p>The left panel shows a comparison of curvature fluctuations from different effects. We see the dominance of fluctuations produced by IR cascading over the wiggles induced by the momentary slowing-down of the inflaton. For illustration we have taken $g^2 = 0.1$, but the dominance is generic for all values of the coupling. The red solid line is the IR cascading curvature power spectrum, while the blue dashed line is the result of a mean field treatment. (The vertical lines show aH at the beginning of particle production and after ~ 3 e-foldings.) The right panel shows the curvature power spectrum resulting from multiple bursts of particle production and IR cascading. Superposing a large number of these bumps produces a broad-band spectrum.</p>	142
5.7	<p>Rescattering diagram.</p>	150
5.8	<p>The bump-like features generated by IR cascading. We plot the feature power spectrum obtained from fully nonlinear lattice field theory simulations (the red points) and also the result of an analytical calculation (the dashed blue curve). We also superpose the fitting function $\sim k^3 e^{-\pi k^2/(2k_*^2)}$ (the solid black curve) to illustrate the accuracy of this simple formula</p>	151
5.9	<p>Marginalized posterior likelihood contours for the parameters A_{IR} and k_{IR} (the magnitude and position of the feature, respectively) in the single-bump model. Black and grey regions correspond to parameter values allowed at 95.4% and 99.7% confidence levels, respectively. At small scales, to the right of the dashed vertical line, our results should be taken with a grain of salt since the nonlinear evolution of the power spectrum may not be modelled correctly in the presence of bump-like distortions.</p>	158

5.10	The left panel shows a sample bump in the power spectrum with amplitude $A_{\text{IR}} = 2.5 \times 10^{-10}$ which corresponds to a coupling $g^2 \sim 0.01$. The feature is located at $k_{\text{IR}} = 0.01 \text{ Mpc}^{-1}$. This example represents a distortion of $\mathcal{O}(10\%)$ as compared to the usual vacuum fluctuations and is consistent with the data at 2σ . The right panel shows the CMB angular TT power spectrum for this example, illustrating that the distortion shows up mostly in the first peak.	161
5.11	Marginalized posterior likelihood contours for the parameters A_{IR} and Δ (the feature amplitude and spacing, respectively) of the multiple-bump model. Black and grey regions correspond to values allowed at 95.4% and 99.7% confidence levels, respectively.	163
5.12	The top panel shows a sample multiple-bump distortion with amplitude $A_{\text{IR}} = 1 \times 10^{-9}$ which corresponds to $g^2 \sim 0.02$. The feature spacing is $\Delta = 0.75$. We take the vanilla parameters to be $A_s = 1.04 \times 10^{-9}$, $n_s = 0.93$ so that the scale of inflation is slightly lower than in the standard scenario and the spectral tilt is slightly redder. The bottom panel shows the CMB angular TT power spectrum for this example.	165
5.13	The behaviour of the function $F(k, t)$ as a function of t . For illustration we have set $\Omega_k = 5k_\star$	182

6.1 A cartoon of the large volume compactification manifold illustrating the ingredients relevant for Kähler moduli inflation and (p)reheating. The modulus $\tau_1 = \text{Re}(T_1)$ controls the overall size of the compactification while the moduli $\tau_i = \text{Re}(T_i)$ ($i \geq 2$) control the size of the blow-up 4-cycles (hole sizes). We have labelled τ_2 as the last 4-cycle to stabilize, and hence this modulus is associated with the final observable phase of inflation. The total volume τ_1 and other cycles (for example τ_3) are assumed to already be stabilized. In the text we consider two possible scenarios for the location of the SM: (i) a D7-brane wrapping the inflationary 4-cycle, τ_2 , and, (ii) a D7-brane wrapping the non-inflationary 4-cycle, τ_3 . We have illustrated these wrappings schematically. 193

6.2 The T_2 potential $V(\tau, \theta)$ surface for a representative choice of parameters, using polar coordinates to illustrate the periodic structure of the potential in the axion direction, θ . Superimposed on the potential surface are three different inflationary trajectories, showing the rich set of possibilities in Roulette inflation. Inflation proceeds in the large τ region where the potential is exponentially flat. On the other hand, preheating after inflation takes place during the phase of oscillations the extremely steep minimum near $\tau = \mathcal{O}(1)$ and $\cos(a_2\theta) = -1$ 195

6.3 The left panel shows the effective potential for the canonical Kähler modulus ϕ along the axion trough, $U(\phi, (2l + 1)\pi/a_2)$ showing the long exponentially flat region relevant for inflation and also the steep minimum relevant for the preheating phase of post-inflationary oscillations. We have labelled the point where inflation ends (where the ϵ slow roll parameter is unity) and also the point where the effective mass-squared $V''(\phi)$ flips sign, corresponding to the cross-over between the tachyonic and non-tachyonic regions. The right panel shows the oscillatory time evolution of the homogeneous inflaton $\phi_0(t)$ at the end of inflation. 201

6.4 The effective mass-squared of both the Kähler modulus ϕ (the dashed blue curve) and axion ψ (the solid red curve) as a function of time. We plot the effective mass in units of m_ϕ , the mass at the minimum of the potential. Note that $M_{\text{eff}}(t)$ actually exceeds m_ϕ during the inflaton oscillations. This corresponds to the steep curvature on the left-hand-side of the potential minimum in Fig. 6.3. 203

6.5 The quantity $|dM_{\text{eff}}/dt|/|M_{\text{eff}}^2|$ for both the Kähler modulus ϕ (the dashed blue curve) and axion ψ (the solid red curve) as a function of time. This quantity provides a measure of the violation of adiabaticity and coincides with the adiabatic invariant $\dot{\omega}_k/\omega_k^2$ in the IR. The Spike structure of the Kähler modulus effective mass leads to extremely strong violations of adiabaticity and particle production. On the other hand, the axion effective frequency varies slowly during the inflaton oscillations and axion particles are not produced. 204

6.6	The dimensionless characteristic exponent μ_k (Floquet exponent) for the exponential instability of the (canonical) Kähler modulus fluctuations $\delta\phi_k$, defined in (6.24). The broad unstable region in the IR comes from the tachyonic regions where $M_{\phi,\text{eff}}^2 < 0$ whereas the UV region displays the band structure that is characteristic of parametric resonance. The behaviour of the modes $\delta\phi_k$ in these two regions is qualitatively different.	206
6.7	The behaviour of linear Kähler fluctuations during preheating after modular inflation illustrating the combination of tachyonic instability and parametric resonance. The left panel shows the mode behaviour for $k = 0.01m_\phi$ (corresponding to the IR tachyonic regime) while the right panel shows the mode behaviour for $k = 0.5m_\phi$ (corresponding to the UV regime of parametric resonance). The middle panel is $k = 0.08m_\phi$, corresponding to the intermediate regime where both effects are active.	207
6.8	The energy spectrum $\sim k^4 n_k$ for $\delta\tau$, calculated with linear theory, showing the rapid and violent production of particles after modular inflation. Within three oscillations of the background field (by $t = 3T$) the energy density is significantly larger than the energy in the homogeneous condensate and at this point nonlinear feedback must be taken into account.	208
6.9	The power in Kähler modulus gradient energy, which is given by $k^5 \mathcal{K}_{,\tau\tau} \delta\tau_k ^2 / (2\pi^2 a^2)$, from our lattice simulations, normalized this to the total background energy density, $\bar{\rho}$. The spectrum is shown for four time steps in the evolution: $t = T$, $t = 2T$, $t = 2.25T$ and $t = 3T$, illustrating the rapid decay of the homogeneous inflaton condensate into inhomogeneous fluctuations. See the text for further discussion.	211
6.10	The left panel shows the time dependence of the effective photon mass, $M_{\gamma,\text{eff}}^2(t)$. The right panel shows the Floquet exponent μ_k for the mode functions $A_k(t) \sim e^{\mu_k t/T}$	216

7.1	Posterior probability density function of the decay rate Γ . Solid line: using all the data sets. Dashed line: CMB + SN + LSS + Ly α . Dotted line: CMB only. The probability density function is normalized as $\int P(\Gamma)d\Gamma = 1$.	240
7.2	Constraints on the early universe CDM density parameter $\Omega_{\text{cdm,e}}$ (defined in Eq. 7.16) and decay rate Γ , using all the data sets, is plotted on the left panel. For comparison, the present day CDM density parameter Ω_{c0} and decay rate Γ is plotted on the right panel. The inner and outer contours correspond to 68.3% and 95.4% confidence levels, respectively.	240
7.3	CMB power spectrum for different dark matter decay rate, assuming the decayed particles are relativistic and weakly interacting. For the CDM density parameter, we choose $\Omega_{\text{cdm,e}}h^2$ to be the same as WMAP-5yr median $\Omega_{\text{c0}}h^2$. For the other cosmological parameters we use WMAP-5yr median values. By doing this, we have fixed the CDM to baryon ratio at recombination. In a similar plot in Ichiki <i>et. al.</i> [9] $\Omega_{\text{c0}}h^2$ is instead fixed. Therefore the height of first peak, which has dependence on CDM to baryon ratio at recombination, will significantly change as one varies the decay rate. In this plot the red line corresponds to a stable dark matter . The blue dotted line corresponds to dark matter with a lifetime 100 Gyr, and the blue dashed line 27 Gyr. The data points are WMAP-5yr temperature auto-correlation measurements.).	242
7.4	The marginalized posterior likelihood of the total optical depth and that of the DM decay reionization parameter.	243
7.5	The marginalized 2D likelihood contours. The contours correspond to 68.3% , 95.4% and 99.7% confidence levels, respectively.	244

Chapter 1

Introduction

1.1 The Standard Model of Cosmology

The past two decades have witnessed a golden age of cosmology. The plethora of observational data has led to a remarkably consistent picture of our universe, often referred to as the standard model of cosmology or the concordance model. The picture of a general-relativity-governed universe composed of about 71% dark energy (DE), 25% dark matter (DM) and 4% baryonic matter, with small inhomogeneities that originated from vacuum fluctuation during the inflation ⁱ, has been confronted with, and passed, a host of observational tests – the measurement of abundances of light elements from Big Bang Nucleosynthesis (BBN), the temperature and polarization anisotropy in Cosmic Microwave Background (CMB) radiation [10, 11] (see Figure 1.1 for an example), the light curves of Type Ia supernova (SN), the large scale structure (LSS) of galaxy clusters, the weak gravitational lensing (WL), and the Lyman- α forest. More comprehensive reviews of the standard cosmological model can be found in Refs. [12, 13, 14].

In spite of the impressive observational success, the concordance model is really a

ⁱFollowing the literature convention, unless otherwise specified, we use the term inflation implicitly for the early-universe inflation, while the term “inflations” in the title refers to both inflation and the late-time cosmic acceleration.

phenomenological model: the dark sectors and the inflaton field that drives inflation are not understood at the level of fundamental particle physics. And because the nature of inflaton is unknown, we do not know the details of preheating or reheating process, i.e., how the universe becomes hot and radiation-dominated, whereas at the end of inflation it is cold and inflaton-dominated.

For dark energy, a cosmological constant Λ , i.e. the vacuum energy is currently the most popular interpretation. For most particle physicists the vacuum energy interpretation is a nightmare, because the value of measured cosmological constant is too small. It is 120 orders of magnitude smaller than the naive estimation from dimensional analysis. Another further embarrassing problem is that the cosmological constant is not only small, but also is fine-tuned to be of the same order of magnitude as the present mass density of the universe. This is the so-called “cosmological constant problem”. It is probably the toughest theoretical problem in cosmology.

In contrast, dark matter is much less problematic for particle physicists. Indeed many dark matter particle candidates have been proposed in extended models of particle physics, with the most popular ones being the weakly interacting massive particles (WIMPs). Experimentally, the laboratory search of dark matter has not been successful yet, but there is much additional evidence for dark matter from astrophysics. This evidence includes: the rotation curves of galaxies [15]; strong gravitational lensing [16]; hot gas in clusters [17]; and the bullet cluster [18]. More information about dark matter research can be found in a recent review article [19].

Cold dark matter (CDM) living in a spatially flat universe with positive cosmological constant Λ , the Λ CDM model, is sometimes referred to as the standard cosmological model in the narrow sense. In a broad sense, the standard cosmological model should also include the pre-BBN history of the universe: the early-universe inflation and (p)reheating.

Thanks to the CMB, the early-universe inflation has become a testable physical model. The major prediction from the simplest scenario, single-field slow-roll inflation, is that

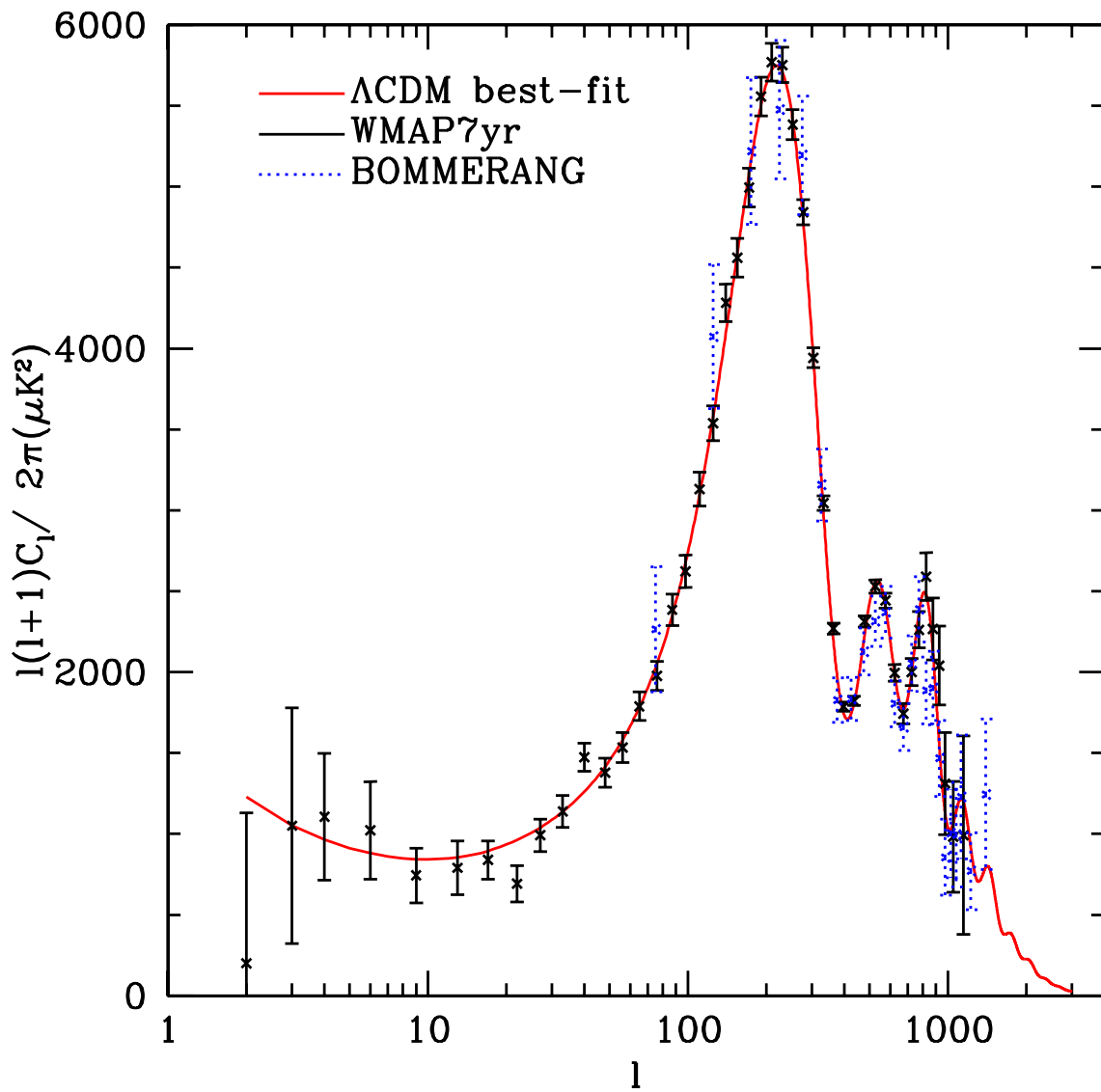


Figure 1.1: CMB temperature auto-correlation angular power spectrum. The solid black data points are Wilkinson Microwave Anisotropy Probe (WMAP) seven-year data [1, 2]. The dotted blue data is from balloon experiment BOOMERANG [3, 4, 5], shown as an example of independent measurements. The solid red line is the theoretical prediction from a best-fit minimal 6-parameter Λ CDM model.

the primordial scalar metric perturbations are almost Gaussian and scale-invariant. This robust prediction, which does not depend on specific models, has been confirmed by CMB and many other cosmological observations. But the model-independence is a double-edged sword. On the one hand, we can make predictions without knowing the details of the inflaton field. On the other hand, the model-independence limits our ability to observationally distinguish between different inflation models. The same situation applies to (p)reheating after inflation, since the current observables are generally insensitive to the details of how inflaton decays into the “primordial soup” of radiation. However, that is not the end of observational early-universe cosmology. Primordial gravitational waves (tensor metric perturbations), primordial non-Gaussianity, and non-trivial features in the primordial scalar power spectrum (e.g. departure from power-law), if any are detected in the future, will open a new window to the physics of inflation, because of the extra information they carry.

Hence the minimal parametrization of cosmic inflations is a cosmological constant Λ plus a slightly tilted primordial scalar power spectrum defined by its amplitude A_s and power-law index n_s . In the last two decades, these parameters are measured to percent-level accuracy by a series of cosmological observations. But this does not tell us much about which inflation/DE model is correct. The aim of the forthcoming precision cosmology is to learn much more details or anomalies about our universe, which are expected to help us pick out the right inflation/DE model. In this thesis we will make novel predictions going beyond the “tilted Λ CDM” from a number of concrete models, and compare them with current and forecast data. These models are listed in the last section of this chapter. In Sections 1.2-1.7 I will give a brief introduction to Λ CDM model, cosmic inflations, and the statistical/computational tools that will be used in later chapters.

1.2 Conventions and Notations

Before we proceed to the technical introduction of Λ CDM model and the topics beyond Λ CDM, let us clarify the conventions and notations. Throughout the thesis, unless otherwise specified, we adopt the $(+, -, -, -)$ metric signature and natural units $c = \hbar = k_B = 1$. The reduced Planck mass is denoted as $M_p = 1/\sqrt{8\pi G_N} = 2.44 \times 10^{18} \text{GeV}$, where $G_N = 1/m_{pl}^2$ is Newton's gravitational constant. We use Einstein summation convention for repeated indices. The Greek alphabet indices α, β, \dots would be implicitly summed over temporal and spatial indices $(0, 1, 2, 3)$; the Roman alphabet indices i, j, k would be summed over spatial indices $(1, 2, 3)$. Perturbed quantities are written with prefix δ . When it does not cause confusion, we use the same notation for the unperturbed quantities and the background quantities. For example, for a field φ , $\delta\varphi$ is the first order perturbation of φ , and the notation φ depending on the context could be either the unperturbed value $\varphi(\mathbf{x}, t)$ or the background value $\bar{\varphi}(t)$. For linear perturbations, in most cases this will not cause confusion. And if it does, I will explicitly use notation $\bar{\varphi}$ for the background value. Unless specified, the constraints on parameters presented in this paper are 68.3% confidence level (CL) bounds, and the inner and outer two-dimensional (2D) contours shown in the figures correspond to 68.3% and 95.4% CL, respectively. The notation $p = \alpha_{-\sigma_l}^{+\sigma_u}$ states that the parameter p has the median value α (i.e. $p > \alpha$ and $p < \alpha$ are equally probable), and the probability that $\alpha - \sigma_l < p < \alpha + \sigma_u$ is 0.683, with $\sigma_u + \sigma_l$ minimized under this constraint. In other words, the interval $(\alpha - \sigma_l, \alpha + \sigma_u)$ is the most compact interval that contains 68.3% probability. The notation $p = \alpha^{+\sigma_1+\sigma_2}$ means that p is always greater than α , and the probability that $p < \alpha + \sigma_1$ is 0.683, while the probability that $p < \alpha + \sigma_2$ is 0.954. And similarly $p = \alpha_{-\sigma_1-\sigma_2}$ states a distribution with a strict upperbound α , a 68.3% CL lower bound $\alpha - \sigma_1$, and a 95.4% CL lower bound $\alpha - \sigma_2$. The Kronecker delta δ_{ij} is unit for $i = j$ and zero otherwise. Finally, I list the abbreviations in Table 1.1.

Table 1.1: ABBREVIATIONS

1D	one-dimensional
2D	two-dimensional
BAO	Baryon Acoustic Oscillations
BBN	Big Bang Nucleosynthesis
CDM	Cold Dark Matter
CMB	Cosmic Microwave Background
CL	confidence level
<i>const.</i>	constant
DE	dark energy
DM	dark matter
EOM	equation of motion
EOS	equation of state
GR	general relativity
L.H.S.	left hand side
LSS	large scale structure
$\text{Ly}\alpha$	Lyman- α forest
r.m.s.	root mean square
QFT	quantum field theory
R.H.S.	right hand side
SN	supernova
SUGRA	supergravity
SUSY	supersymmetry
WL	weak lensing
w.r.t.	with respect to
yr	year

1.3 Basics of FRW Universe

The cosmological principle, a pure hypothesis when it was proposed, and now an observational fact, states that the universe is homogeneous and isotropic on large scales. This leads to the Friedmann-Robertson-Walker (FRW) metric [12, 13, 14]

$$ds^2 = dt^2 - a^2(t) \left[\frac{1}{1 - kr^2} dr^2 + r^2(d\theta^2 + \sin^2 \theta d\phi^2) \right], \quad (1.1)$$

where the constant k is the spatial curvature, t the cosmological time, and r, θ, ϕ the three spatial comoving coordinates. A universe with positive, zero, or negative k is called (spatially) closed, flat, or open universe, respectively. The coordinate r is also called the comoving angular diameter distance, which we will discuss in more details later. A universe on large scales described by FRW metric is called FRW universe.

The wavelength of a photon emitted at time t and received now is stretched by a factor of $a_0/a(t)$, where the subscript 0 denotes quantities at current time. The definition of redshift in astronomy is the fractional increment of wavelength. The cosmological redshift is hence

$$z = \frac{a_0}{a(t)} - 1. \quad (1.2)$$

The choice of normalization of a_0 is completely arbitrary. An oft-used choice is $a_0 = 1$, and hence redshift and the scale factor are related through a simple formula $z = 1/a - 1$.

The dynamics of the homogeneous background is described by the Friedmann equations derived from General Relativity [12, 13, 14]:

$$\left(\frac{\dot{a}}{a}\right)^2 = \frac{8\pi G_N}{3} \rho_{\text{tot}} - \frac{k}{a^2}, \quad (1.3)$$

$$\frac{\ddot{a}}{a} = -\frac{4\pi G_N}{3} (\rho_{\text{tot}} + 3p_{\text{tot}}), \quad (1.4)$$

where ρ_{tot} and p_{tot} are the total energy density and total pressure due to all the components in the universe including all forms of matter, relativistic or non-relativistic, and vacuum if applicable.

The quantity \dot{a}/a is called Hubble parameter or Hubble expansion rate, often denoted as H . Its present value H_0 , the Hubble constant, is often written as $H_0 \equiv 100h \text{ km s}^{-1}\text{Mpc}^{-1}$, with a dimensionless number h of order unity. A measurement of the Hubble constant with the Hubble Space Telescope (HST) from a differential distance ladder gives $h = 0.742 \pm 0.036$ [20]. This result is independent of the cosmological model. In the context of Λ CDM cosmology, a combination of CMB, SN, LSS, WL, Ly α gives $h = 0.692 \pm 0.010$ (see Chapter 2).

The critical density of the universe is defined as

$$\rho_{\text{crit}}(t) = \frac{3H^2(t)}{8\pi G_N}. \quad (1.5)$$

If we regard the spatial curvature term k/a^2 as an “effective energy density” that scales as a^{-2} , we can define the energy-fraction Ω ’s as follows:

$$\Omega_i \equiv \frac{\rho_i}{\rho_{\text{crit}}}, \quad (1.6)$$

where ρ_i is the energy density of the i -th component (baryons, dark matter, dark energy etc.); and

$$\Omega_k \equiv -\frac{k}{a^2 H^2}. \quad (1.7)$$

Some caution needs to be taken here. Even at the homogeneous level, the curvature component is not exactly an effective energy form that scales as a^{-2} . The curvature k also changes the geometry of the universe. We will explicitly show this when we calculate the angular diameter distance.

The first Friedmann equation now can be written as

$$\Omega_\Lambda + \Omega_c + \Omega_b + \Omega_r + \Omega_\nu + \Omega_k = 1, \quad (1.8)$$

where the subscripts “ Λ ”, “ c ”, “ b ”, “ r ”, “ ν ” stand for dark energy, cold dark matter, baryonic matter, radiation, and neutrinosⁱⁱ, respectively. We are often interested in the present values of these Ω ’s, denoted as $\Omega_{\Lambda 0}$, Ω_{c0} , Ω_{b0} , etc.

ⁱⁱHere and in what follows the word “neutrinos” generally refers to neutrinos and anti-neutrinos.

In a simple case where different components only interact through gravity, the scaling of each component as a function of a can be simply derived from energy conservation:

$$\dot{\rho}_i = -3\frac{\dot{a}}{a}(\rho_i + p_i) , \quad (1.9)$$

where $i = 1, 2, 3, \dots$ labels the components. The pressure p_i is related to the energy density ρ_i through equation of state, defined as

$$w_i \equiv \frac{p_i}{\rho_i} . \quad (1.10)$$

In the standard Λ CDM model, at the energy below BBN temperature (\sim MeV) and to sufficiently good accuracy, we have $w_\Lambda = -1$, $w_c = w_b = 0$, and $w_r = 1/3$. The neutrinos are a bit special. They are relativistic in early universe, but at $z \lesssim 1000$ they might become non-relativistic, depending on their mass. Neutrinos decouple from other components before the annihilation of electrons and positrons, which dumps entropy into radiation. A trivial calculation using entropy conservation and the current CMB temperature ($T_{\text{CMB}} = 2.72548 \pm 0.00057$ K [21]) gives the number density of relic neutrinos, which is about a hundred per cubic centimeter per flavor. Therefore the neutrino mass density is

$$\Omega_{\nu 0} h^2 \approx \frac{\sum_i m_{\nu i}}{100\text{eV}} , \quad (1.11)$$

where $m_{\nu i}$ is the mass of neutrino of i -th flavor. The current *laboratory* experimental upper bound on neutrino mass is about 2.3eV [22], which is not sufficient to tell whether neutrinos are relativistic today. Using CMB, LSS and HST data and assuming Λ CDM model, Komatsu *et. al.* [1] improved the constraint to $\sum_i m_{\nu i} < 0.44\text{eV}$. However, in this thesis we will not use this constraint, as we are studying models beyond Λ CDM. Learning about neutrinos in extended models is also an interesting subject, but will not be covered here. In what follows, unless otherwise specified, we will *assume* three generation of light neutrinos ($\sum_i m_{\nu i} \ll \text{eV}$), which means we can safely use $w_\nu = 1/3$ at redshift above a few hundreds where cosmic neutrinos are relevant for the expansion history.

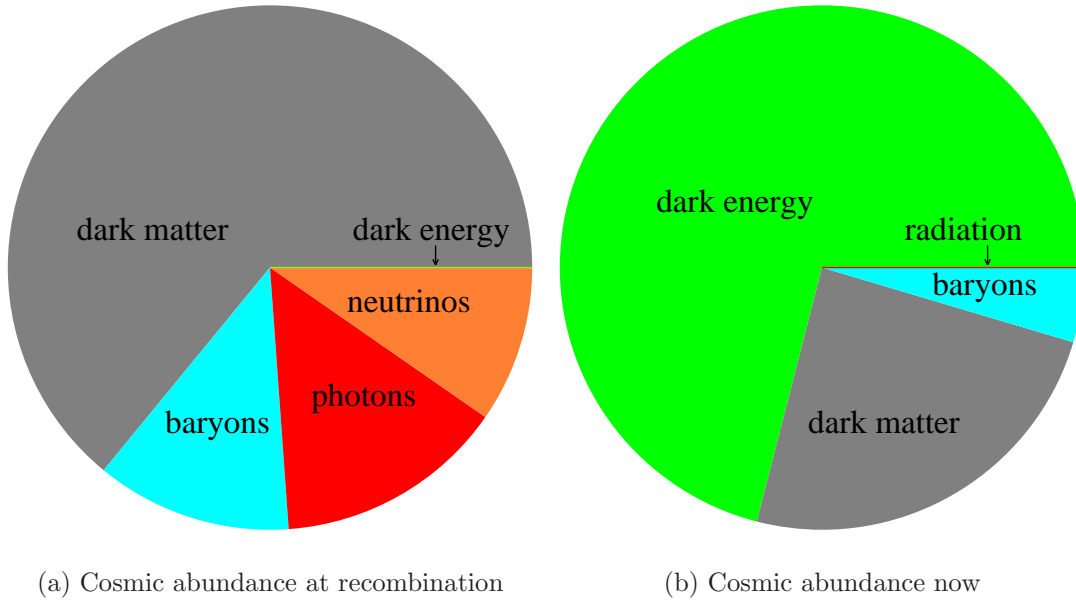


Figure 1.2: Cosmic abundance varies with time. This is assuming a Λ CDM model with three species of light neutrinos.

The parameter Ω_{k0} is predicted to be tiny in almost all inflationary theories. This prediction agrees well with CMB observations [1]. The standard 6-parameter Λ CDM model hence takes $\Omega_{k0} = 0$ as a theoretical prior.

Given all of these, the Hubble parameter and cosmic abundance can be calculated to arbitrary redshift $z < z_{\text{BBN}} \sim 10^9$. Figure 1.2 shows two examples. One is at the “recombination time” when photons decouple from Hydrogen in the universe at redshift about 1100 (this is when CMB forms), and another at present time (redshift zero).

The comoving distance from us to an object at redshift z is obtained by integrating the comoving line element $d\chi = dt/a(t)$ [12, 13, 14]:

$$\chi(z) = \int_0^z \frac{dz'}{H(z')}, \quad (1.12)$$

which is independent of the nature of dark energy and dark matter, and whether the universe is spatially flat or not.

The comoving angular diameter distance, however depends on the spatial curvature

[12, 13, 14]

$$r(z) = \begin{cases} \frac{\sin(\sqrt{k}\chi(z))}{\sqrt{k}} & , \text{ if } k > 0; \\ \chi(z) & , \text{ if } k = 0; \\ \frac{\sinh(\sqrt{-k}\chi(z))}{\sqrt{-k}} & , \text{ if } k < 0. \end{cases} \quad (1.13)$$

The luminosity distance d_L and physical angular diameter distance d_A are given by [12, 13, 14]

$$d_L(z) = (1+z)r(z) , \quad (1.14)$$

$$d_A(z) = \frac{1}{1+z}r(z) . \quad (1.15)$$

These formulas will be used in Chapter 2 where we consider observational constraints on dark energy. The supernova luminosity distances can be connected to their apparent brightness using the inverse square law. The angular diameter distances are related to BAO and weak lensing observables. In addition to those, the mass density fluctuations in the matter content (CDM and baryons) are important cosmological observables. For baryons and CDM, the sound speed is many orders of magnitude smaller than the speed of light. We can safely ignore the Jeans' length on cosmological scales. That means on these scales they are gravitational unstable. But on large scales we have to consider the Hubble expansion that slows down the gravitational collapse. The equation for mass density fluctuation of matter in an expanding universe is [12, 13, 14]

$$\ddot{\delta}_k + 2H\dot{\delta}_k - \frac{3H^2\Omega_m(z)}{2}\delta_k = 0 , \quad (1.16)$$

where $\delta_k(t)$ is the Fourier mode of the fractional mass density fluctuations to the linear order, with k being a comoving wavenumber, and

$$\Omega_m(z) \equiv \Omega_c(z) + \Omega_b(z) \quad (1.17)$$

is the total mass abundance of matter component. I have explicitly used $\Omega_m(z)$ to avoid possible confusion between Ω_m and $\Omega_{m0} \equiv \Omega_m|_{z=0}$.

Given Eq. (1.16), one needs to specify the initial conditions in order to evolve the mass density fluctuations. The “linear growth factor” $D(z)$ is introduced to eliminate the dependency on initial conditions. It is defined as

$$D(z) \equiv \frac{\delta_k(z)}{\delta_{k0}}, \quad (1.18)$$

where δ_{k0} is δ_k at redshift zero. In terms of $D(z)$ we can rewrite Eq. (1.16) as

$$\frac{d^2 D}{dz^2} + \frac{\epsilon - 1}{1 + z} \frac{dD}{dz} - \frac{3\Omega_m(z)}{2(1 + z)^2} D = 0. \quad (1.19)$$

Here we have used a very important ϵ parameter, which is defined as

$$\epsilon \equiv -\frac{\dot{H}}{H^2}. \quad (1.20)$$

It is not only useful for the late-universe cosmology. In next section we will see that ϵ is one of the key parameters that describe early-universe inflation.

Let us round up this section with a few useful formulas for Λ CDM model.

In the standard Λ CDM model, the low-redshift ($z \lesssim 10$) universe is dominated by non-relativistic matter and dark energy, ignoring the tiny contribution from radiation and light neutrinos, we have

$$\Omega_\Lambda = 1 - \Omega_m. \quad (1.21)$$

To very good accuracy, the low-redshift expansion history can be described by only two dimensionless parameters: h and Ω_{m0} . More explicitly, the Hubble expansion rate is given by

$$H(z) = 100h \text{ km s}^{-1} \text{ Mpc}^{-1} \sqrt{1 - \Omega_{m0} + \Omega_{m0}(1 + z)^3}. \quad (1.22)$$

The comoving angular diameter distance and linear growth factor are elliptic integrals that can not be written as elementary functions. But handy fitting formulas can be found for a particularly useful case covering the range $0.2 < \Omega_{m0} < 1$:

$$r(z) = \frac{6243.4h^{-1}}{\Omega_{m0}^{0.395}} \text{ Mpc} \quad (1.23)$$

$$\times \left\{ \frac{1}{(1 + 0.47\Omega_{m0})^{0.105}} - \frac{1}{(1 + z)^{0.185} [1 - \Omega_{m0} + 1.47\Omega_{m0}(1 + z)^3]^{0.105}} \right\}, \quad (1.24)$$

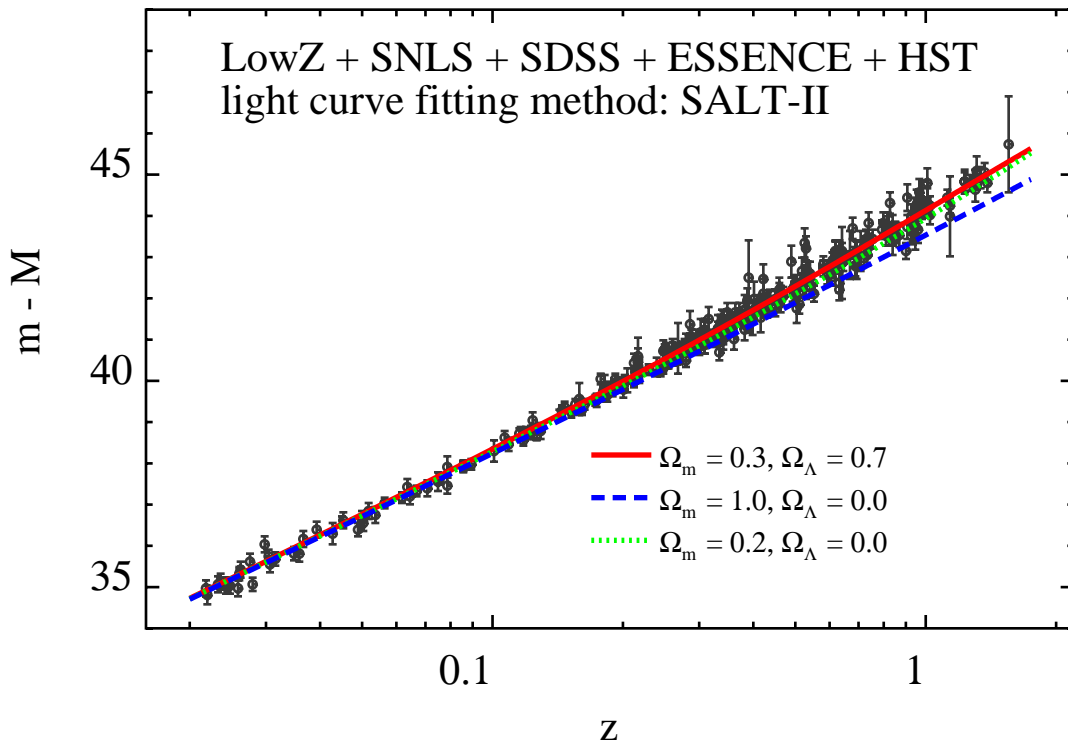


Figure 1.3: The updated Hubble diagram. Here m is the apparent magnitude, and M the absolute magnitude determined by χ^2 fitting, which cancels the dependency of $m - M$ on Hubble constant. See Chapter 2 for more details about the supernova data sets.

and

$$D(z) = \frac{\sqrt{\Omega_{m0}(1+z)^3 + 1 - \Omega_{m0}}}{(1+z)^{1/4}} \left[\frac{10 + \Omega_{m0}}{11\Omega_{m0}(1+z)^3 + 10(1 - \Omega_{m0})} \right]^{3/4}. \quad (1.25)$$

For both formulas the fitting error for a typical value $\Omega_{m0} \sim 0.3$ is about 0.1%.

The current observations of cosmic acceleration are consistent with a constant vacuum energy [1, 23, 24, 25, 26, 27]. At present the strongest evidence is from supernova observations. See Figure 1.3 for the updated Hubble diagram with 288 supernova samples [27].

1.4 Dark Energy: Beyond Λ

Because of the cosmological constant problem, many alternative dark energy models beyond Λ have been proposed (see [28] for a review). Observers often use the simplest phenomenological dark energy parametrization, namely a constant equation of state w_0 . Dark energy equation of state will be one of the major topics of this thesis. For readability I will omit the subscript Λ (or “DE”) for w when it does not cause confusion.

For constant $w = w_0$, the low-redshift expansion history is now determined by three parameters: h , Ω_{m0} and w_0 . The Hubble expansion rate in a flat FRW universe is now

$$H(z) = 100h \text{ km s}^{-1} \text{ Mpc}^{-1} \sqrt{(1 - \Omega_{m0})(1 + z)^{3(1+w_0)} + \Omega_{m0}(1 + z)^3}. \quad (1.26)$$

The comoving angular diameter distance and linear growth factor can be calculated using the general formulas given in the last section. Here I give the fitting formulas for another often useful case, with $|1 + w_0| < 0.2$ and $\Omega_{m0} > 0.2$:

$$r(z) = \frac{5995.8h^{-1}}{\Omega_{m0}^{0.255-0.19w_0-0.05w_0^2}} \text{ Mpc} \quad (1.27)$$

$$\times \left\{ \frac{1}{\left[\Omega_{m0} + \frac{1-\Omega_{m0}}{2(1-6w_0)(0.245+0.19w_0+0.05w_0^2)} \right]^{0.245+0.19w_0+0.05w_0^2}} - \frac{1}{\sqrt{1+z} \left[\Omega_{m0} + \frac{(1-\Omega_{m0})(1+z)^{3w_0}}{2(1-6w_0)(0.245+0.19w_0+0.05w_0^2)} \right]^{0.245+0.19w_0+0.05w_0^2}} \right\},$$

and

$$D(z) = \frac{\sqrt{\Omega_{m0} + (1 - \Omega_{m0})(1 + z)^{3w_0}}}{(1 + z)} \quad (1.28)$$

$$\times \left[\frac{2(1 - 2w_0)(2 - 3w_0)(1 - \Omega_{m0}) - w_0(5 - 6w_0)(4 + w_0)\Omega_{m0}}{2(1 - 2w_0)(2 - 3w_0)(1 - \Omega_{m0})(1 + z)^{3w_0} - w_0(5 - 6w_0)(4 + w_0)\Omega_{m0}} \right]^{1+\frac{w_0}{4}}.$$

An extension of the constant w dark energy model is the following popular linear expansion for dark energy EOS:

$$w = w_0 + w_a(1 - a). \quad (1.29)$$

It is a model-independent parametrization that should work well at very low redshift $z \ll 1$. At higher redshift, it is not likely to be accurate, as no physical model has predicted such a linear $w(a)$ formula. In contrast, even at present we already have plenty of data at $z \sim 1$, where the linear formula of w is not an ideal model to be compared with.

Without a physical model, there is no “best parametrization”. A linear function of a is as good as a linear function of a^2 , etc. Our approach laid out in Chapter 2 is then to start from a physical model of dark energy, and parameterize w with physical parameters. We will focus on one of the most popular dark energy models – the quintessence model, where a scalar field ϕ minimally couples to gravity. The Lagrangian density of a quintessence field is

$$\mathcal{L} = \frac{1}{2} \partial_\mu \phi \partial^\mu \phi - V(\phi) . \quad (1.30)$$

The potential $V(\phi)$, which depends on the underlying physics of the quintessence field, is an unknown function. The subhorizon perturbation of ϕ obeys

$$\ddot{\delta\phi}_k + \left(k^2 + \frac{d^2V}{d\phi^2}\right) \delta\phi_k = 0. \quad (1.31)$$

For a light field with $|d^2V/d\phi^2| \lesssim H^2$, the subhorizon dark energy perturbations do not grow. Assuming no significant primordial quintessence perturbations, we can approximately treat quintessential dark energy as a homogeneous fluid with equation of state

$$w_\phi = \frac{\frac{1}{2}\dot{\phi}^2 - V(\phi)}{\frac{1}{2}\dot{\phi}^2 + V(\phi)} . \quad (1.32)$$

To explicitly write w_ϕ as a function of redshift z or scale factor a , one needs to know the potential $V(\phi)$ and initial field momentum $\dot{\phi}_{\text{ini}}$. In fact, the specific form of the potential is not important. We will use a few physical properties of the potential – the slope of $\ln V$ at some pivot, the curvature (second derivative) of $\ln V$, and the field momentum – to characterize the dynamics of the quintessence field. Using this quintessential dark energy parametrization and the observational data, we are able to study the generic properties of quintessence potentials. The technical details will be presented in Chapter 2.

1.5 Early-universe Inflation

In the previous section we briefly reviewed the late-universe cosmic acceleration. We now tune the clock back to 14 billions years ago, where early-universe inflation took place. In this section we discuss the dynamics of inflaton and the associated metric perturbations. This is the background for the material in Chapters 3-6.

The first model of inflation, which is called “old inflation”, was proposed by Starobinsky [29], Guth [30] and Sato [31]. In the “old inflationary” model, the true-vacuum bubbles appear via quantum tunneling in a false-vacuum-dominated exponentially expanding universe. The problem with this model, soon recognized by Guth himself and others, is that the nucleation rate of true vacuum bubbles cannot be too large, otherwise the total number of expansion e-folds (defined as the increment of $\ln a$) will be insufficient to solve the horizon problem [12, 13, 14], and cannot be too small, otherwise the bubbles do not coalesce to generate radiation.

Soon after the unsuccessful attempt, the second generation of inflation models were proposed by Linde *et. al.* [32] and Albrecht *et. al.* [33]. The idea of a slow-rolling scalar field on a flat potential was proposed. To obtain the flat potential in the so-called “new inflation” model, Linde first assumed the scalar field was in thermal equilibrium, and the flatness arose from the thermal correction of the effective potential. He soon realized that the hypothesis of thermal equilibrium was unnecessary. Inflation can be realized “chaotically” with very simple potentials like $V = \frac{1}{2}m^2\phi^2$. The idea of chaotic inflation is that although classically a displaced field will roll downhill toward the potential minimum, the quantum fluctuations can occasionally bring the field uphill. The small probability of such uphill quantum diffusion is compensated by the much faster exponential expansion of the physical volume. Here we have made an implicit assumption that equal statistical probabilities should be applied on equal physical volumes (not comoving volumes). These probabilities are estimated in Linde’s article “eternally existing self-reproducing chaotic inflationary universe” [34]. The two popular names “eternal inflation” and “chaotic

inflation” are still being used today. The chaotic inflation models belong to a class called large field models, where the field needs to take values larger than the Planck Mass. It remains one of the most popular inflation models, and is the observational target of many CMB experiments.

In the late 90s and early 00s, the CMB observations confirmed the predictions of inflation [35, 36, 37, 38]. And the supernova observations revealed that our universe is now again inflating [23, 24]. The observational evidence for inflation stimulated a further round of theorizing adding to the already exotic ideas in the zoo of inflation models: natural inflation [39, 40], brane inflation [41], moduli inflation [42, 43, 44], and more. See recent reviews [45, 46, 47] for the zoology of existing inflation models.

In the rest part of this section I will briefly summarize how the primordial metric perturbations from inflation are calculated.

The FRW metric (1.1) with $k = 0$ (predicted by inflation, assuming no fine-tuning) will be used. Since we are studying the origin of inhomogeneities, we also have to perturb the FRW metric. Let us first consider scalar metric perturbations. The perturbed metric in the longitudinal gauge [12, 13, 14] is

$$ds^2 = a(\tau)^2 \left[(1 + 2\Phi) d\tau^2 - (1 - 2\Psi) \delta_{ij} dx^i dx^j \right] , \quad (1.33)$$

where we have introduced the conformal time

$$\tau \equiv \int \frac{dt}{a(t)} . \quad (1.34)$$

The conformal Hubble parameter is defined as

$$\mathcal{H} \equiv \frac{a'}{a} = \dot{a} . \quad (1.35)$$

Here and in what follows I use a prime to denote the derivative with respect to conformal time.

The scalar metric perturbations Φ and Ψ are called Bardeen potentials. Physically Φ corresponds to the Newtonian gravitational potential. If the early universe is dominated by one or more scalar fields, the first order perturbed energy momentum tensor is

diagonal, and we can conclude that the two Bardeen potentials are equal. This can be verified by writing down the perturbed Einstein equations to the first order. I will skip this standard exercise, which can be found in Refs. [12, 13, 14].

Now let us assume that inflation is driven by only one scalar field ϕ . In the single-field case, the field perturbation $\delta\phi$ and metric perturbation Φ are related through Einstein equations. There is only one physical scalar perturbation. This can be explicitly shown using the Sasaki-Mukhanov variable [13, 14]

$$\mathcal{R} \equiv \frac{\mathcal{H}}{\phi'} \delta\phi + \Phi . \quad (1.36)$$

The evolution equation for a Fourier mode of \mathcal{R} , derived from the perturbed Einstein equations and the field EOM, can be written as [13, 14]

$$\mathcal{R}_k'' + \frac{2z'}{z} \mathcal{R}_k' + k^2 \mathcal{R}_k = 0 , \quad (1.37)$$

where k is the comoving wavenumber, and z is defined as

$$z \equiv \frac{a\phi'}{\mathcal{H}} . \quad (1.38)$$

When the physical mode is well inside the horizon ($k/a \gg H$), the vacuum mode function for $\delta\phi$ has the standard Minkowski-spacetime form:

$$\delta\phi_k |_{k \gg aH} = \frac{1}{\sqrt{a^3}} \frac{1}{\sqrt{2k/a}} \exp\left(-i \int \frac{k}{a} dt\right) . \quad (1.39)$$

During inflation where \mathcal{H}/ϕ' does not change sign, the mapping from $\delta\phi$ to \mathcal{R} is straightforward:

$$k^{3/2} \mathcal{R}_k |_{k \gg aH} = \frac{k/a}{2\sqrt{\epsilon} M_{\text{p}}} \exp\left(-i \int \frac{k}{a} dt\right) . \quad (1.40)$$

I have explicitly written everything in physical units. During inflation the ϵ parameter defined in (1.20) satisfies

$$0 < \epsilon < 1 . \quad (1.41)$$

Note that $k^{3/2} \mathcal{R}_k$ is physically normalized (independent of the normalization of scale factor a), but \mathcal{R}_k is not. One should use Eq. (1.40) as the initial condition, and evolve

$k^{3/2}\mathcal{R}_k$ with Eq. (1.37). If $z \propto \sqrt{\epsilon}a$ monotonically increases, $k^{3/2}\mathcal{R}_k$ converges to a constant after the mode exits the horizon ($k/a < H$). One can numerically evolve $k^{3/2}\mathcal{R}_k$ until it converges. The primordial scalar power spectrum then can be calculated through

$$\mathcal{P}_S = \frac{1}{2\pi^2} \left| k^{3/2}\mathcal{R}_k \right|_{k \ll aH}^2, \quad (1.42)$$

which is also physically normalized.

For tensor perturbations the analysis is similar. Here we directly give the results. The equation of motion for the amplitude of free gravitational waves is [13, 14]

$$h_k'' + 2\mathcal{H}h_k' + k^2h_k = 0. \quad (1.43)$$

The initial condition is

$$k^{3/2}h_k \Big|_{k \gg aH} = \frac{\sqrt{2}k/a}{M_p} \exp\left(-i \int \frac{k}{a} dt\right). \quad (1.44)$$

And the primordial tensor power spectrum

$$\mathcal{P}_T = \frac{1}{\pi^2} \left| k^{3/2}h_k \right|_{k \ll aH}^2, \quad (1.45)$$

Eqs (1.37-1.42) and Eqs (1.43-1.45) provide a complete scheme to calculate the primordial scalar and tensor perturbations in arbitrary single field inflation models.

For slow-roll inflation, approximate solutions of \mathcal{P}_S and \mathcal{P}_T can be found [12, 13, 14]:

$$\mathcal{P}_S \approx \frac{H^2}{8\pi^2 M_p^2 \epsilon} \Big|_{k=aH}, \quad (1.46)$$

$$\mathcal{P}_T \approx \frac{2H^2}{\pi^2 M_p^2} \Big|_{k=aH}. \quad (1.47)$$

These are zeroth order approximations. In what follows I will derive more accurate formulas with the first order corrections included.

As the universe exponentially expands, the integral $\int^{+\infty} dt/a$ converges. We can choose the conformal time τ to be $\tau(t) = \int_{+\infty}^t d\tilde{t}/a(\tilde{t})$, which implies $-\infty < \tau < 0$. A special but also very useful case is when $\sqrt{\epsilon}a$ is a power-law function of τ .

$$\sqrt{\epsilon}a = C(-\tau)^{-1-\delta}, \quad (1.48)$$

where C and δ are constants. Given Eq. (1.48), the differential equation (1.37) becomes

$$R_k'' - \frac{2(1+\delta)}{\tau} R_k' + k^2 R_k = 0 . \quad (1.49)$$

The generic solution for this Bessel-type differential equation is

$$R_k = C_1 (-k\tau)^{3/2+\delta} H_{3/2+\delta}^{(1)}(-k\tau) + C_2 (-k\tau)^{3/2+\delta} H_{3/2+\delta}^{(2)}(-k\tau) , \quad (1.50)$$

where $H^{(1,2)}$ are the first kind and second kind Hankel functions. Matching the initial condition (1.40) we find

$$C_1 = 0 , \quad (1.51)$$

$$C_2 = \sqrt{\frac{\pi}{8}} \frac{k^{-\delta}}{M_p C} . \quad (1.52)$$

The primordial scalar power spectrum is then

$$\mathcal{P}_S = \frac{k^{-2\delta}}{8\pi^2 M_p^2 C^2} \left(\frac{2^\delta (1+2\delta) \Gamma(\frac{1}{2})}{\cos(\delta\pi) \Gamma(\frac{1}{2}-\delta)} \right)^2 , \quad (1.53)$$

or written in another form

$$\mathcal{P}_S = \frac{H^2}{8\pi^2 M_p^2 \epsilon} \frac{(k\tau)^{-2\delta}}{(\mathcal{H}\tau)^2} \left(\frac{2^\delta (1+2\delta) \Gamma(\frac{1}{2})}{\cos(\delta\pi) \Gamma(\frac{1}{2}-\delta)} \right)^2 . \quad (1.54)$$

So far no approximation has been made, given that the assumption (1.48) holds.

For slow-roll inflation where

$$0 < \epsilon \ll 1 , \quad (1.55)$$

and

$$\left| \frac{d \ln \epsilon}{d \ln a} \right| \ll 1 , \quad (1.56)$$

it is easy to verify that

$$\delta \approx \epsilon + \frac{1}{2} \frac{d \ln \epsilon}{d \ln a} . \quad (1.57)$$

The spectral index can be directly read from the solution (1.53):

$$n_s - 1 \equiv \frac{d \ln \mathcal{P}_S}{d \ln k} = -2\delta \approx -2\epsilon - \frac{d \ln \epsilon}{d \ln a} , \quad (1.58)$$

the standard textbook result. If $d \ln \epsilon / d \ln a$ varies too much within one e-fold, the assumption (1.48) may not hold. But considerable $d \ln \epsilon / d \ln a$ variation over a few e-folds is compatible with the assumption (1.48). That leads to the running of spectral index

$$n_{\text{run}} \equiv \frac{d^2 \ln \mathcal{P}_S}{(d \ln k)^2} \approx -2\epsilon \frac{d \ln \epsilon}{d \ln a} - \frac{d^2 \ln \epsilon}{(d \ln a)^2}. \quad (1.59)$$

In slow-roll scenario we have $\mathcal{H}\tau \approx 1/(1 - \epsilon)$. The first order approximation of solution (1.54) is

$$\mathcal{P}_S \approx \frac{H^2}{8\pi^2 M_{\text{p}}^2 \epsilon} [1 - 2\epsilon + 2(2 - \gamma - \ln 2)\delta] \Big|_{k=aH}, \quad (1.60)$$

where $\gamma = 0.5772\dots$ is the Euler-Mascheroni Constant. Here we have used $\frac{\Gamma'(1/2)}{\Gamma(1/2)} = -\gamma - 2 \ln 2$.

The procedure to find the approximate solution for tensor spectrum is exactly the same. Here we directly give the result:

$$\mathcal{P}_T \approx \frac{2H^2}{\pi^2 M_{\text{p}}^2} [1 - 2(\ln 2 + \gamma - 1)\epsilon] \Big|_{k=aH}, \quad (1.61)$$

and the spectral index

$$n_t \equiv \frac{d \ln \mathcal{P}_T}{d \ln k} \approx -2\epsilon. \quad (1.62)$$

The first-order slow-roll formulas (1.60) and (1.61) were first derived by Stewart and Lyth [48] in 1993 with a slightly different method.

In Figure 1.4 we compare the slow-roll approximations (1.60) and (1.61) with the full numerical solutions. We find the scalar power spectrum has large responses to the scale-dependence of ϵ . This is due to the denominator ϵ in Eq. (1.60). In contrast the tensor power spectrum can be well fit by a power-law function. We will consider this generic feature when we parameterize \mathcal{P}_S and \mathcal{P}_T in Chapter 3. Another more extreme example is shown in Figure 3.1 in Chapter 3, where slow-roll condition is temporarily broken. The glitch in the inflaton potential could be caused by a phase transition in a non-inflaton field, although in Chapter 5 we point out that phase transition during inflation in some cases should be treated more carefully.

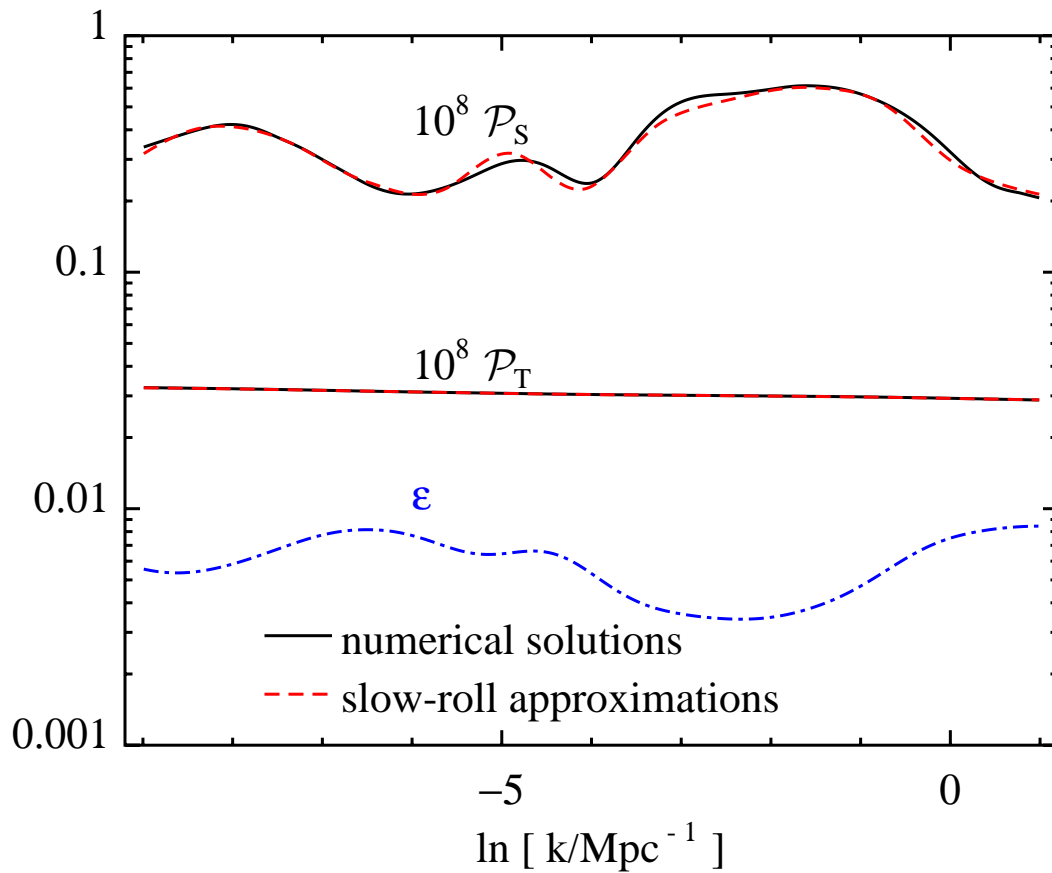


Figure 1.4: When $\epsilon(k) \equiv \epsilon|_{k=aH}$ trajectory has complicated structures, the slow-roll solution (1.60) for scalar power spectrum deviate from the full numerical solution, while the slow-roll approximation (1.61) for tensor power spectrum remains a good fit.

The tensor to scalar ratio at some k_{pivot} is defined as

$$r \equiv \frac{\mathcal{P}_S}{\mathcal{P}_T} \Big|_{k=k_{\text{pivot}}} \approx 16\epsilon \approx -8n_t . \quad (1.63)$$

The relation $r \approx -8n_t$ is the consistency relation for single-field slow-roll models.

Motivated by the slow-roll single-field inflation models, observers often use the following parametrizations for primordial power spectra

$$\mathcal{P}_S = A_S \left(\frac{k}{k_{\text{pivot}}} \right)^{n_s - 1 + \frac{1}{2}n_{\text{run}} \ln(k/k_{\text{pivot}})} , \quad (1.64)$$

$$\mathcal{P}_T = r A_S \left(\frac{k}{k_{\text{pivot}}} \right)^{n_t} . \quad (1.65)$$

Oft-chosen pivots are comoving wavenumber 0.05Mpc^{-1} and 0.002Mpc^{-1} . In many works, including ours in Chapter 3, the pivot for the scalar and that for the tensor are chosen both to be 0.002Mpc^{-1} for simplicity, although it might be more reasonable to use 0.05Mpc^{-1} for the scalar and 0.002Mpc^{-1} for the tensor. The priors $n_{\text{run}} = 0$, $n_t = 0$ or $n_t = -r/8$ are often applied to exclude the poorly measured parameters, or, in the language of Bayesian statistics, to discard bad models. In the standard six-parameter ΛCDM parametrization, the tensor spectrum is also ignored. The remaining six parameters and the current observational constraints on them are listed in Table 1.2. These constraints are derived in Chapter 2 using CMB + SN + LSS + WL + Ly α .

The parameter θ defined in Table 1.2 should not be confused with the comoving coordinate in the metric form (1.1). It is often measured with percent. So $\theta = 1.04$ corresponds to an angle 0.0104 radian. We will stick to this convention throughout this thesis.

In addition to the six standard parameters, a few derived parameters are widely used in the literature. They are listed in Table 1.3.

Other slow-roll parameters directly related to the potential $V(\phi)$ are defined by

$$\epsilon_V \equiv \frac{M_{\text{p}}^2}{2} \left(\frac{dV/d\phi}{V} \right)^2 , \quad (1.66)$$

$$\eta_V \equiv M_{\text{p}}^2 \frac{d^2V/d\phi^2}{V} . \quad (1.67)$$

Table 1.2: Six-parameter Λ CDM model; The current constraints (68.3% CL) are obtained using CMB + SN + LSS + WL + Ly α . See Chapter 2 for more details about the data sets and how these constraints are derived. The cold dark matter and baryonic matter density are normalized to $\rho_{\text{crit}}/h^2 \approx 11.2$ proton mass per cubic meter. The primordial scalar power spectrum is given by Eq. (1.64) with $k_{\text{pivot}} = 0.002\text{Mpc}^{-1}$ and $n_{\text{run}} = 0$. The primordial tensor spectrum is assumed to be negligible ($r = 0$).

parameter	definition	constraints
$\Omega_{\text{c}0}h^2$	current physical density of cold dark matter	$0.02246^{+0.00042}_{-0.00043}$
$\Omega_{\text{b}0}h^2$	current physical density of baryonic matter	$0.1173^{+0.0020}_{-0.0019}$
θ	the angle subtended by sound horizon on CMB sky	$0.01042^{+0.00002}_{-0.00002}$
τ_{re}	the reionization optical depth	$0.089^{+0.014}_{-0.013}$
$\ln(10^{10}A_s)$	logarithm of the amplitude of primordial scalar perturbations	$3.237^{+0.031}_{-0.032}$
n_s	the index of primordial scalar power spectrum	$0.959^{+0.010}_{-0.011}$

Table 1.3: Definition of derived parameters.

parameter	definition
H_0	the Hubble constant (in unit $\text{km s}^{-1}\text{Mpc}^{-1}$)
$\Omega_{\text{m}0}$	current energy-fraction of non-relativistic matter
$\Omega_{\Lambda 0}$	current energy-fraction of dark energy
z_{re}	the redshift where reionization happens
σ_8	current r.m.s. mass fluctuation on $8h^{-1}$ Mpc scale

Table 1.4: Inflation Models

class	definition	typical example
small-field	$\eta_V < 0$	$V = V_0 (1 - e^{- \phi })$
large-field	$0 < \eta_V < 2\epsilon_V$	$V = \frac{1}{2}m^2\phi^2; V = \frac{1}{4}\lambda\phi^4$
hybrid	$\eta_V > 2\epsilon_V$	$V = V_0 + \frac{1}{2}m^2\phi^2$

Assuming the higher order derivatives can be ignored, the potential parameters ϵ_V and η_V can be connected to the geometrical acceleration parameter ϵ through

$$\epsilon \approx \epsilon_V, \quad (1.68)$$

$$\frac{d \ln \epsilon}{d \ln a} \approx 4\epsilon_V - 2\eta_V. \quad (1.69)$$

The slow-roll single-field inflation models can be classified into “large field”, “small field” and “hybrid” ones [49, 50, 51]. The large field models are represented by the most popular chaotic inflation models, where the inflaton starts from a large initial value and rolls down toward the potential minimum at small ϕ . Typically in this class of models, the ϵ parameter is of order 0.01. The variation of field value during the last 50-60 e-folds of inflation is a number of Planck masses. Hybrid inflation models are usually constructed by introducing a second scalar field. The auxiliary field serves as a cosmological constant during inflation. As the inflaton rolls down, phase transition in the second field occurs and inflation ends. The small field models are mostly string theory inspired, such as Kähler moduli inflation [52]. The quantitative description of this classification scheme is summarized in Table 1.4.

The slow-roll assumptions lead to predictions that agree well with current data. However, forthcoming data should allow us to measure the primordial scalar and tensor power spectra much more accurately. In order to address possible deviations from slow-roll single-field inflation models, we would like to have more generic parametrization beyond the (1.64 - 1.65) ansatz. This is the topic discussed in Chapter 3, where the basic ap-

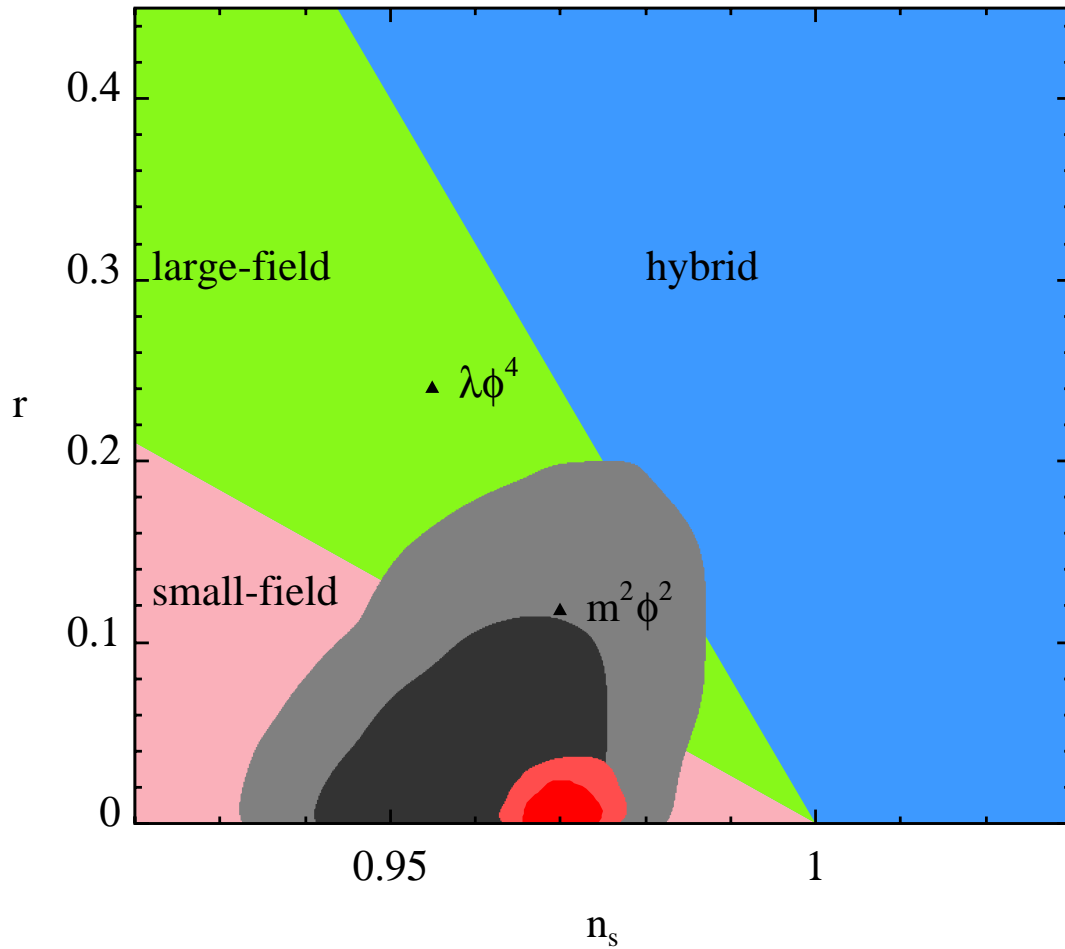


Figure 1.5: The gray contours are the current 68.3% and 95.4% constraints on inflation models. The red contours are constraints using simulated Planck satellite CMB data and EUCLID weak lensing data, for a fiducial $r = 0$ model. See Chapter 2 for the details about the current and forecast data sets.

proach is to use Eqs (1.37-1.42) and Eqs (1.43-1.45) to numerically solve \mathcal{P}_S and \mathcal{P}_T from more generic ϵ trajectories. Numerically calculated power spectra are then used to confront the current and forecast data.

1.6 Parametric Resonance, Preheating, and Particle Production

Another interesting problem associated with scalar field inflation is particle production, either perturbatively or non-perturbatively. The nonperturbative decay of the inflaton into other fields, if it happens at the end of inflation, is called preheating. Preheating is one of the crucial processes that connect the cold, inflaton-dominated universe after inflation to the hot, thermalized universe before BBN. Because preheating typically happens on comoving scales about a centimeter, it was believed that preheating does not produce observable signatures on cosmological scales. We study a classical preheating model in Chapter 4 with a new accurate lattice code, and find that adiabatic comoving curvature perturbations on cosmological scales can be produced, at least in the particular model we have studied. The initial conditions are prepared by inflation, and then amplified by parametric resonance. This is similar to modulated reheating models, but realized in a nonlinear process that had not been studied before.

A few other topics related to parametric resonance are studied in this thesis. In Chapter 6 we study a new preheating model in the context of Roulette Inflation, a string theory motivated inflation model. We find the self-coupling of the inflaton leads to violent preheating. In Chapter 5 we study particle production *during* inflation through a similar mechanism. The usual belief is that any observable signature produced by a burst of particles production, which typically happens at scales much smaller than the Hubble horizon scale, will be damped by exponential expansion. We find that this is not the case. The rescattering of short-wavelength modes allows an energy cascade to

long-wavelength modes, and this process continues until all the relevant modes exit the horizon. The consequence is that large non-Gaussianity will be produced. And if the coupling is strong enough, a big bump in the primordial scalar power spectrum will be produced.

At the end of inflation, the inflaton oscillates around its potential minimum. The scale factor grows as $a \propto t^{1/\langle\epsilon\rangle}$, where $\langle\epsilon\rangle$ is defined as

$$\langle\epsilon\rangle = \lim_{T \rightarrow +\infty} \frac{1}{T} \int_0^T -\frac{\dot{H}}{H^2} dt . \quad (1.70)$$

For a potential $V \propto \phi^n$, and when the oscillating period is much shorter than the Hubble time, $\langle\epsilon\rangle$ can be trivially calculated

$$\langle\epsilon\rangle = \frac{3 \int_0^{\phi_{\max}} \left[1 - \left(\frac{\phi}{\phi_{\max}}\right)^n\right]^{1/2} d\phi}{\int_0^{\phi_{\max}} \left[1 - \left(\frac{\phi}{\phi_{\max}}\right)^n\right]^{-1/2} d\phi} = \frac{3n}{n+2} . \quad (1.71)$$

It follows that the effective equation of state $\langle w \rangle \equiv \frac{2}{3}\langle\epsilon\rangle - 1 = \frac{n-2}{n+2}$.

For a quadratic potential $V = \frac{1}{2}m^2\phi^2$, the dynamics of expansion is the same as that for a dust-dominated universe. However, if we consider structure formation, the coherent oscillating inflaton condensate behaves differently from dust. In a dust dominated universe, structure grows on all subhorizon scales. But if the universe is dominated by a coherent oscillating inflaton, the density perturbations do not grow on most scales. ⁱⁱⁱ

For a quartic potential $V = \frac{\lambda}{4}\phi^4$, the effective EOS is 1/3. The dynamics of background is like that in a radiation-dominated universe, a result that will be used in Chapter 4.

If the inflaton couples to a light field χ , the effective mass m_χ will be modulated by the coherent oscillations of the inflaton. The dynamics of perturbation in the χ field will be described by the theory of parametric resonance, a theory that studies Hill's equation. An introduction to the Hill's equation can be found in [54] and references therein. Here I would like to give a brief summary.

ⁱⁱⁱIt has recently been claimed that non-linear structure will form on very small scales for a $m^2\phi^2$ model without any coupling to other field [53].

Consider an oscillator χ whose mass $M(t)$ is modulated by an external periodic source. The equation of motion of χ is

$$\frac{d\chi^2}{dt^2} + M^2(t)\chi = 0 , \quad (1.72)$$

with

$$M^2(t) = \omega^2 \sum_{n=-\infty}^{+\infty} c_n e^{in\omega t} . \quad (1.73)$$

where $c_{*-n} = c_n$. Thus, $M^2(t)$ is a periodic real function with period $2\pi/\omega$: this is Hill's equation.

A generic solution is

$$\chi(t) = e^{i\nu\omega t} \sum_{n=-\infty}^{+\infty} \chi_n e^{in\omega t} , \quad (1.74)$$

where $i\nu$ is a constant called the Floquet exponent. For our purpose, the exact full solution (1.74) is not important. We are interested in the Floquet exponent that is related to exponential burst of particles in early universe. In the rest part of this section I will introduce two methods to calculate the Floquet exponent. They will be used in Chapter 6 and Chapter 4, respectively.

Plugging (1.74) and (1.73) into (1.72), we obtain

$$\sum_{k=-\infty}^{+\infty} B_{nk} \chi_k = 0, \quad (1.75)$$

where

$$B_{nk}(\nu) = \frac{c_{n-k} - \delta_{nk}(\nu + n)^2}{c_0 - (\nu + n)^2} . \quad (1.76)$$

The existence of a solution for (1.75) requires

$$\Delta(\nu) \equiv \det |B_{nk}(\nu)| = 0 . \quad (1.77)$$

By comparing the poles, and using the theorem that a bounded analytic function on the complex plane must be a constant, one can find

$$\Delta(\nu) = 1 + \frac{1 - \Delta(0)}{2 \cot(\pi\sqrt{c_0})} [\cot(\pi(\nu - \sqrt{c_0})) - \cot(\pi(\nu + \sqrt{c_0}))] . \quad (1.78)$$

Eq. (1.77) is then equivalent to

$$\sin^2(\nu\pi) = \Delta(0) \sin^2(\sqrt{c_0}\pi) . \quad (1.79)$$

Given arbitrary $M^2(t)$, we can in principle calculate $\Delta(0)$, and solve for ν . The imaginary part of ν , if nonzero, leads to exponential growth of χ , which often corresponds to particle production or instability of some structure.

From numerical aspect, the calculation of the determinant of a large matrix is not very efficient. If the structure of $M^2(t)$ is complicated, it is usually easier to numerically solve the original differential equation (1.72), and extract the imaginary part of ν by taking $t \rightarrow \infty$. The brute-force integration method is used in Chapter 6, where $M^2(t)$ with a sharp feature can not be approximated by the sum of a few harmonic oscillators.

For a simple inflaton potentials such as $V = \frac{1}{2}m^2\phi^2$ or $V = \frac{\lambda}{4}\phi^4$, the modulated mass $M^2(t)$ often contains very few numbers of harmonic oscillators. In the case of a single harmonic driver, the Hill's equation becomes Mathieu equation, which is often written as

$$\frac{d^2\chi}{dt^2} + (\lambda - 2q \cos 2t)\chi = 0. \quad (1.80)$$

An iterative algorithm can be used to calculate the Floquet exponent for the Mathieu equation [54]. But it is difficult to extend this algorithm to multiple-frequency case. Here I propose a new algorithm, which is neater, more computer-friendly and can be easily extended to multiple-frequency cases. For readability, here I only discuss its application to the Mathieu equation. In Chapter 4 I will use this method for a multiple-frequency case – the $V = \frac{\lambda}{4}\phi^4 + \frac{1}{2}g^2\phi^2\chi^2$ preheating model.

The Mathieu equation is equivalent to Hill's equation with $c_2 = c_3 = \dots = 0$, for which I define a $(2n + 1) \times (2n + 1)$ matrix

$$Q_{ij}^{(n)}(x) = \begin{cases} x & , \text{ if } i = j = \pm n \\ B_{ij}(0) & , \text{ else} \end{cases} \quad (1.81)$$

Here $-n \leq i, j \leq n$. By definition we have

$$\Delta(0) = \lim_{n \rightarrow +\infty} \det |Q^{(n)}(1)|. \quad (1.82)$$

For $n > 1$, the determinant of $Q_{ij}^{(n)}(x)$ satisfies

$$\det |Q^{(n)}(x)| = x^2 \det \left| Q^{(n-1)} \left(1 - \frac{c_1^2}{(c_0 - n^2)(c_0 - (n-1)^2)x} \right) \right|, \quad (1.83)$$

Using the above formulas and

$$\det |Q^{(1)}(x)| = x^2 \left[1 - \frac{2c_1^2}{c_0(c_0 - 1)x} \right], \quad (1.84)$$

we can iteratively calculate the Floquet exponent for arbitrary c_0, c_1 without solving any differential equations. Figure 1.6 shows the Floquet exponent for the Mathieu equation calculated with this efficient algorithm. The Floquet exponents for about 10^6 points on the λ - q plane are calculated on a desktop computer within a second. For the parameter space shown in Figure 1.6 the Floquet exponent well converge (accuracy ~ 0.01) after 20 iterations.

1.7 Markov Chain Monte Carlo Simulations

In cosmology, the minimal Λ CDM model contains six parameters, and the number of parameters increases as one adds complexity to the model. Markov Chain Monte Carlo (MCMC) simulations, which are proven as a method to do statistics in high-dimensional parameter spaces, have been widely used in cosmology (see Chapters 2, 3, 5, and 7).

Suppose we are given n parameters q_1, q_2, \dots, q_n , and the likelihood (probability density) function $\mathcal{L}(\mathbf{p})$, where \mathbf{p} is a vector in the n dimensional parameter space \mathfrak{R}^n . The idea of MCMC is to draw many “representative random samples” of \mathbf{p} , and use the samples to do *low-dimensional statistics*. As an example, I will introduce the simplest MCMC method – the Metropolis-Hasting algorithm.

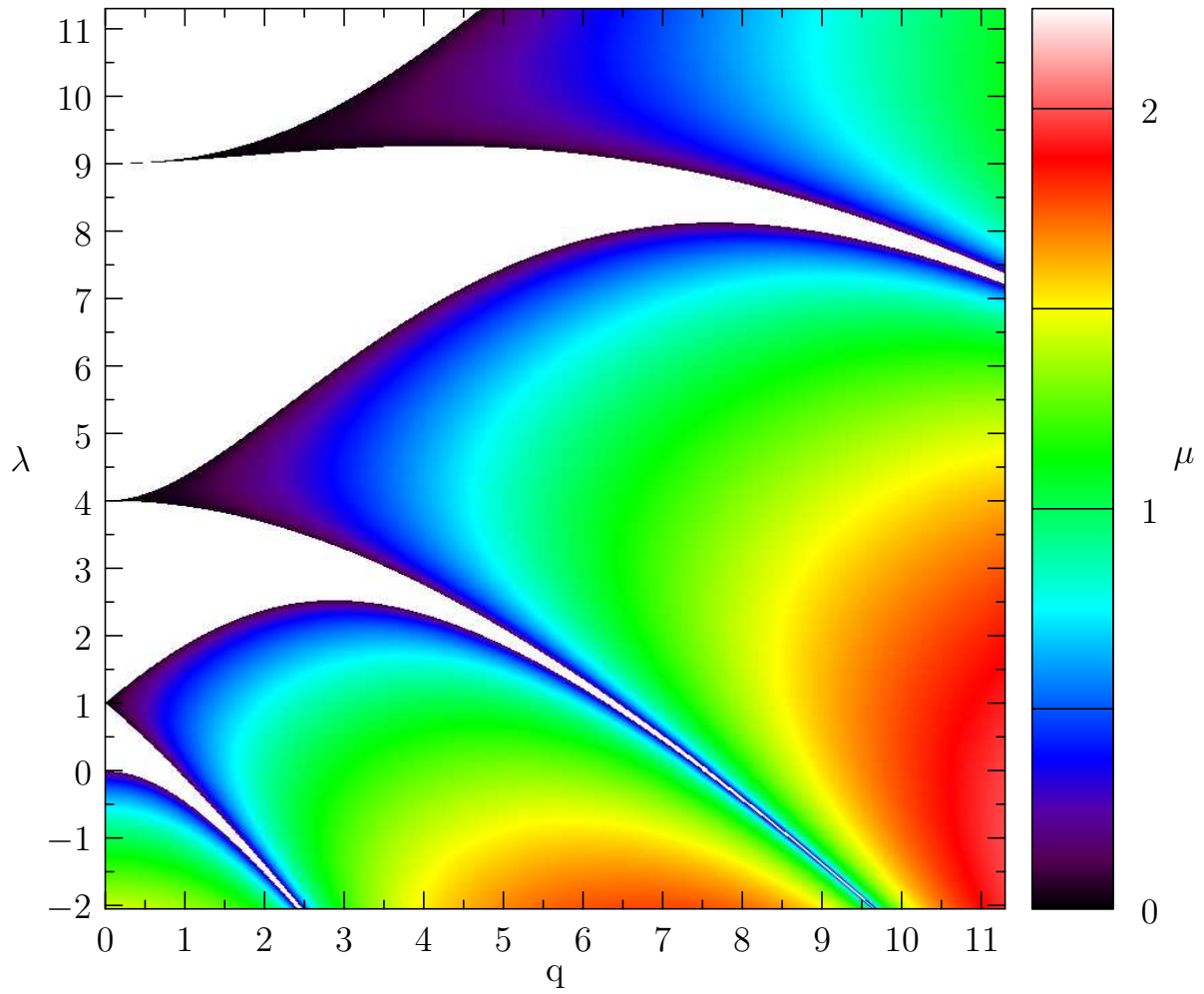


Figure 1.6: The real part of the Floquet exponent for the Mathieu equation $\ddot{\chi} + (\lambda - 2q \cos 2t)\chi = 0$. In the white region the solutions are stable. In the colored region the solutions exponentially grow: $\chi \sim e^{\mu t}$.

For simplicity let us assume there are N possible values of \mathbf{p} (One can always divide the parameter space into small chunks such that the accurate position in the chunk is not relevant.) Suppose the probability that $\mathbf{p} = \mathbf{p}_i$ is \mathcal{L}_i , $i = 1, 2, 3, \dots, N$. The total probability should be normalized

$$\sum_{i=1}^N \mathcal{L}_i = 1. \quad (1.85)$$

The Metropolis-Hasting sampling algorithm is as follows.

1. Choose a irreducible and symmetric matrix $Q_{i,j}$ such that

$$\sum_{j=1}^N Q_{i,j} = 1 \quad (1.86)$$

holds for $i = 1, 2, 3, \dots, N$, and $Q_{ij} > 0$ for all $1 \leq i, j \leq N$. The choice of $Q_{i,j}$ is arbitrary. But once it is chosen, it should not be changed. We may refer to $Q_{i,j}$ as the random-walk probability matrix, since it defines the probability of walking from \mathbf{p}_i to \mathbf{p}_j .

2. Choose an arbitrary starting point \mathbf{p}_i . The sample \mathbf{p}_i is the first element of the Markov Chain.

3. Draw a random number x from a uniform distribution in the interval $(0, 1]$. Find j such that

$$\sum_{k=1}^{j-1} Q_{i,k} < x \leq \sum_{k=1}^j Q_{i,k}. \quad (1.87)$$

In this step, a new sample \mathbf{p}_j is proposed via a random walk.

4. Draw a random number y from a uniform distribution in the interval $(0, 1]$. If $\mathcal{L}_j/\mathcal{L}_i \geq y$, add \mathbf{p}_j into the Markov Chain as the next sample, and let $i = j$ (the proposed sample \mathbf{p}_j is accepted). Otherwise add \mathbf{p}_i into the Markov Chain as the next sample (the proposed sample \mathbf{p}_j is discarded).

5. Go to step 3.

Next I will explain why the Markov chain converges, if it does, to the distribution function \mathcal{L}_i ($i = 1, 2, 3, \dots, N$). Let us assume the distribution of collected samples in the Markov chain converges, and the probability that \mathbf{p}_i appears in the chain is $\tilde{\mathcal{L}}_i$ (for $i = 1, 2, \dots, N$). There are two possible ways to get \mathbf{p}_i in the chain, one is that the previous

sample in the chain is also \mathbf{p}_i , and the proposed sample is rejected. The probability for such a thing to happen is

$$P_{\text{case 1}} = \tilde{\mathcal{L}}_i \sum_{j|\mathcal{L}_j < \mathcal{L}_i} Q_{ij} \left(1 - \frac{\mathcal{L}_j}{\mathcal{L}_i}\right). \quad (1.88)$$

The second possible case will be that the previous sample is \mathbf{p}_j , the proposed sample is \mathbf{p}_i , and it is accepted. The probability for that is

$$P_{\text{case 2}} = \sum_{j|\mathcal{L}_j < \mathcal{L}_i} \tilde{\mathcal{L}}_j Q_{ji} + \sum_{j|\mathcal{L}_j \geq \mathcal{L}_i} \tilde{\mathcal{L}}_j Q_{ji} \left(\frac{\mathcal{L}_i}{\mathcal{L}_j}\right). \quad (1.89)$$

The convergence requires $P_{\text{case 1}} + P_{\text{case 2}} = \tilde{\mathcal{L}}_i$, which is equivalent to

$$\sum_{j=1}^N Q_{ij} \left(\frac{\tilde{\mathcal{L}}_j}{\mathcal{L}_j} - \frac{\tilde{\mathcal{L}}_i}{\mathcal{L}_i}\right) \min(\mathcal{L}_i, \mathcal{L}_j) = 0. \quad (1.90)$$

The above equality should hold for $i = 1, 2, \dots, N$. Apparently $\tilde{\mathcal{L}}_i = \mathcal{L}_i$ (for $i = 1, 2, \dots, N$) is a solution. Again I will skip the proof of uniqueness of the solution. More rigorous discussions and more MCMC algorithms can be found in Ref. [55] and the references therein.

1.8 Outline of the Thesis

In Chapter 2 the quintessence and phantom dark energy models are parameterized, and then confronted with the most current and forecast data. This project is in collaboration with my advisors – Professor Bond and Professor Kofman.

In Chapter 3 the early-universe inflationary expansion history is studied with two approaches: one is the bottom-up approach using blind band-power analyses; another is the top-down approach using numerically calculated primordial power spectra, going beyond the slow-roll assumption. In this project I collaborate with Professor Bond, Professor Kofman, Professor C. Contaldi, and Dr. P. Vaudrevange.

In Chapter 4 the large scale curvature fluctuations from preheating are studied. This work has been published in Phys. Rev. Lett. [56].

Chapter 5 summarizes the published works [6, 7], where we show the rich observable features of particle production during inflation.

In Chapter 6, the work that is published in Ref. [57] studying preheating in Roulette inflation models is discussed.

Chapter 7 is related to published work [58], where we present the cosmological constraints on the lifetime of decaying dark matter.

In Chapter 8 we conclude.

Chapter 2

Parameterizing and Measuring Dark Energy Trajectories from Late-Inflatons

2.1 Introduction

In this chapter we study the quintessence and phantom dark energy models, based on our work [59]. For completeness I include most of the derivations and contents from [59]. Please cite our original paper if these contents are being used.

2.1.1 Running Dark Energy and its Equation of State

One of the greatest mysteries in physics is the nature of dark energy (DE) which drives the present-day cosmic acceleration, inferred to exist from supernovae data [23, 24], and from a combination of cosmic microwave background and large scale structure data [25]. Although there have been voluminous outpourings on possible theoretical explanations of dark energy, recently reviewed in Refs. [28, 60, 61, 62, 63], we are far from consensus. An observational target is to determine if there are temporal (and spatial) variations

beyond the simple constant Λ . Limits from the evolving data continue to roughly center on the cosmological constant case Λ , which could be significantly strengthened in near-future experiments – or ruled out. We explore the class of effective scalar field models for dark energy evolution in this chapter, develop a 3-parameter expression which accurately approximates the dynamical histories in most of those models, and determine current constraints and forecast future ones on these parameters.

The mean dark energy density is a fraction Ω_{de} of the mean total energy density,

$$\rho_{\text{de}}(\ln a) \equiv \rho_{\text{tot}}\Omega_{\text{de}}, \quad 3M_{\text{p}}^2 H^2(a) = \rho_{\text{tot}}(a), \quad (2.1)$$

which is itself related to the Hubble parameter H through the energy constraint equation of gravity theory as indicated. $\Omega_{\text{de}}(a)$ rises from a small fraction relative to the matter at high redshift to its current ~ 0.7 value.

Much observational effort is being unleashed to determine as much as we can about the change of the trajectory ρ_{de} with expansion factor a , expressed through a logarithmic running with respect to $\ln a$:

$$-\frac{1}{2} \frac{d \ln \rho_{\text{de}}}{d \ln a} \equiv \epsilon_{\text{de}}(\ln a) \equiv \frac{3}{2}(1 + w_{\text{de}}) \equiv \frac{3(\rho_{\text{de}} + p_{\text{de}})}{2\rho_{\text{de}}}. \quad (2.2)$$

This ρ_{de} -run is interpreted as defining a phenomenological average pressure-to-density ratio, the dark energy equation of state (EOS). The total “acceleration factor”, $\epsilon \equiv 1 + q$, where the conventional “deceleration parameter” is $q \equiv -a\ddot{a}/\dot{a}^2 = -d \ln(Ha)/d \ln a$, is similarly related to the running of the total energy density:

$$-\frac{1}{2} \frac{d \ln \rho_{\text{tot}}}{d \ln a} \equiv \epsilon = \epsilon_m \Omega_m + \epsilon_{\text{de}} \Omega_{\text{de}}, \quad \Omega_m + \Omega_{\text{de}} = 1. \quad (2.3)$$

Eq. (2.3) shows ϵ is the density-weighted sum of the acceleration factors for matter and DE. Matter here is everything but the dark energy. Its EOS has $\epsilon_m = 3/2$ in the non-relativistic-matter-dominated phase (dark matter and baryons) and $\epsilon_m = 2$ in the radiation-dominated phase.

2.1.2 The Semi-Blind Trajectory Approach

We would like to use the data to constrain $\rho_{\text{de}}(\ln a)$ with as few prior assumptions on the nature of the trajectories as is feasible. However, such blind analyses are actually never truly blind, since ρ_{de} or w_{de} is expanded in a truncated basis of mode functions of one sort or another: necessarily there will be assumptions made on the smoothness associated with the order of the mode expansion and on the measure, i.e., prior probability, of the unknown coefficients multiplying the modes. The most relevant current data for constraining w_{de} , SNIa compilations, extends back only about one e-folding in a , and probes a double integral of w_{de} , smoothing over irregularities. The consequence is that unless w_{de} was very wildly varying, only a few parameters are likely to be extractable no matter what expansion is made.

Low order expansions include the oft-used cases of constant $w_0 \neq -1$ and the 2-parameter linear expansion in a [64, 65, 66, 67, 68, 69, 70],

$$w(a) = w_0 + w_a(1 - a) , \quad (2.4)$$

adopted by the Dark Energy Task Force (DETF) [71]. The current observational data we use in this chapter to constrain our more physically-motivated parameterized trajectories are applied in Figure 2.1 to w_0 and w_a , assuming uniform uncorrelated priors on each. The area of the nearly-elliptical 1-sigma error contour has been used to compare how current and proposed dark energy probes do relative to each other; its inverse defines the DETF “figure of merit” (FOM).

Constant w_{de} and Eq. (2.4) can be considered to be the zeroth and first order polynomial expansion in the variable $1 - a$. Why not redshift z [67, 72] or the scale factor to some power [72] or $\ln a$? Why pivot about $a = 1$.

Why only linear in a ? Why not expand to higher order? Why not use localized spline mode functions, the simplest of which is a set of contiguous top hats (unity in a redshift band, zero outside)? These cases too have been much explored in the literature,

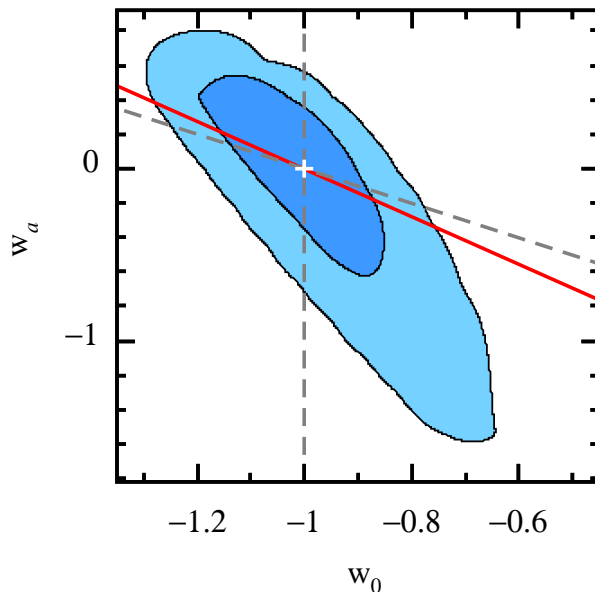


Figure 2.1: The marginalized 68.3% CL (inner contour) and 95.4% CL (outer contour) constraints on w_0 and w_a for the conventional DETF parametrization $w = w_0 + w_a(1 - a)$, using the current data sets described in § 2.4. The white point is the cosmological constant model. The solid red line is a slow-roll consistency relation, Eq. (2.52) derived in § 2.6.2 (for a fixed $\Omega_{m0} = 0.29$, as inferred by all of the current data). The tilted dashed gray line shows $w_a = -1 - w_0$. Pure quintessence models restrict the parameter space to $1 + w_0 > 0$ and w_a above the line, whereas in the pure phantom regime, $1 + w_0 < -0$ and w_a would have to lie below the line. Allowing for equal a priori probabilities to populate the other regions is quite problematical theoretically, and indeed the most reasonable theory prior would allow only the pure quintessence domain.

both for current and forecast data. The method of principal component (parameter eigenmode) analysis takes orthogonal linear combinations of the mode functions and of their coefficients, rank-ordered by the error matrix eigenmodes [73, 74]. As expected only a few linear combinations of mode function coefficients are reasonably determined. Thus another few-parameter approach expands w_{de} in many modes localized in redshift but uses only the lowest error linear combinations. At least at the linearized level, the few new parameters so introduced are uncorrelated. However, the eigenmodes are sensitive to the data chosen and the prior probabilities of the mode parameters. An alternative to the w_{de} expansion is a direct mode expansion in ϵ , considered at low order by Ref. [75]; since the ϵ_m part is known, this is an expansion in $(\epsilon_{\text{de}} - \epsilon_m)\Omega_{\text{de}}$, in which case w_{de} becomes a derived trajectory; for w_{de} parameterizations it is $\epsilon(a)$ that is the derived trajectory.

The partially blind expansions of $1 + w_{\text{de}}$ are similar to the early universe inflation expansions of the scalar power spectrum $\mathcal{P}_s(\ln k)$ [76], except in that case one is “running” in “resolution”, $\ln k$. However there is an approximate relation between the comoving wavenumber k and the time when that specific k -wave went out of causal contact by crossing the instantaneous comoving “horizon” parameterized by Ha . This allows one to translate the power spectra $\ln k$ -trajectories into dynamical $\ln Ha$ -trajectories, $\mathcal{P}_s(\ln Ha)$. Lowest order is a uniform slope $n_s - 1 = d \ln \mathcal{P}_s / \ln k$; next order is a running of that slope, rather like the DETF linear w_{de} expansion. Beyond that, one can go to higher order, e.g., by expanding in Chebyshev polynomials in $\ln k$, or by using localized modes to determine the power spectrum in k -bands. Generally there may be tensor and isocurvature power spectra contributing to the signals, and these would have their own expansions.

In inflation theory, the tensor and scalar spectra are related to each other by an approximate consistency condition: both are derivable from parameterized acceleration factor trajectories defining the inflaton equation of state, $1 + w_\phi(a) = 2\epsilon/3$ (with zero Ω_m in early universe inflation). Thus there is a very close analogy between phenomenological treatments of early and late universe inflation. However, there is a big difference:

power spectra can be determined by over ~ 10 e-foldings in k from CMB and Large Scale Structure data on clustering, hence over ~ 10 e-foldings in a , whereas dark energy data probe little more than an e-folding of a . This means that higher order partially blind mode expansions are less likely to bear fruit in the late-inflaton case.

2.1.3 Physically-motivated Late-inflaton Trajectories

This arbitrariness in semi-blind expansions motivates our quest to find a theoretically-motivated prior probability on general dark energy trajectories characterized by a few parameters, with the smoothness that is imposed following from physical models of their origin rather than from arbitrary restrictions on blind paths. Such a prior has not been much emphasized in dark energy physics, except on an individual-model basis. The theory space of models whose trajectories we might wish to range over include:

- (1) quintessence, with the acceleration driven by a scalar field minimally coupled to gravity with an effective potential with small effective mass and a canonical kinetic energy [77, 78, 79, 80, 81, 82, 83, 84, 85, 86, 87];
- (2) k-essence, late inflation with a non-canonical scalar field kinetic energy as well as a potential [88, 89, 90, 91];
- (3) $F(R, \phi)$ models, with Lagrangians involving a function of the curvature scalar R or a generalized dilaton ϕ , that can be transformed through a conformal mapping into a theory with an effective scalar field, albeit with interesting fifth force couplings to the matter sector popping out in the transform [92, 93, 94, 95, 96, 97];
- (4) phantom energy with $w_{\text{de}} < -1$, and negative effective kinetic energy, also with a potential [28, 98, 99, 100].

In this chapter, we concentrate on the quintessence class of models, but allow trajectories that would arise from a huge range of potentials, with our fitting formula only deviating significantly when $|1 + w_{\text{de}}| > 0.5$. A class of models that are not included due to the limit of our method are ones with dark energy having damped oscillations before

settling into a minimum Λ [101, 102].

We also extend our paths to include ones with $w_{\text{de}} < -1$, the phantom regime where the null energy condition [98] is violated. This can be done by making the kinetic energy negative, at least over some range, but such models are ill-defined. There have been models proposed utilizing extra UV physics, such as with a Lorentz-violating cut-off [103] or with extra fields [104]. Regions with $w_{\text{de}} < -1$ are consistent with current observations, so a semi-blind phenomenology should embrace that possibility. It is straightforward to extend our quintessence fitting formula to the phantom region, so we do, but show results with and without imposing the theoretical prior that these are highly unlikely.

The evolution of w_{de} for a quintessence field ϕ depends on its potential $V(\phi)$ and its initial conditions. For a flat Friedmann-Robertson-Walker (FRW) universe with given present matter density ρ_{m0} and dark energy density $\rho_{\text{de}0}$, any function $w_{\text{de}}(a)$ satisfying $0 \leq 1 + w_{\text{de}} \leq 2$ can be reverse-engineered into a potential $V(\phi)$ and an initial field momentum, $\Pi_{\phi,\text{ini}} \equiv \dot{\phi}_{\text{ini}}$. (The initial field value ϕ_{ini} can be eliminated by a translation in $V(\phi)$, and the sign of $\Pi_{\phi,\text{ini}}$ by a reflection in $V(\phi)$.) Given this one-to-one mapping between $\{V(\phi), |\dot{\phi}_{\text{ini}}|; \rho_{m0}\}$ and $\{w(a), \rho_{\text{de}0}; \rho_{m0}\}$, we may think we should allow for all w_{de} trajectories. Generally, these will lead to very baroque potentials indeed, and unrealistic initial momenta. The quintessence models with specific potentials that have been proposed in the literature are characterized by a few parameters, and have a long period in which trajectories relax to attractor ones, leading to smooth trajectories in the observable range at low redshift. These are the simple class of potentials we are interested in here: our philosophy is to consider “simple potentials” rather than simple mathematical forms of $w_{\text{de}}(a)$. The potentials which we quantitatively discuss in later sections include: power-laws [77, 105]; exponentials [77]; double exponentials [81, 106, 107, 108, 109]; cosines from pseudo-Nambu Goldstone bosons (pnGB) [79, 101]; supergravity (SUGRA) motivated models [82]. Our general method applies to a much broader class than these though: we find the specific global form of the potential is not relevant because the rela-

tively small motions on its surface in the observable range allow only minimal local shape characteristics to be determined, and these we can encode with the three key physical variables parameterizing our w_{de} . Even with the forecasts data to come, we can refine our determinations but not gain significantly more information – unless the entire framework is shown to be at variance with the data.

2.1.4 Tracking and Thawing Models

Quintessence models are often classified into tracking and thawing models [110, 85, 87, 86, 111, 112]. Tracking models were first proposed to solve the coincidence problem, i.e., why the dark energy starts to dominate not very long after the epoch of matter-radiation equality (~ 7.5 e-folds). However, a simple negative power-law tracking model that solves the coincidence problem predicts $w_{\text{de}} \gtrsim -0.5$ today, which is strongly disfavoured by current observational data. In order to achieve the observationally favoured $w_{\text{de}} \approx -1$ today, one has to assume the potential changes at an energy scale close to the energy density at matter-radiation equality. The coincidence problem is hence converted to a fine-tuning problem. In this chapter we take the tracking models as the high-redshift limit, and parameterize it with a “tracking parameter” $\varepsilon_{\phi\infty}$ that characterizes the attractor solution. The thawing models, where the scalar field is frozen at high redshift due to large Hubble friction, can be regarded as a special case of tracking models where the tracking parameter is zero. Because of the nature of tracking behaviour, where all solutions regardless of initial conditions approach an attractor, we do not need an extra parameter to parameterize the initial field momentum.

In either tracking models or thawing models the scalar field has to be slowly-rolling or moderately-rolling at low redshift, so that the late-universe acceleration can be achieved. The main physical quantity that affects the dynamics of quintessence in the late-universe accelerating epoch is the slope of the potential. The field momentum is “damped” by Hubble friction, and the slope of the potential will determine how fast the field will be

rolling down; actually, as we show here, it is the ϕ -gradient of $\ln V$ that matters, and this defines our second “slope parameter” ε_s .

It turns out that a two-parameter formula utilizing just $\varepsilon_{\phi\infty}$ and ε_s works very well, because the field rolls slowly at low redshift, indeed is almost frozen, so the trajectory does not explore changes in the slope of $\ln V$. However, we want to extend our formula to cover the space of moderate-roll as well as slow-roll paths. Moreover, in cases in which $\ln V$ changes significantly, even slow-roll paths may explore the curvature of $\ln V$ as well as its ϕ -gradient. Accordingly, we expanded our formula to encompass such cases, introducing a third parameter ζ_s , which is related to the second ϕ -derivative of $\ln V$, explicitly so in thawing models.

2.1.5 Parameter Priors for Tracking and Thawing Models

Of course, there is one more important fourth parameter, characterizing the late-inflaton energy scale, such as the current dark energy density $\rho_{\text{de},0}$ at redshift 0. This is related to the current Hubble parameter $H_0 \equiv 100h \text{ km s}^{-1}\text{Mpc}^{-1}$, the present-day fractional matter density Ω_{m0} , and the current fractional dark energy density $\Omega_\Lambda \equiv \Omega_{\text{de},0} = 1 - \Omega_{m0}h^2/h^2$: $\rho_{\text{de},0} = 3M_{\text{p}}^2 H_0^2 \Omega_\Lambda$. With CMB data, the sound-crossing angular scale at recombination is actually used, as is the physical density parameter of the matter, $\Omega_{m0}h^2$, which is typically derived from separately determined dark matter and baryonic physical density parameters, $\Omega_{\text{dm}0}h^2$ and $\Omega_{b0}h^2$. With any nontrivial w_{de} EOS, this depends upon the parameters of w_{de} as well as on one of h or the inter-related zero redshift density parameters. The important point here is that the prior measure is uniform in the sound-crossing angular scale at recombination and in $\Omega_{\text{dm}0}h^2$ and $\Omega_{b0}h^2$, not in h or the energy scale of late-inflation. If the quantities are well-measured, as they are, the specific prior does not matter very much.

What to use for the prior probability of the parameters of w_{de} , in which most are not well-determined? The prior chosen does matter, and has to be understood when

assessing the meaning of the derived constraints. Usually a uniform prior in w_0 and w_a is used for the DETF form, Eq. (2.4). The analogue for our parameterization is to be uniform in the relatively well-determined ε_s , but we show what variations in the measure on it do, e.g., using $\sqrt{|\varepsilon_s|}$ or disallowing phantom trajectories, $\varepsilon_s > 0$. The measure for each of the other two parameters is also taken to be uniform. (Our physics-based parameterization leads to an approximate “consistency relation” between w_0 and w_a , a strong prior relative to the usual uniform one.)

In § 2.2, we manipulate the dynamic equations for quintessence and phantom fields to derive our approximate solution, $w_{\text{de}}(a|\varepsilon_s, \varepsilon_{\phi\infty}, \zeta_s, \Omega_{\text{m}0})$. We show how well this formula works in reproducing full trajectories computed for a variety of potentials. In § 2.4 we describe our extension of the CosmoMC program package [113] to treat our parameterized DE and the following updated cosmological data sets: Type Ia Supernova (SN), galaxy power spectra that probe large scale structure (LSS), weak lensing (WL), Cosmic Microwave Background (CMB), and Lyman- α forest (Ly α). The present-day data are used to constrain our dynamical $w_{\text{de}}(a)$. In § 2.5, we investigate how future observational cosmology surveys can sharpen the constraints on $w_{\text{de}}(a|\varepsilon_s, \varepsilon_{\phi\infty}, \zeta_s, \Omega_{\text{m}0})$. We restrict our attention to flat universes. We discuss our results in § 2.6.

2.2 Late-inflation Trajectories and Their Parameterization

2.2.1 The Field Equations in Terms of Equations of State

We assume the dark energy is the energy density of a quintessence (or phantom) field, with a canonical kinetic energy and an effective potential energy $V(\phi)$. This is derived from a Lagrangian density

$$\mathcal{L} = \pm \frac{1}{2} \partial_\mu \phi \partial^\mu \phi - V(\phi) , \quad (2.5)$$

where $+$ is for quintessence ($-$ for phantom). In what follows for readability we implicitly assume a quintessence field, unless otherwise stated. For homogeneous fields the energy density, pressure and equation of state are

$$\rho_\phi = \frac{1}{2}\Pi_\phi^2 + V(\phi), \quad p_\phi = \frac{1}{2}\Pi_\phi^2 - V(\phi), \quad (2.6)$$

$$1 + w_\phi \equiv \frac{\rho_\phi + p_\phi}{\rho_\phi} = \frac{\Pi_\phi^2}{\rho_\phi}, \quad \Pi_\phi \equiv \frac{d\phi}{dt}. \quad (2.7)$$

Since we identify the dark energy with an inflaton, we hereafter use ϕ as the subscript rather than “de”. The field ϕ does not have to be a fundamental scalar, it could be an effective field, an order parameter associated with some collective combination of fields. A simple way to include the phantom field case is to change the kinetic energy sign to minus, although thereby making it a ghost field with unpalatable properties even if it is the most straightforward way to get $1 + w_{\text{de}} < 0$.

The two scalar field equations, for the evolution of the field, $\dot{\phi} = \Pi_\phi$, and of the field momentum, $\dot{\Pi}_\phi = -3H\Pi_\phi - \partial V/\partial\phi$, transform to

$$\dot{\phi}/H : \quad \sqrt{\epsilon_\phi\Omega_\phi} = \pm d\psi/d\ln a, \quad \psi \equiv \phi/(\sqrt{2}M_{\text{p}}), \quad (2.8)$$

$$\begin{aligned} \dot{\Pi}_\phi/H : \quad & \frac{d^2\psi}{(d\ln a)^2} + 3\left(1 - \frac{\epsilon}{3}\right) \frac{d\psi}{d\ln a} \\ & = \pm 3\sqrt{\epsilon_V\Omega_\phi}\sqrt{\Omega_\phi} \left(1 - \frac{\epsilon_\phi}{3}\right). \end{aligned} \quad (2.9)$$

The sign is arbitrary, depending upon whether the field rolls down the potential to larger ψ ($+$) or smaller ψ ($-$) as the universe expands. For definiteness we take it to be positive. The second equation can be recast into a first order equation for $d\ln\sqrt{\epsilon_\phi\Omega_\phi}/d\ln a$ which is implicitly used in what follows, we prefer to work instead with a first integral, the energy conservation equation (2.2).

As long as Π_ϕ is strictly positive, ψ is as viable a time variable as $\ln a$, although it only changes by $\sqrt{\epsilon_\phi\Omega_\phi}$ in an e-folding of a . Thus, along with trajectories in $\ln a$, we could reconstruct the late-inflaton potential $V(\phi)$ as a function of ϕ and the energy density as

a function of the field:

$$\sqrt{\epsilon_V} \equiv -\frac{1}{2} \frac{d \ln V}{d \psi} = \frac{\sqrt{\epsilon_\phi}}{\sqrt{\Omega_\phi}} \left(1 + \frac{d \ln \epsilon_\phi / d \ln a}{6(1 - \epsilon_\phi/3)} \right), \quad (2.10)$$

$$\sqrt{\epsilon_E} \equiv -\frac{1}{2} \frac{d \ln \rho_\phi}{d \psi} = \frac{\sqrt{\epsilon_\phi}}{\sqrt{\Omega_\phi}}. \quad (2.11)$$

$$(2.12)$$

These “constraint” equations require knowledge of both ϵ_ϕ and Ω_ϕ , but the latter runs according to

$$\frac{1}{2} \frac{d \ln [\Omega_\phi^{-1} - 1]}{d \ln a} = \epsilon_\phi - \epsilon_m, \quad (2.13)$$

hence is functionally determined. Eq. (2.13) is obtained by taking the difference of Eqs. (2.2) and (2.3) and grouping all Ω_ϕ terms on the left hand side.

For early universe inflation with a single inflaton, $\Omega_\phi = 1$, and $\epsilon_\phi = \epsilon_E = \epsilon$. The field momentum therefore obeys the relation $\Pi_\phi = -2M_p^2 \partial H / \partial \phi$, which is derived more generally from the momentum constraint equation of general relativity [114].

2.2.2 A Re-expressed Equation Hierarchy Conducive to Approximation

The field equations form a complete system if $V(\psi)$ is known, but what we wish to do is to learn about V . So we follow the running of a different grouping of variables, namely the differential equations for the set of parameters $\sqrt{\epsilon_\phi}$ and $\sqrt{\epsilon_V \Omega_\phi}$, with a third equation for the running of Ω_ϕ , Eq. (2.13):

$$\frac{d \sqrt{\epsilon_\phi}}{d \ln a} = 3(\sqrt{\epsilon_V \Omega_\phi} - \sqrt{\epsilon_\phi})(1 - \epsilon_\phi/3), \quad (2.14)$$

$$\frac{d \ln \sqrt{\epsilon_V \Omega_\phi}}{d \ln a} = (\epsilon_\phi - \epsilon_m)(1 - \Omega_\phi) + 2\gamma \sqrt{\epsilon_\phi} \sqrt{\epsilon_V \Omega_\phi}. \quad (2.15)$$

The reason for choosing Eq. (2.15) for $\sqrt{\epsilon_V \Omega_\phi}$ rather than the simpler running equation in $\sqrt{\epsilon_V}$

$$\frac{1}{2} d \ln \sqrt{\epsilon_V} / d \ln a = \gamma \sqrt{\epsilon_\phi} \sqrt{\epsilon_V \Omega_\phi}, \quad (2.16)$$

is because we must allow for the possibility that the potential could be steep in the early universe, so ϵ_V may be large, even though the allowed steepness now is constrained. For tracking models where a high redshift attractor with constant w_ϕ exists, $\epsilon_V \Omega_\phi$ tends to a constant, and is nicely bounded, allowing better approximations.

(The $\phi \rightarrow -\phi$ symmetry allows us to fix the $\pm\sqrt{\epsilon_\phi}$ and $\pm\sqrt{\epsilon_V \Omega_\phi}$ ambiguity to the positive sign. For phantom energy, we use the negative sign, in Eqs. (2.14 -2.16). In these equations, we have restricted ourselves to fields that always roll down for quintessence, or up for phantom. The interesting class of oscillating quintessence models [101, 102] are thus not considered.)

These equations are not closed, but depend upon a potential shape parameter γ , defined by

$$\gamma \equiv \frac{\partial^2 \ln V / \partial \psi^2}{(\partial \ln V / \partial \psi)^2}. \quad (2.17)$$

It is related to the effective mass-squared in H^2 units through

$$m_{\phi,\text{eff}}^2 / H^2 = 6(1 + \gamma)\epsilon_V \Omega_\phi (1 - \epsilon_\phi / 3), \quad (2.18)$$

Determining how γ evolves involves yet higher derivatives of $\ln V$, ultimately an infinite hierarchy unless the hierarchy is closed by specific forms of V . However, although not closed in $\sqrt{\epsilon_V \Omega_\phi}$, the equations are conducive for finding an accurate approximate solution, which we express in terms of a new time variable,

$$y \equiv \sqrt{\Omega_{\phi\text{app}}}, \quad \Omega_{\phi\text{app}} \equiv \frac{\rho_{\phi\text{eq}}}{\rho_m(a) + \rho_{\phi\text{eq}}} = \frac{(a/a_{\text{eq}})^3}{1 + (a/a_{\text{eq}})^3}, \quad (2.19)$$

where the subscript ‘‘eq’’ defines variables at the redshift of matter-DE equality:

$$a_{\text{eq}} \equiv (\rho_{m0} / \rho_{m,\text{eq}})^{1/3}, \quad \rho_{m,\text{eq}} = \rho_{\phi\text{eq}}, \quad \Omega_{\phi\text{eq}} = \Omega_{m,\text{eq}} = 1/2. \quad (2.20)$$

Thus y is an approximation to $\sqrt{\Omega_\phi}$, pivoting about the expansion factor a_{eq} in the small ϵ_ϕ limit. By definition $y_{\text{eq}} \equiv y|_{a=a_{\text{eq}}} = 1/\sqrt{2}$.

2.2.3 The Parameterized Linear and Quadratic Approximations

We now show how working with these running variables leads to a 1-parameter fitting formula, expressed in terms of

$$\varepsilon_s \equiv \pm \epsilon_V|_{a=a_{\text{eq}}} . \quad (2.21)$$

The 2-parameter fitting formula adds the asymptotic EOS factor

$$\varepsilon_{\phi\infty} \equiv \pm \epsilon_V \Omega_\phi|_\infty . \quad (2.22)$$

The minus sign in Eq. (2.21) and (2.22) is a convenient way to extend the parameterization to cover the phantom case. Here ∞ refers to the $a \ll 1$ limitⁱ. The asymptotic equality of our 2 key variables is derived, not imposed, a consequence of the attractor. In addition, if the initial field momentum is far from the attractor, it would add another variable, but the damping to the attractor goes like a^{-6} in ϵ_ϕ , hence should be well established before we get to the observable regime for trajectories.

The 3-parameter form involves, in addition to these two, a parameter which is a curious relative finite difference of $d\sqrt{\epsilon_V \Omega_\phi}/dy$ about $y_{\text{eq}}/2$:

$$\zeta_s \equiv \frac{d\sqrt{\epsilon_V \Omega_\phi}/dy|_{\text{eq}} - d\sqrt{\epsilon_V \Omega_\phi}/dy|_\infty}{d\sqrt{\epsilon_V \Omega_\phi}/dy|_{\text{eq}} + d\sqrt{\epsilon_V \Omega_\phi}/dy|_\infty} . \quad (2.23)$$

The physical content of the “running parameter” ζ_s is more complicated than that of ε_s and $\varepsilon_{\phi\infty}$. It is related not only to the second derivative of $\ln V$, through γ , thus extending the slope parameter ε_s to another order, but also to the field momentum. As we mentioned in the introduction, the small stretch of the potential surface over which the late-inflaton moves in the observable range make it difficult to determine the second derivative of $\ln V$ from the data (§ 2.6. In thawing models, for which the field momentum locally traces the slope of $\ln V$, the dependence of ζ_s on the field momentum

ⁱFor tracking models $\epsilon_V \Omega_\phi \propto \epsilon_m$ at high redshift varies by a factor of 3/4 from the radiation-dominated era to the matter-dominated era. In practice we actually use $|\varepsilon_{\phi\infty}|/\epsilon_m$ as a parameter, and replace $\varepsilon_{\phi\infty}$ with $\frac{|\varepsilon_{\phi\infty}|}{\epsilon_m} \epsilon_m \text{sgn}(\varepsilon_s)$ in our w_ϕ parametrization.

can be eliminated. However, if the field momentum is sufficiently small, w_ϕ does not respond to $d^2 \ln V/d\phi^2$. We discuss these cases in § 2.6.

What we demonstrate is that a relation linear in y ,

$$\sqrt{\epsilon_V \Omega_\phi} \approx \sqrt{\epsilon_{\phi\infty}} + (\sqrt{\epsilon_s} - \sqrt{2\epsilon_{\phi\infty}})y, \quad (2.24)$$

is a suitable approximation. It yields the 2-parameter formula for ϵ_ϕ , which maintains the basic form linear in parameters,

$$\sqrt{\epsilon_\phi} \approx \sqrt{\epsilon_{\phi\infty}} + (\sqrt{\epsilon_s} - \sqrt{2\epsilon_{\phi\infty}}) F\left(\frac{a}{a_{\text{eq}}}\right), \quad (2.25)$$

with

$$F(x) \equiv \frac{\sqrt{1+x^3}}{x^{3/2}} - \frac{\ln[x^{3/2} + \sqrt{1+x^3}]}{x^3}. \quad (2.26)$$

The 1-parameter case has $\sqrt{\epsilon_{\phi\infty}}$ set to zero, hence the simple $\sqrt{\epsilon_V \Omega_\phi} \approx \sqrt{\epsilon_s \Omega_{\phi\text{app}}}$ and $\epsilon_\phi = \epsilon_s F^2(a/a_{\text{eq}})$, which we regard as the logical physically-motivated improvement to the conventional single- w_0 parameterization, $1+w = (1+w_0)F^2(a/a_{\text{eq}})/F^2(1/a_{\text{eq}})$.

The approximation for the 3-parameter formula adds a quadratic correction in y :

$$\sqrt{\epsilon_V \Omega_\phi} \approx \sqrt{\epsilon_{\phi\infty}} + (\sqrt{\epsilon_s} - \sqrt{2\epsilon_{\phi\infty}})y \left[1 - \zeta_s \left(1 - \frac{y}{y_{\text{eq}}}\right)\right], \quad (2.27)$$

and a more complex form for the DE trajectories,

$$\sqrt{\epsilon_\phi} = \sqrt{\epsilon_{\phi\infty}} + (\sqrt{\epsilon_s} - \sqrt{2\epsilon_{\phi\infty}}) \left[F\left(\frac{a}{a_{\text{eq}}}\right) + \zeta_s F_2\left(\frac{a}{a_{\text{eq}}}\right) \right], \quad (2.28)$$

with

$$F_2(x) \equiv \sqrt{2} \left[1 - \frac{\ln(1+x^3)}{x^3} \right] - F(x). \quad (2.29)$$

To cover the phantom case, we put absolute values everywhere that ϵ_s and $\epsilon_{\phi\infty}$ appears, and multiply $1+w_{\text{de}}$ by the sign, $\text{sgn}(\epsilon_s) = \text{sgn}(\epsilon_{\phi\infty})$.

2.2.4 Asymptotic Properties of $V(\phi)$ & $\sqrt{\epsilon_{\phi\infty}}$

The class of quintessence/phantom models where the field is slow-rolling in the late-universe accelerating phase is of primary interest. Qualitatively this implies $\epsilon_\phi \ll 1$ at

low redshift, but we would like to have a parametrization covering a larger prior space allowing for higher ϵ_ϕ and $|d\psi/d\ln a|$, and let observations determine the allowed speed of the roll. Therefore we also include moderate-roll models in our parametrization, making sure our approximate formula covers well trajectories with values of $|1+w_\phi|$ which extend up to 0.5 and ϵ_ϕ to 0.75 at low redshift.

At high redshift the properties of the potential are poorly constrained by observations, and we have a very large set of possibilities to contend with. Since the useful data for constraining DE is at the lower redshifts, what we really need is just a reasonable shutoff at high redshift. One way we tried in early versions of this work was just to cap ϵ_ϕ at some $\epsilon_{\phi\infty}$ at a redshift well beyond the probe regime. Here we still utilize a cap as a parameter, but let physics be the guide to how it is implemented so that the ϵ_ϕ trajectories smoothly join higher to lower redshifts.

The way we choose to do this here is to restrict our attention to tracking and thawing models for which the asymptotic forms are easily parameterized. Tracking models have an early universe attractor which implies ϵ_ϕ indeed becomes a constant $\epsilon_{\phi\infty}$, which is smaller than ϵ_m . If we apply this attractor to equation (2.14), we obtain $\sqrt{\epsilon_V\Omega_\phi}$ is constant at high redshift, equaling our $\sqrt{\epsilon_{\phi\infty}}$. By definition, thawing models have $\epsilon_{\phi\infty} = 0$.

Consider the two high redshift possibilities exist for the tracking models. One has $\epsilon_\phi = \epsilon_m$, which, when combined with equation (2.15), implies the potential structure parameter γ vanishes, hence one gets an an exponential potential as an asymptotic solution for V , as discussed in Refs. [115, 116, 28]. Another possibility has $\epsilon_\phi < \epsilon_m$, hence from Eq. (2.15) we obtain $\gamma = (\epsilon_m - \epsilon_\phi)/(2\epsilon_\phi)$ is a positive constant. Solving this equation for γ yields a negative power-law potential, $V \propto \psi^{-1/\gamma}$. For both cases, we must have an asymptotically constant $\gamma \geq 0$ to give a constant

$$\epsilon_{\phi\infty} \rightarrow \epsilon_m/(1 + 2\gamma_\infty) , \quad (2.30)$$

where γ_∞ is the high redshift limit of the shape parameter Eq. (2.17). This also shows why $\epsilon_{\phi\infty}/\epsilon_m$ is actually a better parameter choice than $\epsilon_{\phi\infty}$, since the ratio is conserved

as the matter EOS changes.

The difference between tracking and thawing models is not only quantitative, but is also qualitative. For tracking models, the asymptotic limit $\sqrt{\varepsilon_{\phi\infty}}$ has a dual interpretation. One is that the shape of potential has to be properly chosen to have the asymptotic limit of the right hand side of

$$\sqrt{\varepsilon_{\phi\infty}} \rightarrow \sqrt{\varepsilon_V \Omega_\phi}|_\infty = -\frac{1}{2} \frac{d \ln V}{d\psi}|_\infty \sqrt{\Omega_{\phi\infty}}, \quad (2.31)$$

existing. We already know how to choose the potential – it has to be asymptotically either an exponential or a negative power-law. Another interpretation directly relates $\sqrt{\varepsilon_{\phi\infty}}$ to the property of the potential through Eq. (2.30). In the thawing scenario, Eq. (2.15) is trivial, and the shape parameter γ is no longer tied to the vanishing $\varepsilon_{\phi\infty}$, though Eq. (2.31) still holds.

For phantom models the motivation for tracking solutions is questionable. We nevertheless allow for reciprocal ϵ_ϕ -trajectories as for quintessence, just flipping the sign to extend the phenomenology to $1 + w_\phi < 0$, as has become conventional in DE papers. What we do not do, however, is try to parameterize trajectories that cross $\epsilon_\phi = 0$, as is done in the DETF w_0 - w_a phenomenology (see Fig. 2.1).

2.2.5 The Two-Parameter $w_\phi(a|\varepsilon_s, \varepsilon_{\phi\infty})$ -Trajectories

In the slow-roll limit, ε_V does not vary much. As mentioned above, we use $\varepsilon_s \equiv \pm \varepsilon_{V,eq}$ evaluated at the equality of matter and dark energy to characterize the (average) slope of $\ln V$ at low redshift, and Ω_{m0} or h as a way to encode the actual value of the potential V_0 at zero redshift. To model $V(\phi)$ at high redshift for both tracking models and thawing models, we use the interpretation (2.31) characterized by the “tracking parameter” $\varepsilon_{\phi\infty} = (\varepsilon_V \Omega_\phi)|_\infty$, which is bounded by the tracking condition $0 \leq \varepsilon_{\phi\infty}/\varepsilon_m \leq 1$.

Eq. (2.14) shows that to solve for $\epsilon_\phi(a)$ one only needs to know $\sqrt{\varepsilon_V \Omega_\phi}$ plus an initial condition, $\sqrt{\varepsilon_{\phi\infty}}$, but that too is just $\sqrt{\varepsilon_V \Omega_\phi}$ in the $a \rightarrow 0$ limit. We know as well $\sqrt{\varepsilon_V \Omega_\phi}$

at a_{eq} , namely $\sqrt{\varepsilon_s/2}$. If the rolling is quite slow, ε_V will be nearly ε_s , and Ω_ϕ will be nearly $\Omega_{\phi\text{app}} = y^2$, hence

$$\sqrt{\varepsilon_V \Omega_\phi} \approx \sqrt{\varepsilon_s \Omega_{\phi\text{app}}} = \sqrt{\varepsilon_s} y, \quad (2.32)$$

the 1-parameter approximation. But we are also assuming we know the $y = 0$ boundary condition, $\sqrt{\varepsilon_V \Omega_\phi}|_\infty$ as well as this y_{eq} value. If we make the simplest linear- y relation through the two points, we get our first order approximation, Eq. (2.24), for $\sqrt{\varepsilon_V \Omega_\phi}$.

To get the DE EOS w_ϕ , we need to integrate Eq. (2.14), with our $\sqrt{\varepsilon_V \Omega_\phi}$ approximation. In facilitate this, we make another approximation,

$$(\sqrt{\varepsilon_V \Omega_\phi} - \sqrt{\varepsilon_\phi})(1 - \varepsilon_\phi/3) \approx (\sqrt{\varepsilon_V \Omega_\phi} - \sqrt{\varepsilon_\phi}), \quad (2.33)$$

which is always a good one: at high redshift the tracking behaviour enforces $\sqrt{\varepsilon_V \Omega_\phi} - \sqrt{\varepsilon_\phi} \rightarrow 0$; and at low redshift $\varepsilon_\phi/3 \ll 1$. The analytic solution for $\sqrt{\varepsilon_\phi}$ retains the form linear in the two parameters, yielding Eq. (2.25), and hence the w_ϕ approximation

$$1 + w_\phi(a) \approx \frac{2}{3} [\sqrt{\varepsilon_{\phi\infty}} + (\sqrt{\varepsilon_s} - \sqrt{2\varepsilon_{\phi\infty}}) F(\frac{a}{a_{\text{eq}}})]^2, \quad (2.34)$$

where F is defined in (2.26).

The three DE parameters a_{eq} , $\varepsilon_{\phi\infty}$, and ε_s are related to Ω_{m0} through the constraint equation

$$\left[1 + \exp \left(2 \int_{a_{\text{eq}}}^1 (\varepsilon_\phi - \varepsilon_m) \frac{da}{a} \right) \right]^{-1} = 1 - \Omega_{m0} \quad (2.35)$$

obtained by integrating Eq. (2.13) from $a = a_{\text{eq}}$, where by definition $\Omega_{\phi,\text{eq}} = 1/2$, to today, $a = 1$, hence Ω_{m0} is actually quite a complex parameter, involving the entire $w_\phi(a; a_{\text{eq}}, \varepsilon_s, \varepsilon_{\phi\infty})/a$ history, as of course is $a_{\text{eq}}(\Omega_{m0}, \varepsilon_s, \varepsilon_{\phi\infty})$, which we treat as a derived parameter from the trajectories. The zeroth order solution for $a_{\text{eq}}(\Omega_{m0}, \varepsilon_s, \varepsilon_{\phi\infty})$ only depends upon Ω_{m0} :

$$a_{\text{eq}} \approx \left(\frac{\Omega_{m0}}{1 - \Omega_{m0}} \right)^{1/3}, \quad (2.36)$$

In conjunction with the approximate 2-parameter w_ϕ , (2.34), this a_{eq} completes our first approximation for DE dynamics.

2.2.6 The Three-parameter Formula

The linear approximation of $\sqrt{\epsilon_V \Omega_\phi}(y)$ and the zeroth order approximation for a_{eq} rely on the slow-roll assumption. For moderate-roll models ($|1 + w_\phi| \gtrsim 0.2$), the two-parameter approximation is often not sufficiently accurate, with errors sometimes larger than 0.01. We now turn to the improved 3-parameter fit to w_ϕ ; we need to considerably refine a_{eq} as well to obtain the desired high accuracy.

The quadratic expansion Eq. (2.27) of $\sqrt{\epsilon_V \Omega_\phi}$ in y leads to Eq. (2.28) for $\sqrt{\epsilon_\phi}$, in terms of the two functions F and F_2 of a/a_{eq} . Since ζ_s term is a ‘‘correction term’’, we impose a measure restriction on its uniform prior by requiring $|\zeta_s| \lesssim 1$. Thus $w_\phi(a; a_{\text{eq}}, \epsilon_s, \epsilon_{\phi\infty}, \zeta_s)$ follows, with the phantom paths covered by

$$\epsilon_{\phi,\text{phantom}}(a; \epsilon_s, \epsilon_{\phi\infty}, \zeta_s) = \text{sgn}(\epsilon_s) \epsilon_{\phi,\text{quintessence}}(a; |\epsilon_s|, |\epsilon_{\phi\infty}|, \zeta_s). \quad (2.37)$$

We also need to improve a_{eq} , using the constraint Eq. (2.35). We do not actually need the exact solution, but just a good approximation that works for $\Omega_{\text{m}0} \sim 0.3$. For example, the following fitting formula is sufficiently good (error $\lesssim 0.01$) for $0.1 < \Omega_{\text{m}0} < 0.5$:

$$\ln a_{\text{eq}}(\Omega_{\text{m}0}, \epsilon_s, \epsilon_{\phi\infty}, \zeta_s) = \frac{\ln[\Omega_{\text{m}0}/(1 - \Omega_{\text{m}0})]}{3 - \text{sgn}(\epsilon_s)\delta}, \quad (2.38)$$

where the correction to the index is

$$\begin{aligned} \delta &\equiv \left\{ \sqrt{|\epsilon_{\phi\infty}|} + [0.91 - 0.78\Omega_{\text{m}0} + (0.24 - 0.76\Omega_{\text{m}0})\zeta_s] \left(\sqrt{|\epsilon_s|} - \sqrt{2|\epsilon_{\phi\infty}|} \right) \right\}^2 \\ &+ \left[\sqrt{|\epsilon_{\phi\infty}|} + (0.53 - 0.09\zeta_s) \left(\sqrt{|\epsilon_s|} - \sqrt{2|\epsilon_{\phi\infty}|} \right) \right]^2. \end{aligned} \quad (2.39)$$

2.3 Exact DE Paths for Various Potentials Compared with our Approximate Paths

Equations (2.28) and (2.38-2.39) define a three-parameter ansatz for $w_\phi = -1 + 2/3\epsilon_\phi$ (with an implicit fourth parameter for the energy scale, $\Omega_{\text{m}0}$). We numerically solve $w_\phi(a)$

for a wide variety of quintessence and phantom models, and show our $w_\phi(a)$ formula follows the exact trajectories very well. This means we can compress this large class of theories into these few parameters.

The dark energy parameters ε_s , $\varepsilon_{\phi\infty}$ and ζ_s are calculated using definitions (2.21), (2.22) and (2.23). We choose $z = 50$ to calculate the high-redshift quantities such as $\varepsilon_V|_{a\ll 1}$. Unless otherwise specified, the initial condition is always chosen to be at $\ln a = -20$, roughly at the time of BBN, at which point the initial field momentum is set to be zero (although it quickly relaxes). The figures express ϕ in units of the reduced Planck Mass M_p , hence are $\sqrt{2}\psi$. The initial field value is denoted as ϕ_{ini} .

In the upper panel of Figure 2.2 we show that once the memory of the initial input field momentum is lost, our parameterization fits the numerical solution for a negative power-law potential quite well over a vast number of e-foldings, even if $1 + w$ is not small at low-redshift.

We know that in order to achieve both $w_\phi \sim w_m$ at high redshift, which can alleviate the dark energy coincidence problem, and also slow-roll at low redshift, the negative power-law potential (or exponential potential) needs modification to fit the low redshift. One of the best known examples of a potential that does this is motivated by supergravity [82]:

$$V(\phi) = V_0 \left(\frac{M_p}{\phi} \right)^\alpha \exp \left(\frac{\phi^2}{2M_p^2} \right), \quad (2.40)$$

where $\alpha \geq 11$. An example for a SUGRA model is shown in the middle panel of Figure 2.2: it fits quite well for the redshifts over which we have data, with some deviation once ϵ_ϕ exceeds unity at high redshift.

Another popular tracking model is the double exponential model, an example of which is given in the lower panel of Figure 2.2.

In Figures 2.3 we show how robust our parametrization is for slow-roll and moderate-roll cases, taking examples from a variety of examples of popular thawing models. The horizontal axis is now chosen to be linear in a , since there is no interesting early universe

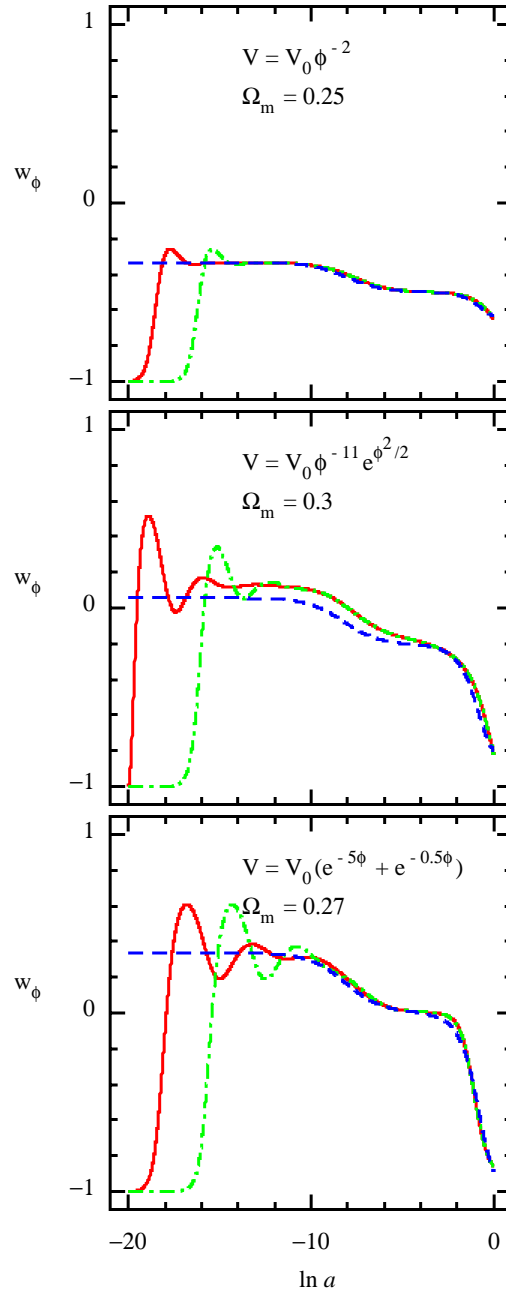


Figure 2.2: Examples of tracking models. The solid red lines and dot-dashed green lines are numerical solutions of w_ϕ with different ϕ_{ini} . Upper panel: $\phi_{\text{ini;red}} = 10^{-7}M_{\text{p}}$, and $\phi_{\text{ini;green}} = 10^{-6}M_{\text{p}}$. Middle panel: $\phi_{\text{ini;red}} = 0.01M_{\text{p}}$, and $\phi_{\text{ini;green}} = 0.03M_{\text{p}}$. Lower panel: $\phi_{\text{ini;red}} = -12.5M_{\text{p}}$, and $\phi_{\text{ini;green}} = -10.5M_{\text{p}}$. The dashed blue lines are $w(a)$ trajectories calculated with the three-parameter $w(a)$ ansatz (2.28). The rapid rise at the beginning is the a^{-6} race of ϵ_ϕ from our start of zero initial momentum towards the attractor.

dynamics in thawing models. The different realizations of the w_ϕ trajectories are produced by choosing different values for the potential parameters – λ for the upper panel, and V_0 for the middle and lower panels. The initial values of ϕ are chosen to ensure $\Omega_\phi(a = 1) = 1 - \Omega_{m0}$ is satisfied. We see that in general our $w_\phi(a)$ parametrization works well up to $|1 + w| \sim 0.5$. The case shown in the bottom panel is the potential of a pseudo Nambu Goldstone boson, which has been much discussed for early universe inflation due to ϕ being an angular variable with a 2π shift symmetry that is easier to protect from acquiring large mass terms, and has been invoked for late universe inflation as well [101].

In Figure 2.4 we demonstrate how the parameter ζ_s improves our parametrization to sub-percent level. In the slow-roll regime, the ζ_s correction is small, and both the two- and three-parameter formulas can fit the numerical solution well. But the ζ_s correction becomes important in the moderate-roll regime.

The last example, shown in Figure 2.5, is a phantom model.

2.4 Observational Constraints

In this section we compile the updated cosmological data sets and use them to constrain the quintessence and phantom models.

2.4.1 Current Data Sets Used

For each of the data sets used in this chapter we either wrote a new module to calculate the likelihood or modified the CosmoMC likelihood code to include dynamic w models.

Cosmic Microwave Background (CMB)

Our complete CMB data sets include WMAP-7yr [1, 2], ACT [117], BICEP [118], QUaD [119], ACBAR [120, 121, 122, 123], CBI [124, 125, 126, 127], BOOMERANG [3, 4, 5], VSA [128], and MAXIMA [129].

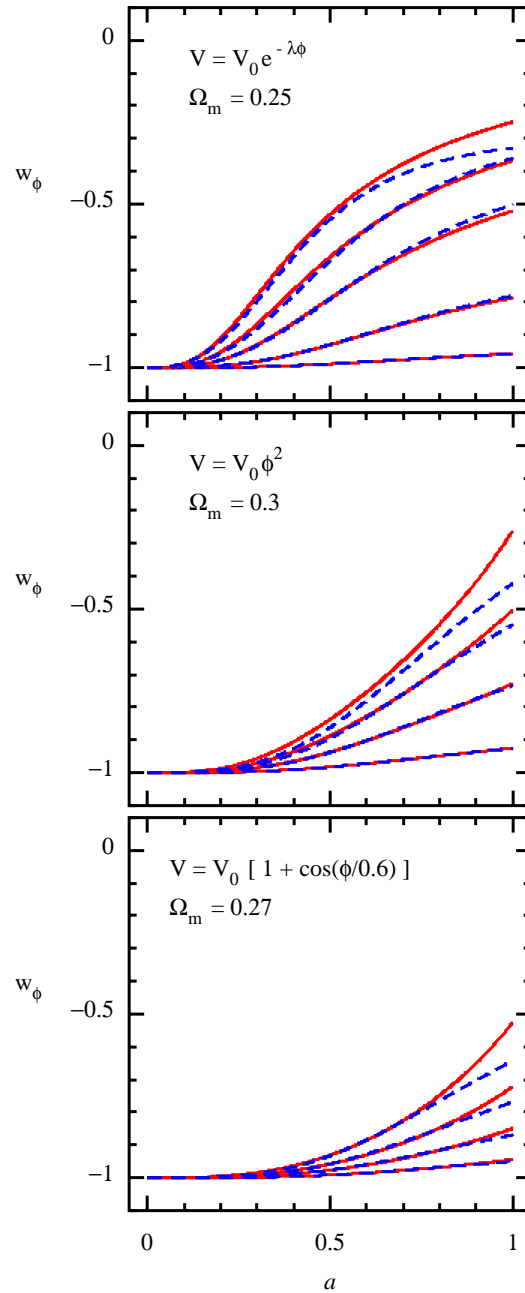


Figure 2.3: Examples of thawing models. The solid red lines are numerical solutions of w_ϕ . The dashed blue lines are calculated using the three-parameter $w(a)$ formula (2.28). See the text for more details.

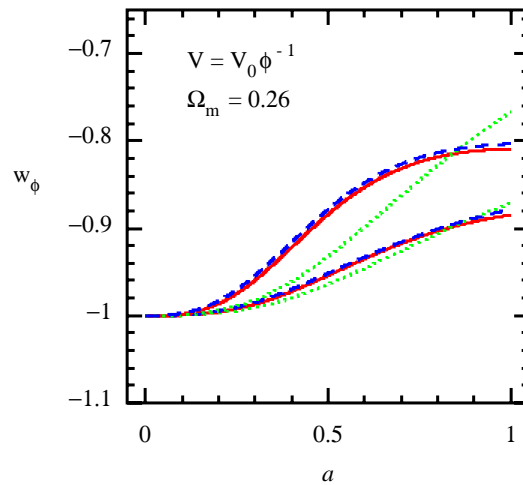


Figure 2.4: An example showing how the ζ_s parameter improves our parametrization in the moderate-roll case. The solid red lines are numerical solutions of w_ϕ . The dashed blue lines are $w(a)$ trajectories calculated with the three-parameter ansatz (2.28). The dotted green lines are two-parameter approximations obtained by forcing $\zeta_s = 0$.

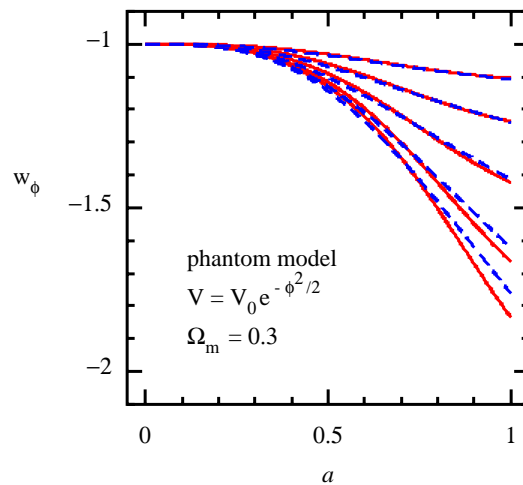


Figure 2.5: An example of phantom model. The solid red lines are numerical solutions of w_ϕ . The dashed blue lines are $w(a)$ trajectories calculated with the three-parameter $w(a)$ formula (2.28).

For high resolution CMB experiments we need to take account of other sources of power beyond the primary CMB. We always include the CMB lensing contribution even though with current data its influence is not yet strongly detected [120]. For most high resolution data sets, radio sources have been subtracted and residual contributions have been marginalized over [117]. However, other frequency-dependent sources will be lurking in the data, and they too should be marginalized over. We follow a well-worn path for treating the thermal Sunyaev-Zeldovich (SZ) secondary anisotropy [130, 131]: we use a power template from a gasdynamical cosmological simulation (with heating only due to shocks) described in [132, 133] with an overall amplitude multiplier A_{SZ} , as was used in the CBI and ACBAR papers. This template does not differ by much from the more sophisticated ones obtained by [134] that include cooling and feedback. Other SZ template choices with different shapes and amplitudes [135, 136] have been made by WMAP and ACT and SPT, and as a robustness alternative by CBI. A key result is that as long as the “nuisance parameter” A_{SZ} is marginalized, other cosmological parameters do not vary much as the SZ template changes. We make no other use of A_{SZ} here, although it can encode the tension between the cosmology derived from the CMB primary anisotropy and the predictions for the SZ signal in that cosmology.

In addition to thermal SZ, there are a number of other sources: kinetic SZ with a power spectrum whose shape roughly looks like the thermal SZ one [134]; sub-mm dusty galaxy sources, which have clustering contributions in addition to Poisson fluctuations. Thermal SZ is a small effect at WMAP and Boomerang resolution. At CBI’s 30 GHz, kinetic SZ is small compared with thermal SZ, but it is competitive at ACBAR, QUaD’s and ACT’s 150 GHz and of course dominates at the ~ 220 GHz thermal-SZ null, but the data is such that little would be added by separately modelling the frequency dependence and shape difference of it, so de facto it is bundled into the generic A_{SZ} of the frequency-scaled thermal-SZ template. We

chose not to include the SPT data in our treatment because the influence of the sub-mm dusty galaxy sources should be simultaneously modelled, and where its band-powers lie (beyond $\ell \sim 2000$), the primary SZ power is small.

Type Ia Supernova (SN)

We use the Kessler et al [27] data set, which combines the SDSS-II SN samples with the data from the ESSENCE project [137, 138], the Supernova Legacy Survey (SNLS) [26], the Hubble Space Telescope (HST) [139, 140, 141, 142], and a compilation of nearby SN measurements. Two light curve fitting methods, MLCS2K2 and SALT-II, are employed in [27]. The different assumptions about the nature of the SN color variation lead to a significant apparent discrepancy in w . For definiteness, we choose the SALT-II-fit results in this chapter, but caution that if we had tried to assign a systematic error to account for the differences in the two methods the error bars we obtain would open up, and the mean values for $1 + w$ may not centre as much around zero as we find.

Large Scale Structure (LSS)

The LSS data are for the power spectrum of the Sloan Digital Sky Survey Data Release 7 (SDSS-DR7) Luminous Red Galaxy (LRG) samples [143]. We have modified the original LSS likelihood module to make it compatible with time-varying w models.

Weak Lensing (WL)

Five WL data sets are used in this chapter. The effective survey area A_{eff} and galaxy number density n_{eff} of each survey are listed in Table 2.1.

For the COSMOS data, we use the CosmoMC plug-in written by Julien Lesgourgues [145] with our modifications for dynamic dark energy models.

For the other four weak lensing data sets we use the covariance matrices given by

Table 2.1: Weak Lensing Data Sets

Data sets	A_{eff} (deg ²)	n_{eff} (arcmin ⁻²)
COSMOS[144, 145]	1.6	40
CFHTLS-wide[146, 147]	22	12
GaBODS[148, 149]	13	12.5
RCS[148, 149]	53	8
VIRMOS-DESCART[150, 147]	8.5	15

[151]. To calculate the likelihood we wrote a CosmoMC plug-in code. We take the best fit parameters α, β, z_0 for $n(z) \propto (z/z_0)^\alpha \exp[-(z/z_0)^\beta]$, and marginalize over z_0 , assuming a Gaussian prior with a width such that the mean redshift z_m has an uncertainty of $0.03(1+z_m)$. We have checked that further marginalizing over other $n(z)$ parameters (α and β) has no significant impact [58].

Lyman- α Forest ($Ly\alpha$)

Two $Ly\alpha$ data sets are applied: i) the set from [152] consisting of the LUQAS sample [153] and the data given in [154]; ii) the SDSS $Ly\alpha$ data presented in [155] and [156]. To calculate the likelihood we interpolate the χ^2 table in a three dimensional parameter space, where the three parameters are amplitude, index, and the running of linear CDM power spectrum at pivot $k = 0.9h \text{ Mpc}^{-1}$.

Other Constraints

We have also used in CosmoMC the following observational constraints: i) the distance-ladder constraint on Hubble parameter, obtained by the Hubble Space Telescope (HST) Key Project [20]; ii) constraints from the Big Bang Nucleosynthesis (BBN): $\Omega_b h^2 = 0.022 \pm 0.002$ (Gaussian prior) and $\Omega_\Lambda(z = 10^{10}) < 0.2$ [157, 158, 159, 160, 28]; iii) an isotopic constraint on the age of universe $10\text{Gyr} <$

Age < 20Gyr [161]. For the combined data sets, none of these add much. They are useful if we are looking at the impact of the various data sets in isolation on constraining our parameters.

2.4.2 CosmoMC Results for Current Data

Using our modified CosmoMC, we ran Markov Chain Monte Carlo (MCMC) calculations to determine the likelihood of cosmological parameters, which include the standard six, A_{SZ} and our DE parameters, w_0-w_a for Fig. 2.1 and the new ones ε_s , $|\varepsilon_{\phi\infty}|/\epsilon_m$ and ζ_s for most of the rest. Here we use $|\varepsilon_{\phi\infty}|/\epsilon_m$ as a fundamental parameter to eliminate the dependence of $\varepsilon_{\phi\infty}$ on ϵ_m and the sign of ε_s , whereas $\varepsilon_{\phi\infty}$ adjusts as one evolves from a relativistic to non-relativistic matter EOS. The main results are summarized in Table 2.2. The basic six are: $\Omega_{b0}h^2$, proportional to the current physical density of baryons; $\Omega_{c0}h^2$, the physical cold dark matter density; θ , the angle subtended by sound horizon at “last scattering” of the CMB, at $z \sim 1100$; $\ln A_s$, with A_s the primordial scalar metric perturbation power evaluated at pivot wavenumber $k = 0.002\text{Mpc}^{-1}$; n_s , the spectral index of primordial scalar metric perturbation; τ , the reionization Compton depth. The measures on each of these variables is taken to be uniform. Derived parameters include z_{re} , the reionization redshift; Age/Gyr, the age of universe in units of gigayears; σ_8 , today’s amplitude of the linear-extrapolated matter density perturbations over an top-hat spherical window with radius $8h^{-1}\text{Mpc}$. And, of great importance for DE, Ω_{m0} ; and H_0 in unit of $\text{km s}^{-1}\text{Mpc}^{-1}$, which set the overall energy scale of late-inflatons.

We begin with our versions of the familiar contour plots that show how the various data sets combine to limit the size of the allowed parameter regions. Figures 2.6 and 2.7 shows the best-fit cosmological parameters do depend on the specific subset of the data that is used. We find most cosmological parameters are stable when we vary the choice of data sets, The data making the largest differences are: the SDSS-DR7-LRG data driving Ω_m up, and the Ly α data driving σ_8 up. We take SN+CMB as a “basis”, for which

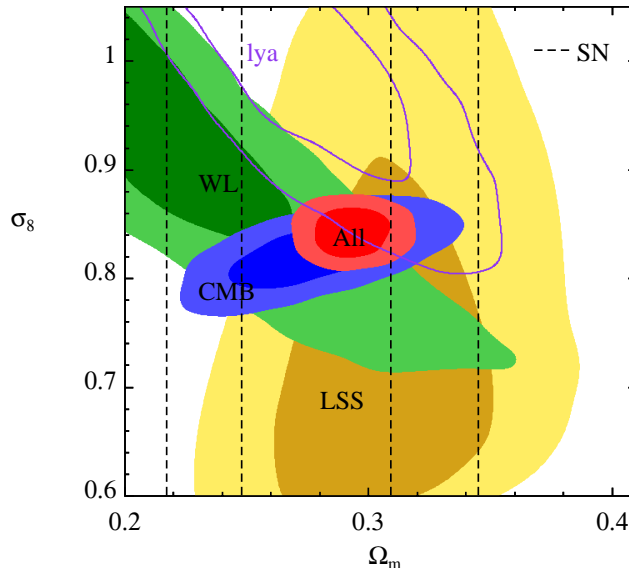


Figure 2.6: The marginalized 68.3% CL and 95.4% CL constraints on σ_8 and Ω_{m0} for the Λ CDM model vary with different choices of data sets. For each data set a HST constraint on H_0 and BBN constraint on $\Omega_{b0}h^2$ have been used.

$\Omega_{m0} = 0.267^{+0.019}_{-0.018}$ and $\sigma_8 = 0.817^{+0.023}_{-0.021}$. Adding LSS pushes Ω_{m0} to $0.292^{+0.011}_{-0.010}$; whether or not WL and Ly α are added or not is not that relevant, as Figure 2.6 shows. Ly α pushes σ_8 to $0.844^{+0.015}_{-0.016}$. These drifts of best-fit values are at the $\sim 2\sigma$, level in terms of the σ 's derived from using all of the data sets, as is evident visually in Figure 2.6.

Figure 2.7 shows how the combination of complementary data sets constrains ε_s and Ω_{m0} , the two key parameters that determine low-redshift observables. The label “All” refers to all the data sets described in this section, and “CMB” refers to all CMB data sets, and so forth. In Figure 2.9, marginalized 2D likelihood contours are shown for all our DE parameters. The left panel shows that the slope parameter ε_s and tracking parameter $\varepsilon_{\phi\infty}$ are both constrained. The constraint on ε_s limits how steep the potential could be at low redshift. The upper bound of $\varepsilon_{\phi\infty}$ indicates that the field can not be rolling too fast at intermediate redshift $z \sim 1$. The right panel shows that ζ_s is not constrained, and is almost uncorrelated with ε_s . This is because the current observational data favors

Table 2.2: Cosmic Parameter Constraints: Λ CDM, w_0 -CDM, w_0 - w_a -CDM, ε_s - $\varepsilon_{\phi\infty}$ - ζ_s -CDM

	Λ CDM	$w = w_0$	$w=w_0+w_a(1-a)$	track+thaw	thaw
Current Data: CMB+LSS+WL+SN1a+Ly α					
$\Omega_{b0}h^2$	$0.0225^{+0.0004}_{-0.0004}$	$0.0225^{+0.0004}_{-0.0004}$	$0.0225^{+0.0004}_{-0.0004}$	$0.0225^{+0.0004}_{-0.0004}$	$0.0225^{+0.0004}_{-0.0004}$
$\Omega_{c0}h^2$	$0.1173^{+0.0020}_{-0.0019}$	$0.1172^{+0.0024}_{-0.0024}$	$0.1177^{+0.0025}_{-0.0023}$	$0.1174^{+0.0029}_{-0.0029}$	$0.1175^{+0.0023}_{-0.0022}$
θ	$1.042^{+0.002}_{-0.002}$	$1.042^{+0.002}_{-0.002}$	$1.042^{+0.003}_{-0.002}$	$1.042^{+0.003}_{-0.002}$	$1.0417^{+0.0021}_{-0.0021}$
τ	$0.089^{+0.014}_{-0.013}$	$0.090^{+0.015}_{-0.014}$	$0.088^{+0.014}_{-0.013}$	$0.090^{+0.015}_{-0.014}$	$0.088^{+0.015}_{-0.014}$
n_s	$0.96^{+0.01}_{-0.01}$	$0.96^{+0.01}_{-0.01}$	$0.96^{+0.01}_{-0.01}$	$0.96^{+0.01}_{-0.01}$	$0.958^{+0.011}_{-0.011}$
$\ln(10^{10}A_s)$	$3.24^{+0.03}_{-0.03}$	$3.24^{+0.03}_{-0.03}$	$3.24^{+0.03}_{-0.03}$	$3.24^{+0.03}_{-0.03}$	$3.239^{+0.033}_{-0.033}$
A_{SZ}	$0.56^{+0.11}_{-0.15}$	$0.56^{+0.11}_{-0.14}$	$0.57^{+0.11}_{-0.14}$	$0.56^{+0.11}_{-0.14}$	$0.56^{+0.11}_{-0.14}$
Ω_m	$0.292^{+0.011}_{-0.010}$	$0.294^{+0.012}_{-0.012}$	$0.293^{+0.012}_{-0.012}$	$0.293^{+0.015}_{-0.014}$	$0.293^{+0.013}_{-0.011}$
σ_8	$0.844^{+0.015}_{-0.016}$	$0.841^{+0.026}_{-0.026}$	$0.847^{+0.026}_{-0.026}$	$0.844^{+0.035}_{-0.036}$	$0.844^{+0.024}_{-0.023}$
z_{re}	$10.8^{+1.2}_{-1.1}$	$10.9^{+1.2}_{-1.2}$	$10.7^{+1.1}_{-1.1}$	$10.9^{+1.2}_{-1.2}$	$10.8^{+1.2}_{-1.2}$
H_0	$69.2^{+1.0}_{-1.0}$	$69.0^{+1.4}_{-1.4}$	$69.2^{+1.4}_{-1.4}$	$69.0^{+1.9}_{-1.8}$	$69.1^{+1.4}_{-1.4}$
w_0	...	$-0.99^{+0.05}_{-0.06}$	$-0.98^{+0.14}_{-0.11}$
w_a	$-0.05^{+0.35}_{-0.58}$
ε_s	$0.00^{+0.18}_{-0.17}$	$-0.00^{+0.27}_{-0.29}$
$ \varepsilon_{\phi\infty} /\varepsilon_m$	$0.00^{+0.21+0.58}$...
ζ_s	n.c.	...
Forecasted Data Planck2.5yr + low-z-BOSS + CHIME + Euclid-WL + JDEM-SN					
$\Omega_{b0}h^2$	$0.02200^{+0.00007}_{-0.00007}$	$0.02200^{+0.00007}_{-0.00007}$	$0.02200^{+0.00007}_{-0.00008}$	$0.02200^{+0.00007}_{-0.00008}$	$0.02200^{+0.0007}_{-0.0007}$
$\Omega_{c0}h^2$	$0.11282^{+0.00024}_{-0.00023}$	$0.11280^{+0.00027}_{-0.00027}$	$0.11282^{+0.00026}_{-0.00029}$	$0.1128^{+0.0003}_{-0.0003}$	$0.1128^{+0.0003}_{-0.0003}$
θ	$1.0463^{+0.0002}_{-0.0002}$	$1.0463^{+0.0002}_{-0.0002}$	$1.0463^{+0.0003}_{-0.0002}$	$1.0463^{+0.0002}_{-0.0002}$	$1.0463^{+0.0002}_{-0.0002}$
τ	$0.090^{+0.003}_{-0.003}$	$0.090^{+0.004}_{-0.004}$	$0.090^{+0.004}_{-0.004}$	$0.090^{+0.005}_{-0.005}$	$0.090^{+0.004}_{-0.004}$
n_s	$0.970^{+0.002}_{-0.002}$	$0.970^{+0.002}_{-0.002}$	$0.970^{+0.002}_{-0.002}$	$0.970^{+0.002}_{-0.002}$	$0.970^{+0.002}_{-0.002}$
$\ln(10^{10}A_s)$	$3.115^{+0.008}_{-0.008}$	$3.115^{+0.009}_{-0.009}$	$3.115^{+0.009}_{-0.009}$	$3.115^{+0.010}_{-0.010}$	$3.115^{+0.009}_{-0.009}$
Ω_m	$0.260^{+0.001}_{-0.001}$	$0.261^{+0.002}_{-0.002}$	$0.260^{+0.003}_{-0.003}$	$0.2609^{+0.0022}_{-0.0022}$	$0.2605^{+0.0027}_{-0.0024}$
σ_8	$0.7999^{+0.0016}_{-0.0017}$	$0.7994^{+0.0023}_{-0.0025}$	$0.800^{+0.003}_{-0.003}$	$0.7992^{+0.0027}_{-0.0027}$	$0.7996^{+0.0026}_{-0.0029}$
z_{re}	$10.9^{+0.3}_{-0.3}$	$10.9^{+0.3}_{-0.3}$	$10.9^{+0.3}_{-0.3}$	$10.9^{+0.3}_{-0.4}$	$10.9^{+0.3}_{-0.3}$
H_0	$72.0^{+0.1}_{-0.1}$	$71.9^{+0.3}_{-0.3}$	$72.0^{+0.4}_{-0.4}$	$71.85^{+0.37}_{-0.29}$	$71.94^{+0.34}_{-0.36}$
w_0	...	$-1.00^{+0.01}_{-0.01}$	$-1.00^{+0.03}_{-0.03}$
w_a	$0.01^{+0.08}_{-0.08}$
ε_s	$0.005^{+0.031}_{-0.025}$	$0.008^{+0.056}_{-0.054}$
$ \varepsilon_{\phi\infty} /\varepsilon_m$	$0.000^{+0.034+0.093}$...
ζ_s	n.c.	n.c.

Tracking + thawing models use $w_{de}(a|\varepsilon_s, \varepsilon_{\phi\infty}, \zeta_s)$ of Eq. (2.28). Thawing enforces $\varepsilon_{\phi\infty} = 0$. n.c. stands for “not constrained”. H_0 has unit $\text{km s}^{-1}\text{Mpc}^{-1}$. θ is in unit $\text{rad}/100$.

Table 2.3: The marginalized 68.3%, 95.4%, and 99.7% CL constraints on ε_s under different prior assumptions.

Prior	Constraint
flat prior on ε_s	$\varepsilon_s = 0.00^{+0.18+0.39+0.72}_{-0.17-0.44-0.82}$
flat prior on $\sqrt{ \varepsilon_s }$	$\varepsilon_s = 0.00^{+0.09+0.27+0.46}_{-0.07-0.28-0.52}$
thawing prior $\varepsilon_{\phi_\infty} = 0$	$\varepsilon_s = 0.00^{+0.27+0.53+0.80}_{-0.29-0.61-0.98}$
slow-roll thawing $\varepsilon_{\phi_\infty} = \zeta_s = 0$	$\varepsilon_s = -0.01^{+0.26+0.50+0.70}_{-0.28-0.59-0.86}$
quintessence $\varepsilon_s > 0$	$\varepsilon_s = 0.00^{+0.18+0.39+0.76}$

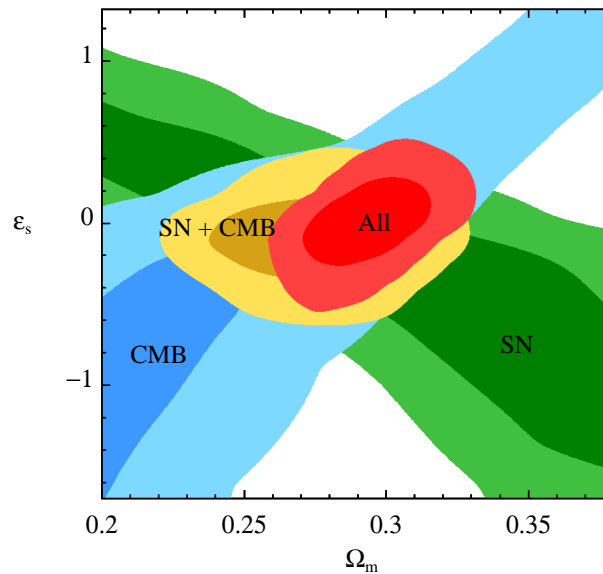


Figure 2.7: The marginalized 68.3% CL and 95.4% CL constraints on ε_s and Ω_{m0} , using different (combinations) of data sets. This is the key DE plot for late-inflaton models of energy scale, encoded by $1 - \Omega_{m0}$ and potential gradient defining the roll-down rate, $\sqrt{\varepsilon_s}$.

slow-roll ($|1 + w_\phi| \ll 1$), in which case the ζ_s correction in w_ϕ is very small. Another way to interpret this is that a slowly rolling field does not “feel” the curvature of potential. In Section 2.6 we will discuss the meaning and measurement of ζ_s in more detail.

Because of the correlation between ε_s and $\varepsilon_{\phi\infty}$, the marginalized likelihood of ε_s depends on the prior of $\varepsilon_{\phi\infty}$. On the other hand, the constraint on ε_s will also depend on the prior on ε_s itself. For example, we can apply a flat prior on $d \ln V / d\phi|_{a=a_{\text{eq}}}$, rather than a flat prior on the squared slope ε_s . Other priors we have tried are the “thawing prior” $\varepsilon_{\phi\infty} = 0$, the “quintessence prior” $\varepsilon_s > 0$, and “slow-roll thawing prior” $\varepsilon_{\phi\infty} = \zeta_s = 0$. The results are summarized in Table 2.3.

In Figure 2.8 we show the reconstructed trajectories of the dark energy EOS, Hubble parameter, distance moduli, and the growth factor D of linear perturbations. The w_ϕ information has also been compressed into a few bands with errors, although that is only to guide the eye. The off-diagonal correlation matrix elements between bands is large, encoding the coherent nature of the trajectories. As well, the likelihood surface in all w_ϕ -bands is decidedly non-Gaussian, and should be characterized for this information to be statistically useful in constraining models by itself. The other variables shown involve integrals of w_ϕ , and thus are not as sensitive to detailed rapid change aspects of w_ϕ , which, in any case, our late-inflaton models do not give. The bottom panels show how impressive the constraints on trajectory bundles should become with planned experiments, a subject to which we now turn.

2.5 Future Data Forecasts

In this section ,we discuss the prospects for further constraining the parameters of the new $w(a)$ parameterization using a series of forthcoming or proposed cosmological observations: from the Planck satellite CMB mission [162, 163, 51]; from a JDEM (Joint Dark Energy Mission, [71]) for Type Ia supernova observations; from a weak lensing sur-

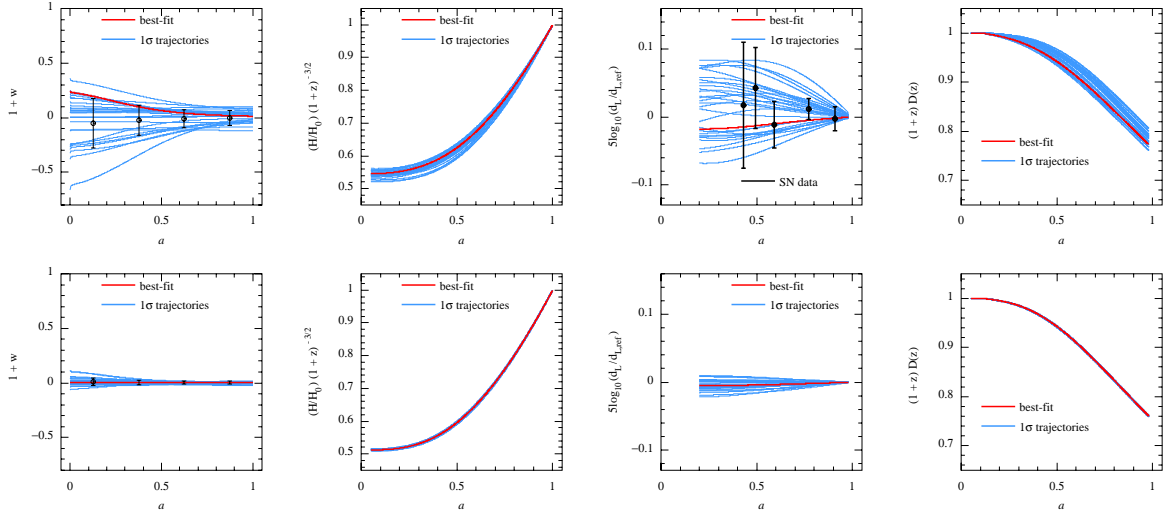


Figure 2.8: The best-fit trajectory (heavy curve) and a sample of trajectories that are within one-sigma (68.3% CL). In the upper panels the current data sets are used, and lower panels the forecast mock data. From left to right the trajectories are the dark energy equation of state, the Hubble parameter rescaled with $H_0^{-1}(1+z)^{3/2}$, the distance moduli with a reference Λ CDM model subtracted, and the growth factor of linear perturbation rescaled with a factor $(1+z)$ (normalized to be unit in the matter dominated regime). The current supernova data is plotted against the reconstructed trajectories of distance moduli. The error bars shown in the upper-left and lower-left panels are one- σ uncertainties of $1+w$ in bands $0 < a \leq 0.25$, $0.25 < a \leq 0.5$, $0.5 < a \leq 0.75$ and $0.75 < a \leq 1$.

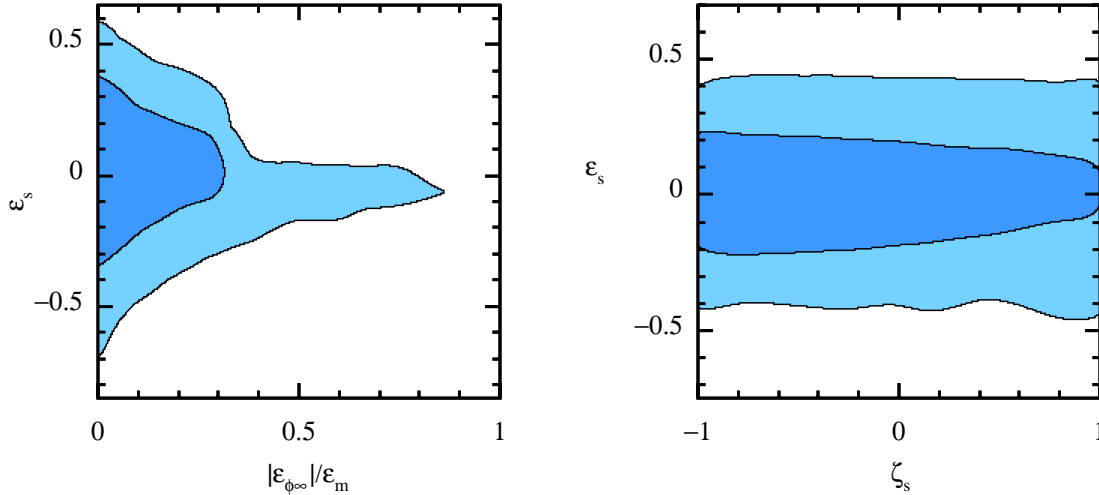


Figure 2.9: Marginalized 2D likelihood contours for our three DE parameters derived using “ALL” current observational data. The inner and outer contours are 68.3% CL and 95.4% CL contours. (We actually show $|\epsilon_{\phi\infty}|/\epsilon_m$ since that is the attractor whether one is in the relativistic $\epsilon_m = 2$ or non-relativistic $\epsilon_m = 3/2$ regime.)

Table 2.4: Fiducial model used in future data forecasts

$\Omega_{b0}h^2$	$\Omega_{c0}h^2$	h	σ_8	n_s	τ
0.022	0.1128	0.72	0.8	0.97	0.09

vey by the Euclid satellite [164]; and from future BAO data that could be obtained by combining low-redshift galaxy surveys with a redshifted-21-cm survey of moderate $z \sim 2$. The low-redshift galaxy surveys for BAO information can be achieved by combining a series of ground-based galaxy observations, such as BOSS [165]. For the 21-cm survey, we assume a $200\text{m} \times 200\text{m}$ ground-based cylinder radio telescope [166, 167, 168], which is the prototype of the proposed experiment CHIME (Canadian Hydrogen Intensity Mapping Experiment).

Table 2.5: Planck Instrument Characteristics

Channel Frequency (GHz)	70	100	143
Resolution ^a (arcmin)	14	10	7.1
Sensitivity ^b - intensity (μK)	8.8	4.7	4.1
Sensitivity - polarization (μK)	12.5	7.5	7.8

- a. Full width at half maximum (FWHM) assuming Gaussian beams.
b. This is for 30 months of integration.

2.5.1 The mock data sets

Planck CMB simulation

Planck 2.5 years (5 sky surveys) of multiple (CMB) channel data are used in the forecast, with the instrument characteristics for the channels used listed in Table 2.5 using Planck “Blue Book” detector sensitivities and the values given for the full width half maxima.

For a nearly full-sky (we use $f_{\text{sky}} = 0.75$) CMB experiment, the likelihood \mathcal{L} can be approximated with the following formula [169]:

$$\begin{aligned}
-2 \ln \mathcal{L} = & \sum_{l=l_{\min}}^{l_{\max}} (2l+1) f_{\text{sky}} \left[-3 + \frac{\hat{C}_l^{BB}}{C_l^{BB}} + \ln \left(\frac{C_l^{BB}}{\hat{C}_l^{BB}} \right) + \ln \left(\frac{C_l^{TT} C_l^{EE} - (C_l^{TE})^2}{\hat{C}_l^{TT} \hat{C}_l^{EE} - (\hat{C}_l^{TE})^2} \right) \right. \\
& \left. + \frac{\hat{C}_l^{TT} C_l^{EE} + \hat{C}_l^{EE} C_l^{TT} - 2\hat{C}_l^{TE} C_l^{TE}}{C_l^{TT} C_l^{EE} - (C_l^{TE})^2} \right], \tag{2.41}
\end{aligned}$$

where $l_{\min} = 3$ and $l_{\max} = 2500$ have been used in our calculation. Here, \hat{C}_l is the observed (or simulated input) angular power spectrum, and C_l is the theoretical power spectrum plus noise.

We use the model described in [170] and [169] to propagate the effect of polarization foreground residuals into the estimated uncertainties on the cosmological parameters. For simplicity, only the dominating components in the frequency bands we are using, i.e., the synchrotron and dust signals, are considered in our simulation. The fraction of

the residual power spectra are all assumed to be 5%.

JDEM SN simulation

For the JDEM SN simulation, we use the model given by the Dark Energy Task Force (DETF) forecast [71], with roughly 2500 spectroscopic supernova at $0.03 < z < 1.7$ and 500 nearby samples. The apparent magnitude of SN is modelled as

$$m = M + 5 \log_{10} \left(\frac{d_L}{\text{Mpc}} \right) + 25 - \mu^L z - \mu^Q z^2 - \mu^S \delta_{\text{near}} , \quad (2.42)$$

where δ_{near} is unity for the nearby samples and zero otherwise.

There are four nuisance parameters in this model. The supernova absolute magnitude is expanded as a quadratic function $M - \mu^L z - \mu^Q z^2$ to account for the possible redshift dependence of the SN peak luminosity, where M is a free parameter with a flat prior over $-\infty < M < +\infty$; and for μ^L and μ^Q , Gaussian priors $\mu^{L,Q} = 0.00 \pm 0.03/\sqrt{2}$ (the ‘‘pessimistic’’ case in the DETF forecast) are applied. Finally, given that the near by samples are obtained from different projects, an offset μ^S is added to the nearby samples only. For μ^S we apply a Gaussian prior $\mu^S = 0.00 \pm 0.01$.

The intrinsic uncertainty in the supernova absolute magnitude is assumed to be 0.1, to which an uncertainty due to a peculiar velocity 400 km/s is quadratically added.

BAO simulation

The ‘‘Baryon Acoustic Oscillations’’ (BAO) information can be obtained by combining a series of ground-based low-redshift galaxy surveys with a high-redshift 21-cm survey. We assume a fiducial galaxy survey with comoving galaxy number density $0.003h^3\text{Mpc}^{-3}$ and sky coverage $20,000 \text{ deg}^2$, which is slightly beyond, but not qualitatively different from the specification of SDSS-III BOSS (Baryon Oscillation Spectroscopic Survey) project. The 21-cm BAO survey using a ground-based cylinder radio telescope has been studied by [166, 167] and [171]. The specifications we have used are listed in Table 2.6.

Table 2.6: 21-cm BAO Survey Specifications

Parameter	Specification
shot noise	$0.01h^3\text{Mpc}^{-3}$
survey area	15,000 deg ²
number of receivers	4000
integration time	4 years
cylinder telescope	200 m \times 200 m
antenna temperature	50K
bias	1

For more details about the BAO forecast technique, the reader is referred to [172] and [171].

EUCLID Weak Lensing Simulation

We assume a weak lensing survey with the following ‘‘Yellow Book’’ EUCLID specifications [164]:

$$f_{\text{sky}} = 0.5, \langle \gamma_{\text{int}}^2 \rangle^{1/2} = 0.35, \bar{n} = 40 \text{ galaxies/arcmin}^2, \quad (2.43)$$

where $\langle \gamma_{\text{int}}^2 \rangle^{1/2}$ is the intrinsic galaxy ellipticity, and \bar{n} is the average galaxy number density being observed. At high ℓ , the non-Gaussianity of the dark matter density field becomes important [173]. For simplicity we use a ℓ -cutoff $\ell_{\text{max}} = 2500$ to avoid modelling the high- ℓ non-Gaussianity, which will provide more cosmic information, hence the weak lensing constraints shown in this chapter are conservative.

We use a fiducial galaxy distribution,

$$n(z) \propto \left(\frac{z}{z_0}\right)^2 \exp\left[-\left(\frac{z}{z_0}\right)^{1.5}\right], \text{ with } z_0 = 0.6. \quad (2.44)$$

The galaxies are divided into four tomography bins, with the same number of galaxies in each redshift bin. The uncertainty in the median redshift in each redshift bin is assumed to be $0.004(1 + z_m)$, where z_m is the median redshift in that bin.

In the ideal case in which the galaxy redshift distribution function is perfectly known, the formula for calculating weak lensing tomography observables and covariance matrices can be found in e.g. [174]. In order to propagate the uncertainties of photo-z parameters onto the uncertainties of the cosmological parameters, we ran Monte Carlo simulations to obtain the covariance matrices due to redshift uncertainties, which are then added to the ideal covariance matrices.

2.5.2 Results of the Forecasts

The constraints on cosmological parameters from future experiments are shown in Table 2.2 below those for current data. The future observations should improve the measurement of ε_s significantly – about five times better than the current best constraint. There is also a significant improvement on the upper bound of $\varepsilon_{\phi\infty}$, which together with the constraint on ε_s can be used to rule out many tracking models. The running parameter ζ_s remains unconstrained.

To compare different dark energy probes, in Figure 2.10 we plot the marginalized constraints on Ω_{m0} and ε_s for different data sets. To break the degeneracy between dark energy parameters and other cosmological parameters, we apply the Planck-only CMB constraints as a prior on each of the non-CMB data sets.

The forecasted BAO, WL, and SN results, when combined with the Planck prior, are all comparable. We note in particular that the ground-based BAO surveys deliver similar measurements at a fraction of the cost of the space experiments, although of course much useful collateral information will come from all of the probes.

The shrinkage in the allowed parameter space is visualized in Figure 2.8 through the decrease in area of the trajectory bundles from current to future data, showing trajectories

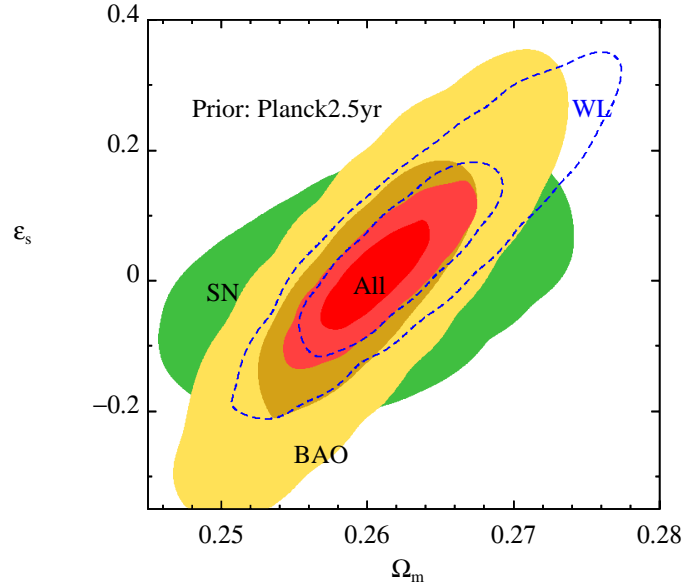


Figure 2.10: Marginalized 2D likelihood contours; Using mock data and assuming thawing prior ($\varepsilon_{\phi\infty} = 0$); The inner and outer contours of each color correspond to 68.3% CL and 95.4% CL, respectively. See the text for more details.

of $1 + w_\phi$ sampled down to the one-sigma level. We also show the mean and standard deviation of $1 + w$ at the center of four uniform bands in a . As mentioned above, the bands are highly correlated because of the coherence of the trajectories, a consequence of their physical origin. We apply such band analyses to early (as well as late) universe inflation that encodes such smoothing theory priors in future papers.

Figure 2.8 also plots $(1 + z)^{-3/2}(H/H_0) = \sqrt{\rho_{\text{tot}} a^3 / \rho_{\text{tot},0}}$ trajectories, which are flat in the high redshift matter-dominated regime. They are less spread out than the w bundle because H depends upon an integral of w . One of the observable quantities measured with supernovae is the luminosity distance. What we plot is something more akin to relative magnitudes of standard candles, $5 \log_{10}(d_L/d_{L,\text{ref}})$, in terms of $d_{L,\text{ref}}$, the luminosity distance of a reference Λ CDM model. For luminosity distance trajectories reconstructed with the current data we choose a reference model with $\Omega_{m0} = 0.29$, which the SDSS LSS data drove us to; for forecasts, we chose $\Omega_{m0} = 0.26$, what the other

current data is more compatible with, for the reference. Because the supernova data only measure the ratio of luminosity distances, for each trajectory we normalize $d_L/d_{L,\text{ref}}$ to be unit in the low-redshift limit by varying H_0 in the reference model. The error bars shown are for the current supernova data [27], showing compatibility with Λ CDM, and, based upon the coherence of the quintessence-based prior and the large error bars, little flexibility in trying to fit the rise and fall of the data means.

The rightmost panels of Figure 2.8 shows the linear growth factor for dark matter fluctuations relative to the expansion factor, $(1+z)D(z)$. The normalization is such that it is unity in the matter-dominated regime. It should be determined quite precisely for the quintessence prior with future data.

2.6 Discussion and Conclusions

2.6.1 Slow-roll Thawing Models, Their One-parameter Approximation and the Burn-in to It

In slow-roll thawing models, to first order $w(z)$ only depends on two physical quantities: one determining “when to roll down”, quantified mostly by $1 - \Omega_{m0}$, and one determining “how fast to roll down”, quantified by the slope of the potential, *i.e.*, ε_s , since $\varepsilon_{\phi\infty} = 0$, and $\zeta_s \approx 0$:

$$1 + w_\phi|_{\text{slowroll,thawing}} \approx \frac{2\varepsilon_s}{3} F^2\left(\frac{a}{a_{\text{eq}}}\right), \quad (2.45)$$

where F is an analytical function given by Eq. (2.26), and

$$a_{\text{eq}}|_{\text{slowroll,thawing}} \approx \left(\frac{\Omega_{m0}}{1 - \Omega_{m0}}\right)^{1/[3-1.08(1-\Omega_{m0})\varepsilon_s]}, \quad (2.46)$$

to sufficient accuracy. We plot $F^2(x)$ in the left panel of Figure 2.11. It is zero in the small a regime and unity in the large a regime, and at a_{eq} is $F^2(1) = [\sqrt{2} - \ln(1 + \sqrt{2})]^2 \approx 0.284$. The right panel of Figure 2.11 plots the derivative dF^2/dx showing $|dw/da|$

maximizes around $a = a_{\text{eq}}$ (at redshift ~ 0.4). Three stages are evident in the significant time-dependence of dw/da : the Hubble-frozen stage at $a \ll a_{\text{eq}}$, where w has the asymptotic value -1 ; the thawing stage when the dark energy density is comparable to the matter component; and the future inflationary stage where dark energy dominates ($a \gg a_{\text{eq}}$) and a future attractor with $1 + w \rightarrow 2\varepsilon_s/3$ is approached, agreeing with the well-known early-inflation solution $1 + w = 2\varepsilon_V/3$.

Even with such models, there is in principle another parameter: the initial field momentum is unlikely to be exactly on the $\varepsilon_{\phi\infty} = 0$ attractor. In that case, $\dot{\phi}$ falls like a^{-3} until the attractor is reached, a “burn-in” phase. (Such burn-in phases are evident in Fig. 2.2 for tracking models.) In early work on parameterizing late-inflatons we added a parameter a_s to characterize when this drop towards the attractor occurred, and found it could be (marginally) constrained by the data to be small relative to the a -region over which the trajectories feel the DE-probing data. However, we decided to drop this extra parameter for this chapter since the expectation of late-inflaton models is that the attractor would have been established long before the redshift range relevant for DE-probes.

The 3-parameter, 2-parameter and 1-parameter fits all give about the same result for the statistics of ε_s derived from current data. Figure 2.12 illustrates why we find $\varepsilon_s \approx 0.0 \pm 0.28$. It shows the confrontation of banded supernova data on distance moduli defined by

$$\mu \equiv 25 + 5 \log_{10} \left(\frac{d_L}{\text{Mpc}} \right), \quad (2.47)$$

where d_L is the physical luminosity distance, with trajectories in μ with differing values of ε_s (for the h (or $\Omega_{\text{m}0}$) values as described.) The current DE constraints are largely determined by SN, in conjunction with the $\Omega_m h^2$ -fixing CMB.

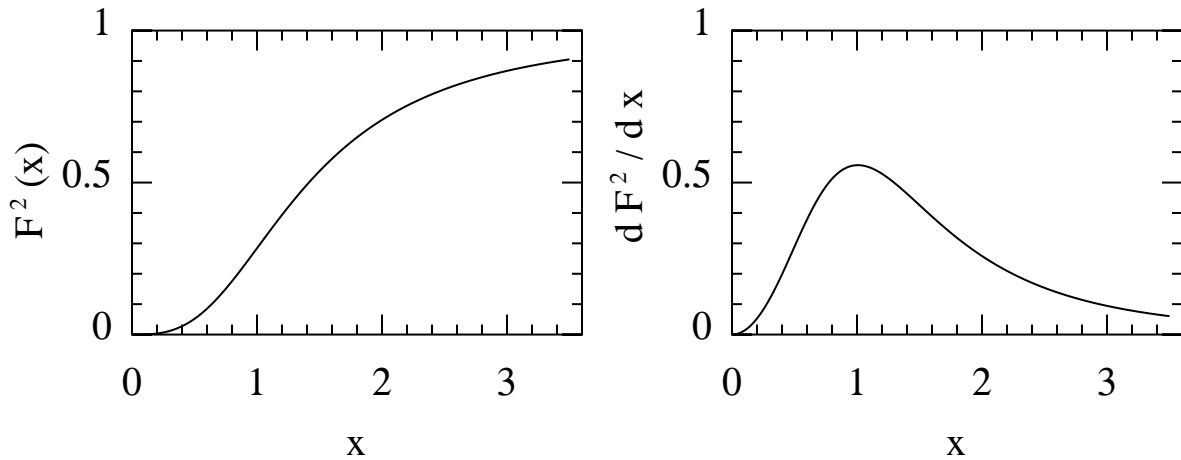


Figure 2.11: Left panel: the function $F^2(x)$ with $x = a/a_{\text{eq}}$ defined by Eq. (2.26). Right Panel: the derivative dF^2/dx , showing where w_ϕ changes most quickly in thawing models, namely near a_{eq} .

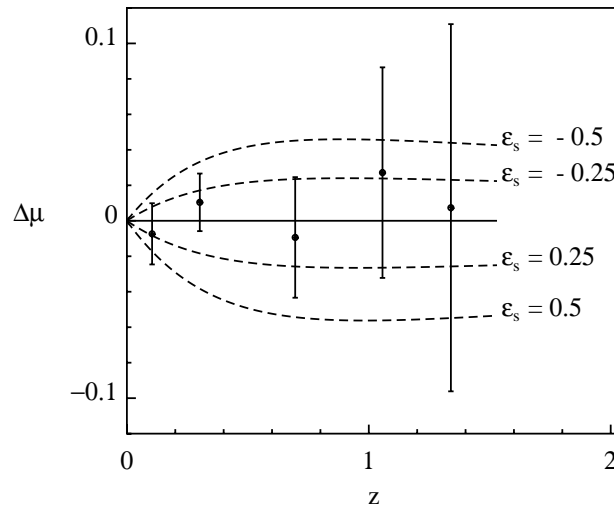


Figure 2.12: The dependence of distance moduli $\mu(z)$ on the slope parameter ε_s for slow-roll thawing models. The prediction of $\mu(z)$ from a reference Λ CDM model with $\Omega_{\text{m}0} = 0.29$ is subtracted from each line. The supernova samples are binned into redshift bins with bin width $\Delta z = 0.3$.

2.6.2 A w_0 - w_a Degeneracy for the Slow-roll Thawing Model Prior

The parameterization (2.45) can be simply related to the phenomenological w_0 - w_a parameterization by a first order Taylor series expansion about a redshift zero pivot:

$$1 + w_0 \equiv \frac{2}{3}\varepsilon_s F^2\left(\frac{1}{a_{\text{eq}}}\right), \quad (2.48)$$

and

$$w_a \equiv -\frac{2}{3}(\varepsilon_s/a_{\text{eq}}) \left. \frac{dF^2(x)}{dx} \right|_{x=1/a_{\text{eq}}}. \quad (2.49)$$

From formula (2.45), it follows that w_0 and w_a should satisfy the linear relation

$$1 + w_0 + w_a(1 - a^*) = 0, \quad (2.50)$$

where

$$a^* = 1 - \frac{\sqrt{1 + a_{\text{eq}}^3} - a_{\text{eq}}^3 \ln\left(\frac{1 + \sqrt{1 + a_{\text{eq}}^3}}{a_{\text{eq}}^{3/2}}\right)}{6a_{\text{eq}}^3 \left[\ln\left(\frac{1 + \sqrt{1 + a_{\text{eq}}^3}}{a_{\text{eq}}^{3/2}}\right) - \frac{1}{\sqrt{1 + a_{\text{eq}}^3}} \right]} \quad (2.51)$$

is roughly the scale factor where the field is unfrozen. Over the range of $0.17 < \Omega_m < 0.5$, this constraint equation (2.50) can be well-approximated by the formula

$$1 + w_0 + w_a \left(0.264 + \frac{0.132}{\Omega_{m0}} \right) = 0. \quad (2.52)$$

Such a degeneracy line is plotted in Figure 2.1. Rather than a single w_0 parameter, constraining to this line based on a more realistic theoretical prior obviously makes for a more precise measurement of w . On the other hand, once the measurements of w_0 and w_a are both sufficiently accurate, the slow-roll thawing models could be falsified if they do not encompass part of the line. Obviously though it would be better to test deviations relative to true thawing trajectories rather than the ones fit by this perturbation expansion about redshift zero. One way to do this is to demonstrate that $1 + w_\infty$ is not compatible with zero, as we now discuss.

2.6.3 Transforming w_0 - w_a and ε_s - $\varepsilon_{\phi\infty}$ Contours into w_0 - w_∞ Contours

The DETF w_0 - w_a parameterization which is linear in a can be thought of as a parameterization in terms of w_0 and $w_\infty = w_a + w_0$ (or $\varepsilon_{\text{de},0}$ and $\varepsilon_{\text{de},\infty}$ in the DE acceleration factor language). The upper panel w_0 - w_a contour map in Fig. 2.13 shows that it is only a minor adjustment of the w_0 - w_a of Fig. 2.1. If we said there is a strict dichotomy between trajectories that are quintessence and trajectories that are phantom, as has been the case in our treatment in this chapter, only the two of the four quadrants of Fig. 2.13 would be allowed. (In the w_0 - w_a figures, the prior looks quite curious visually, in that the line $w_a = -(1 + w_0)$ through the origin has only the region above it allowed in the $1 + w_0 > 0$ regime, and only the region below it allowed in the $1 + w_0 < 0$ regime.)

To make this issue more concrete, we show in the lower panel of Fig. 2.13 what happens for our physics-motivated 2-parameter linear model, Eq. 2.34, except it is linear for $\pm\sqrt{|1 + w_{\text{de}}|}$, and in the “time variable” F not in a . In terms of $w_{\phi 0}$ and $w_{\phi\infty}$, we have $\sqrt{\varepsilon_\phi} = \sqrt{\varepsilon_{\phi 0}} + (\sqrt{\varepsilon_{\phi\infty}} - \sqrt{\varepsilon_{\phi 0}}) [1 - F(a/a_{\text{eq}})/F(1/a_{\text{eq}})]$. The prior measure on $1 + w_{\phi 0}$ and $w_{\phi\infty}$ are uniform as in the linear- a case. Once the prior that only 2 quadrants are allowed is imposed upon the linear- a case, it looks reasonably similar to the lower panel.

To illustrate that the determination of our various parameters actually depends upon an extended redshift regime, one can construct window functions, that is redshift-filters, for the parameters. These determine how an error in a parameter is built up by a sum of deviations of the observational data from the observable constructed using the model for w_{de} , using the maximum likelihood formula. This shows that the window functions are quite extended, not concentrated around zero redshift for w_0 , not concentrated at high redshift for w_∞ or $\varepsilon_{\phi\infty}$ and not concentrated at a_{eq} for ε_s . An illustration of the redshift reach of the ε_s parameter is Fig. 2.12 for the Supernova observable, namely a magnitude difference. The specific window functions are very data-dependent of course.

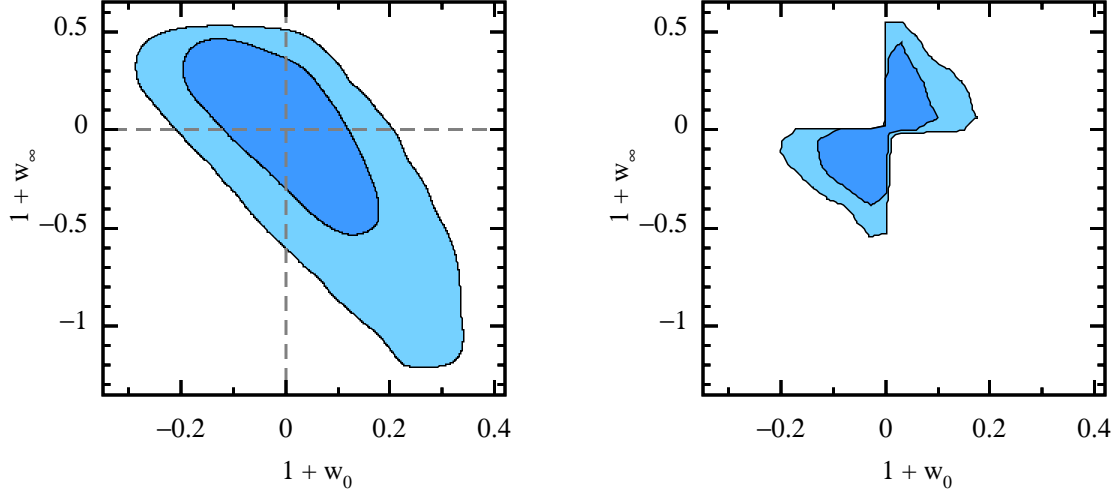


Figure 2.13: The upper panel shows the marginalized 68.3% (inner contour) and 95.4% (outer contour) constraints on w_0 and w_∞ for the conventional linear DETF parametrization, recast as $w = w_\infty + (w_0 - w_\infty)a$, using the current data sets described in § 2.4. It is a slightly tilted version of the w_0 - w_a version in Fig. 2.1. The demarcation lines transform to just the two axes, with the upper right quadrant the pure quintessence regime, and the lower right quadrant the pure phantom regime. If the cross-over of partly phantom and partly quintessence are excluded, as they are for our late-inflaton treatment in this chapter, the result looks similar to the lower panel, in which the 2-parameter ε_s - $\varepsilon_{\phi_\infty}$ formula has been recast into $2\varepsilon_0/3$ and $2\varepsilon_\infty/3$, via $\sqrt{\varepsilon_0} = \sqrt{\varepsilon_{\phi_\infty}} + (\sqrt{\varepsilon_s} - \sqrt{2\varepsilon_{\phi_\infty}})F(1/a_{\text{eq}})$. However, as well the prior measure has also been transformed, from our standard uniform $d\varepsilon_s d\varepsilon_{\phi_\infty}$ one to a uniform $d\varepsilon_0 d\varepsilon_{\phi_\infty}$ one. The quadrant exclusions are automatically included in our re-parameterization.

2.6.4 ζ_s , the Potential Curvature and the Difficulty of Reconstructing $V(\phi)$

For slow-roll thawing quintessence models, the running parameter ζ_s can be related to the second derivative of $\ln V$. Using the single-parameter approximation we can approximately calculate $d\phi/d\ln a$ at $a = a_{\text{eq}}$. The result is:

$$\left. \frac{d\phi}{d\ln a} \right|_{a=a_{\text{eq}}} = \sqrt{2}M_{\text{p}} \sqrt{\epsilon_\phi \Omega_\phi} \Big|_{a=a_{\text{eq}}} \approx 0.533 \sqrt{\epsilon_s} M_{\text{p}} . \quad (2.53)$$

An immediate consequence is that the amount that ϕ rolls, at least at late time, is small compared with the Planck mass. In the slow-roll limit, to the zeroth order, Eq. (2.27) can be reformulated as

$$\left. \frac{d\sqrt{2\epsilon_V}}{dN} \right|_{a=a_{\text{eq}}} \approx \frac{3}{2\sqrt{2}} \zeta_s \sqrt{\epsilon_s} . \quad (2.54)$$

Combining Eqs. (2.53-2.54), and that $M_{\text{p}}^2 d^2 \ln V / d\phi^2 = -d\sqrt{2\epsilon_s} / d\phi$, we obtain

$$\zeta_s \approx -\frac{CM_{\text{p}}^2}{2} \frac{d^2 \ln V}{d\phi^2} = -\frac{C}{4} \frac{d^2 \ln V}{d\psi^2} , \quad (2.55)$$

where

$$C \equiv \frac{8}{3} \left(1 - \frac{\ln(1 + \sqrt{2})}{\sqrt{2}} \right) \approx 1.005 . \quad (2.56)$$

For phantom models C is negative.

We have shown in § 2.5 that, for the fiducial Λ CDM model (with $\epsilon_s = \epsilon_{\phi_\infty} = 0$), the running parameter ζ_s cannot be measured. For a nearly-flat potential, the field momentum is constrained to be very small, hence so is the change $\delta\phi$, so the second order derivative of $\ln V$ is not probed. To demonstrate what it takes to probe ζ_s , we ran simulations of fiducial models with varying ϵ_s (0, 0.25, 0.5, and 0.75). The resulting forecasts for the constraints on ϵ_s and ζ_s , are shown in Figure 2.14. We conclude that unless the true model has a large $\epsilon_s \gtrsim 0.5$, which is disfavored by current observations at nearly the 2σ level, we will not be able to measure ζ_s . Thus if the second derivative of $\ln V$ is of order unity or less over the observable range, as it has been engineered

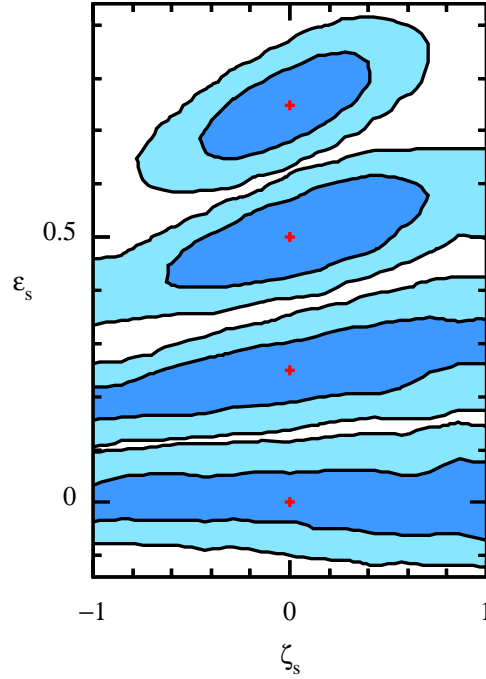


Figure 2.14: The 68.3% CL (inner contours) and 95.4% (outer contours) CL constraints on ε_s and ζ_s , using forecasted CMB, WL, BAO and SN data. The thawing prior ($\varepsilon_{\phi\infty} = 0$) has been used to break the degeneracy between ε_s and $\varepsilon_{\phi\infty}$. The four input fiducial models labeled with red points have $\zeta_s = 0$ and, from bottom to top, $\varepsilon_s = 0, 0.25, 0.5,$ and 0.75 , respectively. Only for large gradients can ζ_s be measured and a reasonable stab at potential reconstruction be made

to be in most quintessence models, its actual value will not be measurable. However, if $|M_p^2 d^2 \ln V / d\phi^2| \gg 1$, the field would be oscillating. Though in their own right, oscillatory quintessence models are not considered in this work.

2.6.5 Field Momentum and the Tracking Parameter $\varepsilon_{\phi\infty}$

The late universe acceleration requires the field to be in a slow-roll or at most a moderate-roll at low redshift. In tracking models, the high redshift ε_ϕ constancy implies the kinetic energy density follows the potential energy density of the scalar field: $\Pi_\phi^2/2V \rightarrow \varepsilon_{\phi\infty}/(3-$

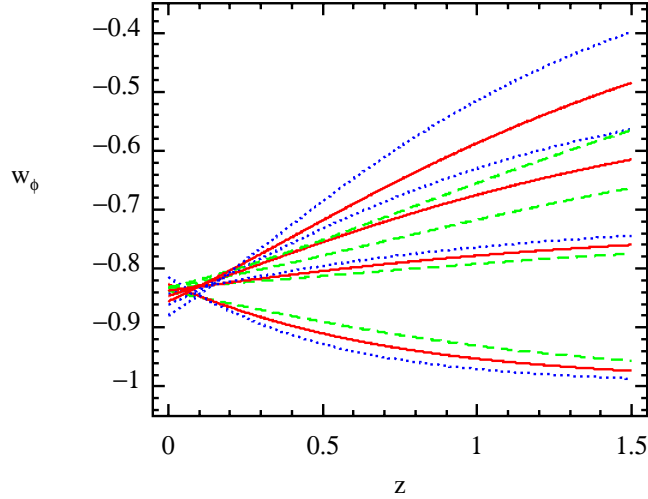


Figure 2.15: The dependence of $w_\phi(z)$ on $\varepsilon_{\phi_\infty}$ and ζ_s . We have fixed $\Omega_{m0} = 0.27$ and $\varepsilon_s = 0.5$. The red solid lines correspond to $\zeta_s = 0$, green dashed lines $\zeta_s = -0.5$, and blue dotted lines $\zeta_s = 0.5$. For each fixed ζ_s , the lines from bottom to top correspond to $\varepsilon_{\phi_\infty} = 0, 0.3, 0.6$, and 0.9 .

$\varepsilon_{\phi_\infty}$). The field could be fast-rolling in the early universe, with large $\varepsilon_{\phi_\infty}$ and a steep potential, and indeed is the case for many tracking models. If the potential is very flat, field momenta fall as a^{-3} , The rate of Hubble damping in the flat potential limit is $\dot{\phi} \propto a^{-3}$. However, as proposed in most tracking models, the potential is steep at high redshift, and gradually turns flat at low redshift. The actual damping rate itself is related to the field momentum, which again relies on how steep potential is at high redshift. The complicated self-regulated damping behavior of field momentum is encoded in the tracking parameter $\varepsilon_{\phi_\infty}$ in Eq. (2.28) (see Figure 2.15 where the damping of field momentum is visualized in $w(z)$ space). At high redshift the approximation $\dot{\phi} \sim a^{-3}$ completely fails, but at low redshift the damping rate asymptotically approaches $\dot{\phi} \sim a^{-3}$.

Since dark energy is subdominant at high redshift, the observational probes there are not very constraining. In the 3-parameter approximation, instead of an asymptotic $\varepsilon_{\phi_\infty}$, we could use a moderate redshift ($z \sim 1$) pivot z_{pivot} , with variables $\varepsilon_{\phi_{\text{pivot}}}$, ε_s ,

and the curvature parameter ζ_s , and the asymptotic regime a controlled extrapolation. Indeed, using the method of § 2.6.3, we could define everything in terms of pivots of ϵ_ϕ , for example at $a = 1$ as we used in § 2.6.3, and a third about half way in between, for example at a_{eq} , which is about 0.7, so $z_{\text{eq}} \sim 0.4$. The formula would remain the same, but the measure (prior on the parameters) would be different. At very high redshift where dark energy is negligible, there is essentially no observational constraint. The reconstructed $w(z)$ trajectories in Figure 2.8 should really be regarded as low-redshift observational constraints extrapolated to high-redshift. The tracking assumption that we have used throughout this chapter provides one, but not a unique extrapolation method that extrapolates $w(z)$ to high redshift. The extrapolation method defines the prior of $\dot{\phi}_{\text{pivot}}$ and the details how the damping rate of $\dot{\phi}$ approaches a^{-3} . These may affect the marginalized posterior likelihood of ϵ_s . An example is that a flat prior $0 \leq \epsilon_{\phi\infty} < 1$ gives $0.00_{-0.17}^{+0.18}$, while the “thawing prior” ($\epsilon_{\phi\infty} = 0$ or equivalently $\dot{\phi}_{\text{pivot}} \approx 0$) gives $\epsilon_s = -0.00_{-0.29}^{+0.27}$. However, the high-redshift observables, such as the Hubble parameter $H(z)$, the luminosity distance $d_L(z)$, and the linear perturbation growth rate $D(z)$, as shown in Figure 2.8, are not sensitive to the high-redshift extrapolation of $w(z)$. For a model that has time-varying attractor, such as the SUGRA model shown in the middle panel of Figure 2.2, the high redshift extrapolation will be inaccurate. But the lack of data at very high redshift allows us to apply our parametrization to these models.

2.6.6 Using Our w_ϕ Parametrization

We believe the FOM of future DE experiments should not be evaluated using only *ad hoc* parametrizations, when we do have physical models to follow. The physics-based dark energy EOS parametrization $w_\phi(a|\epsilon_s, \epsilon_{\phi\infty}, \zeta_s, \Omega_{\text{m}0})$ provides an alternative to the widely used phenomenological w_{de} parametrizations, e.g., Eq. (2.4), although using it generally requires more sophisticated calculations. To facilitate general-purpose use of our parametrization, we wrote a fortran90 module that calculates $w_\phi(a|\epsilon_s, \epsilon_{\phi\infty}, \zeta_s, \Omega_{\text{m}0})$

(<http://www.cita.utoronto.ca/~zqhuang/work/wphi.f90>).

Suppose that one has in mind a specific quintessence potential $V(\phi)$. How can our constraints, in particular on ϵ_s , be used to test viability? The first thing is to see what ϵ_V looks like as a function of ϕ . One does not know ϕ_{eq} of course, but it had better lie in the range for ϵ_s allowed by the data. The model would be ruled out if no ϕ has ϵ_V penetrating the allowed region. Otherwise, the field equation of motion has to be solved to get ϕ_{eq} , and hence ϵ_s from its definition. Such a calculation is inevitable because quintessence models do not solve the fine-tuning problem. For tracking models, the low-redshift dynamics is usually designed (i.e., are fine-tuned) to deviate from an attractor. For thawing models, the initial value of ϕ_∞ (to which ϕ is frozen at high redshift) needs to be fine-tuned as well.

2.7 Appendix: Comparison with Other Parameterizations

The constant w model and the linear w models, $w = w_0 + w_a(1 - a)$ or $w = w_0 + w_1 z$ with a cutoff [67, 72], are the simplest w_{de} parameterizations widely used in the literature. An advantage is that they can fit many dark energy models, including those beyond scalar field models, at low redshifts. A disadvantage is that they fail at $z \gtrsim 1$ for most physical models, and in this high-precision cosmology era we cannot ignore adequate inclusion of the $z \sim 1$ information. For this reason there are various three-parameter or four-parameter approximations proposed to improve w at higher redshifts. Some examples are simple extensions of w_0 - w_a :

An expansion quadratic in $(1 - a)$ with a w_b parameter added to w_0, w_a [175, 67, 72],

$$w(a) = w_0 + w_a(1 - a) + w_b(1 - a)^2. \quad (2.57)$$

Replacement of $(1 - a)$ by $(1 - a^b)$, with b a parameter added to w_0, w_a [72],

$$w(a) = w_0 + w_a(1 - a^b) . \quad (2.58)$$

Four parameter models include:

$$w(a) = w_0 w_1 \frac{a^p + a_s^p}{w_1 a^p + w_0 a_s^p}, \quad (2.59)$$

where w_0, w_1, a_s, p are the parameters [176];

$$w(a) = w_0 + (w_m - w_0) \frac{1 + e^{a_c/\Delta}}{1 + e^{(a_c - a)/\Delta}} \frac{1 - e^{(1-a)/\Delta}}{1 - e^{1/\Delta}}, \quad (2.60)$$

where w_0, w_m, a_c, Δ are constants [177];

$$w(a) = w_f + \frac{\Delta w}{1 + (a/a_t)^{1/\tau}}, \quad (2.61)$$

where $w_f, \Delta w, a_t, \tau$ are the parameters [72].

Many of these four-parameter models describe a w_ϕ -transition characterized by an initial w , today's w , a transition redshift, and a duration of transition. For the tracking models they are meant to describe, such a phenomenology introduces three parameters to describe essentially one degree of freedom (the tracking attractor). Instead our parametrization consistently solves the tracking $w_\phi(a)$.

[178] has done similar work for the negative power-law tracking models, though did not model the low-redshift slow-roll regime, making his parameterization much less useful than ours for comparing with data.

Slow-roll quintessence models have been studied by, e.g., [179, 112, 180], but our work makes significant improvements. Firstly, we have chosen a more optimal pivot $a = a_{\text{eq}}$ to expand $\ln V(\phi)$, whereas the other works expand $V(\phi)$ at either $a \ll 1$ or

$a = 1$. As a result, we approximate w_ϕ at the sub-percent level in the slow-roll regime $|1+w| < 0.2$ compared with the other approximations failing at $|1+w_\phi| > 0.1$. Secondly, with the field momentum from the tracking regime incorporated, our three-parameter $w_\phi(a)$ ansatz can also fit the more extreme moderate-roll and tracking models with an accuracy of a few percent. Since current data allow a relatively large region of parameter space ($|1+w_\phi| \lesssim 0.2$ at 99.7% CL), a slow-roll prior with $|1+w_\phi| \ll 1$ should not be imposed as other papers have done. Thirdly, we have extended the parameterization to cover phantom models, though that is arguably not a virtue.

2.7.1 $\rho_{\text{de}}(z)$ and $H(z)$ reconstruction

One has to integrate $w_\phi(z)$ once to get the the dark energy density $\rho_\phi(z)$ and the Hubble parameter $H(z)$. Observational data are often directly related to either $H(z)$ or $\rho_{\text{de}}(z)$, and not sensitive to $w_{\text{de}}(z)$ variations. Thus one may prefer to directly parameterize $\rho_{\text{de}}(z)$ [66, 181] or $H(z)$ [182, 181, 183] on phenomenological grounds. A semi-blind expansion of $H(z)$ or $\rho_{\text{de}}(z)$, e.g., in polynomials or in bands, differs from one in $w_{\text{de}}(z)$, since the prior measures on the coefficients are radically altered. By contrast, a model such as ours for $w_{\text{de}}(z; \varepsilon_s, \varepsilon_{\phi\infty}, \zeta_s)$ characterized by physical parameters is also a model for $H(z; \varepsilon_s, \varepsilon_{\phi\infty}, \zeta_s)$ or $\rho_{\text{de}}(z; \varepsilon_s, \varepsilon_{\phi\infty}, \zeta_s)$, obtained by integration.

Where the freedom does lie is in the prior measures imposed on the parameters, a few examples of which were discussed in Section 2.4.

2.7.2 $V(\phi)$ reconstruction

For thawing models, our parameters ε_s and ζ_s are based on a local expansion of $\ln V(\phi)$ at low redshift. One should obtain similar results by directly reconstructing the local $V(\phi)$. An attempt at local $V(\phi)$ reconstruction was done in [184], where a polynomial expansion was used,

$$V(\phi) = V_0 + V_1\phi + V_2\phi^2 + \dots, \quad (2.62)$$

with ϕ chosen to be zero at present. A result highlighted in that paper is that there is a strong degeneracy between V_1 and $\dot{\phi}_0$. We shall see that this degeneracy is actually a result of the prior, and not something that observational data is telling us, as we now show.

For simplicity we assume that Ω_{m0} and h are known, hence the parameter V_0 is hence fixed. Although V_1 is defined at the pivot $a = 1$, it is approximately proportional to $\sqrt{\varepsilon_s}$ since ε_V varies slowly. Because $\dot{\phi}_0$ is a function of $1 + w|_{z=0}$, the degeneracy between V_1 and $\dot{\phi}_0$ is roughly the degeneracy between ε_s and $\varepsilon_{\phi 0}$, an expression of the low-redshift dynamics being mainly dependent upon the slope of $\ln V$. This is explicitly shown in Figure 2.15.

Huterer et al [86] tried to do $V(\phi)$ reconstruction using what was then recent observational data. They used RG flow parameters ε_V , η_V , etc. expanded about the initial redshift $z_{\text{start}} = 3$. The constraint they found on the parameter $\varepsilon_V|_{z=3}$ is very weak. From our work, this is understandable because the high-redshift dynamics are determined by the tracking parameter rather than by ε_V . They also calculated the posterior probability of ε_V at redshift zero, which is much better constrained. Their result is consistent with what we have obtained for ε_s . Also the large uncertainty in $\eta_V|_{z=0}$ they found is similar to our result for ζ_s .

Recently [185] have proposed Chebyshev expansions of $V(z)$ or $w_\phi(z)$, a method we have applied to treat early universe inflation [76], but as we have discussed in the introduction there is de facto much less information in the \sim one e-folding in a that DE probes cover than the ~ 10 e-foldings in a that CMB+LSS power spectrum analyses cover.

Chapter 3

Scanning Inflationary Trajectories

3.1 Introduction

In previous chapter we studied the accelerated expansion in late universe, for which we are mostly interested in the homogeneous expansion history $\epsilon(t)$ defined in Eq. (1.20). In addition to the obvious fact that the accelerated expansion changes the geometrical distances, it can also change the CMB power spectra via Integrated Sachs-Wolf effect [186] and the growth factor $D(z)$ via Hubble friction. Very similarly the expansion history during early-universe inflation is imprinted on the superhorizon comoving curvature perturbations, which later enter the horizon and become observable. In this chapter we will discuss the parametrization of the primordial power spectra from inflation.

The expansion history of early-universe inflation is fully defined through the ϵ trajectory. By definition of accelerated inflation the ϵ trajectory satisfies $0 < \epsilon(t) < 1$. The endpoint $\epsilon = 1$ formally ends the inflation.

Traditionally the inflationary dynamics are described via the slow-roll approximation through expansion in orders of variables ϵ and $d \ln \epsilon / d \ln a$, defining a restricted set of spectral parameters such as scalar power law index n_s , running $n_{\text{run}} \equiv dn_s / d \ln k$ and tensor index $n_t \equiv d \ln \mathcal{P}_T(k) / d \ln k$. In addition, the amplitude is usually parametrized

by a scalar power A_s and a tensor-to-scalar ratio r . These parameters are defined at a given pivot point, a wavenumber k_{pivot} . A typical pivot point is $k_{\text{pivot}} = 0.05\text{Mpc}^{-1}$ or $k_{\text{pivot}} = 0.002\text{Mpc}^{-1}$. At low order $r \approx -8n_t$ defines the consistency relation for single-field inflation. These are used to parametrize the form of the scalar (curvature) \mathcal{P}_S and tensor (gravity wave) \mathcal{P}_T power spectra which determine cosmic observables such as CMB, WL and LSS.

Major efforts are currently under way to detect the tensor modes in the CMB polarization. This is a challenging signal to observe given the potential foreground contamination of the B-type polarization where a pure tensor contribution is found. A detection of r however is crucial for inflationary model building as it fixes the energy scale of inflation and breaks the degeneracy in the determination of the shape of the underlying potential. So far, the only theoretical limits on the energy scale of inflation come from arguments from reheating, while the scalar power spectrum does not provide any information about the energy scale of inflation.

Here, we advocate a different approach to reconstruct the primordial power spectra. Instead of starting off with (a family) of scalar field potentials, we aim at reconstructing the shape of the primordial tensor and scalar power spectra independent of theoretical priors (in the sense of expecting certain shapes of the scalar field potential). Instead, we let observational data almost freely decide the shapes of the power spectra, using two different paradigms. The goal is to reconstruct – in a model-independent way – nontrivial features in the primordial power spectra, if there are any, without imposing strong theoretical priors. On the other hand, if no interesting features are found with our method, the slow-roll assumption will be robustly supported, rather than being defined as a prior.

To this end, we consider spectra features produced by some non-standard processes. Examples of such models are particle production during inflation [6, 7] that we will discuss in Chapter 5, cosmological fluctuations from preheating [56] that will be discussed

in Chapter 4, and “curvaton” models [187, 188]. In these models the consistency relation between tensor and scalar spectra breaks down. We hence let the scalar and tensor spectrum vary independently. In order to generate spectra with a finite number of parameters, we have to impose certain smoothing conditions (priors), implicitly defined by the interpolation method. We vary the interpolation method to show that the dependence on the smoothness prior is weak, provided that proper number of knots are used ⁱ.

Secondly, we consider spectra produced by single-field inflation with exotic features in the potential that can break down the slow roll approximation. Some extreme examples are discussed in e.g. Ref. [189], and we show one of these in Figure 3.1. For these kinds of models we will impose the single field consistency condition, in effect forcing all observables to be derivable from a single real scalar field potential. Once again, we will strive to be agnostic about the shape of the potential. All that we require is an inflationary period.

This chapter is structured as follows. In Section 3.2 we introduce the current and forecast data sets used in this chapter, and update the constraints on the traditional parametrization of primordial power spectra. Section 3.3 briefly introduce different statistical methods to study trajectories. Section 3.4 introduces the different possible parameterizations of background trajectories for the scalar and tensor power spectra without assuming a consistency condition between them. Section 3.5 discusses the trajectories in the case of inflation driven by a single real scalar field. We summarize our results and conclude in Section 3.6.

ⁱThe criterion is that the reduced χ^2 is not significantly smaller than 1, or expressed in the Bayesian language, the Bayesian evidence is not too low.

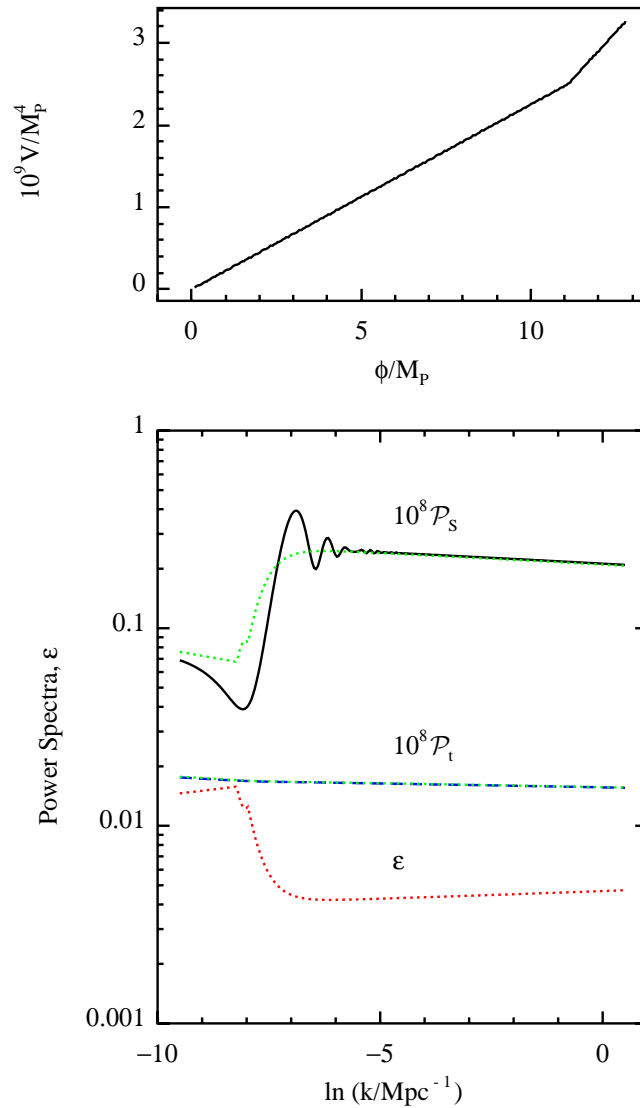


Figure 3.1: Top panel: the “Starobinsky potential”. The two linear pieces of potential $V(\phi)$ are connected by a quadratic piece with width $0.04M_p$. Bottom panel: the power spectra generated in this inflation model. The solid black line and dashed blue line are numerically calculated \mathcal{P}_S and \mathcal{P}_T , respectively. The dotted green lines are the slow-roll approximations (1.60) and (1.61). The dotted red line at the bottom is the ϵ trajectory.

3.2 Updating the Traditional Parametrization

3.2.1 Data Sets

We run MCMC simulations to determine the likelihood of cosmological parameters, using the publicly available parallel code CosmoMC [113] with our modifications for arbitrary input of primordial power spectra.

The current data sets we have used are described in Section 2.4 (see also [59]), although for weak lensing and Ly α we use different treatment to allow more general primordial power spectra. For weak lensing data we use the Halofit formula [190] to map the linear matter power spectrum to nonlinear power spectrum. Because we are considering non-standard forms of primordial spectra, the Halofit formula can be inaccurate, potentially washing out bump features by non-linear dynamics. To model this additional uncertainty, we introduce two nuisance parameters α_h and β_h

$$\begin{aligned} \ln P_{\text{nl}} = & e^{-k^2 r_{\text{nl}}^2} \ln P_{\text{halofit}} + \left(1 - e^{-k^2 r_{\text{nl}}^2}\right) \\ & \times (\ln P_{\text{smooth}} + \alpha_h + \beta_h k r_{\text{nl}}) , \end{aligned} \quad (3.1)$$

where P_{halofit} is calculated using the original halofit formula code, with the nonlinear scale r_{nl} as a byproduct. Here $\ln P_{\text{smooth}}$ is obtained by fitting $\ln P_{\text{halofit}}$ as a quadratic function of $\ln k$ in the range where $\ln(k r_{\text{nl}}) > -1$ and $k < \text{Mpc}^{-1}$. We used priors $-0.2 < \alpha_h < 0.2$ and $-0.2 < \beta_h < 0.2$, allowing about 20% uncertainty of P_{nl} on scales $\sim 1/r_{\text{nl}}$, and even larger uncertainties on smaller scales. By doing this we are effectively discarding most of the information on non-linear scales, with only a rough amplitude of the matter power spectrum being used. For α data we only use the likelihood given in [155] and [156]. This likelihood code does *not* assume a strictly power-law primordial power spectrum. It can be used as long as the cosmology models we are considering are close to WMAP favored Λ CDM model, and the linear matter power spectrum around $k \sim 0.9 \text{Mpc}^{-1}$ can be approximated by a quadratic expansion. To

calculate the likelihood, we interpolate the χ^2 table in a three dimensional parameter space, where the three parameters are amplitude, index, and the running of linear matter power spectrum at pivot point $k_{\text{lva}} = 0.9h \text{ Mpc}^{-1}$. To extract these parameters from more general power spectra that are allowed in our parametrization, we perform a quadratic fitting of $\ln P_{\text{matter}}$ for $\ln k_{\text{lva}} - 1/2 < \ln k < \ln k_{\text{lva}} + 1/2$, and marginalize over 2% uncertainty of the amplitude and 5% uncertainty of the spectral index.

The future data forecasts used in this chapter are described in Section 2.5. For weak lensing forecasts we do not do further marginalization on Halofit mapping, assuming the future N-body simulations can precisely predict nonlinear matter power spectra for general primordial power spectra.

3.2.2 Constraints on the Conventional Parameters

Let us start with the traditional parametrizations (1.64-1.65), and update the observational constraints on the primordial power spectra using the latest available data. It is unrealistic to measure the small deviation of scale invariance in the tensor power spectrum. We therefore use a prior $n_t = 0$ as an approximation. We also tried turning off the running parameter (by imposing a prior $n_{\text{run}} = 0$). The results with and without running are shown in Table 3.1. The marginalized posterior likelihoods are shown in Figure 3.2.

In the left panel of Figure 3.3 we show that the spectral index of tensor is so poorly measured that the single-field consistency relation ($r \approx -8n_t$, red line) is not tested. We also have tried using the simulated forecast data, this conclusion does not change.

The weak degeneracy between n_s and r are shown in the right panel of Figure 3.3. When tested with the simulated forecast data, we find the degeneracy vanishes, as shown in Figure 3.4. We also simulate the SPIDER CMB data to show the further improvement of constraint on r . SPIDER is a proposed balloon experiment targeting at CMB polarizations at large scales [191]. We have assumed 580 hours integration time and 9% coverage of the sky. We use the same foreground model that we have adopted for Planck.

Table 3.1: The 68.3% CL constraints on cosmological parameters (for r the 68.3%CL and 95.4% CL upperbounds are shown). A Λ CDM model with $n_t = 0$ has been assumed. The scalar power spectrum is expanded at $k_{\text{pivot}} = 0.002\text{Mpc}^{-1}$.

	with n_{run}	without n_{run}
$\Omega_{\text{b}0}h^2$	$0.02262^{+0.00043}_{-0.00044}$	$0.02260^{+0.00044}_{-0.00044}$
$\Omega_{\text{c}0}h^2$	$0.1179^{+0.0020}_{-0.0020}$	$0.1171^{+0.0019}_{-0.0019}$
θ	$1.0425^{+0.0019}_{-0.0020}$	$1.0420^{+0.0019}_{-0.0019}$
τ_{re}	$0.094^{+0.015}_{-0.014}$	$0.090^{+0.014}_{-0.014}$
n_s	$1.006^{+0.029}_{-0.029}$	$0.962^{+0.011}_{-0.011}$
n_{run}	$-0.017^{+0.010}_{-0.010}$...
$\ln(10^{10}A_s)$	$3.184^{+0.043}_{-0.047}$	$3.226^{+0.033}_{-0.034}$
r	$0.00^{+0.14+0.27}$	$0.00^{+0.08+0.17}$
$\Omega_{\text{m}0}$	$0.293^{+0.012}_{-0.011}$	$0.290^{+0.011}_{-0.010}$
σ_8	$0.844^{+0.014}_{-0.014}$	$0.843^{+0.014}_{-0.016}$
z_{re}	$11.2^{+1.2}_{-1.2}$	$10.8^{+1.2}_{-1.2}$
H_0	$69.3^{+1.0}_{-1.0}$	$69.4^{+1.0}_{-1.0}$

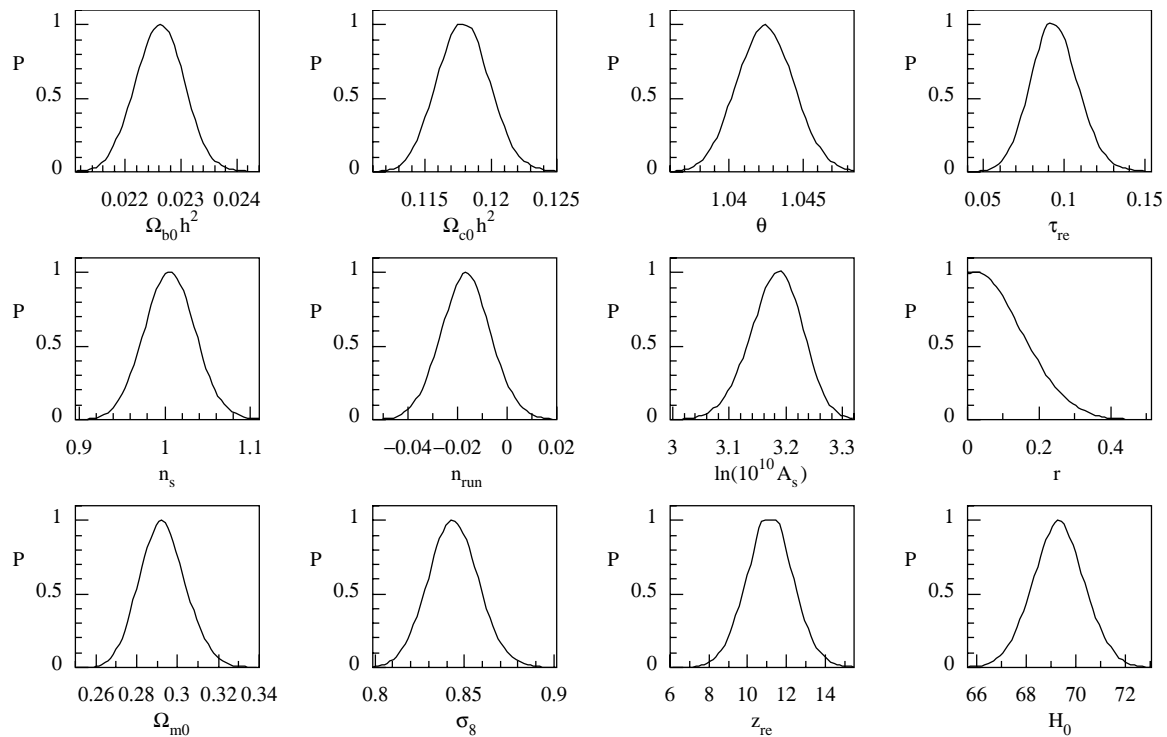


Figure 3.2: The marginalized posterior likelihood of cosmological parameters. They are normalized such that the maximum likelihood is 1. A Λ CDM model with $n_t = 0$ has been assumed. The scalar power spectrum is expanded at $k_{\text{pivot}} = 0.002 \text{Mpc}^{-1}$. The solid red line in the left panel shows the single-field inflation consistency.

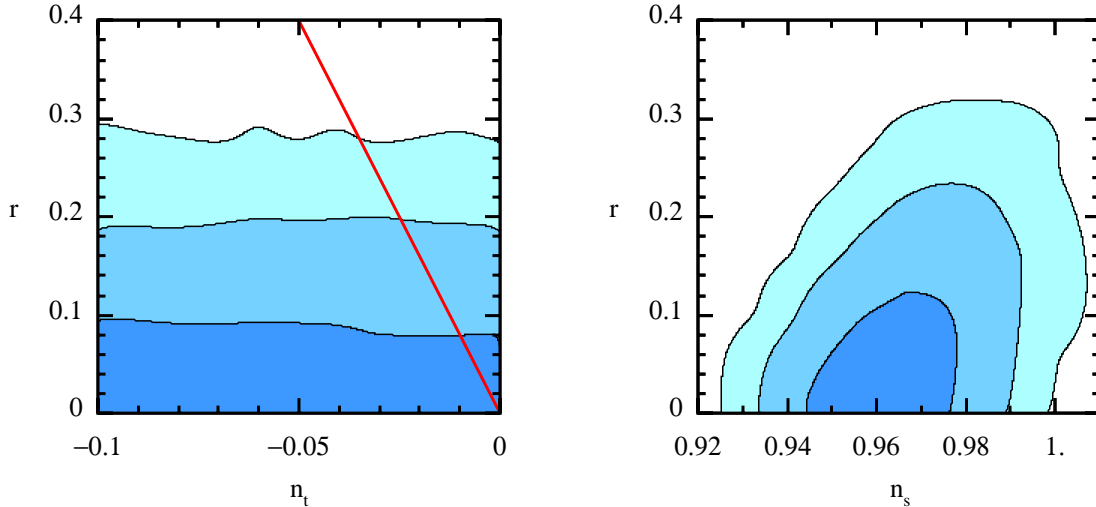


Figure 3.3: Left panel: the single-field consistency relation (red line) is not tested by the data. Right panel: the degeneracy between n_s and r . A Λ CDM model with $-0.1 < n_t < 0$ and $n_{\text{run}} = 0$ has been assumed. The spectra are expanded at $k_{\text{pivot}} = 0.002\text{Mpc}^{-1}$. The three contours are 68.3% CL, 95.4% CL and 99.7% CL, respectively.

See subsection 2.5.1 for the details.

3.3 Statistics of Trajectories

Let us consider the case when the likelihood is a functional of a trajectory (function) $f(x)$ defined on $x \in [a, b]$.

Unlike usual Bayesian parameters that can be imposed a flat prior, the trajectories does not have a natural “flat” prior. It can be defined only if we have a natural measure in the infinite-dimension functional space. We do not search for such a natural measure, since doing statistics on infinite number of parameters is not meaningful. Bayesian evidence will always exclude a model with too many parameters. Moreover, given so many degrees of freedom, the posterior likelihood will strongly depends on the prior, making the result meaningless.

The practical solution is to use a few parameters to generate trajectories. The gener-

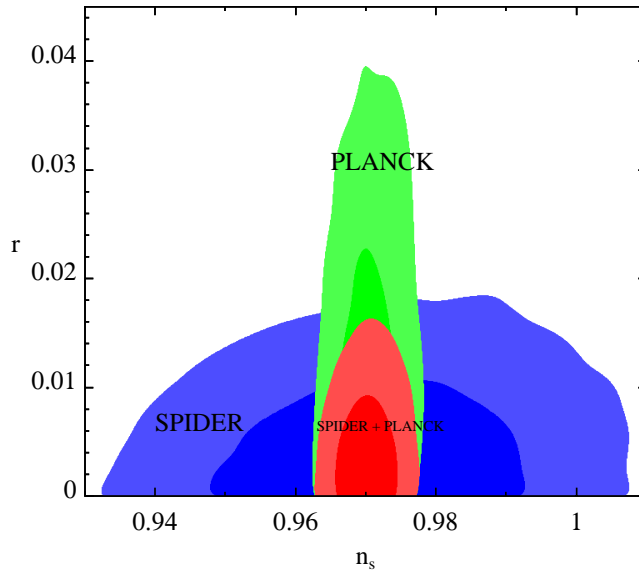


Figure 3.4: The marginalized 68.3% CL and 95.4% CL constraints on n_s and r using simulated Planck and SPIDER CMB data.

ated trajectories do not exhaust the original infinite-dimensional trajectory space. The hope is that the subset of trajectories is representative enough. That means

1). Any physically meaningful trajectory can be approximated by a trajectory in the subset;

2). Most trajectories in the subset are physically meaningful.

Condition (2) is as important as (1), because we do not want the reconstructed posterior trajectories to be dominated by the nonphysical trajectories strongly favored by the prior.

The most widely used series expansion approach generates trajectories through basis functions

$$f(x) = \sum_{i=0}^n c_k b_k(x) , \quad (3.2)$$

where $b_k(x)$ ($k = 1, 2, \dots, n$) are pre-chosen independent basis functions. The samples of trajectories are obtained by varying the coefficients c_k 's, on which usually flat priors are applied. Oft-used basis functions are power series x^k , Fourier mode $\cos kx$, Chebyshev

polynomial $T_k(x)$ ($i = 1, 2, \dots, n$), etc.

Often in a physics problem the physically meaningful trajectories are bounded: $A < f(x) < B$, with certain smoothness constraint. The series expansion has a disadvantage that it is difficult to choose the prior bounds for c_1, c_2, \dots, c_n , such that most generated trajectories are physically meaningful. This problem can be fixed by pre-excluding the trajectories that do not fall in the band between A and B . However, this leads to complicated priors on c_1, c_2, \dots, c_n , making it difficult to understand and interpret the posteriors.

A better method is to sample $f(x)$ on a few knots, and generate the trajectories via interpolations between the knots. With this approach, the parameters all have clear physical meanings, the smoothness constraint can be tuned by choosing proper interpolation methods, and the bounds $A < f(x) < B$ can be directly applied on the parameters. Often with certain smoothness constraint most of the interpolated $f(x)$'s fall in the band $A < f(x) < B$. Finally, the proper number of knots can be determined by examining the reduced χ^2 . This approach, namely the “scanning method”, is therefore ideal for statistics on a general bounded function.

The scanning method has its disadvantage, too. The generated trajectories have the feature that most of them are oscillatory. The mean of the “scanning parameters” ($f(x)$ values at the knots) is driven towards $(A + B)/2$ by a very strong prior (if n is large). A false-detection can occur if we are interested in the mean amplitude of $f(x)$, when the data does not constrain $f(x)$ piecewisely (i.e. too many knots have been used). In some cases we want to explicitly avoid these disadvantages. One example is that the primordial tensor power spectrum $\mathcal{P}_T(k)$ should be a monotonically decreasing function of k , and we want to avoid false detection of \mathcal{P}_T . We will not be using the scanning approach directly on \mathcal{P}_T . As the current and near-future data do not constrain \mathcal{P}_T piecewisely. A subtle case is when we scan ϵ trajectory and apply the single-field inflation prior. A false-detection of gravitational waves tends to occur because the well measured scalar

power spectrum only constrains $n_s - 1 \approx -2\epsilon - d \ln \epsilon / d \ln k$, but not ϵ . The average amplitude of ϵ can be easily driven by the prior imposed by scanning method. We can avoid this problem by scanning $d \ln \epsilon / d \ln k$ or $2\epsilon + d \ln \epsilon / d \ln k \approx 1 - n_s$, which are less prior-dependent.

3.4 The Bottom-Up Approach: Phenomenological Expansion of \mathcal{P}_S and \mathcal{P}_T

3.4.1 Method

The current observational data explore about ten e-folds of comoving wave-length, roughly corresponding to the interval $-9 < \ln(k/\text{Mpc}^{-1}) < 1$. Let us define this interval as “observable interval”. The spectra on scales outside the observable interval do not have essential impact on the cosmic observables. Any reasonable extrapolation will do as good. We simply use constant \mathcal{P}_S for these extra-large and extra-small scales. Natural cubic spline interpolation is our default option to interpolate $\ln \mathcal{P}_S$ within the observable interval. Alternative interpolation methods are Chebyshev interpolation and monotonic cubic Hermite interpolation. The Chebyshev interpolation defines a unique $n - 1$ -th order polynomial passing the n given points at the $\ln k$ knots. Both natural cubic spline interpolation and monotonic cubic Hermite interpolation assume third order polynomial between two neighbor knots. Natural cubic spline defines a unique interpolated curve by matching the second order derivatives across the knots, with an additional assumption that the second order derivative vanishes at the two boundaries. The cubic Hermite interpolation only requires the first order derivative to be continuous across the knots. The extra n degrees of freedom is fixed by choosing the first order derivative at the i -th knot. For generic cubic Hermite interpolation where the piecewise monotonicity is not

required, the derivatives can be chosen as

$$\Delta_i \equiv \begin{cases} [f(x_2) - f(x_1)] / (x_2 - x_1) & , \text{ if } i = 1 \\ [f(x_n) - f(x_{n-1})] / (x_n - x_{n-1}) & , \text{ if } i = n \\ [f(x_{i+1}) - f(x_{i-1})] / (x_{i+1} - x_{i-1}) & , \text{ else} \end{cases} \quad (3.3)$$

where x_i is the i -th knot. For monotonic cubic Hermite interpolation, the piecewise monotonicity of $f(x)$ between two neighbor knots is achieved by further adjusting Δ_i . First, for $i = 1, 2, \dots, n - 1$, if $f(x_i) = f(x_{i+1})$, set $\Delta_i = \Delta_{i+1} = 0$. Second, for $i = 1, 2, \dots, n - 1$ where $f(x_i) \neq f(x_{i+1})$, define $\alpha_i = \Delta_i(x_{i+1} - x_i) / [f(x_{i+1}) - f(x_i)]$ and $\beta_i = \Delta_{i+1}(x_{i+1} - x_i) / [f(x_{i+1}) - f(x_i)]$; If $\alpha_i^2 + \beta_i^2 > 9$, update Δ_i and Δ_{i+1} to be $3\alpha_i\Delta_i / \sqrt{\alpha_i^2 + \beta_i^2}$ and $3\beta_i\Delta_{i+1} / \sqrt{\alpha_i^2 + \beta_i^2}$, respectively.

To summarize, the parametrization is

$$\ln \mathcal{P}_S(\ln k) = \ln \mathcal{P}_S |_{\ln(k/\text{Mpc}^{-1})=-9} , \text{ if } \ln(k/\text{Mpc}^{-1}) < -9 ;$$

$$\ln \mathcal{P}_S(\ln k) = \ln \mathcal{P}_S |_{\ln(k/\text{Mpc}^{-1})=1} , \text{ if } \ln(k/\text{Mpc}^{-1}) > 1 ;$$

$$\text{flat prior } 1 < \ln [10^{10}\mathcal{P}_S] < 5 , \text{ if } \ln k \text{ is a knot;}$$

$$\text{interpolate } \ln \mathcal{P}_S(\ln k) , \text{ if } \ln k \text{ is not a knot, and } -9 < \ln(k/\text{Mpc}^{-1}) < 1 .$$

Uniformly distributed knots from $\ln(k/\text{Mpc}^{-1}) = -9$ to $\ln(k/\text{Mpc}^{-1}) = 1$ are used for natural cubic spline interpolation and monotonic cubic Hermite interpolation. For Chebyshev interpolation we choose the nodal points of Chebyshev polynomials, i.e., the n roots of n -th order Chebyshev polynomial $T_n(x)$, with $x \equiv \frac{\ln(k/\text{Mpc}^{-1})+4}{5}$. The Chebyshev polynomials along with the particular pattern of knots are used for better fitting and numerical stability [192].

For the tensor power spectrum we use $\mathcal{P}_T = A_T(k/k_{\text{pivot}})^{n_t}$ with prior $-0.1 < n_t < 0$ and $A_T \geq 0$.

3.4.2 Reconstructed Power Spectra

The reconstructed primordial power spectra are shown in the left panel of Figure 3.5. We also have shown as contrasts the theoretical prediction from a quadratic potential ($V = 1/2m^2\phi^2$) chaotic inflation model, which lies well inside the $1\text{-}\sigma$ band. Another notable result is that once we allow more degrees of freedom in \mathcal{P}_S , the tensor spectrum \mathcal{P}_T is no longer tightly constrained to be less than 20% of the \mathcal{P}_S . We calculate the posterior probability of r at $k_{\text{pivot}} = 0.002\text{Mpc}^{-1}$. The 95.4% CL upper bound is $r < 0.68$. The interesting question is of course whether the large tensor spectra are consistent with single-field inflation models. We will address this issue in Section 3.5.

The reconstructed trajectories can be mapped into CMB angular power spectra, as shown in the left panels of Figure 3.6.

For the forecast data, the reconstructed \mathcal{P}_S and \mathcal{P}_T trajectories are shown in Figure 3.7. We also have tried Chebyshev interpolation and Monotonic Cubic Hermite interpolation to test the dependency of result on the interpolation method. The constraints on $r(0.002\text{Mpc}^{-1})$ using different interpolation methods are listed in Table 3.2. For the future data, the constraints on scalar power spectrum are very stringent. If the number of knots is about ten or less, the choice of interpolation method (prior) is not important. But the measurement of index of tensor power spectrum is still challenging. No constraint is found for a fiducial model $r = 0$ or $r = 0.13$. This is true even when we assume a simple power-law scalar power spectrum to avoid possible degeneracy.

3.4.3 Searching for nontrivial features in the power spectra

Although any specific choice of algorithm to generate “random” trajectories may be challenged by prior issues as discussed above, we are interested in methods that can practically detect nontrivial features in the primordial power spectra. To show that the method we are advocating in this paper is a viable candidate, we produce mock data

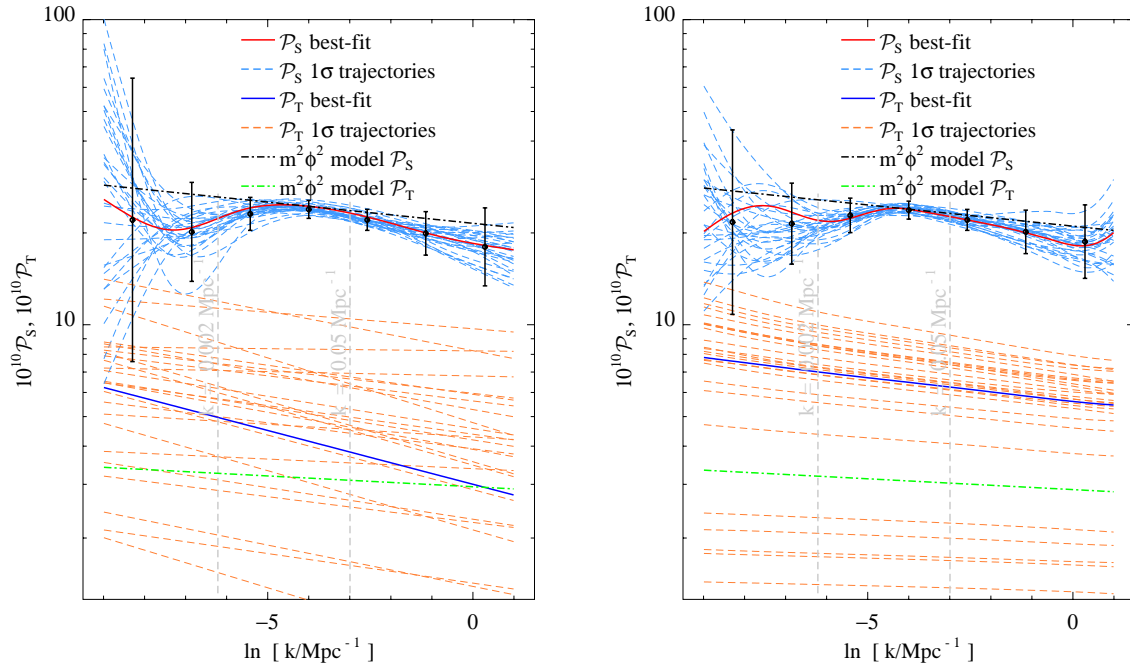


Figure 3.5: The reconstructed primordial spectra with current data. In the left panel we have used the bottom-up approach with natural cubic spline interpolation. See Section 3.4 for the details of the parametrization. In the right panel the top-down approach with single-field inflation prior is applied. See Section 3.5 for the details about the parametrization. The 1- σ error bars are uncertainties of the band powers. The band powers are defined as the convolutions of the power spectrum and top-hat window functions in seven uniform bins.

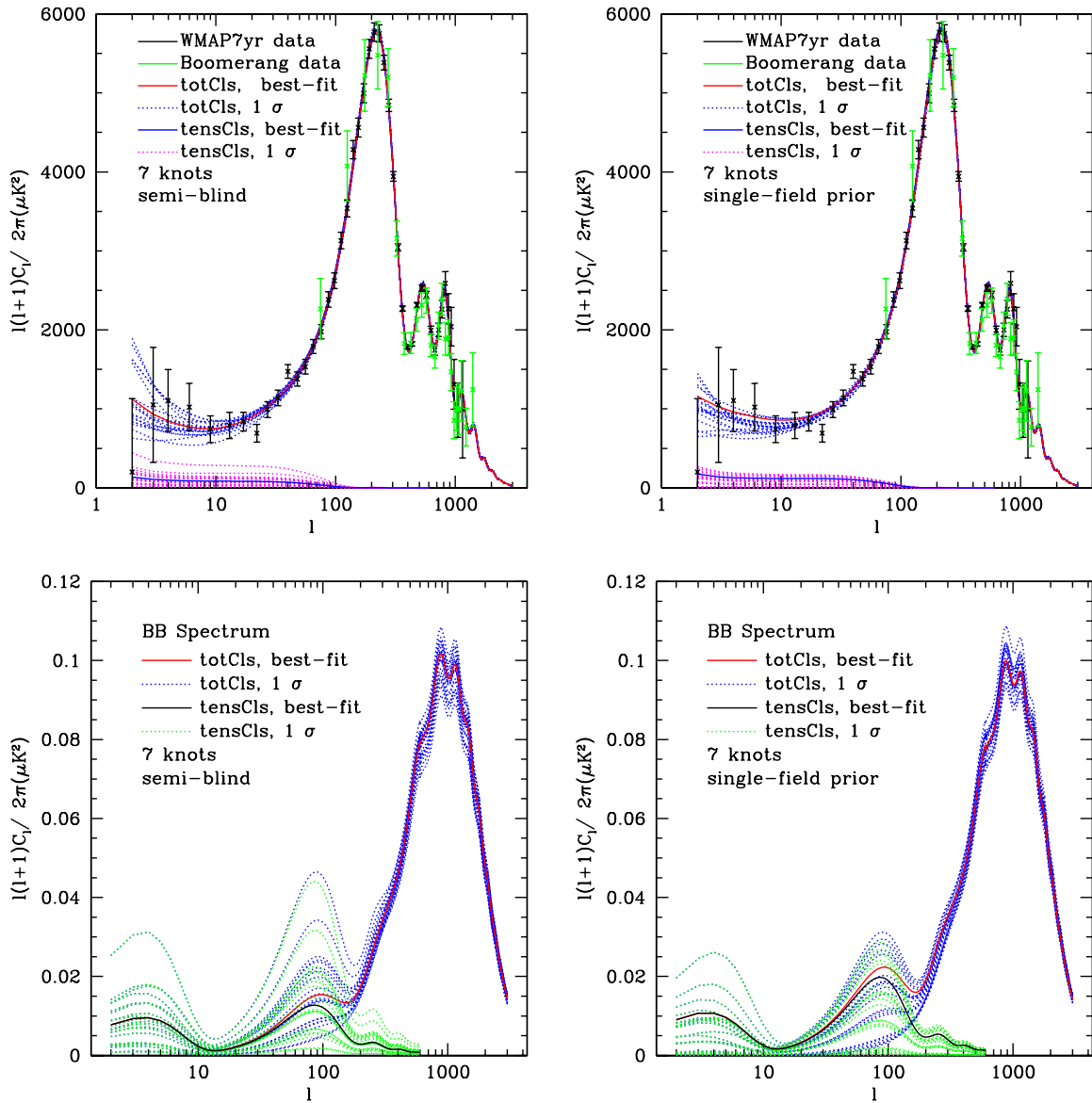


Figure 3.6: This CMB angular power spectra mapped from reconstructed trajectories (see Figure 3.5). The upper-left and lower-left panels are TT and BB power spectra reconstructed with bottom-up approach, and the upper-right and lower-right panels are using top-down approach. See the text for more details.

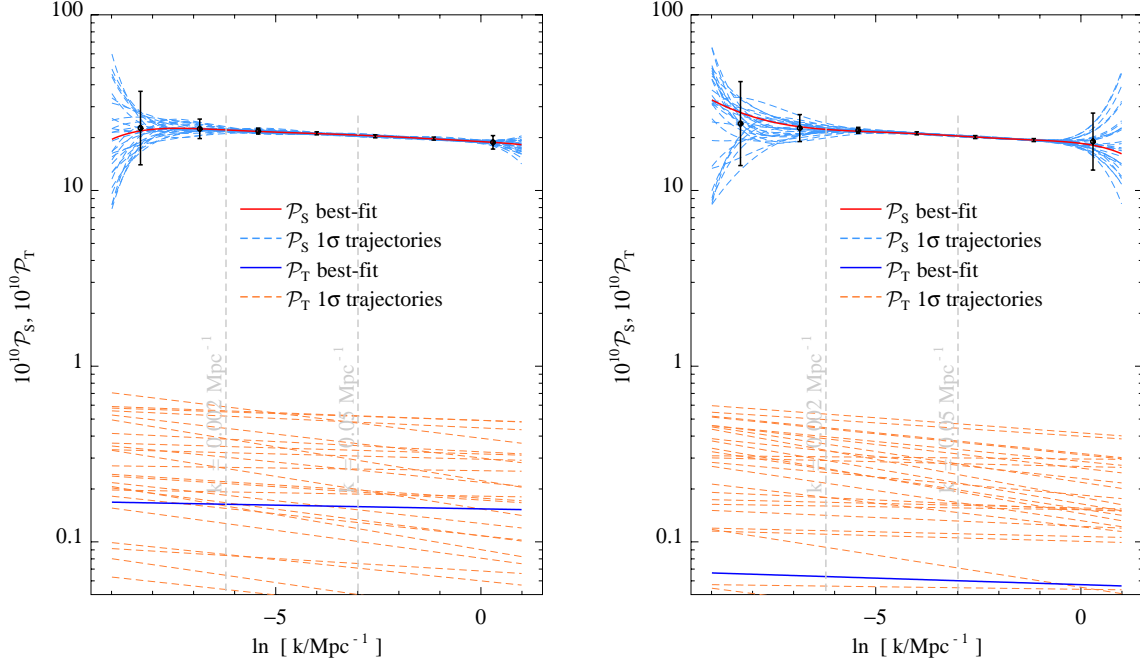


Figure 3.7: The reconstructed primordial spectra with mock data. The fiducial model has $\mathcal{P}_T = 0$ and a power-law \mathcal{P}_S with $n_s = 0.97$. The left panel uses natural cubic spline interpolation on $\ln \mathcal{P}_S$, while the right panel uses Chebyshev interpolation. The $1\text{-}\sigma$ error bars are uncertainties of the band powers. The band powers are defined as the convolutions of the power spectrum and top-hat window functions in seven uniform bins.

Table 3.2: The constraints on r using different parametrizations. Here “consistency” stands for the single-field inflation prior (see Section 3.5).

knots	interpolation method	consistency	fiducial model	constraint
7	natural cubic spline	no	$r = 0$	$0.000^{+0.017+0.035}$
7	Chebyshev	no	$r = 0$	$0.000^{+0.014+0.027}$
7	monotonic cubic Hermite	no	$r = 0$	$0.000^{+0.018+0.036}$
11	natural cubic spline	no	$r = 0$	$0.000^{+0.018+0.037}$
7	natural cubic spline	no	$r = 0.126$	$0.130^{+0.023}_{-0.021}$
7	monotonic cubic Hermite	yes	$r = 0.126$	$0.129^{+0.020}_{-0.018}$

with \mathcal{P}_S having an “IR-cascading” bump [6, 7], approximated by

$$P_{\text{bump}} = A \left(\frac{k}{k^*} \right)^3 e^{-\frac{\pi}{2}(k/k^*)^2} . \quad (3.4)$$

The shape of such a bump can be calculated in the theory, and should be parameterized accordingly in power spectrum reconstruction attempts if we consider this particular model. Here we examine whether such a bump is detectable without knowing the theoretical priori.

The reconstructed power spectra using monotonic cubic Hermite interpolation between 11 knots are shown in Figure 3.8. The bump in the scalar spectrum has no effect on the reconstructed tensor spectra, we hence only show scalar trajectories in the plot for a clear view of the details of the reconstructed bump. We notice that the bump is successfully reconstructed. However, the spectrum close to the bump is slightly twisted by the smoothness assumption (prior) we have chosen. We have also tried natural cubic spline interpolation and varying the number of the knots. We find that the twisting varies with different choices of interpolation method and number of knots, confirming our conjecture that it is a prior-driven effect. Despite these prior issues that persist in any trajectory reconstruction methods, we are able to find the main feature in the power spectrum without knowing the theoretical priori.

3.5 The Top-down Approach: Scanning the Expansion History

3.5.1 Method

To numerically calculate the primordial power spectra, it is more convenient to write everything as a function of comoving wavenumber k , by defining

$$f(k) = f|_{aH=k} , \quad (3.5)$$

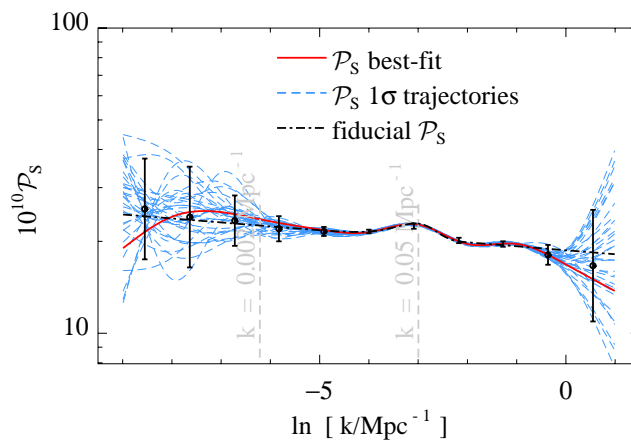


Figure 3.8: The reconstructed primordial power spectra, using mock data with a feature in the scalar power spectrum. A fiducial $r = 0$ and $n_s = 0.97$ model has been used, on top of which an IR-cascading bump [6, 7] with amplitude about 10% of the total \mathcal{P}_S and with position $k^* = 0.05\text{Mpc}^{-1}$ is added to the scalar power spectrum, as shown in dot-dashed black color. Monotonic cubic Hermite interpolation is used to interpolate $\ln \mathcal{P}_S$ between 11 knots.

where f represent arbitrary inflationary variables such as ϵ , H , etc.

We generate the expansion history with a similar technique. Random values of $d \ln \epsilon / d \ln k$ are drawn at a few knots in the observable interval. A trajectory of $d \ln \epsilon / d \ln k$ obtained via interpolation is then integrated into an $\epsilon(k)$ trajectory, with a constant of integration $\epsilon(k_{\text{pivot}})$ being an additional parameter. One more integral is performed to obtain the H trajectory, requiring again a new parameter. Instead of $H(k_{\text{pivot}})$ that is poorly determined by the observations, we use the the logarithm of zero-th order approximation of the well determined amplitude of scalar power spectrum, i.e. $\ln(H^2/\epsilon)|_{aH=k_{\text{pivot}}}$, as another parameter.

The scalar and tensor power spectra are then calculated using Eqs (1.37-1.42) and Eqs (1.43-1.45). Using the variable

$$\tilde{N} \equiv \ln(aH) , \quad (3.6)$$

we can write the evolution equations of \mathcal{R}_k and h_k as

$$\frac{d^2 \mathcal{R}_k}{d\tilde{N}^2} + \mu(\tilde{N}) \frac{d\mathcal{R}_k}{d\tilde{N}} + \frac{k^2}{(1-\epsilon)^2 e^{2\tilde{N}}} \mathcal{R}_k = 0 , \quad (3.7)$$

$$\frac{d^2 h_k}{d\tilde{N}^2} + \nu(\tilde{N}) \frac{dh_k}{d\tilde{N}} + \frac{k^2}{(1-\epsilon)^2 e^{2\tilde{N}}} h_k = 0 , \quad (3.8)$$

where the friction coefficients $\mu(\tilde{N})$ and $\nu(\tilde{N})$ are defined as

$$\mu(\tilde{N}) \equiv 3 + \frac{2\epsilon}{1-\epsilon} + \frac{1-2\epsilon}{1-\epsilon} \frac{d \ln \epsilon}{d\tilde{N}} , \quad (3.9)$$

$$\nu(\tilde{N}) \equiv 3 + \frac{2\epsilon}{1-\epsilon} - \frac{\epsilon}{1-\epsilon} \frac{d \ln \epsilon}{d\tilde{N}} . \quad (3.10)$$

There formulas can be directly used for numerical calculations, since we have already generated the trajectories of $d \ln \epsilon / d \tilde{N}$, $\epsilon(\tilde{N})$, and $H(\tilde{N})$.

We reconstruct \mathcal{P}_S and \mathcal{P}_T trajectories using the current observational data. The results are shown in the right panel of Figure 3.5. The earlier question whether a large tensor spectrum is allowed in the context of single-field inflation thus has an positive answer. The implication is that the quartic potential ($V = \frac{\lambda}{4} \phi^4$) chaotic inflation model,

which “over predicts” r in the traditional parametrization for single-field inflation, is consistent with the data in the extended parameter space. This conclusion addressed in a more precise way is: *$\lambda\phi^4$ model is ruled out by current data only if we restrict ourselves to a power-law scalar power spectrum.*

Of great interest is the ability of present and future CMB experiments to detect primordial gravitational waves. We produce mock data with a single-field inflation model - the $V = \frac{1}{2}m^2\phi^2$ model, which has r about 0.13 and n_s about 0.97. This value of r is promised to be detected by Planck, assuming a power-law \mathcal{P}_S . The reconstructed spectra with both bottom-up approach and top-down approach are shown in Figure 3.9. We find that this tensor power spectrum can be detected even we allow almost arbitrary shapes of scalar power spectrum. For the top-down approach we have also tried varying the interpolation methods, the number of knots, and scanning $2\epsilon + d\ln\epsilon/d\ln k \approx 1 - n_s$ trajectories. The similar results we find show the robustness of our method.

3.6 Discussion and Conclusions

The reconstruction of primordial power spectra is a conceptually simple problem. We are aware that the choice of statistical tools should not be unique; or otherwise the results will not be robust and convincing. However, this does not mean that we can ignore this problem and choose arbitrary statistical tools. Many statistical treatments of the trajectories implicitly impose strong priors that might mimic the physics of interest. One example is the false detection of gravitational waves if we assume flat priors on \mathcal{P}_T on a few knots, and impose the monotonicity condition $d\mathcal{P}_T/d\ln k < 0$. The statistical methods we proposed in this work are better choices than many others. We have shown that the robust results do not depend on the choice of interpolation method and the number of knots, provided that we keep the reduced χ^2 or Bayesian evidence at a reasonable level. Also, successful reconstructions are shown with mock data.

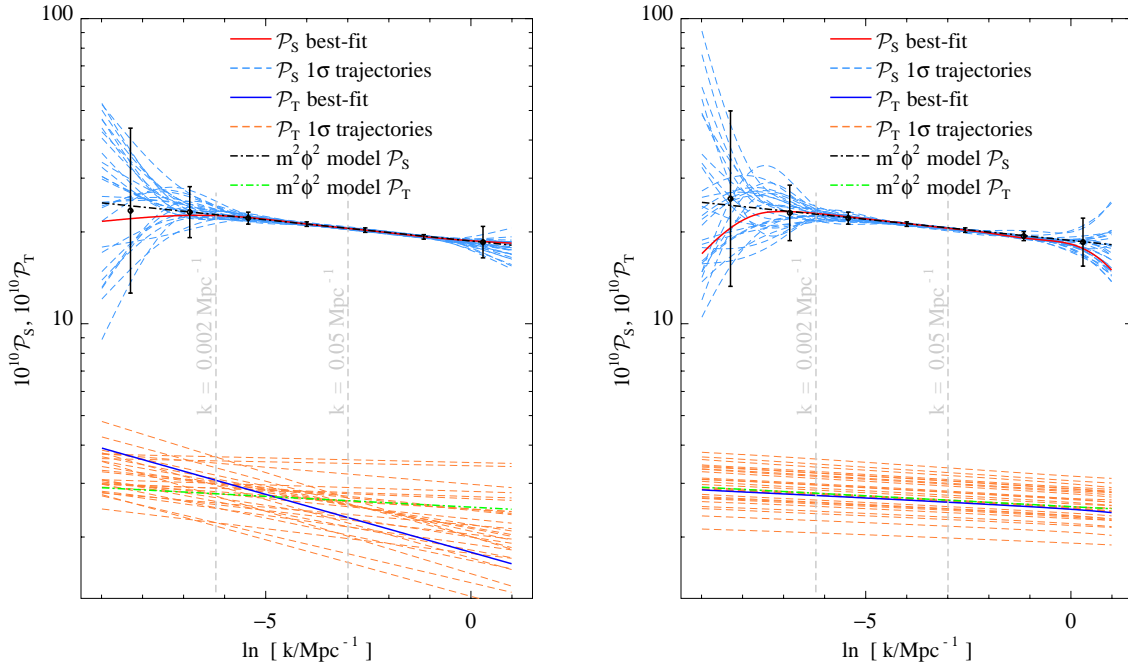


Figure 3.9: The reconstructed primordial spectra with mock data. The fiducial model that has been used to generate the mock data is the quadratic potential ($V = \frac{1}{2}m^2\phi^2$) model. The left panel shows the reconstructed power spectra using the bottom-up approach described in Section 3.4, with natural cubic spline interpolation method applied. The right panel shows the reconstructed power spectra using the top-down approach scanning $d \ln \epsilon / d \ln k$, as described in Section 3.5. The $1\text{-}\sigma$ error bars are uncertainties of the band powers. The band powers are defined as the convolutions of the power spectrum and top-hat window functions in seven uniform bins.

Previous attempts on this problem can be put into three categories:

1. Top-down approach using basis expansion [36, 193, 194, 195, 196, 197].
2. Bottom-up approach using basis expansion [198, 199, 200, 201, 202, 203, 204, 205, 206, 207, 208].
3. Bottom-up approach using interpolation [209, 210, 211, 212, 38, 213, 214, 215, 216].

Our work differs from these works from the following aspects: i) We have shown that the obviously missing method – top-down approach using interpolation is a viable method; ii) For the bottom-up approach we have shown the independency of the results on the choice of interpolation method, with three concrete examples – natural cubic spline interpolation, monotonic cubic Hermite interpolation, and Chebyshev interpolation; iii) We have used the most current data sets including weak lensing and $\text{Ly}\alpha$ that have not been included in earlier works.

Also we have explicitly shown, via a concrete example, that nontrivial features in the primordial power spectra can be practically detected using our method. This has not been studied before in the aforementioned works.

Another also very interesting method that is not covered here is the principal components analysis (PCA) method [217]. We leave this topic, and many others, in our future work.

Chapter 4

Non-Gaussian Curvature

Fluctuations from Preheating

4.1 Introduction

In chaotic inflation models, the inflaton field ϕ starts from a large initial value, a number of Planck masses, and rolls toward the potential minimum. Inflation ends when ϕ is close to the potential minimum, and soon after that the inflaton field starts to oscillate. The oscillating inflaton field decays into other particles, either perturbatively (reheating) or non-perturbatively (preheating), via some form of couplings. An oft-studied model is the $\frac{1}{2}g^2\phi^2\chi^2$ coupling, where χ is a light scalar field, and g a dimensionless coupling constant. In the last chapter, we studied the metric perturbations derived from the inflaton fluctuations $\delta\phi$. Fluctuations in χ , generated via the same mechanism, were not thought to be responsible for the metric perturbations, since during inflation the energy contribution from χ is negligible. During preheating, the fluctuations in the χ field are magnified through parametric resonance. It is difficult to track such full non-linear process, in which all the modes χ_k in the broad resonance band are magnified and come to interact with each other. Metric perturbations from this process can be generated

only if the local expansion rate or the local equation of state is modulated by the χ field. Before our work, which I will discuss in this chapter, it was widely believed that in such a complicated non-linear system the initial condition (the local χ value) will not be remembered, but this had not been proved, either theoretically or numerically. Early in 2007's, I used LATTICEEASY [218] to simulate preheating for such a model. With a brute-force calculation, I found spiky patterns in the expanding e-folds as a function of χ . But the signal was weak, and no tests were done to show that the spikes are not numerical glitches. In 2008 Professor Frolov and Professor Bond participated in the project. With Frolov's new code DEFROST [219] similar spiky patterns were found. By that time we (Professor Bond, Professor Kofman, Professor Frolov and I) all started to take this seriously, as it might be the first hint that preheating can produce large scale metric fluctuations. Progress was made in parallel. I was not satisfied by these brute-force calculations. The conversations with Professor Frolov stimulated me to write a new lattice simulation code with superb high accuracy of energy conservation (improved our previous code by about 8 orders of magnitude). This code again verified the spiky patterns we found before. We came up with a full theory of the physical origin of this phenomenon, and how to visualize it. This "billiard model" was soon verified in details by Frolov's DEFROST code and my new code "HLattice".

This Chapter is based on the work published in the journal *physics review letter*. Hence it is very terse. A longer paper expanding on this material is in development. For completeness we will include here most of the contents that has already been published [56]. Please cite our original paper for the use of these contents.

4.2 The Preheating Model

During inflation, vacuum fluctuations in the light field χ are transformed on super-horizon scales into homogeneous and isotropic Gaussian random fields. These are fully

defined by their power spectra $\frac{d\sigma_\chi^2(k)}{d\ln k} \equiv \langle |\chi_k|^2 \rangle \frac{k^3}{2\pi^2}$, whose magnitude, $\sim [H/(2\pi)]^2$, is related to the Hubble parameter H at expansion factor a when Ha first equals the wavenumber k in question. Here and in what follows, we use the notation $\langle \cdot \rangle$ for ensemble average and σ_x for r.m.s. of random variable x . In standard scenarios, metric curvature fluctuations ζ_ϕ , defined as $H\delta\rho/\dot{\rho}$ in spatial flat gauge [220]ⁱ, are derived from the inflaton ϕ and are nearly Gaussian and often nearly scale invariant, with power $d\sigma_\zeta^2(k) \approx d\sigma_\phi^2(k)/(2M_p^2\epsilon)$, in terms of the acceleration parameter ϵ defined in Eq (1.20) [10, 12, 13, 14]. Observationally ϵ is below 0.03 at the 95.4% confidence limit from the large angle CMB, hence ζ is considerably amplified over $\delta\phi/M_p$. Alternative mechanisms utilizing light “non-inflatons” χ must overcome this ϵ effect. Examples are “curvatons” which temporarily dominate the energy density after inflation [187, 188], and fields which induce spatial variations of couplings which modulate the timing of the now-inhomogeneous post-inflation (p)reheating [221], but are not gravitationally dominant.

The ζ -source first proposed in [222] and studied here is nonlinear resonant preheating inducing expansion factor variations from the end of inflation at $\epsilon = 1$ to when the equation of state settles to $w = 1/3$. A sample framework [223] for this has a potential

$$V(\phi, \chi) = \frac{1}{4}\lambda\phi^4 + \frac{1}{2}g^2\phi^2\chi^2, \quad (4.1)$$

with inflation driven by the first and particle creation by the second term. Here $\lambda \sim 10^{-13}$ gives the right amplitude of CMB fluctuations.

If g^2/λ is of order unity, the non-inflaton $\chi(\mathbf{x})$ is light during inflation and accumulates quantum fluctuations varying on scales much greater than the Hubble scale at the end of inflation

$$H_e \equiv H|_{\epsilon=1} \sim 10^{-7}M_p. \quad (4.2)$$

Figure 4.1 shows the amplitude of mode functions χ_k in the spatial flat gauge at the end of inflation, for k/a_e covering the range from H_e to scales much bigger than today’s

ⁱIn the large scale limit, it coincides with the comoving curvature fluctuations \mathcal{R} .

cosmological scales ($k/a_e \sim e^{-60} H_e$), where a_e is the scale factor at the end of inflation. We note for $g^2/\lambda = 2$ that corresponds to a SUSY model, the amplitude of χ fluctuation on scales much larger than H_e^{-1} but within the current observable universe is about $H_e \sim 10^{-7} M_p$. On scales shorter than H_e^{-1} , this $\chi(\mathbf{x})$ is nearly homogeneous, defining “separate universes” with specified background χ_i as initial conditions for lattice simulations of the fully coupled fields to determine the nonlinear evolution of the EOS, which imprints itself on $\ln a(\chi_i)$. The resulting curvature perturbations $\zeta_{\text{preh}}(\mathbf{x})$ are different in the number of e-folds on uniform Hubble (*i.e.* uniform energy density) time hypersurfaces, $\zeta \equiv \delta \ln a|_H = \delta N(\chi_i)$ [224, 114, 225]. If such variations exist, they would be in addition to the standard ones.

Preheating in the model begins with parametric resonance amplifying the fluctuations in the mode function $\chi_k(t)e^{i\mathbf{k}\cdot\mathbf{x}}$ describing vacuum excitations of the χ -particles. The problem can be reduced to a flat space-time model by conformal transformations:

$$\tilde{\phi} \equiv \sqrt{\lambda} a \phi , \quad (4.3)$$

$$\tilde{\chi} \equiv a \chi . \quad (4.4)$$

$$\tau \equiv \int \frac{dt}{a} . \quad (4.5)$$

The inflaton EOM is

$$\tilde{\phi}'' + \left(\frac{a''}{a} + \tilde{\phi}^2 \right) \tilde{\phi} = 0 , \quad (4.6)$$

where a prime denotes the derivative w.r.t. the conformal time τ .

Recall that during coherent oscillations the effective EOS for $\lambda\phi^4$ model is 1/3 (see Section 1.6). We can ignore the a''/a term, as this term is decaying as a^{-2} and has zero average. The solution of Eq. (4.6) with the a''/a term ignored is

$$\tilde{\phi} = \tilde{\phi}_{\text{max}} \text{Cn} \left(\phi_{\text{max}} \tau; \frac{1}{\sqrt{2}} \right) , \quad (4.7)$$

where $\tilde{\phi}_{\text{max}}$ is the amplitude of the $\tilde{\phi}$ oscillation. If we define $a = 1$ at the end of inflation,

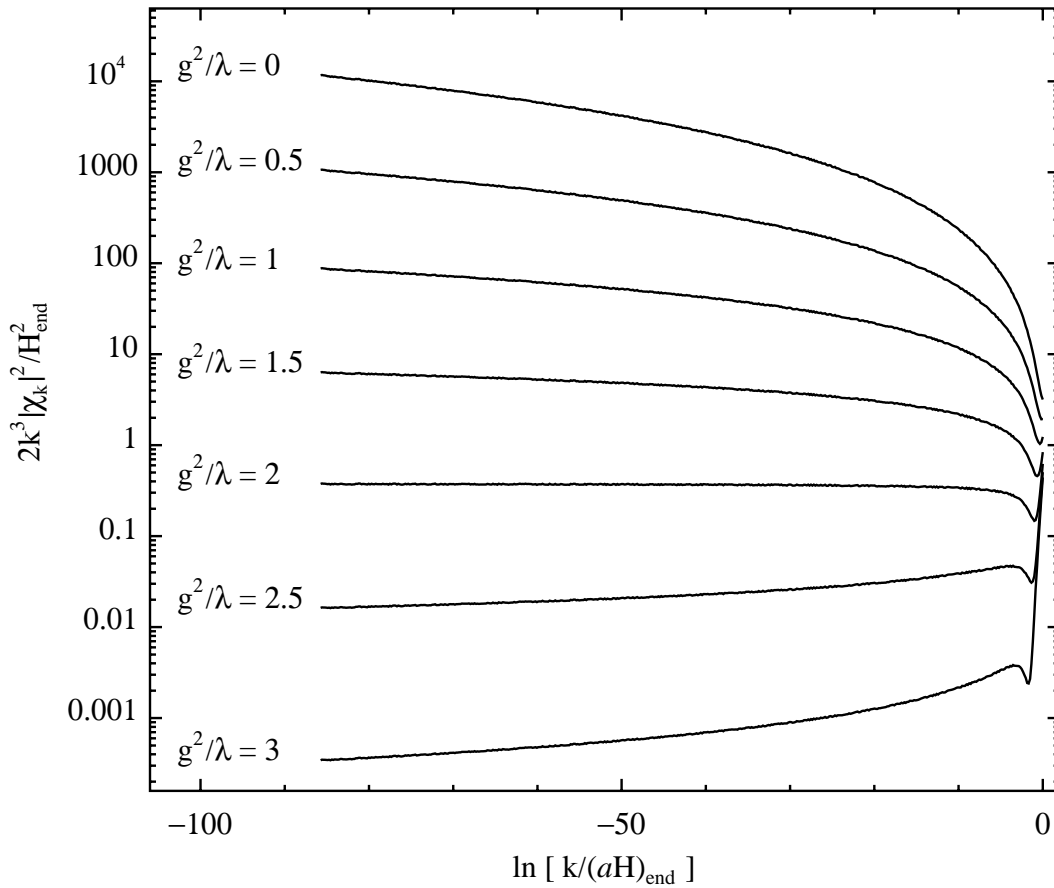


Figure 4.1: The amplitude of mode functions of χ in the spatial flat gauge at the end of inflation, for the inflation model $V = \frac{\lambda}{4}\phi^4 + \frac{1}{2}g^2\phi^2\chi^2$ with $\lambda = 10^{-13}$ and various values of g^2/λ . The rising tails around $k \sim (aH)_{\text{end}}$ are the vacuum mode functions that have not passed the quantum-decoherence phase. These tails should be renormalized away when calculating the classical r.m.s. of the χ field.

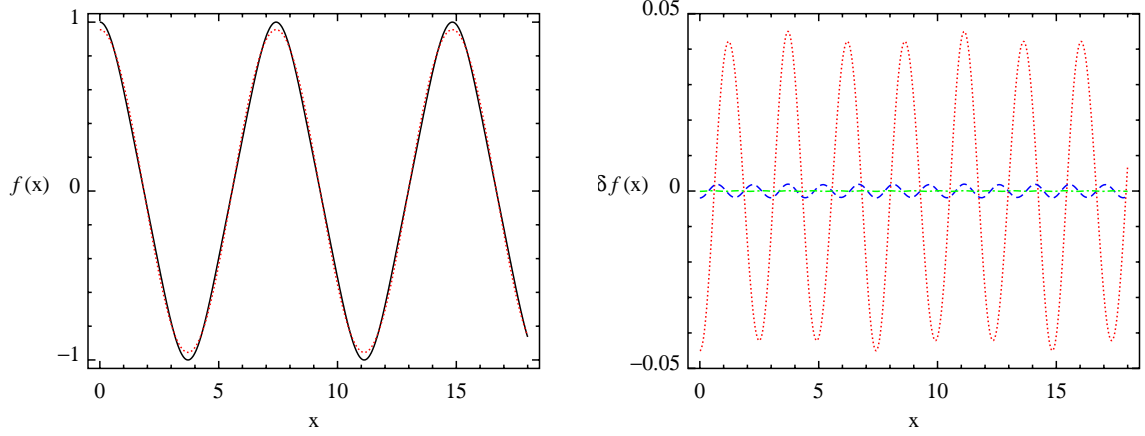


Figure 4.2: In left panel the solid black line is $\text{Cn}(x; 1/\sqrt{2})$, the dotted red line shows the first ($n = 1$) term on the R.H.S. of Eq. (4.8). In the right panel we show the residuals $\delta f_n(x) \equiv \text{Cn}(x; 1/\sqrt{2}) - f_n(x)$, where $f_n(x)$ is the sum of the first n terms in the R.H.S. of Eq (4.8). The dotted red line, the dashed blue line, and the dot-dashed green line are $\delta f_1(x)$, $\delta f_2(x)$ and $\delta f_3(x)$, respectively.

$\tilde{\phi}_{\max}$ is about $0.1\sqrt{\lambda}M_p$. The elliptical cosine Cn is given by

$$\text{Cn}\left(x; \frac{1}{\sqrt{2}}\right) = \frac{8\pi\sqrt{2}}{T} \sum_{n=1}^{+\infty} \frac{e^{-\pi(n-\frac{1}{2})}}{1 + e^{-\pi(2n-1)}} \cos \frac{2\pi(2n-1)x}{T}, \quad (4.8)$$

where the period $T = \frac{\Gamma^2(1/4)}{\sqrt{\pi}} \approx 7.4163$ [223] (The Fourier expansion of $\text{Cn}(x; 1/\sqrt{2})$ given in Ref. [223] has a typo and should be corrected as above.) In Figure 4.2 the approximations using the first one, first two and first three terms are shown.

The conformal mode function $\tilde{\chi}_k \equiv a\chi_k$ obeys an oscillator equation with a periodic frequency controlled by the background inflaton oscillations:

$$\frac{d^2\tilde{\chi}_k}{d\tau^2} + \left(k^2 + \frac{g^2}{\lambda}\tilde{\phi}^2\right)\tilde{\chi}_k = 0, \quad (4.9)$$

where again we have ignored the tiny a''/a term.

In the resonant bands, $\tilde{\chi}_k \sim e^{\mu_k\tau}$ is unstable, with the real part of the Floquet exponent μ_k being a function of $g^2/\lambda\tilde{\phi}_{\max}^2$ and k^2 . It is more convenient to use $\tilde{\phi}_{\max}$ as a mass unit, and write $\tilde{\mu}_k \equiv \mu_k/\tilde{\phi}_{\max}$ as a function of g^2/λ and $\tilde{k} \equiv k/\tilde{\phi}_{\max}$. Note

that $\tilde{\mu}_k$ and \tilde{k} are both physical, i.e., they do not depend on the normalization of a . Using the technique described in Section 1.6, I calculate the Floquet chart and show the result in Figure 4.3. The growth of superhorizon modes on $\phi = \text{const.}$ hypersurfaces does not violate causality. It is generated by coherent inflaton oscillations prepared during inflation.

4.3 The Comoving Curvature Fluctuations

If $g^2/\lambda \sim 2$, the maximum of μ_k in the first resonant band is located close to $k = 0$ (see Figure 4.3). Hence a nearly homogeneous χ_i will be exponentially unstable in each separate universe, and soon becomes entangled in the complicated mode-mode dynamics of preheating driven by the back-reaction effects of copiously produced χ and $\delta\phi$ particles. To determine $\delta N(\chi)$ at the part per million level, we need non-linear lattice simulations with energy conservation accuracy (ECA) well below this. The early attempt by [222] used an energy-leaking algorithm and got a wrong result with $\delta N \sim 10^{-3}$, with a dominantly-quadratic form $\delta N \approx f_\chi \chi_i^2$ characterized by a constant f_χ similar to f_{NL} used in non-Gaussianity (nG) studies of the CMB sky [226, 227]. We do not confirm the large quadratic nG of [222], but do find a nontrivial $\delta N(\chi_i)$ with a regular sharp-spiked pattern at the observationally interesting $\sim 10^{-5}$ level, as shown in Fig. 4.4, with a radically different impact on the sky than the f_{NL} story. Although our discovery of the spiked $\delta N(\chi_i)$ function was a truly numerical one, a posteriori we can explain it by a combination of chaotic zero-mode dynamics after t_e and the abrupt onset of inhomogeneous nonlinearity at a preheating time t_{preh} , allowing us to conjecture for which models it works.

To accurately compute the very low levels of $\delta N(\chi_i)$, especially since we are in finding and validation mode for such tiny effects, we needed to go well beyond the ECA practically achievable in second-order preheating codes (typically $\sim 10^{-3}$ for LATTICEEASY

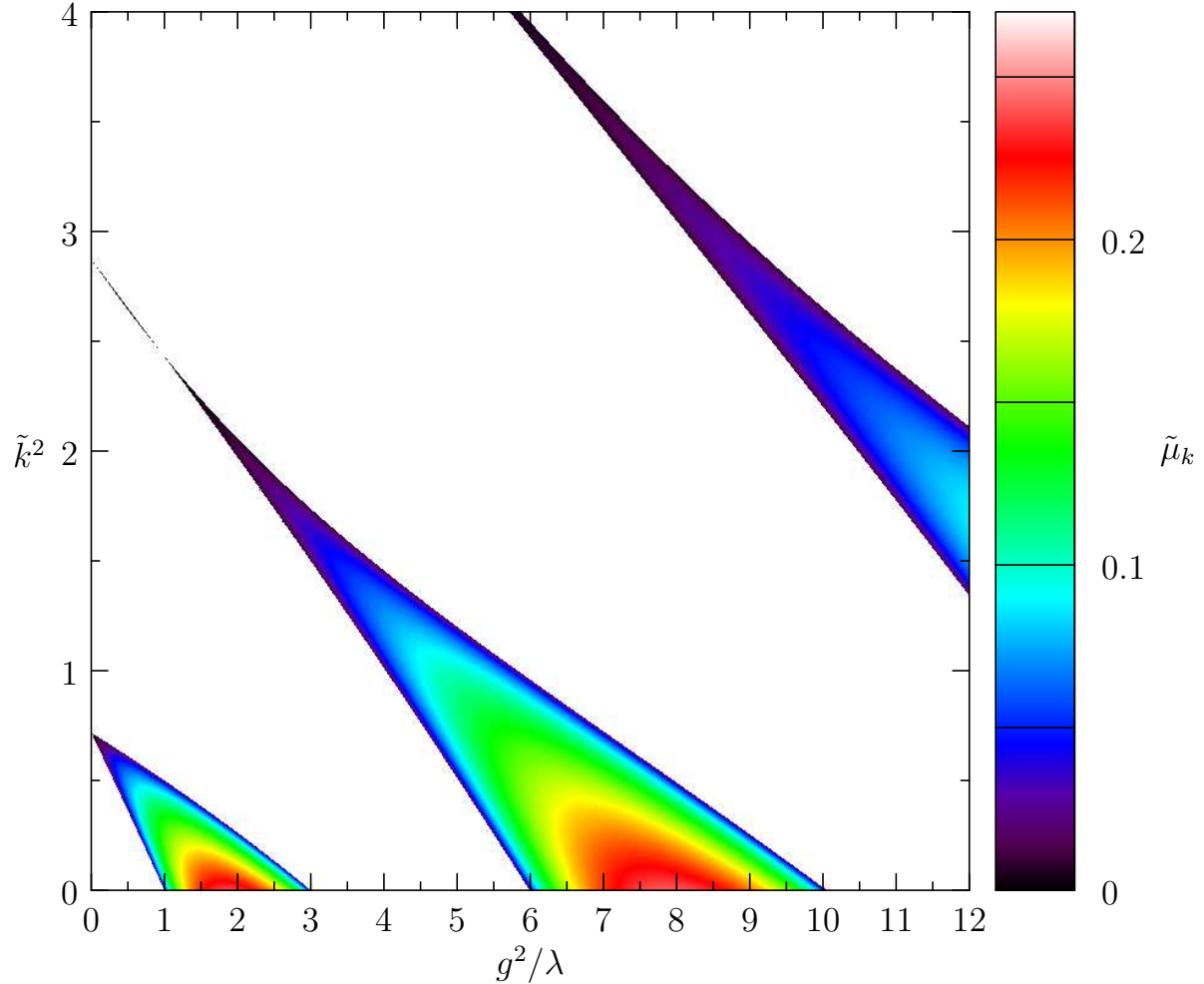


Figure 4.3: The Floquet chart for $V = \frac{1}{4}\lambda\phi^4 + \frac{1}{2}g^2\phi^2\chi^2$ preheating model. The white regions give the stable bands where the mode function χ_k does not grow. The coloured regions are the instability bands. Here \tilde{k} is defined as $k/(a\sqrt{\lambda}\phi_{\max})$, where $\phi_{\max} \propto a^{-1}$ is the amplitude of the ϕ oscillation. In the instability bands the growth of mode function χ_k is described by $a\chi_k \sim e^{\tilde{\mu}_k \sqrt{\lambda} \int \phi_{\max} dt}$, where t is the physical time.

[218] and $\sim 10^{-5}$ for DEFROST [219]). We developed a new high-order symplectic PDE solver with adaptive time steps, which can reach machine precision levels (ECA $\sim 10^{-13}$!) to address this problem. In retrospect, we find that ECA of 10^{-7} would suffice, which is achievable with shorter timesteps in DEFROST. The lattice simulations begin at expansion factor a_e when $\epsilon = 1$; we have shown that variations of the start do not affect results. The calculations are stopped at a uniform Hubble value H_f when the EOS $w = p/\rho$ is nearly $1/3$, the radiation-dominated value. Although the average w is asymptotically approaching $1/3$, it has small oscillations during preheating, leading to a fluctuations to average over to determine $N(\chi_i)$ for use in the curvature formula. To deal with this, we used an accurate extrapolation template for the averaged $a(\tau)$ or, for superb accuracy, a Kaiser window filter to suppress high frequency oscillations in $a(\tau)$ by a factor 10^{-8} . With either, we showed that provided we calculate for 5-6 e-folds after a_e , the specific H_f is not important. An accuracy test was to show δN is effectively zero ($\ll 10^{-6}$) and not modulated by χ_i for g^2/λ out of the resonant band, *e.g.* at $g^2/\lambda = 1$ and 3 , for which the real part of the Floquet exponent for $k = 0$ is zero ($\mu_0 = 0$). With the symplectic code, we ran a lattice simulation in a box of size $64/H_e$ with resolution 256^3 to check that our conclusions derived using a very large number of lower resolution simulations using DEFROST to build up statistics in χ_i are accurate. The essential effects can indeed be captured with lower resolution and box size. Fig. 4.4 showing a spiky pattern in $\delta N(\chi_i)$ for $g^2/\lambda = 2$ was produced with 11563 simulations with box size $20/H_e$ and resolution 32^3 . The amplitude of the spikes increases as χ_i increases. The spikiest pattern is at $g^2/\lambda \approx 1.88$ corresponding to the maximum of the real part of the Floquet exponent for $k = 0$ in the band $1 < g^2/\lambda < 3$ (see Figure 4.3), with the spikes broadening away from that, finally disappearing at the $g^2/\lambda = 1$ and 3 borders.

For Fig. 4.4, we explored a large range in input χ_i/M_P , from 10^{-8} up to 2×10^{-5} . $\chi_i(\mathbf{x}) = \chi_{<h} + \chi_{>h}$ has a sub-horizon contribution $\chi_{<h}$ from eigenmodes with wavenumbers between $k_e \sim H_e a_e$ to the current horizon scale, $k_h \sim H_h a_h$, and a super-horizon

contribution $\chi_{>h}$ with waves from k_h to a k_{\min} whose value will depend upon the inflation model. The corresponding variances are $\sigma_{<h}^2 = \int_{k_h}^{k_e} d\sigma_\chi^2$ and $\sigma_{>h}^2 = \int_{k_{\min}}^{k_h} d\sigma_\chi^2$. As shown in Figure 4.1, $d\sigma_\chi^2/d\ln k$ is nearly constant over ~ 100 e-folds for $1.5 < g^2/\lambda < 2.5$, drops substantially as $a \rightarrow a_e$ for $g^2/\lambda = 0$, and actually rises for $g^2/\lambda = 3$. The numerical result agrees well with a simple analytical estimation $k^3|\chi_k|^2 \propto k^{(g^2/\lambda-2)/N}$ (valid only for $k \ll a_e H_e$ and $g^2/\lambda \lesssim O(1)$), where $N \sim \ln[(a_e H_e)/k]$ is the number of efoldings from the horizon-crossing of mode k to the end of inflation. The least number of e-folds $\ln a_h/a_e$ must exceed $\sim 50 - 60$, and since $H > H_e$ during inflation, $\sigma_{<h}^2 \gtrsim \ln k_e/k_h [H_e/(2\pi)]^2$ gives a $\chi_{<h}$ enhanced over H_e by $\sim \sqrt{55}$. The super-horizon power, $\sigma_{>h}^2 \gtrsim \ln k_h/k_{\min} [H_e/(2\pi)]^2$ is also log-enhanced, and considerably so in our illustrative $\lambda\phi^4$ example. Thus, the log factors give larger χ_i , including a $\chi_{>h}$ random number which is nearly constant within our Hubble patch, but has a $\sim \pm\sigma_{>h}$ patch-to-patch ‘‘cosmic variance’’.

4.4 Analog to Chaotic Billiard Motions

We now show how the features of $\delta N(\chi_i)$ can be understood qualitatively from trajectories in the two-dimensional space of homogeneous modes $(\phi(\tau), \chi(\tau))$. The excited inhomogeneous degrees of freedom do back-react on these $k \approx 0$ modes, but only later in the evolution, *e.g.* at $t \sim 10T$ for $g^2/\lambda = 2$. The $(\phi(\tau), \chi(\tau))$ space is effectively bounded by potential energy barriers $\frac{1}{4}\lambda\phi^4 + \frac{1}{2}g^2\phi^2\chi^2 = \text{const}$, as shown in Fig. 4.5. Initially the trajectories oscillate mostly in the ϕ direction, with only very small initial amplitudes in χ , as illustrated in the insets in Fig. 4.5.

These oscillations are akin to billiard motions between the potential walls. Precession of the initial oscillations causes the χ amplitude to grow exponentially in a chaotic manner: $\chi(\tau) = \chi_i e^{\Lambda t}$, where Λ is the Lyapunov exponent. This gives us new insight on the parametric resonant $k = 0$ solution in terms of the Lyapunov instability. For $g^2/\lambda = 2$, we find $\Lambda = \mu_0 = 0.235$. This conjecture also works for the cases in which $k = 0$ is

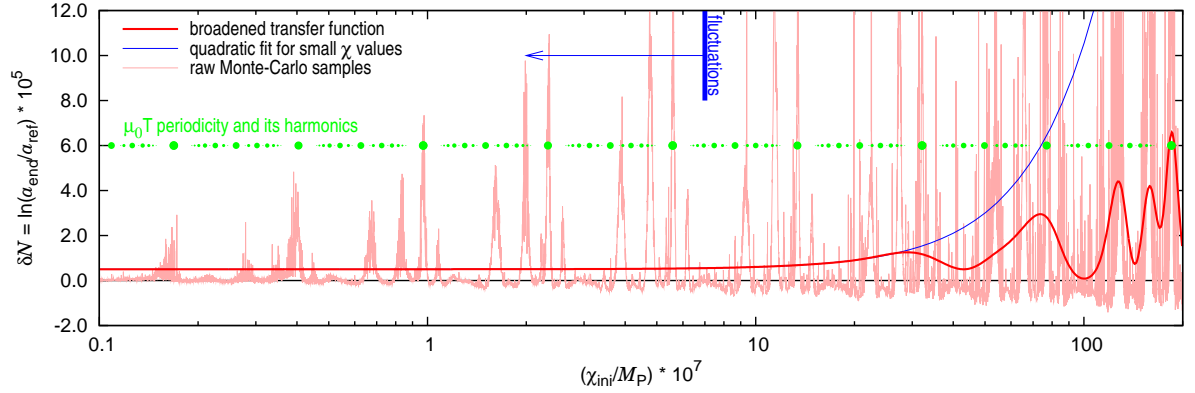


Figure 4.4: The structure of $\delta N(\chi_i)$ on uniform Hubble hypersurfaces probed with $\sim 10^4$ lattice simulations from the end-of-inflation through the end-of-preheating for varying homogeneous χ_i initial conditions, for $g^2/\lambda = 2$. The periods $n\mu_0 T$ in $\ln \chi_i$ are marked by the large green circles, and the higher harmonics (revealed by the Fourier analysis) by smaller green circles. These locate the spikes in $\delta N(\chi_i)$. The effective field $\langle F_{\text{NL}} | \chi_b + \chi_{>h} \rangle$ marginalized over high spatial frequencies with $\sigma_{\text{HF}} = 7 \times 10^{-7} M_P$ (vertical line) yields the solid curve. Here χ_b etc. are defined in Section 4.5. A quadratic fit, $f_\chi(\chi_b + \chi_{>h})^2$, is also shown. An issue for *our* Hubble patch is whether the ultra-large scale $\chi_{>h}$ is large enough that the large scale structure fluctuations about it, $\pm \sigma_{b<h}$, encompass smoothed peaks in field space, or not. A typical value for $\sigma_{b<h}$ is $\sim 3 \times 10^{-7} M_P$.

not in the resonant band; *e.g.* for $g^2/\lambda = 3$ we have $\mu_0 = 0$ and do indeed find periodic trajectories so $\Lambda = 0$.

As χ grows beyond the linear regime, the bouncing billiard experiences the negative curvature of the potential walls and a bifurcation of the trajectories occurs, with a few entering the arms in between walls, and most do not. If there were only homogeneous modes the impact of this would be temporary because eventually all trajectories would be chaotically mixed. However, the excitation of the inhomogeneous modes results in exponential growth of $\langle\chi^2\rangle$ and $\langle\delta\phi^2\rangle$, as $e^{2\mu_*t}$ and $e^{4\mu_*t}$ respectively, where μ_* is an effective resonant exponent [223]. These induce enhanced effective masses in the fields, abruptly changing the potential, with the arms in between walls closing exponentially quickly, as shown in Fig. 4.5.

The trajectories which happen to get into the arms before arm-closure evolve very different from those which never get into the arms. The billiard picture breaks down when the gradient terms in χ and $\delta\phi$ occur, at arm-closure time, but the bifurcation determined by the initial conditions at the linear stage has already happened. The two pre-closure classes of in-arm and not-in-arm trajectories result in different equations of state, and hence a χ_i -dependent $\delta N(\chi_i)$. In-arm trajectories experience kinetic energy kicks from the closing arms, which translates into a transient decrease in w , inducing a jump in δN . The no-spike trajectories of the upper panel of Fig. 4.5 are much more numerous than the rarer sort in the lower panel corresponds that give spikes. The billiard picture predicts the spike pattern as one periodic in $\ln \chi$ which works extremely well: the same “spiky” trajectory labelled by χ_i is repeated for initial values $\chi_i e^{n\mu_0 T}$ for integer n . The origin of the higher harmonics is more complex. Our spike pattern formula works very well for other values of g^2/λ , with the requisite $\mu_0(g^2/\lambda)$.

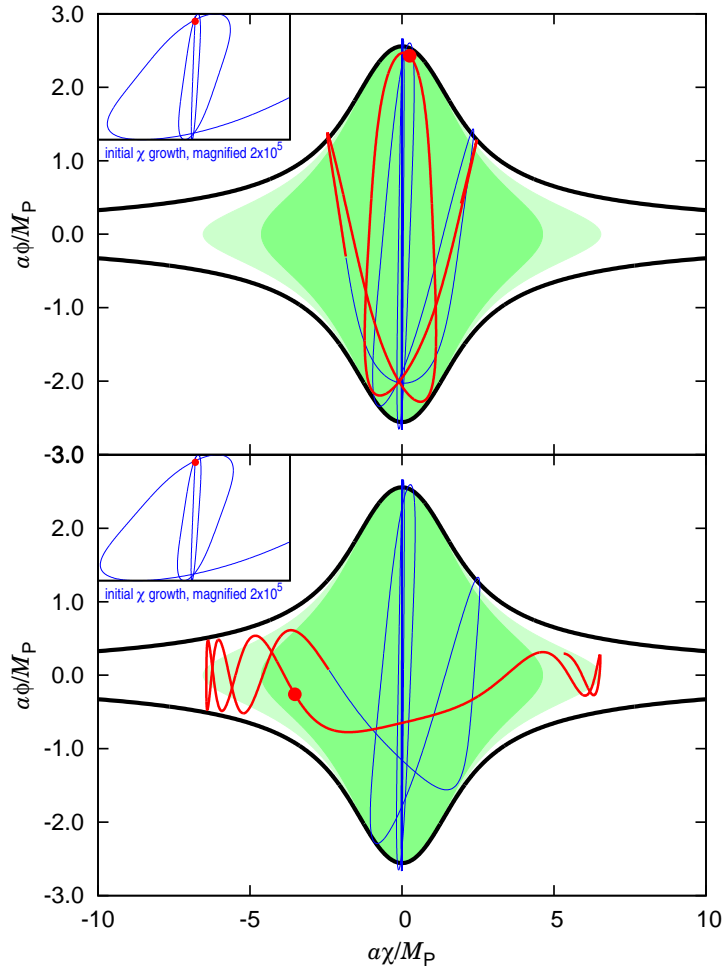


Figure 4.5: Billiard trajectories of the $k = 0$ modes $\phi(\tau)$ and $\chi(\tau)$ within the $\lambda\phi^4/4 + g^2\chi^2\phi^2/2$ potential well. Upper panel has a “no-spike” initial value $\chi_i = 3.6 \times 10^{-7} M_P$, and the bottom panel has a “spike” $\chi_i = 3.9 \times 10^{-7} M_P$. The solid curves are the (fuzzy) potential walls without the inclusion of mass terms induced by field nonlinearities; the pale green and brighter green border areas include the induced masses at the instances $t = 10.8T$ and asymptotically. Thin and thick parts of the trajectories denote before after $t = 9.7T$, and up to $11.8T$, with the circle on it at $t = 10.8T$. The inserts in the left upper corners of the panels show the first several periods of linear oscillations.

4.5 Non-Gaussianity

Let us denote ζ_{preh} by $F_{\text{NL}}(\chi_i(\mathbf{x}))$, where the capital F is used to distinguish it from the usual constant f_{NL} parameter. These are added to the conventional inflaton curvature fluctuations ζ_ϕ : $\zeta_{\text{tot}}(\mathbf{x}) \approx \zeta_\phi(\mathbf{x}) + F_{\text{NL}}(\chi(\mathbf{x})) - \langle F_{\text{NL}} \rangle$ (The ensemble average $\langle F_{\text{NL}} \rangle$ over all values of χ , is subtracted so ζ_{tot} fluctuates about zero.) Structure in χ_i and hence in F_{NL} , exists on a vast range of resolution scales, from k_{min} through k_h to k_e . Observed large scale structure (LSS), as probed by the CMB, redshift surveys, weak lensing, and rare event abundances such as of clusters probe ~ 10 e-folds in $\ln k$ below k_h^{-1} , and about the same number of e-folds just below this can be probed with the more uncertain astrophysical observables involving earlier stages in the nonlinear hierarchy, galaxies, dwarves, and the “first stars” within them. The superhorizon scales beyond k_h^{-1} have no impact on ζ_ϕ -structure, but do have a large impact on F_{NL} through the specific value $\chi_{>h}$ built from waves $k_{\text{min}} < k < k_h$. To explore the astrophysical consequences of F_{NL} , we marginalize over high frequency components χ_{HF} of $\chi \equiv \chi_{\text{HF}} + \chi_{\text{LF}}$ to form the conditional non-Gaussian “effective field”, $\langle F_{\text{NL}} | \chi_{\text{LF}} \rangle$, with about 40-50 e-folds of “short distance” substructure in F_{NL} filtered out. The mean-field, $\langle F_{\text{NL}} | \chi_{\text{LF}} \rangle = \int F_{\text{NL}}(\chi) P(\chi | \chi_{\text{LF}}) d\chi$, is a Gaussian-smoothing of F_{NL} in field-space, via $P(\chi | \chi_{\text{LF}}) = \frac{1}{\sqrt{2\pi}\sigma_{\text{HF}}} \exp[-(\chi - \chi_{\text{LF}})^2 / (2\sigma_{\text{HF}}^2)]$, with variance $\sigma_{\text{HF}}^2 = \langle \chi_{\text{HF}}^2 \rangle$. Using it will give reliable LSS inferences, if the Fourier transform of the deviation $\Delta F_{\text{NL}} \equiv F_{\text{NL}} - \langle F_{\text{NL}} | \chi_{\text{LF}} \rangle$ is small for $k^{-1} \gg k_{\text{LF}}^{-1}$, the χ_{LF} filter scale. Since $\chi_{\text{LF}} = \chi_b + \chi_{>h}$ contains a spatially varying part χ_b built from waves with $k_h < k < k_{\text{LF}}$ and a constant superhorizon part $\chi_{>h}$. Which aspects of the spiky patterns of Fig. 4.4 that would be realized in our Hubble patch is quite dependent on the luck of our $\chi_{>h}$ -draw from a Gaussian distribution with variance $\sigma_{>h}^2 = \langle \chi_{>h}^2 \rangle$, in particular whether $\chi_{>h}$ is near a smoothed-peak, or small ($\lesssim \sigma_{\text{HF}}$).

The analytic model, $F_{\text{NL}} = \sum_p F_p \exp[-(\chi - \chi_p)^2 / (2\gamma_p^2)]$, approximates each spike of Fig. 4.4 with a Gaussian “line profile” of width γ_p centred on χ_p , with peak amplitude

F_p and integrated line strength $u_p = F_p \sqrt{2\pi} \gamma_p$. The $\chi \rightarrow -\chi$ symmetry means that for each peak at χ_p there is a mirror peak at $-\chi_p$ of the same strength. The conditional n -point moments of F_{NL} , $\langle \prod_{i=1}^n F_{\text{NL}}(\mathbf{x}_i) | \chi_{\text{LF}} \rangle$ are then easily computable Gaussians, with quadratic terms in $\chi_i - \chi_p$ linked through the HF 2-point function of χ_{HF} . The mean field has $n = 1$:

$$\langle F_{\text{NL}} | \chi_{\text{LF}} \rangle = \sum_p U_p e^{-\frac{\chi_b^2(\mathbf{x})}{2\sigma_{p\text{HF}}^2}} \cosh\left\{ \frac{\chi_{p>h}}{\sigma_{p\text{HF}}^2} \chi_b(\mathbf{x}) \right\}. \quad (4.10)$$

Here $\sigma_{p\text{HF}}^2 \equiv \gamma_p^2 + \sigma_{\text{HF}}^2$ can be approximated by σ_{HF}^2 for the typical γ_p we find, and $U_p = \frac{2u_p \gamma_p}{\sigma_{p\text{HF}}} \exp\left\{-\frac{\chi_{p>h}^2}{2\sigma_{p\text{HF}}^2}\right\}$, with $\chi_{p>h} = \chi_p - \chi_{>h}$. The χ_{HF} correlation function dependence of the fluctuation variance $\langle \Delta F_{\text{NL}}(\mathbf{x}_1) \Delta F_{\text{NL}}(\mathbf{x}_2) | \chi_{\text{LF}} \rangle$ precludes an analytic harmonic analysis, but we have investigated this numerically: *e.g.* for a 1-spike version, this F_{NL} variance is 1% of $\langle F_{\text{NL}} | \chi_{\text{LF}} \rangle^2$ if it is smoothed on $\sim k_{\text{LF}}^{-1}$, and $\sim 0.1\%$ with $\sim 10k_{\text{LF}}^{-1}$ smoothing. (We have checked the effective field works even better for F_{NL} quadratic and exponential in χ .) The HF structure is very relevant to first-object formation, but what actually happens will be model-dependent. However, HF will not impinge upon LSS observables, since they are convolved with experimentally-determined or theoretically-imposed windows $\gg k_e^{-1}$ in scale.

A fundamental character of the resonant mechanism is the delay of in-arm preheating completion, translating into positive large excursions in $\delta \ln a|_H$. The associated perturbed Newtonian gravitational potential Φ_{N} is negative. The CMB sky temperature $T(\hat{q})$, an angular function of the CMB photon direction \hat{q} towards us, is a projected image of various sources whose 3D Fourier transforms involve various form factors $\mathcal{F}(|\mathbf{k}|)$ times $\Phi_{\text{N}}(\mathbf{k}, t_0)/3$. The dominant \mathcal{F} terms are from two CMB decoupling effects, and one late-time effect: the combined ‘naive Sachs-Wolfe (NSW) effect plus photon compression-rarefaction’; the Doppler effect from flowing electrons; and the integrated Sachs-Wolfe (ISW) effect with \mathcal{F} a k -dependent time-integral of $6\dot{\Phi}_{\text{N}}/\Phi_{\text{N}}$ [10, 12, 13, 14]. The upper panels in Fig. 4.6 correspond to $\mathcal{F} = 1$ and the lower panels are convolved with a CMB transfer function and smoothing on 1° , appropriate if the CMB sky is a direct map of

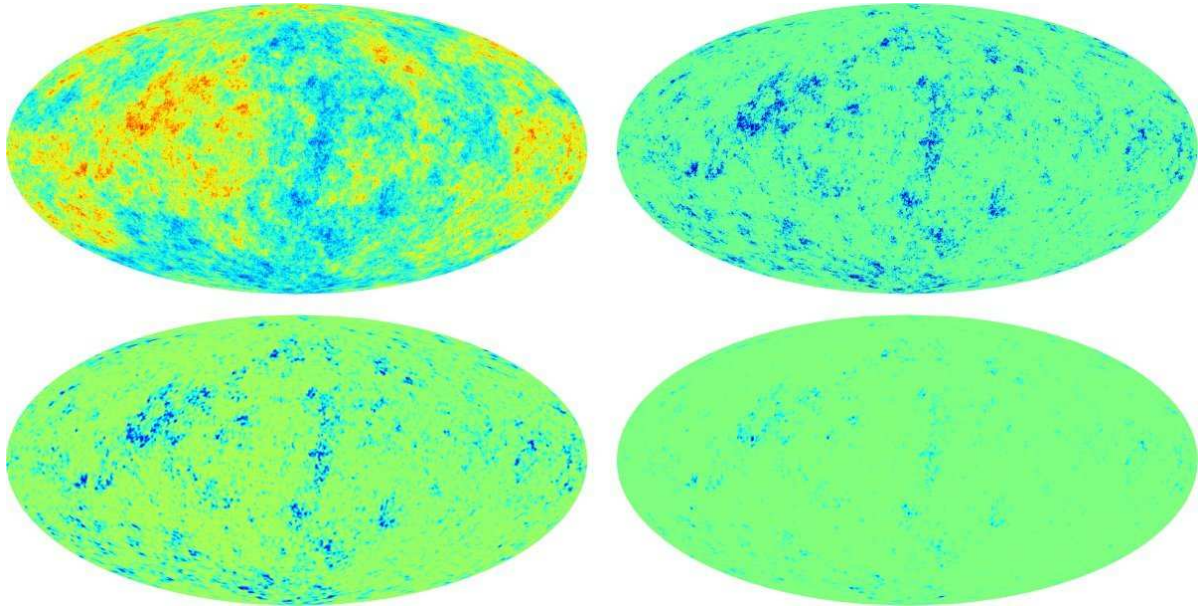


Figure 4.6: Realizations of the nG map $\langle F_{\text{NL}} | \chi_b \rangle$ on the CMB sky. Top left shows a scale-invariant Gaussian random field realization $\chi_b(d_{\gamma_{\text{dec}}}\hat{q})$ in direction \hat{q} on a sphere at the comoving distance to photon decoupling, $d_{\gamma_{\text{dec}}}$. Top right shows the action of $\langle F_{\text{NL}} | \chi_b \rangle$ on it, using our Gaussian-line-profile approximation with 2 peaks at $\chi_p = \pm\nu_p\sigma_b$, for $\nu_p = 3.5$. Middle left shows the map convolved with a CMB transfer function, and smoothed on a 1° scale, right with $\nu_p = 4.5$; both show “cold spot” intermittency.

the photon decoupling surface, ignoring its fuzziness (valid for the 1° smoothing) and a correct implementation of the ISW effect, which will affect the largest scales. However, the essential intermittent cold spot nature following from negative Φ_N will persist. Such cold spots will be polarized just as those deriving from ζ_ϕ are, and have a CMB spectrum, a prediction for the $\sim 6^\circ$ COBE/WMAP cold spot [226, 227] if it is a smoothed remnant of resonant preheating.

Another non-intermittent nG regime is that of extreme “line blending”: Fig. 4.4 shows $f_\chi \chi_{\text{LF}}^2/M_P^2$ with $f_\chi = 2 \times 10^6$ is a good fit to $\langle F_{\text{NL}} | \chi_{\text{LF}} \rangle$ below $\sim \sigma_{\text{HF}}$. (Such a quadratic form also follows from Eq. (4.10).) For $\chi_{>h} \lesssim \sigma_{\text{HF}}$, we will get a power law in χ_b , $\beta_\chi \chi_b/M_P + f_\chi \chi_b^2/M_P^2$, with $\beta_\chi = 2f_\chi \chi_{>h}/M_P$. The conventional WMAP $-9 < F_{\text{NL}} < 111$ constraints [226, 227] use $\sim \zeta_\phi + f_{\text{NL}} \zeta_\phi^2$. In our case, $f_\chi \chi^2$ is uncorrelated with ζ_ϕ^2 so the constraint on f_χ will be considerably relaxed, as long as the linear $\beta_\chi \chi_b$ term is subdominant to ζ_ϕ , as is expected.

4.6 Discussion

Further exploration is needed of how spiked F_{NL} from resonant preheating may arise in more general inflation models and on the rich nG impact and observable constraints of such F_{NL} on short and long cosmic scales. For now, we note SUSY models provide light non-inflaton fields of the sort we need, and future CMB experiments could test whether nG cold spots are polarized, as predicted with this mechanism for their productions.

Chapter 5

Infra-red Cascading During Inflation

5.1 Introduction

In this chapter we will discuss another mechanism that could produce large scale metric perturbations via particle production. This time we consider a model where the particle production occurs during inflation. For completeness we will include here most of the contents that has already been published in [6, 7]. Please cite our original papers for the use of these contents.

Physical processes during inflation may leave their imprint as features in the cosmological fluctuations. These can in principle be observed if they fall in the range of the wavelengths between 10^4 Mpc and 100 kpc, which corresponds to about ten e-folds during inflation. Relevant dynamical models were studied in the early days of the inflationary theory, e.g. the model with phase transitions during inflation yielding associated features in the cosmological fluctuations [228, 229, 230] (see also [231, 232]). There the time-dependent dynamics of the inflaton field ϕ can trigger a phase transition in the iso-inflaton χ field. The growth of χ inhomogeneities induces curvature fluctuations on scales leaving the horizon at the moment of the phase transition.

Recently, several studies [228, 233, 234, 8, 235] considered features in the cosmological

fluctuations from the effect of particle creation during inflation, which can be modelled by the simple interaction

$$\mathcal{L}_{int} = -\frac{g^2}{2}(\phi - \phi_0)^2\chi^2 \quad (5.1)$$

with some value of the scalar field ϕ_0 which the rolling $\phi(t)$ crosses during inflation that must be tuned to give a signal in the observable range of e-folds. There are different motivations for the model (5.1). The early study introduced the possibility of slowing down the fast rolling inflaton using particle creation via the interaction (5.1). Imagine there are a number of field points ϕ_{0i} , $i = 1, 2, \dots, n$, where the iso-inflaton field becomes massless and χ particles are created. The produced χ particles are diluted by the expansion of the universe, however, the back-reaction effect from multiple bursts of particle creation may slow down the motion of ϕ sufficiently to allow for slow-roll inflation. This is called trapped inflation. A more concrete string theory realization of trapped inflation, based on a sequence of $D3$ brane interactions, was discussed in [234]. The work [235], which is complimentary to this study, provides a detailed realization of trapped inflation in the context of the string theory model [236].

The instant of χ -particle creation and the slow-down of the rolling inflaton generates a feature in the power spectrum $P_\zeta(k)$ of scalar curvature fluctuations from inflation. This was noticed in [233], where the features in the power spectrum were estimated from the simple-approximate formula $P_\zeta(k) \sim \left(\frac{H^2}{\phi}\right)^2$. The inflaton slow-down was described by the mean-field equation

$$\ddot{\phi} + 3H\dot{\phi} + V_{,\phi} + g^2(\phi - \phi_0)\langle\chi^2\rangle = 0. \quad (5.2)$$

The vacuum average $\langle\chi^2\rangle$ can be calculated with the analytic machinery of particle creation with the coupling (5.1), which was developed in the theory of preheating after inflation [237, 238]. The QFT of χ particles interacting with the time-dependent condensate $\phi(t)$ deals with the eigenmodes $\chi_k(t)e^{i\mathbf{k}\cdot\mathbf{x}}$, where the time-dependent mode function

obeys an oscillator-like equation in an expanding universe

$$\ddot{\chi}_k + 3H\dot{\chi}_k + \left[\frac{\mathbf{k}^2}{a^2} + g^2(\phi(t) - \phi_0)^2 \right] \chi_k = 0, \quad (5.3)$$

with time-dependent frequency $\omega_k(t)$. When $\phi(t)$ crosses the value ϕ_0 , the χ_k mode becomes massless and $\omega_k(t)$ varies non-adiabatically. Around this point $(\phi(t) - \phi_0) \approx \dot{\phi}_0(t - t_0)$, where $t = t_0$ is corresponding time instant. With this very accurate [238] approximation, one can solve the equation (5.3) analytically to obtain the occupation number of created χ particles

$$n_k = \exp\left(-\frac{\pi k^2}{k_\star^2}\right), \quad k_\star^2 = g|\dot{\phi}_0|, \quad (5.4)$$

presuming that $k_\star > H$. The latter condition requires coupling constant $g > H^2/|\dot{\phi}_0| \sim 10^{-4}$. It is useful to note that, independent of the details of $V(\phi)$ and $\phi(t)$, the scale k_\star can be related to the naively estimated amplitude of vacuum fluctuations as $k_\star/H = \sqrt{g/(2\pi P_\zeta^{1/2})}$. Thus $k_\star/H \sim 20$ if $P_\zeta^{1/2} = 5 \times 10^{-5}$ as suggested by the CMB and the coupling is $g^2 \sim 0.1$.ⁱ

The VeV $\langle \chi^2 \rangle$, which controls the back-reaction on the homogeneous field $\phi(t)$, can be calculated from (5.4) and estimated as $\langle \chi^2 \rangle = \int \frac{d^3k}{(2\pi)^3} |\chi_k|^2 \approx \int \frac{d^3k}{(2\pi)^3} \frac{n_k}{\omega_k} \approx \frac{n_\chi a^{-3}}{g|\dot{\phi} - \dot{\phi}_0|}$ for $\phi > \phi_0$. Substitution of this result back into (5.2) gives the expected velocity dip of $\phi(t)$ and, correspondingly, a bump in the power spectrum $P_\zeta(k)$. In Fig. 5.1 we illustrate this velocity dip for the model (5.1) with $g^2 = 0.1$.

The calculation of curvature fluctuations was re-considered in [8], where the linearized equations of motion for the quantum fluctuations $\delta\phi$ coupled with the metric fluctuations were treated again in the mean-field approximation, using $\langle \chi^2 \rangle$ to quantify the back-reaction. This study shows that the bump in the curvature power spectrum is the most prominent part of an otherwise wiggling pattern. Similar to us, the work [235] further refined the calculation of the curvature perturbation in this model, going beyond the

ⁱWe are assuming that supersymmetry protects the inflaton potential from radiative corrections at $t = t_0$.

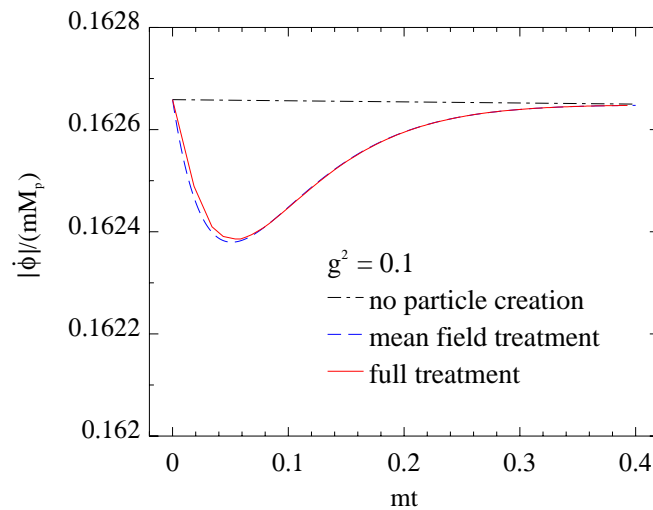


Figure 5.1: $|\dot{\phi}|/(M_p m)$ plotted against mt for $g^2 = 0.1$ (where $m = V_{,\phi\phi}$ is the effective inflaton mass). Time $t = 0$ corresponds to the moment when $\phi = \phi_0$ and χ -particles are produced copiously. The solid red line is the lattice field theory result taking into account the full dynamics of re-scattering and IR cascading while the dashed blue line is the result of a mean field theory treatment which ignores re-scattering [8]. The dot-dashed black line is the inflationary trajectory in the absence of particle creation.

mean-field treatment of ϕ .ⁱⁱ

In a parallel development, scalar field interactions of the type (5.1) are the subject of studies in non-equilibrium QFT and its application to the theory of preheating after inflation, as we mentioned above. In this context χ particles are usually created with large occupation numbers (For example, in the case of parametric resonant preheating due to the oscillating inflaton background $\phi(t)$, χ particles are created in successive bursts whenever $\phi(t)$ crosses zero.) The full dynamics of interacting scalars also includes re-scattering effects where $\delta\phi$ fluctuations (particles) are created very quickly due to the interaction of χ particles with the condensate $\phi(t)$ [238, 239, 240, 241, 242, 243]. The diagram for this process is illustrated in Fig. 5.7. The $\delta\phi$ particles produced by re-scattering are far from equilibrium and evolve towards an intermediate regime which is well described by the scaling “turbulent” solution. To understand the dynamics, one needs to use lattice numerical simulations of the time-evolution of the classical scalar fields based on the LATTICEASY [218] or DEFROST [219] codes, designed for this purpose. The turbulent regime of interacting scalars was investigated in several recent works. The papers [244, 245] used numerical simulations to demonstrate the scaling regime in the model of a self-interacting classical scalar $\lambda\phi^4$. The papers [246, 247] show numerically the scaling solution for the fully QFT treatment of the same model, and advocate a new regime, the non-thermal fixed point, which may be asymptotically long – and before the system evolves, if ever, to another fixed point, namely thermal equilibrium.

In this chapter we will study in detail the back-reaction of created χ particles on the inflaton field resulting in bremsstrahlung radiation and IR cascading of $\delta\phi$ fluctuations.

ⁱⁱBelow we use QFT methods to study correlators of inhomogeneous fluctuations $\delta\phi$ induced by χ^2 inhomogeneities. Ref. [235] considers the effect induced by quantum mechanical fluctuations of the total particle number n_χ . Owing to the relationship between χ^2 and n_χ , our calculations below capture this effect.

5.2 Re-scattering, numerics

To study the creation of $\delta\phi$ fluctuations by re-scattering of produced χ particles off the condensate $\phi(t)$ in the model (5.1) we have adapted the numerical DEFROST code for the problem of a single burst of instantaneous particle creation during inflation.ⁱⁱⁱ To run the classical scalar field simulation, we must first choose the appropriate initial conditions. The field χ on the lattice is modelled by the random Gaussian field realized as the superposition of planar waves $\chi_k(t)e^{i\mathbf{k}\mathbf{x}}$ with random phases. The initial conditions for the modes $\chi_k(t)$ are chosen to emulate the exact quantum mode functions corresponding to the physical occupation number (5.4) (see appendix A for more details) while ensuring that the source term for the $\delta\phi$ fluctuations turns on smoothly at $t = 0$. The box size of our 512^3 simulations corresponds to a comoving scale which initially is $\frac{20}{2\pi} \sim 3$ times the horizon size $1/H$, while $k_* \cong 60\sqrt{g}H$. We run our simulations for roughly 3 e-folding from the initial moment t_0 when χ -particles are produced, although a single e-folding would have been sufficient to capture the effect. We are interested in the power spectrum of inflaton fluctuations $P_\phi = k^3|\delta\phi|^2/(2\pi^2)$, and also the number density of inflaton fluctuations $n_\phi(k) = \frac{\Omega_k}{2} \left(\frac{|\dot{\phi}_k|^2}{\Omega_k^2} + |\delta\phi_k|^2 \right)$ (where we introduce the notation $\Omega_k = \sqrt{V_{,\phi\phi} + k^2}$ for the inflaton frequency). For the sake of illustration we have chosen the standard chaotic inflationary potential $V = m^2\phi^2/2$ with $m = 10^{-6}m_{pl}$ and $\phi_0 = 3.2m_{pl}$, however, our qualitative results will be independent of the choice of background inflation model and, in particular, are applicable to trapped inflation. We have considered three different values of the coupling constant, $g^2 = 0.01, 0.1, 1$, although we focus most of our attention on the case $g^2 = 0.1$. Fig. 5.2 shows time evolution of the re-scattered inflaton power spectrum $P_\phi(k)$ for three different time steps, while Fig. 5.3 shows the

ⁱⁱⁱSince the production of long wavelength $\delta\phi$ modes is so energetically inexpensive, a major requirement for successfully capturing this effect on the lattice is respecting energy conservation to very high accuracy. In our modified version of DEFROST energy conservation is respected with an accuracy of order 10^{-8} , compared to $10^{-3} - 10^{-5}$ obtained using previous codes. A minimum accuracy of roughly 10^{-4} is required for this problem.

corresponding evolution of the particle number density $n_\phi(k)$. In Fig. 5.4 we illustrate the dependence of our results on the coupling constant g^2 .

In Fig. 5.2 we see clearly how multiple re-scatterings lead to a cascading of power into the IR. These re-scattered inflaton perturbations are complimentary to the usual long-wavelength inflaton modes produced by quantum fluctuations. As long as $g^2 > 0.06$ the re-scattered power spectrum outside the horizon comes to dominate over the usual vacuum fluctuations within a single e-folding. At much later times the IR portion of the power spectrum remains frozen while the UV portion is damped out by the Hubble expansion. The effect of IR cascading on the power spectrum is much more significant than features which are produced by the momentary slowing-down of the background $\phi(t)$.^{iv}

Fig. 5.1 illustrates the impact of re-scattering on the dynamics of the velocity of the background field. The evolution of $\dot{\phi}(t)$ including re-scattering is not changed significantly (as compared to the mean field theory result), which show the energetic cheapness of IR cascading.

The long-wavelength inflaton fluctuations produced by IR cascading are non-Gaussian. This is illustrated in Fig. 5.5 where we study the probability density function and compare to a Gaussian fit.

5.3 Re-scattering, analytics

We now develop an analytical theory of this effect. Here we provide only a cursory discussion, the reader is referred to Appendices A and B for a detailed exposition and technical details of the calculation.

^{iv}To avoid confusion: here we use “cascading” to refer to the dynamical process of building up $\delta\phi$ fluctuations in the IR. If the universe were not expanding, a scaling turbulent regime would be established. Here we see this scaling regime only in an embryonic form, see the envelope in Fig. 5.3.

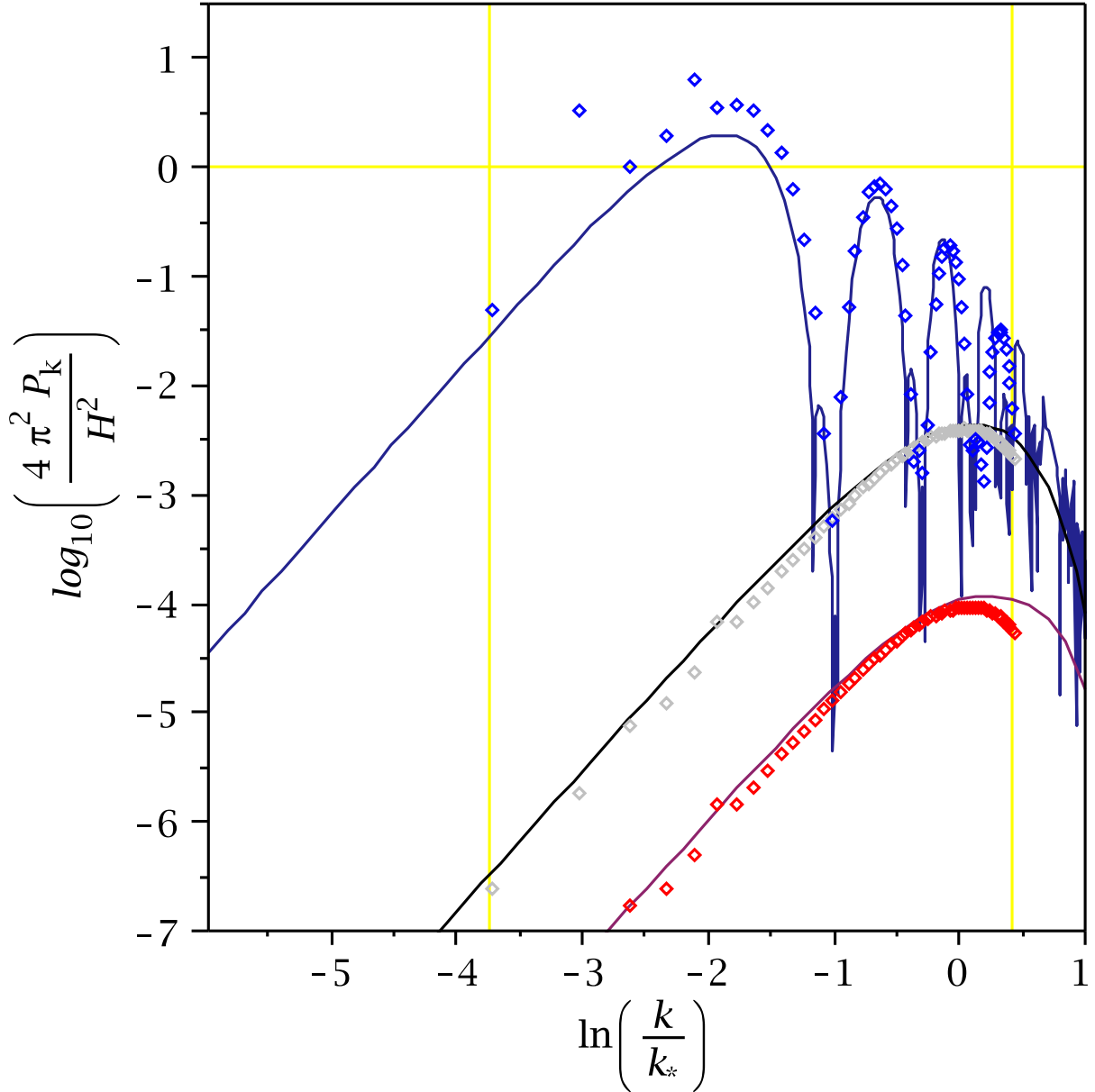


Figure 5.2: The power spectrum of inflaton modes induced by re-scattering (normalized to the usual vacuum fluctuations) as a function of $\ln(k/k_*)$, plotted for three representative time steps in the evolution, showing the cascading of power into the IR. For each time step we plot the analytical result (the solid line) and the data points obtained using lattice field theory simulations (diamonds). The time steps correspond to the following values of the scale factor: $a = 1.03, 1.04, 2.20$ (where $a = 1$ at the moment when $\phi = \phi_0$). By this time the amplitude of fluctuations is saturated due to the expansion of the universe. The vertical lines show the range of scales from our lattice simulation.

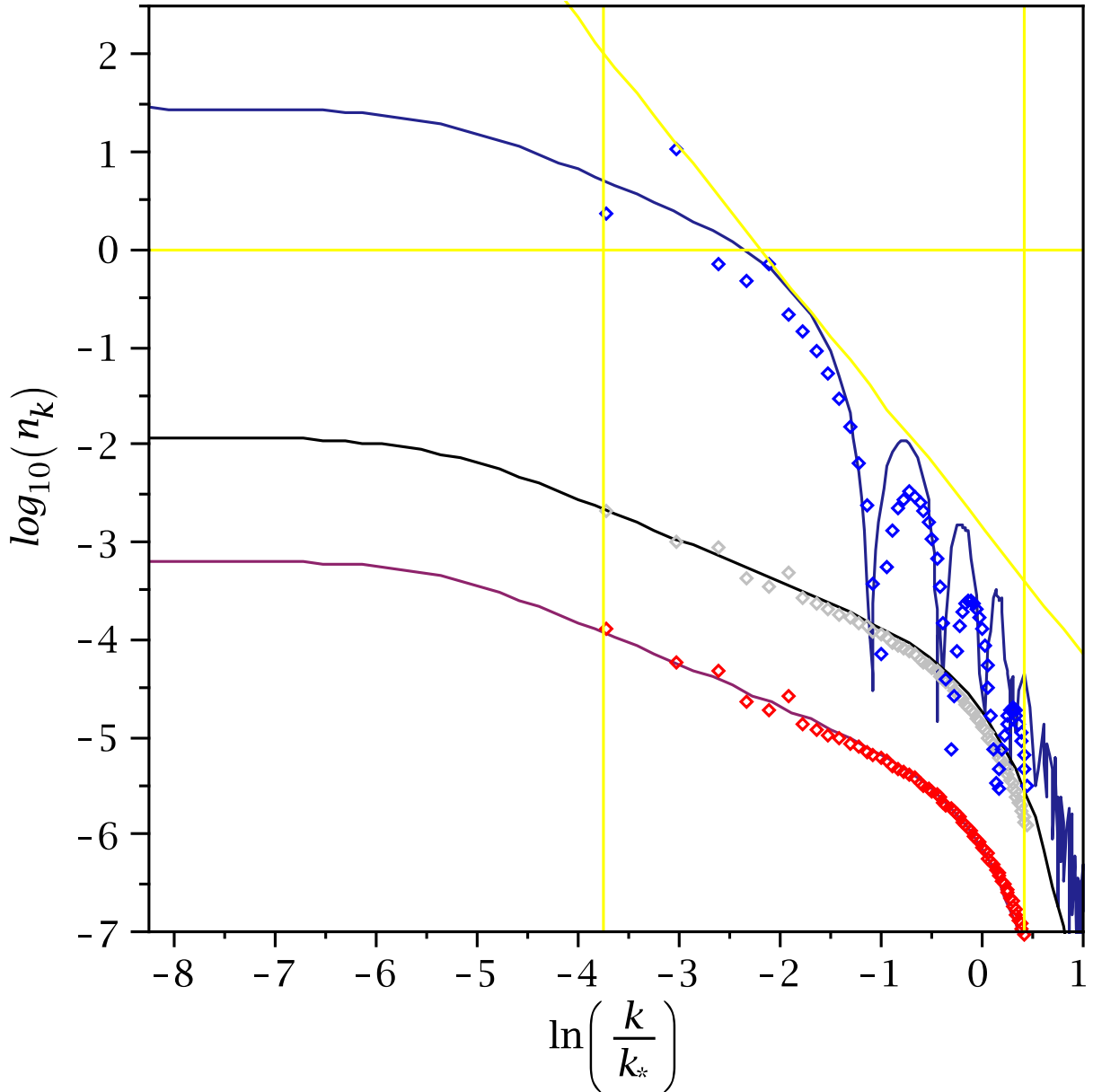


Figure 5.3: Physical occupation number n_k as a function of $\ln(k/k_*)$ for $g^2 = 0.1$. The three curves correspond to the same series of time steps used in Fig. 5.2, and demonstrate the growing number of long wavelength inflaton modes which are produced as a result of IR cascading. Because the same χ -particle can undergo many re-scatterings off the background condensate $\phi(t)$, the $\delta\phi$ occupation number is larger than the initial χ particle number (for $g^2 = 0.1$ one can achieve $n_\phi(k) \sim 30$ even though initially $n_\chi(k) \leq 1$). When $g^2 = 0.06$ the IR $\delta\phi$ occupation number exceeds unity within a single e-folding. The yellow envelope line shows the onset of scaling behaviour associated with the scaling turbulent regime.

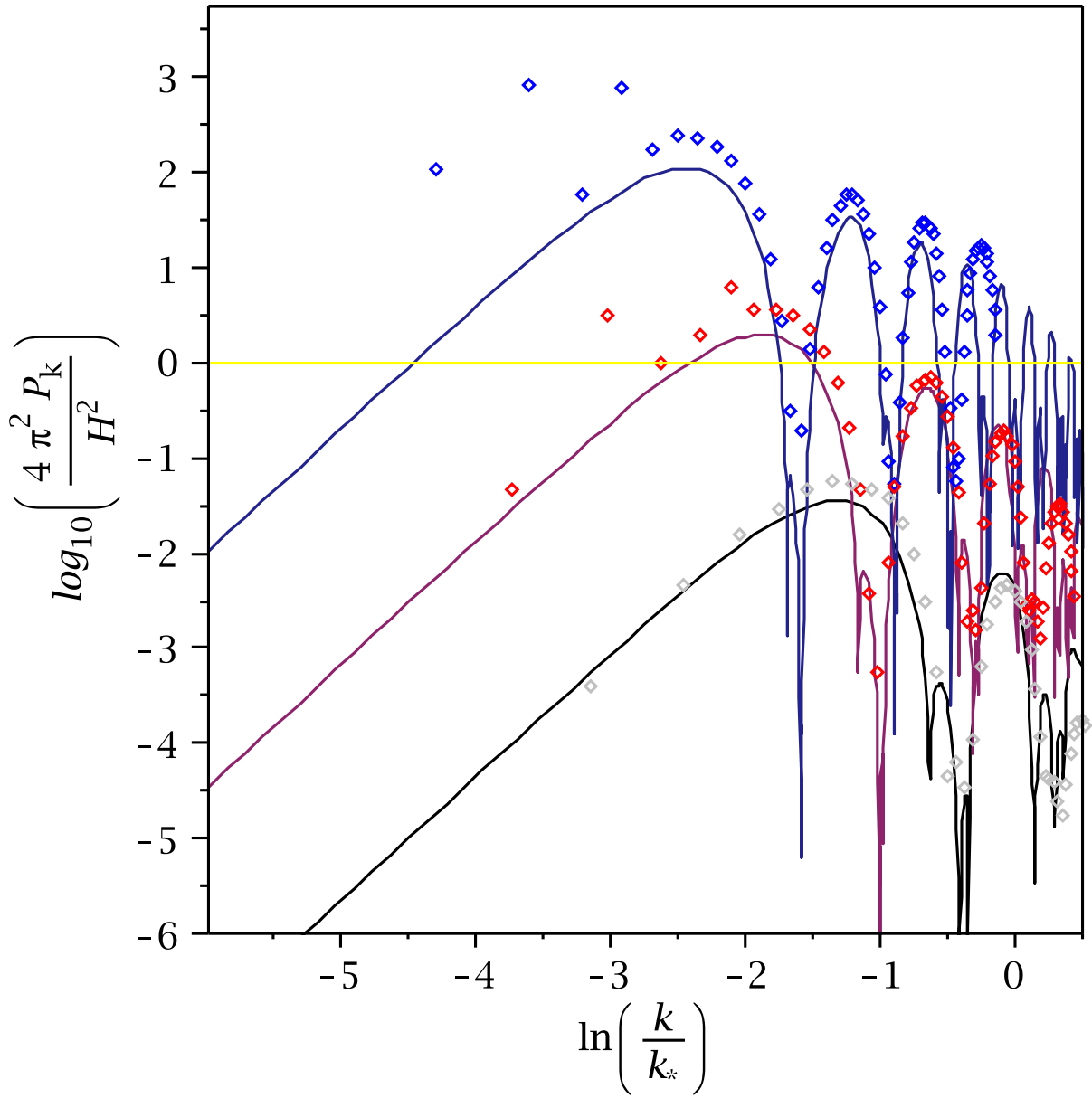


Figure 5.4: The dependence of the power spectrum P_ϕ on the coupling g^2 . The three curves correspond to P_ϕ for $g^2 = 0.01, 0.1, 1$, evaluated at a fixed value of the scale factor, $a = 2.20$. We see that even for small values of g^2 the inflaton modes induced by re-scattering constitute a significant fraction of the usual vacuum fluctuations after only a single e-folding.

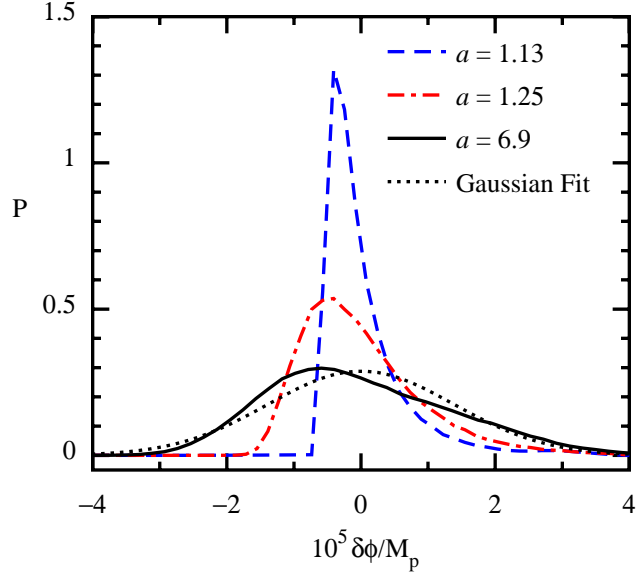


Figure 5.5: Probability density function of $\delta\phi$ for $g^2 = 0.1$ at a series of different values of the scale factor, a . The dotted curve shows a Gaussian fit at late time $a = 6.9$.

At leading order the physics of re-scattering (see Fig. 5.7) is described by the equation

$$\delta\ddot{\phi} + 3H\delta\dot{\phi} - \frac{1}{a^2}\nabla^2\delta\phi + m^2\delta\phi \cong -g^2[\phi(t) - \phi_0]\chi^2, \quad (5.5)$$

where we introduce the notation $m^2 = V_{,\phi\phi}$ for the effective inflaton mass. The solution of (5.5) consists of two components: the solution of the homogeneous equation which simply corresponds to the usual vacuum fluctuations produced during inflation and the particular solution which is due to the source term. We will focus our attention on this latter solution which, physically, corresponds to re-scattered inflaton perturbations. Since the process of IR cascading takes less than a single e-folding, we can safely neglect the expansion of the universe when studying analytically the particular solution of (5.5). (In all of our lattice simulations the inflationary expansion of the universe is taken into account consistently.) Solving for the particular solution $\delta\phi_k$ of (5.5) and defining the re-scattered power spectrum P_ϕ in terms of the QFT correlation function in the usual manner we arrive at an expression for P_ϕ in terms of the c-number mode functions χ_k

which obey equation (5.3).^v The result is

$$P_\phi = \frac{g^4 \dot{\phi}_0^2 k^3}{8\pi^5 \Omega_k^2} \int dt' dt'' t' t'' \sin[\Omega_k(t-t')] \sin[\Omega_k(t-t'')] \times \int d^3 k' \chi_{k-k'}(t') \chi_{k-k'}^*(t'') \chi_{k'}(t') \chi_{k'}^*(t'') \quad (5.6)$$

where again we have $\Omega_k = \sqrt{k^2 + m^2}$ for the $\delta\phi$ -particle frequency.

To evaluate this power spectrum we need an expression for the solutions of (5.3) in the regime of interest. Let us choose the origin of time so that $t = 0$ corresponds to the moment when $\phi = \phi_0$. At the moment $t = 0$ the parameter $|\dot{\omega}_k|/\omega_k^2$ is order unity or larger and ω_k varies non-adiabatically. At this point χ_k modes are produced in the momentum band $k \lesssim k_*$. However, within a time $\Delta t \sim k_*^{-1}$ (which is tiny compared to the Hubble time H^{-1}) the χ particles become extremely heavy and their frequency again varies adiabatically. At times $t \gtrsim k_*^{-1}$ we can safely approximate $\omega_k = \sqrt{k^2 + k_*^4 t^2} \cong k_*^2 t$ for the modes of interest and χ_k takes the simple form

$$\chi_k(t) \cong \sqrt{1+n_k} \frac{e^{-i(k_* t)^2/2}}{k_* \sqrt{2t}} - i\sqrt{n_k} \frac{e^{+i(k_* t)^2/2}}{k_* \sqrt{2t}}, \quad (5.7)$$

where the occupation number was defined in (5.4). The factors $\sqrt{1+n_k}$, $-i\sqrt{n_k}$ are the Bogoliubov coefficients while the factors proportional to $e^{\pm i(k_* t)^2/2}$ come from the positive and negative frequency adiabatic mode solutions [238]. As we see, very quickly after $t = 0$ the χ particles become very massive and their multiple re-scatterings off the condensate $\phi(t)$ generates bremsstrahlung radiation of IR $\delta\phi$ particles.

We have computed the full renormalized power spectrum analytically in closed form and the result is presented in equation (5.46). This formula is used for all of our figures. Since the exact analytical result is quite cumbersome, it is useful to consider the following representative contribution to (5.6):

$$P_\phi \simeq \frac{g^2 k^3 k_*^3}{32\sqrt{2} \pi^5} \left[\frac{1 - \cos(\Omega_k t)}{\Omega_k^2} \right]^2 e^{-\pi k^2/(2k_*^2)}, \quad (5.8)$$

^vWe are only interested in connected contributions to the correlation functions, which is equivalent to subtracting the expectation value from the source term in (5.5): $\chi^2 \rightarrow \chi^2 - \langle \chi^2 \rangle$. Thus, our re-scattered inflaton modes are only sourced by the variation of χ^2 from the mean $\langle \chi^2 \rangle$.

which captures the properties of the full analytical solution. In particular, the simple expression (5.8) nicely describes the IR cascade. The spectrum has a peak which initially (near $t \sim k_\star^{-1}$) is close to k_\star . As time evolves the peak moves to smaller-and-smaller k as power builds up in the IR. From (5.8) we see that modes with $\Omega_k t < 1$ gain power as $P_\phi(k) \sim t^4$. For a given k -mode the growth of the power spectrum saturates when $\Omega_k t \sim 1$, however, the cascade still continues at some lower k . If we had $m = 0$ then the cascade would continue forever, otherwise formula (5.8) predicts that the growth of the spectrum saturates at $t \sim m^{-1}$ when the peak has reached $k \sim m$. After this point the character of the IR cascade is expected to change, however, our analytic calculation is no longer reliable because $m \ll H$ and we have neglected the expansion of the universe.

5.4 Discussion of Curvature Fluctuations from IR Cascading

Any inflaton fluctuations $\delta\phi$, independently on their origin, evolve qualitatively similarly during inflation. When their physical wavelength is smaller than the Hubble radius $1/H$, $\delta\phi$ is oscillating while their amplitude is diluted as $1/a$. As far as the wavelength exceeds the Hubble radius, the amplitude of $\delta\phi$ freezes out. Fluctuations of $\delta\phi$ induce the curvature metric fluctuations. Inflationary expansion of the universe further stretch the wavelengths of the fluctuations frozen outside the horizon, making them potentially of the cosmological scales, depending on the wavelength. The inflaton fluctuations produced by the IR cascading, therefore, are the potential sources for observable curvature fluctuations. To calculate curvature fluctuations generated by the IR cascading, we have to solve self-consistent system of linearized Einstein equations for metric and the fields fluctuations.

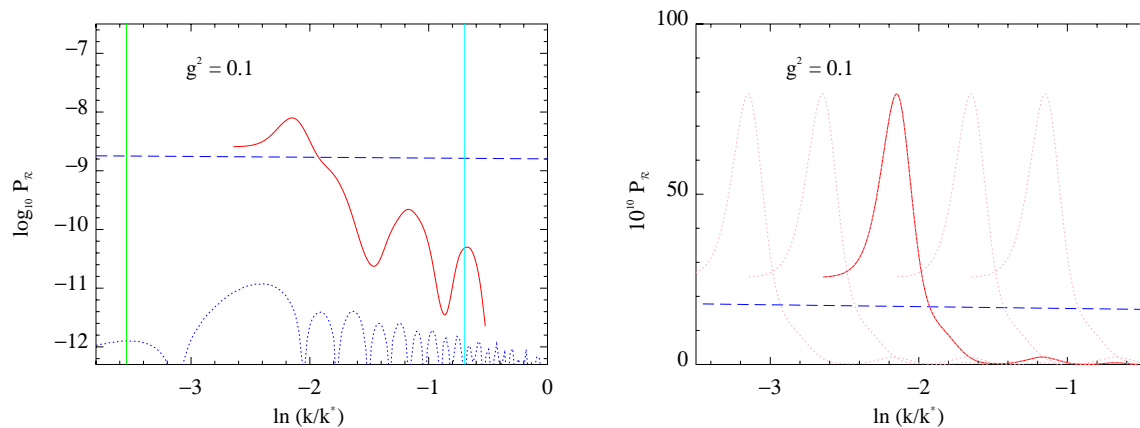


Figure 5.6: The left panel shows a comparison of curvature fluctuations from different effects. We see the dominance of fluctuations produced by IR cascading over the wiggles induced by the momentary slowing-down of the inflaton. For illustration we have taken $g^2 = 0.1$, but the dominance is generic for all values of the coupling. The red solid line is the IR cascading curvature power spectrum, while the blue dashed line is the result of a mean field treatment. (The vertical lines show aH at the beginning of particle production and after ~ 3 e-foldings.) The right panel shows the curvature power spectrum resulting from multiple bursts of particle production and IR cascading. Superposing a large number of these bumps produces a broad-band spectrum.

For example, the (0, 0) linearized Einstein equation for our model reads

$$\delta G_0^0 = \frac{8\pi}{M_p^2} (\delta T_0^0(\phi) + \delta T_0^0(\chi)) . \quad (5.9)$$

where δG_0^0 is the perturbed Einstein tensor and in the R.H.S. $\delta T_0^0(\phi)$ corresponds to the fluctuations of the inflaton energy density, containing familiar terms linear with respect to $\delta\phi$, like $\dot{\phi}\delta\dot{\phi}$ etc. Second term corresponds to the contribution from χ particles

$$\delta T_0^0(\chi) = \frac{1}{2}\dot{\chi}^2 + \frac{1}{2}(\nabla\chi)^2 + \frac{1}{2}g^2(\phi - \phi_0)^2\chi^2 - \langle T_0^0(\chi) \rangle . \quad (5.10)$$

Although this expression is bi-linear *w.r.t.* χ , it turns out taking $\delta T_0^0(\chi)$ into account is important. To begin the investigation the equation (5.9), it is convenient to use its Fourier transformation. While the Fourier components of $\delta T_0^0(\phi)$ contains linear terms of $\delta\phi_k$, the Fourier transform of $\delta T_0^0(\chi)$ contains convolutions like $\sim \int d^3\mathbf{k}' \dot{\chi}_{\mathbf{k}'} \dot{\chi}_{\mathbf{k}-\mathbf{k}'}^*$ etc. As a result, despite the fact that χ particles amplitude is peaked at $k \sim k_*$, this type of convolution gives significant contribution at small k , which are of interest for the theory of generation of cosmological fluctuations. Preliminary estimations based on the analytical formulas for χ_k involved in the convolution, show that contribution of $\delta T_0^0(\chi)$ is at least the same order of magnitude as $\delta T_0^0(\phi)$. Rigorous treatment of the curvature fluctuations in our model is therefore rather complicated, and will be leave it for separated project.

Since both terms in R.H.S. in (5.9) are the same order of magnitude, here for the crude estimations we will use the simple-minded formula $P_\zeta \sim \left(\frac{H^2}{\phi}\right)^2$. The curvature fluctuations generated by the IR cascading, are illustrated in the left panel of Fig. 5.6. The curvature fluctuations from the instance of the IR cascading has the bump-like shape within the interval of the wavelength, roughly corresponding to one e-folding. They are significantly, by orders of magnitude, dominated over the fluctuations generated by the momentary slowing down of $\phi(t)$. If we pick up the background inflationary model to be chaotic inflation with the standard quadratic potential, the ratio of the power spectra from IR cascading and the standard fluctuations is estimates as $P_{IR}/P_s \sim 700 \times g^{4.5}$.

Thus, depending on the coupling g^2 , the IR bump can dominate (for $g^2 > 0.06$) over the standard fluctuations, or just contribute to them for smaller g^2 .

Suppose that we have a sequence of the particles creation events at different moments t_{0i} , $i = 1, 2, 3, \dots$. Each of those events generate, through IR cascading, corresponding bumps in the spectrum, as illustrated in the right panel of Fig. 5.6. Depending on the density of t_{0i} moments, superposition of such IR bumps results in broad band contribution to the curvature power spectrum.

We also estimated non-Gaussianity of $\delta\phi$ fluctuations from IR cascading. They are quite significant, we estimate the non-Gaussianity parameter $f_{NL} \sim 2 \times 10^4 g^{2.25}$. Therefore the non-Gaussian signal from individual bump can be strongly non-Gaussian. In the model with multiple instances of particle creations, the broad-band IR cascading fluctuations dominated over the standard fluctuations, apparently, are ruled out because of the strong non-Gaussianity. However, the broad-band IR cascading fluctuations can be considered as additional subdominant component to the standard fluctuations. In this case the non-Gaussianity of the net curvature fluctuations can be acceptable but different from that of the standard fluctuations alone.

Another important parameter of the IR cascading fluctuations is the wavelength of the bump, which depend on the value of ϕ_0 . there are interesting possibilities to consider them at small CMB angular scales (small-scale non-Gaussianity?), at scales of galaxies, at near the horizon scales (CMB anomalies at large scales?). We leave all of these possibilities for further discussion.

5.5 Summary of Theoretical Part

We find the following new results for interacting scalars during inflation in the model (5.1).

i) In the early stages of re-scattering, when the back-reaction can be treated linearly, the

spectrum of inflaton fluctuations $\delta\phi$ and the corresponding particle number density $n_\phi(k)$ can be rigorously calculated with QFT with the diagram in Fig. 5.7. We perform such QFT calculations and compare with lattice simulations of the classical field dynamics. The results are highly compatible with each other, even well into the late time nonlinear regime. This signals the dominance of Fig. 5.7 in the dynamics of re-scattering, while the analytic estimate gives a handy fitting formula.

ii) While the stationary scaling turbulent solution for the scalar fields was established previously, the way this regime appears dynamically was not traced out in detail. For our example we show how the scaling regime emerges, what is the timing of IR cascade propagation and what is the profile of the spectra resulting from the IR cascading.

iii) The most unexpected result, which is of interest outside of the inflationary theory, is that even an insignificant amount of out-of-equilibrium particles with $n_\chi(k) \leq 1$, being re-scattered off the scalar field condensate, can generate IR cascade of the inhomogeneous condensate fluctuations with large occupation number $n_\phi(k)$ in the IR region. This is explained by fact that multiple production of the IR modes is energetically cheap.

iv) IR fluctuations of the light fields have special significance in the context of inflationary theory. These fluctuations evolve in time similar to the evolution of the usual inflationary fluctuations. Their amplitude is oscillating while their wavelengths is inside the Hubble radius and is frozen out once their wavelengths exceed the Hubble radius H^{-1} . However, the amplitude of IR cascading fluctuations is different from that of the usual quantum fluctuations. Frozen fluctuations $\delta\phi$, regardless of their origin, will induce cosmological curvature fluctuations. Thus, we get a new mechanism for generating frozen long wavelength $\delta\phi$ fluctuations from IR cascading. Therefore, IR cascading will lead to observable features in the CMB power spectrum. For generic choices of parameters, these re-scattered fluctuations are much more significant than the features induced by the momentary slowing-down of the background $\phi(t)$, see the left panel of Fig. 5.6.

v) Since the solution $\delta\phi$ of (5.5) depends nonlinearly on the Gaussian field χ , the curva-

ture fluctuations induced by IR cascading will be non-Gaussian. This non-Gaussianity is illustrated in Fig. 5.5. We estimate this non-Gaussianity to be significant. However, this non-Gaussian signal is related to the IR cascading bump of the spectrum and peaks on the range of scales corresponding to roughly one e-folding after $t = t_0$. This type of non-Gaussianity, which is large only over a small range of scales, is not well constrained by observation.

vi) The strength and location of our effect is model-dependent (through g^2 and ϕ_0), however, the very fact that subtle QFT effects of interaction during inflation may lead to an observable effect is intriguing.

vii) In our analysis we have focused on a single burst of instantaneous particle production during inflation. This scenario is interesting in its own right, however, our results could also be extended in a straightforward manner to study trapped inflation models where there are numerous bursts of particle production; see [235] for more detailed discussion.

viii) Suppose we have a sequence of points ϕ_{0i} ($i = 1, \dots, N$) where particles χ_i become massless. In this case the curvature fluctuation profiles generated from individual bursts of IR cascading can superpose to form a smooth spectrum of cosmological fluctuations, see the right panel of Fig. 5.6. This provides us with a new mechanism for generating long wavelength curvature fluctuations during inflation from IR cascading. The amplitude and non-Gaussianity of these curvature fluctuations will depend on the coupling, g^2 . These fluctuations are interesting on their own, although they may generate too much non-Gaussianity. They also can be considered as an extra component of the standard vacuum fluctuations, introducing an interesting non-Gaussian signal to the net fluctuations.

ix) The transfer of energy into fluctuations via successive bursts of particle production can lead to trapped inflation. Our new mechanism of generating cosmological fluctuations from IR cascading can, but need not, be associated with trapped inflation.

x) Varying the location, strength and non-Gaussianity of the IR cascading bump, it will

be interesting to consider other potential implication to the cosmological fluctuations, e.g. their impact on the horizon scale fluctuations or on small scale fluctuations where they might effect primordial Black Hole formation or the generation of gravitational waves.

Finally, let us return to the old story of how cosmological fluctuations are affected by phase transition during inflation, which we discussed at the beginning of this paper. We project that our results concerning re-scattering and IR cascading will radically change the conventional picture.

5.6 Introduction for the Observational Part

Recently, there has been considerable interest in inflationary models where the motion of the inflaton triggers the production of some non-inflation (iso-curvature) particles *during* inflation [233, 248, 249, 8, 6, 250, 228, 229, 230, 231, 232, 251, 252, 253, 254, 234, 235, 255, 256]. Examples have been studied where this particle production occurs via parametric resonance [233, 248, 249, 8, 6, 250], as a result of a phase transition [228, 229, 230, 231, 232, 251, 252, 253, 254], or otherwise. In some scenarios, back-reaction effects from particle production can slow the motion of the inflaton on a steep potential [234, 235, 255], providing a new inflationary mechanism. Moreover, inflationary particle production arises naturally in a number of realistic microscopic models from string theory [234, 235, 255, 236, 257, 258] and also supersymmetry (SUSY) [259].

In previous sections of this chapter it was shown that the production of massive iso-curvature particles during inflation (and their subsequent interactions with the slow roll condensate) provides a qualitatively new mechanism for generating cosmological perturbations. This new mechanism leads to a variety of novel observable signatures. Here we study in detail the observational constraints on such distortions of the primordial power spectrum for a variety of scenarios.

One motivation for this study is to determine whether features generated by particle

production during inflation can explain some of the anomalies in the observed primordial power spectrum, $P(k)$. A number of different studies have hinted at the possible presence of some localized features in the power spectrum [248, 254, 210, 204, 205, 260, 261, 198, 207, 201, 202, 262, 263, 203], which are not compatible with the simplest power law $P(k) \sim k^{n_s-1}$ model. Although such glitches may simply be statistical anomalies, there is also the tantalizing possibility that they represent a signature of primordial physics beyond the simplest slow roll inflation scenario. Forthcoming polarization data may play a crucial role in distinguishing between these possibilities [254]. However, in the meantime, it is interesting to determine the extent to which such features may be explained by microscopically realistic inflation models.

We consider a very simple model where the inflaton, ϕ , and iso-inflaton, χ , fields interact via the coupling given in Eq. (5.1). We focus on this simple prototype model in order to illustrate the basic phenomenology of particle production during inflation, however, we expect our results to generalize in a straightforward way to more complicated scenarios. Models of the type (5.1) have been considered as a probe of Planck-scale effects [233] and offer a novel example of the non-decoupling of high energy physics during inflation.^{vi}

At the moment when $\phi = \phi_0$ (which we assume occurs during the observable range of e -foldings of inflation) the χ particles become instantaneously massless and are produced by quantum effects. This burst of particle production drains energy from the condensate $\phi(t)$, temporarily slowing the motion of the inflaton background and violating slow roll. Shortly after this moment the χ particles become extremely non-relativistic, so that their number density dilutes as a^{-3} , and eventually the inflaton settles back onto the slow roll attractor.

^{vi}For reasonable values of g^2 the χ particles are *extremely* massive for almost the entire duration of inflation excepting a tiny interval, much less than an e -folding, about the point $\phi = \phi_0$. However, the χ field cannot be integrated out due to the non-adiabatic time dependence of the mode functions, see [264] for further discussion.

Several previous papers [233, 248, 249, 8] have studied the temporary slowing-down of the inflaton background using the mean-field equation (5.2), where the vacuum average $\langle\chi^2\rangle$ is computed following [237, 238]. Using this approach one finds that the transient violation of slow roll leads to a “ringing pattern” (damped oscillations) in the spectrum of cosmological fluctuations leaving the horizon near the moment when $\phi = \phi_0$ [8]. In [248, 249] observational constraints on particle production during inflation were discussed in the context of this mean field treatment.

However, in previous part of this chapter we re-considered cosmological fluctuations for this model, going beyond the mean-field treatment of ϕ .^{vii} It was pointed out that the massive χ particles can rescatter off the condensate to generate bremsstrahlung radiation of long-wavelength $\delta\phi$ fluctuations via diagrams such as Fig. 5.7. Multiple rescattering processes lead to a rapid cascade of power into the infra-red (IR) - *IR cascading*. The inflaton modes generated by IR cascading freeze once their wavelength crosses the horizon and lead to a bump-like feature in the cosmological perturbations that is illustrated in Fig. 5.8. This feature is complimentary to the usual (nearly) scale-invariant quantum vacuum fluctuations from inflation. The bump dominates over the ringing pattern discussed above by many orders of magnitude, independently of the value of g^2 .

In light of the results of [6] it is clear that the observational constraints on the model (5.1) need to be reconsidered. Since previous studies have suggested marginal evidence for localized power excesses in the CMB using both parametric [248, 263] and non-parametric [202, 201] techniques, it is interesting to determine if a simple and well-motivated model such as (5.1) can explain these anomalies. To answer this question we provide a simple semi-analytic fitting function that accurately captures the shape of the feature generated by particle production and IR cascading during inflation. Next, we confront this modified power spectrum with a variety of observational data sets. We find no evidence for a detection, however, we note that observations are consistent with relatively large

^{vii}See also [235] for a complimentary analysis and for a detailed analytical treatment of the dynamics.

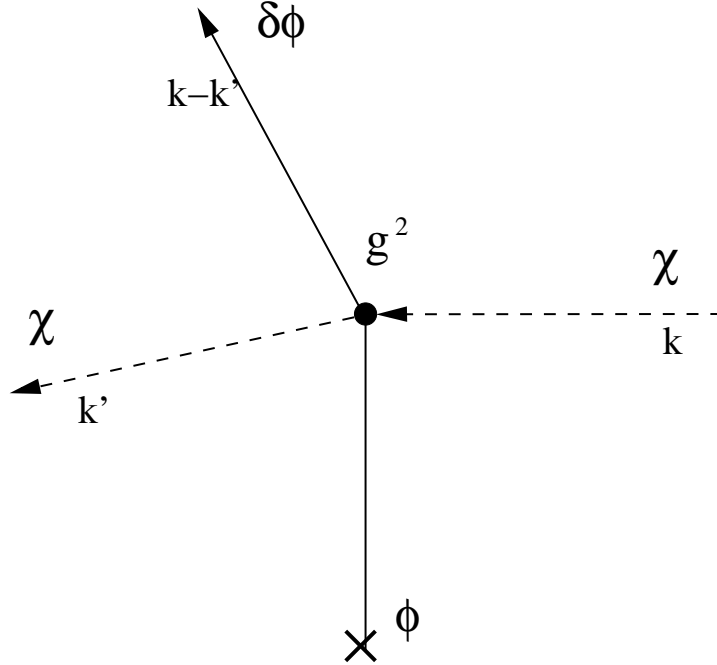


Figure 5.7: Rescattering diagram.

spectral distortions of the type predicted by the model (5.1). If the feature is located on scales relevant for Cosmic Microwave Background (CMB) experiments then its amplitude may be as large as $\mathcal{O}(10\%)$ of the usual scale-invariant fluctuations, corresponding to $g^2 \sim 0.01$. Our results translate into a ϕ_0 -dependent bound on the coupling g^2 which is crucial in order to determine whether the non-Gaussian signal associated with particle production and IR cascading is detectable in future missions.

We also consider the more complicated features which result from multiple bursts of particle production and IR cascading. Such features are a prediction of a number of string theory inflation models, including brane/axion monodromy [236, 257, 258]. For appropriate choice of the spacing between the features, we find that the constraint on g^2 in this scenario is even weaker than the single-bump case.

Although we focus on the interaction (5.1), our findings may have some bearing also on models with phase transitions during inflation. A simple prototype model for the

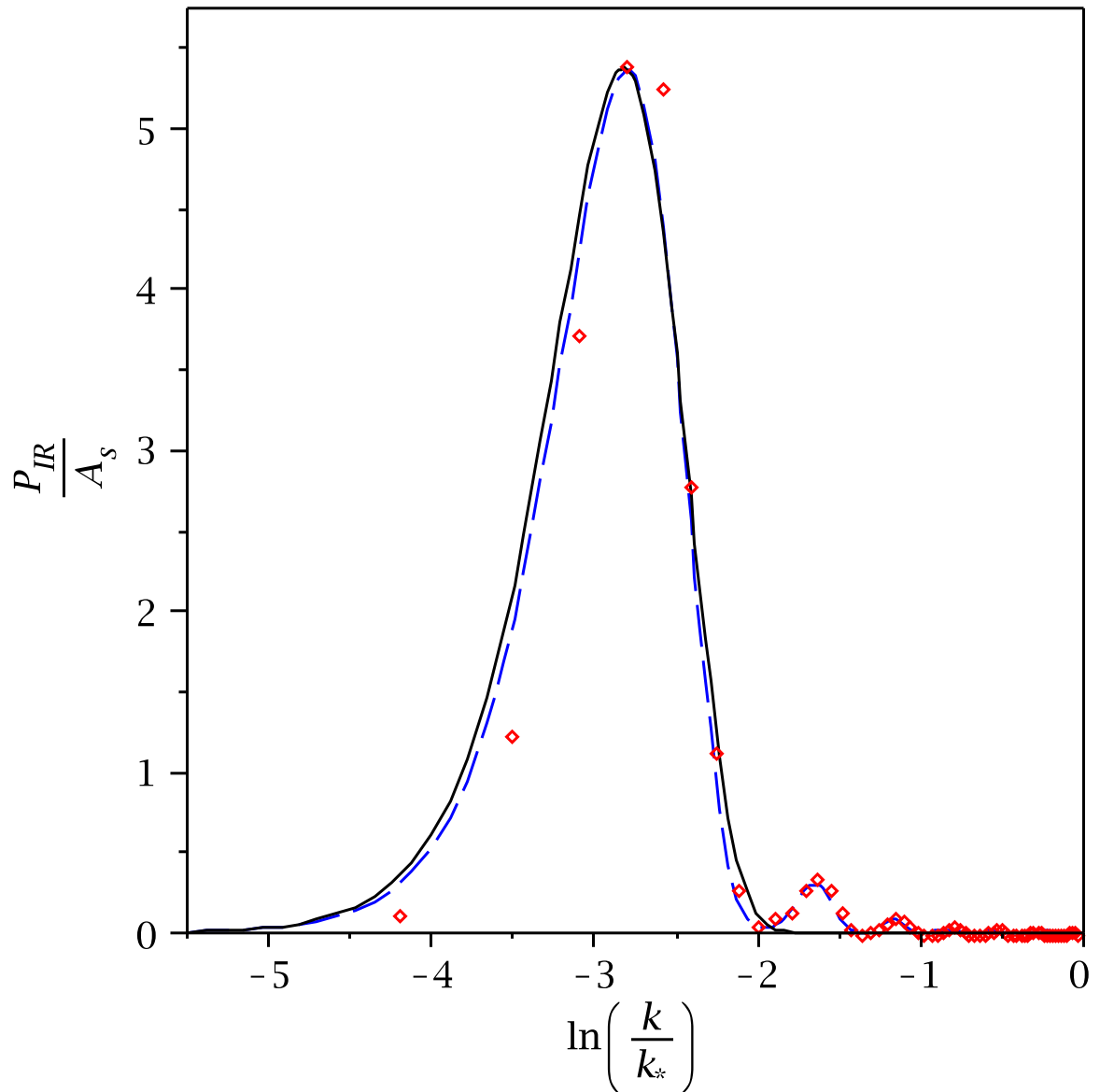


Figure 5.8: The bump-like features generated by IR cascading. We plot the feature power spectrum obtained from fully nonlinear lattice field theory simulations (the red points) and also the result of an analytical calculation (the dashed blue curve). We also superpose the fitting function $\sim k^3 e^{-\pi k^2/(2k_*^2)}$ (the solid black curve) to illustrate the accuracy of this simple formula

latter scenario is

$$V(\phi, \chi) = \frac{\lambda}{4}(\chi^2 - v^2)^2 + \frac{g^2}{2}\chi^2\phi^2 + V_{\text{inf}}(\phi)$$

At the moment when $\phi = \sqrt{\lambda}v/g$ massive iso-inflaton χ particles are produced copiously by tachyonic (spinodal) instability [265, 266]. These produced particles will subsequently interact with the condensate via rescattering diagrams similar to Fig. 5.7. Hence, we expect the features produced by inflationary phase transitions to be qualitatively similar to the bumps considered in this work. (This intuition is consistent with a second order computation of the cosmological perturbations in a closely related model [231, 232]. See [263] for a discussion of the observational consequences.)

In the literature it is sometimes argued that inflationary phase transitions can be studied using a toy model with a sharp step-like feature in the inflaton potential. This potential-step model predicts a ringing pattern in the power spectrum, very much analogous to the mean field treatment of resonant particle production during inflation, discussed above. This treatment does not take into account the violent growth of inhomogeneities of the fields that occurs during realistic phase transitions [265, 266] and, in particular, does not capture rescattering effects and IR cascading. In the case of resonant particle production, these nonlinear effects have a *huge* impact on the cosmological fluctuations [6]. Hence, it is far from clear if the potential-step model provides a good effective description of inflationary phase transitions.^{viii}

Of course, inflation models with steps in $V(\phi)$ (or its derivatives) may be considered on phenomenological grounds, irrespective of the motivation from inflationary phase transitions. In [268] cosmological perturbations from models with step-like features and discontinuities in higher derivatives were considered, as were the microscopic motivations for such constructions. See [269, 270] for a study of the non-Gaussianities induced in a variety of single-field models with steps or oscillations in the inflaton potential.

The outline of this chapter is as follows. In section 5.7 we provide a simple parametriza-

^{viii}See also [267] for a related discussion.

tion of the features that are imprinted on the primordial power spectrum by one or more bursts of particle production during inflation. In section 5.8 we describe our method and discuss the observational data sets employed to derive constraints on this modified power spectrum. In section 5.9 we present observational constraints on various scenarios. In section 5.10 we present some microscopic realizations of our scenario and discuss the implications of our findings for popular string theory/SUSY inflation models with a special emphasis on brane monodromy. Finally, in section 5.11 we conclude.

5.7 A Simple Parametrization of the Power Spectrum

In [6] it was shown that particle production and IR cascading during inflation in the model (5.1) generates a bump-like contribution to the primordial power spectrum. As shown in Fig. 5.8, this feature can be fit with a very simple function $P_{\text{bump}} \sim k^3 e^{-\pi k^2/(2k_*^2)}$. The bump-like contribution from IR cascading is complimentary to the usual (nearly) scale-invariant contribution to the primordial power spectrum $P_{\text{vac}} \sim k^{n_s-1}$ coming from the quantum vacuum fluctuations of the inflaton. The total, observable, power spectrum in the model (5.1) is simply the superposition of these two contributions: $P(k) \sim k^{n_s-1} + k^3 e^{-\pi k^2/(2k_*^2)}$. This simple formula can be motivated from analytical considerations [6] and provides a good fit to lattice field theory simulations near the peak of the feature and also in the IR tail.^{ix}

It is straightforward to generalize this discussion to allow for multiple bursts of particle production during inflation. Suppose there are multiple points $\phi = \phi_i$ ($i = 1, \dots, n$) along

^{ix}This fitting formula does *not* capture the small oscillatory structure in the UV tail of the feature (see Fig. 5.8) which does not concern us since that region is not phenomenologically interesting.

the inflationary trajectory where new degrees of freedom χ_i become massless:

$$\mathcal{L}_{\text{int}} = - \sum_{i=0}^n \frac{g_i^2}{2} (\phi - \phi_i) \chi_i^2 \quad (5.11)$$

For each instant t_i when $\phi = \phi_i$ there will be an associated burst of particle production and subsequent rescattering of the produced massive χ_i off the condensate $\phi(t)$. Each of these events proceeds as described above and leads to a new bump-like contribution to the power spectrum. These features simply superpose owing to that fact that each field χ_i is statistically independent (so that the cross terms involving $\chi_i \chi_j$ with $i \neq j$ in the computation of the two-point function must vanish). Thus, we arrive at the following parametrization of the primordial power spectrum in models with particle production during inflation:

$$P(k) = A_s \left(\frac{k}{k_0} \right)^{n_s-1} + \sum_{i=1}^n A_i \left(\frac{\pi e}{3} \right)^{3/2} \left(\frac{k}{k_i} \right)^3 e^{-\frac{\pi}{2} \left(\frac{k}{k_i} \right)^2} \quad (5.12)$$

where A_s is the amplitude of the usual nearly scale invariant vacuum fluctuations from inflation and k_0 is the pivot, which we choose to be $k_0 = 0.002 \text{ Mpc}^{-1}$ following [271]. The constants A_i depend on the couplings g_i^2 and measure the size of the features from particle production. We have normalized these amplitudes so that the power in the i -th bump, measured at the peak of the feature, is given by A_i . The location of each feature, k_i , is related to the number of e -foldings N from the end of inflation to the time when the i -th burst of particle production occurs: roughly $\ln(k_i/H) \sim N_i$ where $N = N_i$ at the moment when $\phi = \phi_i$. From a purely phenomenological perspective the locations k_i are completely arbitrary.

We compare (5.12) to lattice field theory simulations in order to determine the amplitude A_i in terms of model parameters. We find

$$A_i \cong 1.01 \times 10^{-6} g_i^{15/4} \quad (5.13)$$

Assuming standard chaotic inflation $V = m^2\phi^2/2$ we have tested this formula for $g^2 = 1, 0.1, 0.01$, taking both $\phi_0 = 2m_{pl}$ and $\phi_0 = 3.2m_{pl}$. We found agreement up to factors order unity in all cases.

Theoretical consistency of our calculation of the shape of the feature bounds the coupling as $10^{-7} \lesssim g_i^2 \lesssim 1$ (For smaller g^2 the theoretical calculation ignoring the expansion of universe is invalid.) Hence, the power spectrum (5.12) can be obtained from sensible microphysics only when $10^{-20} \lesssim A_i \lesssim 10^{-6}$.^x This constraint still allows for a huge range of observational possibilities: near the upper bound the feature is considerably larger than the vacuum fluctuations while near the lower bound the feature is completely undetectable.

Note that for each bump in (5.12) the IR tail $P_{\text{bump}} \rightarrow k^3$ as $k \rightarrow 0$ is similar to the feature considered by Hoi, Cline & Holder in [263], consistent with causality arguments about the generation of curvature perturbations by local physics.

5.8 Data Sets and Analysis

The primordial power spectrum for our model is parametrized as (5.12). Our aim is to derive observational constraints on the various model parameters A_s, n_s, k_i and A_i using CMB, galaxy power spectrum and weak lensing data. To this end we use the CosmoMC package [113] to run Markov Chain Monte Carlo (MCMC) calculations to determine the likelihood of the cosmological parameters, including our new parameters A_i and k_i . We employ the following data sets.

Cosmic Microwave Background (CMB)

Our complete CMB data sets include WMAP-5yr [226, 271], BOOMERANG [3, 4,

^xFor $10^{-7} < g^2 \lesssim 10^{-4}$ the feature in power spectrum will be too small to be observed. For $g^2 < 10^{-7}$ our theoretical calculation is not reliable, and it is difficult to track such a tiny effect with lattice simulations. We expect for $g^2 < 10^{-7}$ the power spectrum is also negligible, and leave this conjecture to be verified in our future work.

5], ACBAR [122, 123, 121, 120], CBI [127, 125, 126, 124], VSA [128], DASI [272, 273], and MAXIMA [129]. We have included the Sunyaev-Zeldovic (SZ) secondary anisotropy [130, 131] for WMAP-5yr, ACBAR and CBI data sets. The SZ template is obtained from hydrodynamical simulation [133]. Also included for theoretical calculation of CMB power spectra is the CMB lensing contribution.

Type Ia Supernova (SN)

We employ the Union Supernova Ia data (307 SN Ia samples) from The Supernova Cosmology Project [274].

Large Scale Structure (LSS)

The 2dF Galaxy Redshift Survey (2dFGRS) data [275] and Sloan Digital Sky Survey (SDSS) Luminous Red Galaxy (LRG) data release 4 [276] are utilized.

Note that we have used the likelihood code based on the non-linear modelling by Tegmark et al. [276] (marginalizing the bias b and the Q parameter). However with a large bump in the linear power spectrum, this naive treatment may be not sufficient to characterize the non-linear response to the feature on small scales. Ideally, this should be obtained from N-body simulations, however, such a study is beyond the scope of the current work.

There are several other caveats on our results in the high- k regime. First, we assume linear bias for the galaxies, which may not be entirely safe at sufficiently small scales. Moreover, sharp features in the matter power spectrum can cause sharp features in the bias as a function of k .

Keeping in mind these caveats our constraints on small scales $k \gtrsim 0.1 \text{ Mpc}^{-1}$ should be taken with a grain of salt and considered as accurate only up to factors order unity.

Weak Lensing (WL)

See Section 2.4 for five WL data sets used here.

As for the LSS data, for small scales $k \gtrsim 0.1 \text{ Mpc}^{-1}$ there is the caveat that the nonlinear evolution of the power spectrum in the presence of bump-like distortions may not be treated accurately.

5.9 Observational Constraints

We now present our results for the observational constraints on particle production during inflation, assuming two different scenarios.

5.9.1 A Single Burst of Particle Production

The minimal scenario to consider is a single burst of particle production during inflation, which corresponds to taking $n = 1$ in (5.11). The power spectrum is given by (5.12) with $n = 1$ and, with some abuse of notation, we denote $k_1 \equiv k_{\text{IR}}$ and $A_1 \equiv A_{\text{IR}}$. The prior we have used for A_{IR} is $0 \leq A_{\text{IR}} \leq 25 \times 10^{-10}$, and for k_{IR} is $-9.5 \leq \ln[k/\text{Mpc}^{-1}] \leq 1$. The former condition ensures that the bump-like feature from IR cascading does not dominate over the observed scale invariant fluctuations while the latter is necessary in order to have the feature in the observable range of scales. In Fig. 5.9 we plot the marginalized posterior likelihood for the new parameters A_{IR} and k_{IR} describing the magnitude and location of the bump while in Table 5.1 we give the best fit values for the remaining (vanilla) cosmological parameters.

For very large scales $\lesssim \text{Gpc}^{-1}$, the data do not contain much information (due to cosmic variance) and hence the constraint on any modification of the power spectrum is weak. In this region the spectral distortion may be larger than 100% of the usual scale invariant fluctuations and couplings g^2 order unity are allowed. For smaller scales $k \gtrsim \text{Gpc}^{-1}$ the constraints are stronger and we have, very roughly, $A_{\text{IR}}/A_s \lesssim 0.1$ corresponding to $g^2 \lesssim 0.01$. For very small scales, $k \gtrsim 0.1 \text{ Mpc}^{-1}$ our constraints should be

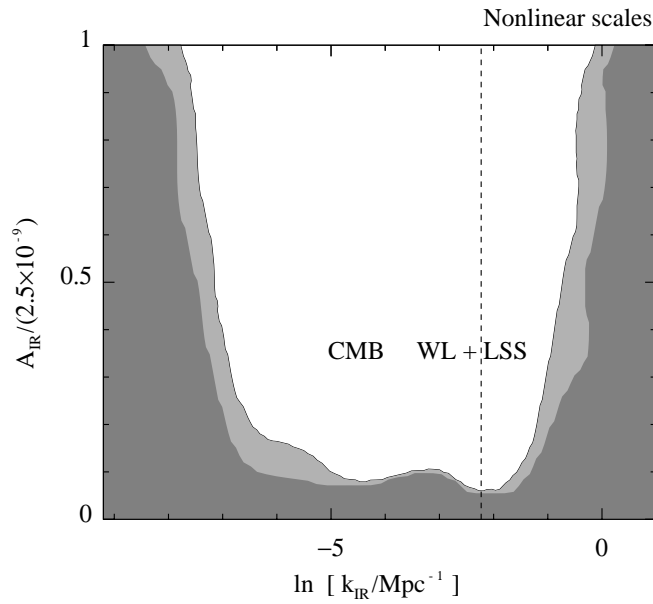


Figure 5.9: Marginalized posterior likelihood contours for the parameters A_{IR} and k_{IR} (the magnitude and position of the feature, respectively) in the single-bump model. Black and grey regions correspond to parameter values allowed at 95.4% and 99.7% confidence levels, respectively. At small scales, to the right of the dashed vertical line, our results should be taken with a grain of salt since the nonlinear evolution of the power spectrum may not be modelled correctly in the presence of bump-like distortions.

Table 5.1: Constraints on the standard (“vanilla”) cosmological parameters for the single-bump model. For comparison we also show the standard Λ CDM constraints using the same data sets. All errors are 95.4% confidence level. (*Note we are showing 2- σ constraints here.*)

	single bump	Λ CDM (no bump)
$\Omega_{\text{b}0}h^2$	$0.0227^{+0.0010}_{-0.0010}$	$0.02270^{+0.0009}_{-0.0009}$
$\Omega_{\text{c}0}h^2$	$0.1122^{+0.0050}_{-0.0044}$	$0.1120^{+0.0045}_{-0.0048}$
θ	$1.0424^{+0.0042}_{-0.0043}$	$1.0421^{+0.0043}_{-0.0036}$
τ_{re}	$0.08^{+0.03}_{-0.03}$	$0.089^{+0.026}_{-0.025}$
n_s	$0.956^{+0.024}_{-0.024}$	$0.957^{+0.026}_{-0.023}$
$\ln[10^{10}A_s]$	$3.21^{+0.08}_{-0.07}$	$3.23^{+0.07}_{-0.07}$
$\Omega_{\text{m}0}$	$0.264^{+0.026}_{-0.022}$	$0.264^{+0.021}_{-0.025}$
σ_8	$0.81^{+0.04}_{-0.03}$	$0.81^{+0.04}_{-0.03}$
z_{re}	$10.5^{+2.5}_{-2.7}$	$11.4^{+2.1}_{-2.4}$
H_0	$71.6^{+2.3}_{-2.4}$	$71.5^{+2.8}_{-2.1}$

taken with a grain of salt since the nonlinear evolution of the power spectrum may not be modelled correctly in the presence of bump-like distortions. At small scales nonlinear effects tend to wipe out features of this type (see, for example, [277]) and hence observational constraints for $k \gtrsim 0.1 \text{ Mpc}^{-1}$ may be weaker than what is presented in Fig. 5.9. Note that in most of this nonlinear regime we find essentially no constraint on A_{IR} , which is consistent with what would be expected in a more comprehensive treatment.

The IR cascading bump in the primordial power spectrum will be accompanied by a corresponding non-Gaussian feature in the bispectrum [6]. From the perspective of potentially observing this signal it is most interesting if this feature is located on scales probed by CMB experiments. (There is also the fascinating possibility that the non-Gaussianity from IR cascading could show up in the large scale structure as in [278, 279, 280, 281]. We leave a detailed discussion to future studies.) To get some intuition into what kinds of features in the CMB scales are still allowed by the data we focus on an example with $A_{\text{IR}} = 2.5 \times 10^{-10}$ which, using (5.13), corresponds to a reasonable coupling value $g^2 \sim 0.01$. We take the bump to be located at $k_{\text{IR}} = 0.01 \text{ Mpc}^{-1}$ and fix the remaining model parameters to $A_s = 2.44 \times 10^{-9}$, $n_s = 0.97$ (which are compatible with the usual values). This sample bump in the power spectrum is illustrated in the left panel of Fig. 5.10 and is consistent with the data at 2σ . In the right panel of Fig. 5.10 we plot the associated angular CMB TT spectrum. This example represents a surprisingly large spectral distortion: the total power in the feature as compared to the scale invariant vacuum fluctuations is $P_{\text{bump}}/P_{\text{vac}} \sim 0.1$, evaluated at the peak of the bump. We will discuss the non-Gaussianity associated with this feature.

5.9.2 Multiple Bursts of Particle Production

Next, we consider a slightly more complicated scenario: multiple bursts of particle production leading many localized features in the power spectrum. For simplicity we assume that all bumps have the same magnitude $A_i \equiv A_{\text{IR}}$ and we further suppose a fixed num-

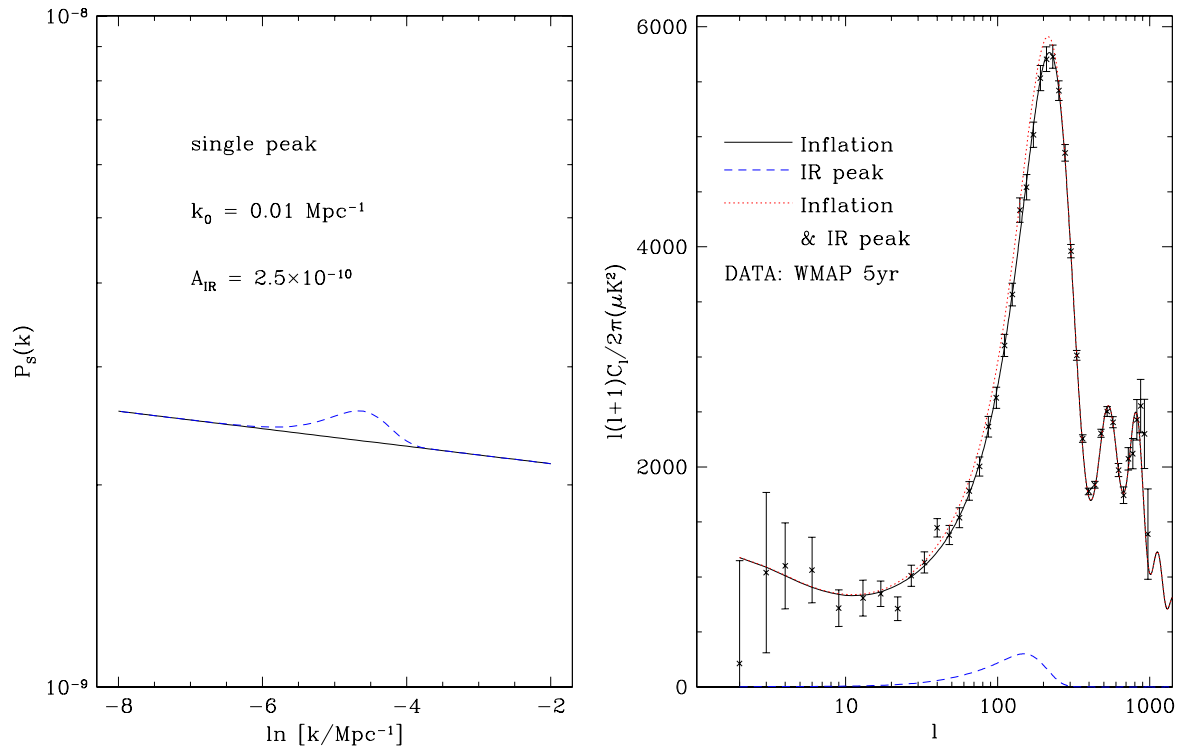


Figure 5.10: The left panel shows a sample bump in the power spectrum with amplitude $A_{\text{IR}} = 2.5 \times 10^{-10}$ which corresponds to a coupling $g^2 \sim 0.01$. The feature is located at $k_{\text{IR}} = 0.01 \text{ Mpc}^{-1}$. This example represents a distortion of $\mathcal{O}(10\%)$ as compared to the usual vacuum fluctuations and is consistent with the data at 2σ . The right panel shows the CMB angular TT power spectrum for this example, illustrating that the distortion shows up mostly in the first peak.

ber of e -foldings δN between each burst of particle production. This implies that the location of the i -th bump will be given by $k_i = e^{(i-1)\Delta} k_1$ where Δ is a model parameter controlling the density of features. We take the number of bursts, n , to be sufficiently large that the series of features extends over the whole observable range. In the next section we will see that these assumptions are not restrictive and that many well-motivated models are consistent with this simple set-up.

Our multi-bump model, then, has three parameters: A_{IR} , k_1 and Δ . We take the prior on the amplitude to be $A_{\text{IR}} \leq 25 \times 10^{-10}$ as in section 5.9.1. If the features are very widely spaced, $\Delta \gtrsim 1$, then the constraint on each bump will obviously be identical to the results for the single-bump case presented in the section 5.9.1. Hence the most interesting case to consider is $\Delta \lesssim 1$ so that the bumps are partially overlapping. Our prior for the density of features is therefore $0 \leq \Delta \leq 1$. Finally, the location of the first bump will be a historical accident in realistic models, hence we marginalize over all possible values of k_1 and present our constraints and 2-d likelihood plots in the space of A_{IR} and Δ . This marginalized likelihood plot is presented in Fig. 5.11. In table 5.2 we present the best-fit values for the vanilla cosmological parameters.

From the likelihood plot, Fig. 5.11, there is evidently a preferred value of the feature spacing, roughly $\Delta \sim 0.75$, for which the constraints are weakest. This can be understood as follows. For very high density $\Delta \rightarrow 0$ the localized features from IR cascading smear together and the total power spectrum (5.12) is $P(k) \sim A_s(k/k_0)^{n_s-1} + C$ where the size of the constant deformation scales linearly with the density of features: $C \propto \Delta^{-1}$. Therefore, the upper bound on the amplitude A_{IR} should scale linearly with Δ . Indeed, this linear trend is very evident from Fig. 5.11 in the small- Δ regime. This linear behaviour must break down at some point since for $\Delta \gtrsim 1$ the peaks no longer overlap, generating a non-flat spectrum that is strongly disfavored by the data. The upperbound on A_{IR} will again be stringent. This explains the bump in the likelihood plot, Fig. 5.11, near $\Delta \sim 0.75$.

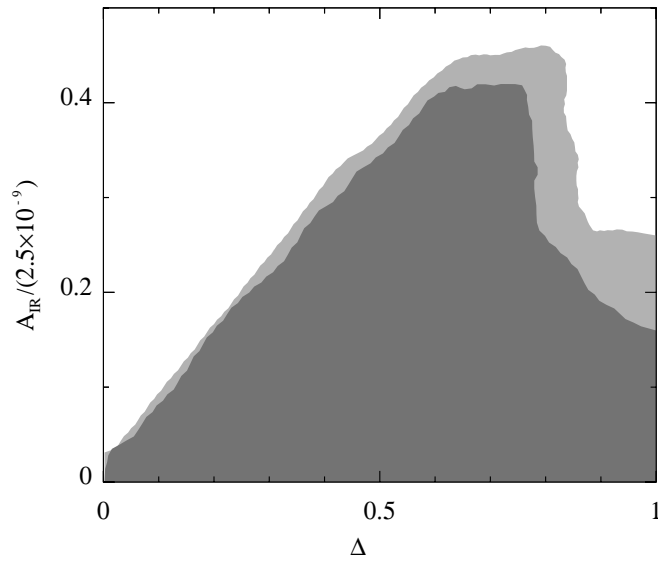


Figure 5.11: Marginalized posterior likelihood contours for the parameters A_{IR} and Δ (the feature amplitude and spacing, respectively) of the multiple-bump model. Black and grey regions correspond to values allowed at 95.4% and 99.7% confidence levels, respectively.

Table 5.2: constraints on the standard (“vanilla”) cosmological parameters for the multiple-bump model. All error bars are 95.4% confidence level.

$\Omega_{\text{b}0}h^2$	$0.0227^{+0.0009}_{-0.0009}$
$\Omega_{\text{c}0}h^2$	$0.1126^{+0.0049}_{-0.0044}$
θ	$1.0424^{+0.0039}_{-0.0043}$
τ_{re}	$0.078^{+0.031}_{-0.026}$
n_s	$0.93^{+0.04}_{-0.17}$
$\ln[10^{10}A_s]$	$2.8^{+0.4}_{-0.9}$
$\Omega_{\text{m}0}$	$0.265^{+0.026}_{-0.021}$
σ_8	$0.807^{+0.034}_{-0.030}$
H_0	$71.4^{+2.2}_{-2.4}$

In passing, notice that the behaviour $P(k) \sim A_s(k/k_0)^{n_s-1} + C$ for $\Delta \ll 1$ also explains why the best-fit A_s in table 5.2 is somewhat lower than the standard value and why the spectral tilt $n_s - 1$ is somewhat more red.

To get some intuition for the kinds of multi-bump distortions that are allowed by the data, we consider an example with $A_{\text{IR}} = 1 \times 10^{-9}$, $\Delta = 0.75$ and fix the vanilla parameters to $A_s = 1.04 \times 10^{-9}$, $n_s = 0.93$. This choice of parameters is consistent with the data at 2σ and corresponds to a reasonable coupling $g^2 \sim 0.02$. In Fig. 5.12 we plot the primordial power spectrum $P(k)$ and also the CMB TT angular power spectrum for this example.

5.10 Particle Physics Models

From the low energy perspective one expects interactions of the type (5.1) to be rather generic, hence particle production during inflation may be expected in a wide variety of

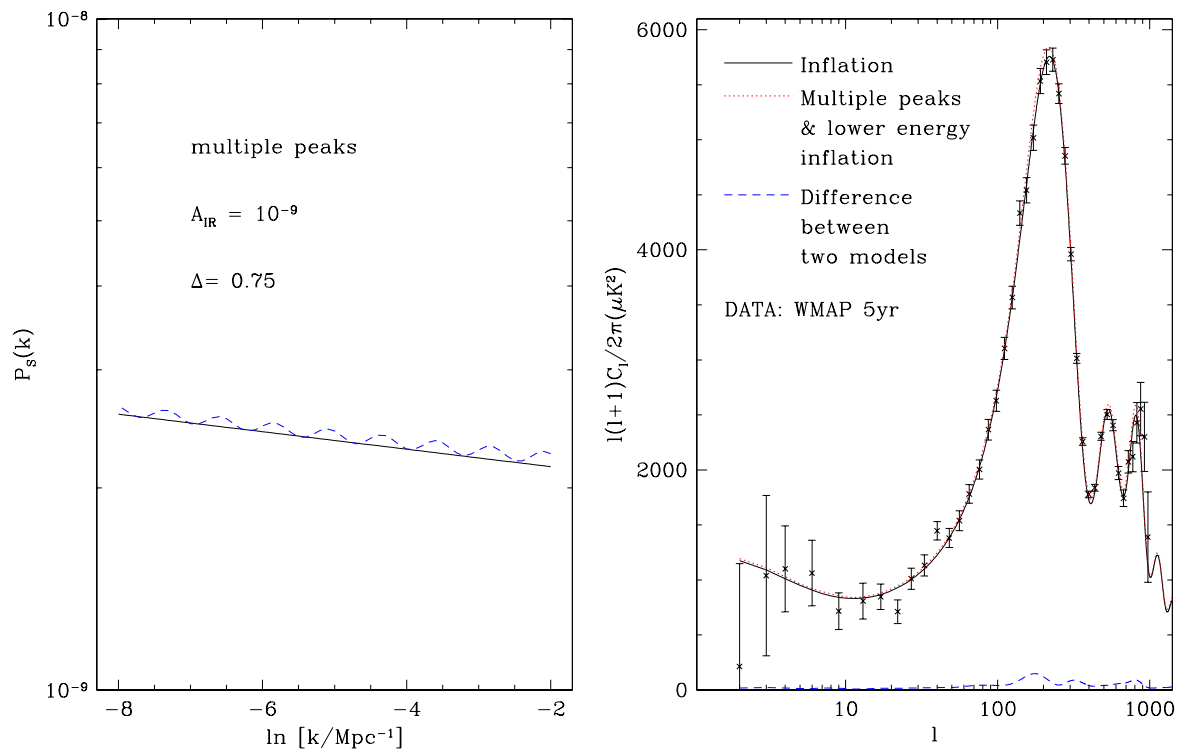


Figure 5.12: The top panel shows a sample multiple-bump distortion with amplitude $A_{\text{IR}} = 1 \times 10^{-9}$ which corresponds to $g^2 \sim 0.02$. The feature spacing is $\Delta = 0.75$. We take the vanilla parameters to be $A_s = 1.04 \times 10^{-9}$, $n_s = 0.93$ so that the scale of inflation is slightly lower than in the standard scenario and the spectral tilt is slightly redder. The bottom panel shows the CMB angular TT power spectrum for this example.

models. In this section we consider some explicit examples in string theory and SUSY in order to show how such models may be obtained microscopically and also to provide the proof of concept that realistic models do exist where ϕ_i are in the observable range.

5.10.1 Open String Inflation Models

String theory inflation models may be divided into two classes depending on the origin of the inflaton: closed string models and open string models. In the former case the inflaton is typically a geometrical modulus associated with the compactification manifold (examples include racetrack inflation [282], Kähler modulus inflation [52] and Roulette inflation [44]). In the latter case the inflaton is typically the position modulus of some mobile D-brane^{xi} living in the compactification manifold (examples include brane inflation [41] such as the warped KKLM model [288], D3/D7 inflation [289] and DBI inflation [290]). In open string inflation models there may be, in addition to the mobile inflationary brane, some additional “spectator” branes. If the mobile brane collides with any spectator brane during inflation then some of the stretched string states between these branes will become massless at the moment when the branes are coincident [234, 235], precisely mimicking the interaction (5.1). Thus, we expect particle production, IR cascading and the bump-like features described above to be a reasonably generic prediction of open string inflation.

5.10.2 String Monodromy Models

A concrete example of the heuristic scenario discussed in the last subsection is provided by the brane monodromy and axion monodromy string theory inflation models proposed in [236, 257, 258]. In the original brane monodromy model [236] one considers type IIA string theory compactified on a nil manifold that is the product of two twisted tori. The

^{xi}One notable exception is inflation driven by the open string tachyon, for example nonlocal string field theory models [283, 284, 285, 286, 287].

metric on each of these twisted tori has the form

$$\frac{ds^2}{\alpha'} = L_{u_1}^2 du_1^2 + L_{u_2}^2 du_2^2 + L_x^2 (dx' + Mu_1 du_2)^2 \quad (5.14)$$

where $x' = x - \frac{M}{2}u_1u_2$ and M is an integer flux number. The dimensionless constants L_{u_1} , L_{u_2} and L_x determine the size of the compactification.

Inflation is realized by the motion of a D4-brane along the direction u_1 of the internal manifold. The D4 spans our large 3-dimensions and wraps a 1-cycle along the direction u_2 of the internal space. The size of this 1-cycle, in string units, is given by

$$L = \sqrt{L_{u_2}^2 + L_x^2 M^2 u_1^2} \quad (5.15)$$

Hence, the brane prefers to minimize its world-volume by moving to the location $u_1 = 0$ where this 1-cycle has minimal size. This preference gives a potential to the D4-brane position which goes like $V \sim u_1$ in the large u_1 regime that is relevant for large field inflation.

In [235] it was shown that this scenario allows for the inclusion of a number of spectator branes stabilized at positions $u_1 = i/M$ (with i integer) along the inflationary trajectory. As the mobile inflationary D4 rolls through these points particles (strings) will be produced and the resulting distribution of features will look nearly identical to the simple multi-bump scenario studied in section 5.9.2. To see this, let us now determine the distribution of features that is predicted from brane monodromy inflation. The canonical inflaton ϕ can be related to the position of the mobile D4 as

$$\phi = B u_1^{1/p} \quad (5.16)$$

where B is a constant with dimensions of mass that depends on model parameters. Hence, the effective potential during inflation has the power-law form

$$V(\phi) = \mu^{4-p} \phi^p \quad (5.17)$$

For the simplest scenario described above one has $p = 2/3$. However, the formulas (5.16,5.17) still hold for the variant considered in [236] with $p = 2/5$ as long as one

replaces u_1 by a more complicated linear combination of coordinates. These relations also hold for axion monodromy models [257] with $p = 1$ and u_1 replaced by the axion, c , arising from a 2-form RR potential $C^{(2)}$ integrated over a 2-cycle Σ_2 . For *all* models of the form (5.17) the number of e -foldings N from $\phi = \phi(N)$ to the end of inflation (which occurs at $\phi = p/\sqrt{2}$ when the slow roll parameter $\epsilon(\phi) = 1$) is given by

$$\begin{aligned} N &= \frac{1}{2p} \frac{\phi^2(N)}{M_p^2} - \frac{p}{4} \\ &= \frac{1}{2p} \frac{B^2}{M_p^2} u_1^{2/p} - \frac{p}{4} \end{aligned} \quad (5.18)$$

Since the spectator branes are located at $u_1 = i/M$ the bursts of particle production must occur at times $N = N_i$ where

$$N_i = \frac{1}{2p} \frac{B^2}{M_p^2} \left(\frac{i}{M} \right)^{2/p} - \frac{p}{4} \quad (5.19)$$

The location $k = k_i$ of the i -th feature is defined, roughly, by the scale leaving the horizon at the moment $N = N_i$. Hence, the distribution of features for brane/axion monodromy models is given by

$$\ln \left[\frac{k_i}{H} \right] \cong \tilde{B}^2 i^{2/p} - \frac{p}{4} \quad (5.20)$$

with $p = 2/3$ or $p = 2/5$ for brane monodromy and $p = 1$ for axion monodromy. In (5.20) the dimensionless number \tilde{B} depends on model parameters.

Although the distribution of features (5.20) is not exactly the same as the evenly space distribution considered subsection 5.9.2, the two are essentially indistinguishable over the range of scales which are probed observationally (corresponding to roughly 10 e -foldings of inflation). The reason for this is simple: the inflaton is nearly constant during the first 10 e -foldings of inflation and hence $\delta N \sim \delta\phi \sim \delta u_1$ within the observable region. It follows that $k_i \cong e^{(i-1)\Delta} k_1$ to very good approximation for a huge class of models. To see this more concretely in the case at hand, let us compute dN/du_1 from (5.18). It is straightforward to show that

$$\frac{dN}{du_1} = \frac{1}{p^p} \frac{1}{[2\epsilon(\phi)]^{1-p/2}} \left(\frac{B}{M_p} \right)^p \quad (5.21)$$

where

$$\epsilon(\phi) \equiv \frac{M_p^2}{2} \left(\frac{V'}{V} \right)^2 = \frac{p^2}{2} \left(\frac{M_p}{\phi} \right)^2 \quad (5.22)$$

is the usual slow roll parameter. Observational constraints on the running of the spectral index imply that $\epsilon(\phi)$ cannot change much over the observable 10 e -foldings of inflation. Since $dN/du_1 \cong \text{const}$ to very high accuracy it follows trivially that $N = N(u_1)$ is very close to linear and $k_i \cong e^{(i-1)\Delta} k_1$ as desired.

In the context of axion monodromy inflation models [257] the multiple bump features discussed here will be complimentary to the oscillatory features described in [258] which result from the sinusoidal modulation of the inflaton potential by instanton effects. If the bursts of particle production are sufficiently densely spaced, then signal from IR cascading may appear oscillatory, however, it differs from the effect discussed in [258] in both physical origin and also in functional form.

Let us now estimate the effective value of the couplings g_i^2 appearing in the prototype interaction (5.11) that are predicted from the simplest brane monodromy model. A complete calculation would involve dimensionally reducing the DBI action describing the brane motion and requires knowledge of the full 10-dimensional geometry with the various embedded branes. For our purposes, however, a simple heuristic estimate for the collision of two D4-branes will suffice. When N D-branes become coincident the symmetry is enhanced from $U(1)^N$ to a $U(N)$ Yang Mill gauge theory. The gauge coupling for this Yang Mills theory is given by

$$g_{\text{YM}}^2 = \frac{g_s (2\pi)^2}{L} \quad (5.23)$$

where L is the volume of the 1-cycle that the D4 branes wrap and is given by (5.15). If the inflationary brane is at position u_1 and the i -th spectator brane is at $u_{1,i}$ then the distance between the two branes is given by

$$d^2 = \alpha' L_{u_1}^2 (u_1 - u_{1,i})^2 \quad (5.24)$$

The mass of the gauge bosons corresponding to the enhanced symmetry is

$$M_i^2 = g_{\text{YM}}^2 \frac{d^2}{(2\pi)^2 (\alpha')^2} = \frac{g_s L_{u_1}^2 (u_1 - u_{1,i})^2}{\alpha' \sqrt{L_{u_2}^2 + L_x^2 M^2 u_1^2}} \quad (5.25)$$

To put this in the prototype form $M_i^2 = g_i^2 (\phi - \phi_i)^2$ we must first convert to the canonical variable ϕ using the formula (5.16) with $p = 2/3$ and

$$B = \frac{M^{1/2} L_{u_1} L_x^{1/2}}{6\pi^2 \sqrt{g_s \alpha'}} \quad (5.26)$$

Next, we must Taylor expand the resulting equation about the minimum $\phi = \phi_i$. We find

$$M_i^2 \cong g_i^2 (\phi - \phi_i)^2 + \dots \quad (5.27)$$

$$\begin{aligned} g_i^2 &= \frac{16g_s^2 \pi^4}{ML_x u_{1,i}} \frac{1}{\sqrt{L_{u_2}^2 + L_x^2 M^2 u_{1,i}^2}} \\ &= \frac{16g_s^2 \pi^4}{L_x i} \frac{1}{\sqrt{L_{u_2}^2 + L_x^2 i^2}} \end{aligned} \quad (5.28)$$

where on the second line of (5.28) we have used the fact that $u_{1,i} = i/M$ (with i integer) in the simplest models. We see that the effective couplings g_i^2 become larger as the D4 unwinds during inflation. (The apparent divergence for $u_{1,i} = 0$ in the formula (5.28) is an artifact of the fact that the relation (5.16) is not valid at small values of u_1 . This will not concern us here since inflation has already terminated at the point that our formulas break down.)

To compute the amplitude of the bump-like feature produced by brane monodromy inflation we should take into account also combinatorial factors. When two branes become coincident the symmetry is enhanced from $U(1)^2$ to $U(2)$ so there are $2^2 - 2 = 2$ additional massless spin-1 fields appearing at the brane collision. Thus, using equation (5.13), the amplitude of the feature that will be imprinted in the CMB is

$$A_{i,\text{eff}} = 2 \times (2^2 - 2) \times \left[1.01 \cdot 10^{-6} \cdot g_i^{15/4} \right] \quad (5.29)$$

where the extra factor of 2 counts the polarizations of the massless spin-1 fields. This combinatorial enhancement can be much larger if the inflationary brane collides with a *stack* of spectators.

The above discussion is predicated on the assumption that the original brane monodromy set-up [236] is supplemented by additional spectator branes. This may seem like an unnecessary contrivance, however, in order for this model to reheat successfully it may be *necessary* to include spectator branes. For example, with the reheating mechanism proposed in [291] semi-realistic particle phenomenology can be obtained by confining the standard model (SM) to a D6 brane which wraps the compact space. In order to reheat into SM degrees of freedom we orient this brane so that its world-volume is parallel to the mobile (inflationary) D4. In this case the end of inflation involves multiple oscillations of the D4 about the minimum of its potential. At each oscillation the D4 collides with the D6 and SM particles are produced by parametric resonance preheating [237, 238]. However, due to the periodic structure of the compactification, D4/D6 collisions will necessarily occur also *during* inflation, leading to IR cascading features in the CMB.

The timing of these D4/D6 collisions was computed in [291] for the minimal $p = 2/3$ brane monodromy model, assuming the same choices of parameters used in [236]. For this particular case there is only one collision (and hence one feature) during the first 10 e -foldings of inflation and the phenomenology is essentially the same as that considered in subsection 5.9.1. What is the amplitude of this feature? Assuming, again, the parameters employed in [236] and noting that the first collision takes place at $i = 13$ [291] equation (5.28) gives $g_1^2 \cong 0.001$. From (5.29) we find the effective amplitude of the feature to be $A_{1,\text{eff}}/A_s \cong 0.01$. This value is well within the observational bounds derived in subsection 5.9.1

We stress that the conclusions in the previous paragraph apply *only* for the particular choice of model parameters employed in [236]. There exist other consistent parameter choices for which the simplest brane monodromy model predicts a much higher density

of features with much larger amplitude.

Note that both brane and axion monodromy models may be used to realize trapped inflation [235]. Here we are restricting ourselves to the large-field regime where the potential $V = \mu^{4-p}\phi^p$ is flat enough to drive inflation without the need for trapping effects. For a given choice of parameters one should verify that this classical potential dominates over the quantum corrections from particle production.

5.10.3 A Supersymmetric Model

Another microscopic realization of multiple bursts of particle production and IR cascading during inflation which does not rely on string theory can be obtained from the so-called “distributed mass” model derived in [259] with warm inflation [256] in mind, however, the theory works equally well for our scenario. This model is based on $\mathcal{N} = 1$ global SUSY and allows for the inclusion of multiple points along the inflationary trajectory where both scalar degrees of freedom and also their associated fermion superpartners become massless. The distribution of features in this set-up is essentially arbitrary.

5.11 Conclusions for the Observational Part

We have studied the observational constraints on models with particle production during inflation. We have focused on the simple prototype model (5.1) for each burst of particle production, however, we expect that our qualitative results will apply also to more complicated models (for example with gauged interactions or fermion iso-inflaton fields) and perhaps also to the case of inflationary phase transitions. We find no evidence for a detection of the features associated with particle production and IR cascading, however, it is interesting to note that rather large localized features are still compatible with the data. Our results differ significantly from previous studies as a result of a more realistic treatment of the cosmological perturbations in models with particle production. The

bounds we have derived on g^2 will play a crucial role in assessing the detectability of the non-Gaussianity produced by particle production and IR cascading.

We have also discussed the implications of our results for popular brane/axion monodromy string theory inflation models. Successful reheating in these constructions may require the inclusion of spectator branes which collide with the mobile D4-brane during inflation and hence we expect CMB features to be a fairly generic prediction. We have shown that brane/axion monodromy models predict a distribution of bump-like features which are evenly spaced in $\ln k$ over the observable range of scales. In the case of axion monodromy this multiple-bump spectral distortion is complimentary to the oscillatory features discussed in [258]. We have also estimated the magnitude of these bump-like features in terms of model parameters.

One motivation for the present study was to determine the extent to which microscopically realistic models such as (5.1) can reproduce the localized “glitches” in the power spectrum that have been detected (albeit with marginal significance) by several previous studies. These anomalies can be classified as follows:

1. *Localized power excesses:*

In both [248] and [263] power spectra with localized spikes were studied and in both cases marginal evidence was found for a detection of such features. In [202] a non-parametric reconstruction of the power spectrum was performed and the result is marginally consistent with a power law everywhere, however, several localized spikes are evident in the reconstruction.

Localized excesses are naturally obtained in our model (5.1). Sadly, however, we did not find that our model fits the data significantly better than the simplest slow roll inflation scenario. This does not necessarily imply a disagreement with [248, 263] since we use a different shaped feature and different data sets. Indeed, when the authors of [263] repeat their analysis using the WMAP 5-year data they do not obtain a detection, consistent with our findings.

2. *Localized power deficits:*

In [204] the Richardson-Lucy deconvolution algorithm was used to perform a non-parametric reconstruction of the primordial power spectrum which displayed a prominent IR cut-off near the horizon. In [203] a similar analysis was performed and the reconstructed power spectrum displays a localized dip in power near $k \sim 0.002 \text{ Mpc}^{-1}$.

Localized deficits *can* be produced by our model (5.11) but only in a rather contrived way. Hence, we have not focused on such features in section 5.9.

3. *Damped oscillations:*

In [251, 205, 260, 254] power spectra with superimposed ringing patterns were studied. Such features provide a marginally improved fit over the simplest power-law model.

As we have discussed in the introduction, damped oscillatory “ringing” features are not predicted by inflationary particle production. Nor is it clear if such features are predicted by models with phase transitions. (Of course damped oscillations *can* be obtained from a toy model with a step in $V(\phi)$. However, it may be difficult to obtain such a potential from realistic micro-physics; generically one expects that any sharp features in $V(\phi)$ will be smoothed out by quantum corrections.)

Finally, let us note that features of the type studied here will lead to other observables beyond the distortion of the primordial power spectrum. In particular, bumps in $P(k)$ will lead to features in the tensor spectrum (resulting from the sourcing of gravitational waves by scalar fluctuations at second order in perturbation theory) and also, possibly, black hole production. In [292, 293] these effects were estimated assuming a power spectrum which is qualitatively similar to ours. As discussed in [6], inflationary particle production will also lead to potentially large localized non-Gaussian features in the bispectrum (and

higher order statistics) of the cosmological fluctuations. These non-Gaussianities will be discussed in detail in an upcoming work.

5.12 APPENDIX A: Analytical Theory of Re-scattering

In this appendix we develop an analytical theory of re-scattering which is in good agreement with the result of fully nonlinear lattice field theory simulations. As usual we split the inflaton field into a classical homogeneous component and quantum inhomogeneities as $\phi(t, \mathbf{x}) = \phi(t) + \delta\phi(t, \mathbf{x})$ such that $\langle\phi(t, \mathbf{x})\rangle = \phi(t)$ and we further suppose that $\langle\chi(t, \mathbf{x})\rangle = 0$. Since IR cascading occurs within a single e-folding we can safely neglect the expansion of the universe. However, there is no obstruction to consistently including this effect.

At leading order the physics of re-scattering is described by equation (5.5), which corresponds to the diagram in Fig. 5.7. There is a correction to (5.5) corresponding to a diagram where two $\delta\phi$ particles interact with two χ particles, however, this effect is sub-leading [238]. It is understood that one must subtract from (5.5) the expectation value of the right-hand-side in order to consistently define the quantum operators $\delta\phi$ such that $\langle\delta\phi\rangle = \langle\chi\rangle = 0$. Subtracting off this expectation value is equivalent to only considering connected diagrams when we compute correlation functions.

5.12.1 Production of χ -Particles

To solve equation (5.5) we first require explicit expressions for the background field $\phi(t)$ and the wavefunction $\chi(t, \mathbf{x})$. Let us choose the origin of time so that $\phi = \phi_0$ at $t = 0$. Near the moment of particle production we can expand $\phi(t) - \phi_0 \cong \dot{\phi}_0 t$. The interaction term in (5.1) induces a mass for the χ -field

$$m_\chi^2 = g^2 [\phi(t) - \phi_0]^2 \cong g^2 \dot{\phi}_0^2 t^2 \equiv k_\star^4 t^2 \quad (5.30)$$

which vanishes at $t = 0$. At this moment particles will be copiously produced by quantum effects.

The mode functions $\chi_k(t)$ obey the following equation

$$\ddot{\chi}_k(t) + \omega_k^2(t)\chi_k(t) = 0 \quad (5.31)$$

where the time-dependent frequency is

$$\omega_k(t) = \sqrt{k^2 + m_\chi^2} = \sqrt{k^2 + k_\star^2(k_\star t)^2} \quad (5.32)$$

The theory of equation (5.31) is well-studied in the literature [238, 234]. As long as the frequency (5.32) varies adiabatically $|\dot{\omega}_k|/\omega_k^2 \ll 1$ the modes of χ will not be excited and are well described by the adiabatic solution $\chi_k(t) = f_k(t)$ where we have defined

$$f_k(t) \equiv \frac{1}{\sqrt{2\omega_k(t)}} \exp \left[-i \int^t dt' \omega_k(t') \right] \quad (5.33)$$

However, very close to $t = 0$, roughly within the interval $-k_\star^{-1} < t < +k_\star^{-1}$, the parameter $|\dot{\omega}_k|/\omega_k^2$ can become order unity or larger for low momenta $k \lesssim k_\star$ and χ_k modes within this band will be produced. The general solution of (5.31) can be written in terms of the adiabatic modes (5.33) and the time-dependent Bogoliubov coefficients as

$$\chi_k(t) = \alpha_k(t)f_k(t) + \beta_k(t)f_k(t)^\star \quad (5.34)$$

where the Bogoliubov coefficients obey a set of coupled ordinary differential equations with initial conditions $|\alpha_k(0^-)| = 1$, $\beta_k(0^-) = 0$. Near $t = 0$ the adiabaticity condition is violated and β_k grows rapidly away from zero as a step-like function. Very shortly after this burst of particle production the frequency again varies adiabatically and α_k , β_k become constant, taking the following values [238]:

$$\alpha_k(t > 0) = \sqrt{1 + n_k} \quad (5.35)$$

$$\beta_k(t > 0) = \sqrt{n_k} e^{i\delta_k} \quad (5.36)$$

where the physical occupation number is defined by (5.4). The phase δ_k has been computed analytically in [237] and depends nontrivially on k . However, since most of the

particle production occurs for momenta $k \lesssim k_*$ it is an excellent approximation to use the simple result $e^{i\delta_k} \cong -i$. (We have verified that changing the relative phase will at most alter factors order unity in the final results.)

We are now in a position to write out the solution for the χ_k modes in the outgoing adiabatic regime $t \gtrsim k_*^{-1}$. Since most of our interest is in IR modes with $k \lesssim k_*$ it is a good approximation to expand the frequency (5.32) as $\omega_k(t) \cong k_*(k_*t)$. Using the equations (5.35) and (5.36) we can write the solution (5.34) in the region of interest as

$$\chi_k(t) \cong \sqrt{1+n_k} \frac{e^{-i(k_*t)^2/2}}{k_*\sqrt{2t}} - i\sqrt{n_k} \frac{e^{+i(k_*t)^2/2}}{k_*\sqrt{2t}} \quad (5.37)$$

5.12.2 Equations for Re-scattering

Having reviewed the solutions for $\phi(t)$ and $\chi_k(t)$ we now turn our attention to solving (5.5). Let us first briefly discuss our conventions for fourier transforms and mode functions. We write the q-number valued fourier transform of χ as

$$\chi(t, \mathbf{x}) = \int \frac{d^3k'}{(2\pi)^{3/2}} e^{i\mathbf{k}\cdot\mathbf{x}} \xi_{\mathbf{k}}^\chi(t) \quad (5.38)$$

Because χ is Gaussian we can expand $\xi_{\mathbf{k}}^\chi$ into c-number mode functions χ_k (discussed above) and annihilation/creation operators $a_{\mathbf{k}}, a_{\mathbf{k}}^\dagger$ as

$$\xi_{\mathbf{k}}^\chi(t) = a_{\mathbf{k}} \chi_k(t) + a_{-\mathbf{k}}^\dagger \chi_k^*(t) \quad (5.39)$$

In the theory of preheating/moduli trapping without re-scattering the distinction between q-number fourier transform and c-number mode functions is not important because both obey the same equation of motion (equation (5.31) in the case at hand). However, once re-scattering is taken into account this distinction is crucial. To see why, note that the solution $\delta\phi$ of equation (5.5) will not be Gaussian and hence will not admit an expansion of the form (5.39).

Finally, we return to the equation for re-scattering, eqn. (5.5). We can solve for the q-number fourier transform of $\delta\phi$ (defined analogously to (5.38)) using the retarded Green

function

$$\begin{aligned} \xi_{\mathbf{k}}^{\phi}(t) &= \frac{g^2 \dot{\phi}}{(2\pi)^{3/2} \Omega_k} \int_0^t dt' t' \sin[\Omega_k(t-t')] \\ &\quad \times \int d^3 k' \xi_{\mathbf{k}-\mathbf{k}'}^{\chi}(t') \xi_{\mathbf{k}'}^{\chi}(t') \end{aligned} \quad (5.40)$$

where we have introduced the notations $\Omega_k = \sqrt{k^2 + m^2}$ for the $\delta\phi$ -particle frequency and $m^2 = V_{,\phi\phi}$ for the effective $\delta\phi$ mass. Carefully carrying out the Wick contractions yields

$$\begin{aligned} \langle \xi_{\mathbf{k}_1}^{\phi}(t) \xi_{\mathbf{k}_2}^{\phi}(t) \rangle &= \frac{2g^4 \dot{\phi}^2}{(2\pi)^3 \Omega_{k_1}^2} \delta^{(3)}(\mathbf{k}_1 + \mathbf{k}_2) \\ &\quad \times \int dt' dt'' t' t'' \sin[\Omega_{k_1}(t-t')] \sin[\Omega_{k_1}(t-t'')] \\ &\quad \times \int d^3 k' \chi_{\mathbf{k}_1-\mathbf{k}'}(t') \chi_{\mathbf{k}_1-\mathbf{k}'}^*(t'') \chi_{\mathbf{k}'}(t') \chi_{\mathbf{k}'}^*(t'') \end{aligned} \quad (5.41)$$

where the χ -particle mode functions χ_k are defined by (5.39). Defining the power spectrum in terms of the two-point function in the usual manner

$$\langle 0 | \xi_{\mathbf{k}}^{\phi}(t) \xi_{\mathbf{k}'}^{\phi}(t) | 0 \rangle \equiv \delta^{(3)}(\mathbf{k} + \mathbf{k}') \frac{2\pi^2}{k^3} P_{\phi} \quad (5.42)$$

we can extract the power in re-scattered ϕ modes.

Alternatively one could compute the power spectrum of re-scattered inflaton modes using the Schwinger's "in-in" formalism which was implemented to compute cosmological perturbations by Weinberg in [294]. We have verified that the tree level contribution to P_{ϕ} obtained using this formalism reproduces our result (5.41). Our approach is analogous to computing the cosmological perturbation from the field equations using the Seery et al. approach [295]. The consistency of this method with the in-in approach at tree level is in accordance with the general theorem of [296].

5.12.3 Renormalization

To compute the spectrum of re-scattered $\delta\phi$ -particles we simply need to insert the solution (5.37) into (5.41) and evaluate the integrals. However, there is one subtlety. The resulting

power spectrum is formally infinite, moreover, it contains the effect of both particle production as well as vacuum fluctuations of the χ field. We are only interested in the re-scattered $\delta\phi$ which are due to particle production, thus, we need to subtract off the contribution due to nonlinear $\delta\phi$ production by χ vacuum fluctuations.

To properly define the two-point function of $\delta\phi$ we need to renormalize the four-point function of the Gaussian field χ . As a warm-up, let us first consider how to renormalize the two point function of the Gaussian field χ . We use the following scheme

$$\langle \xi_{k_1}^\chi(t_1) \xi_{k_2}^\chi(t_2) \rangle_{\text{ren}} = \langle \xi_{k_1}^\chi(t_1) \xi_{k_2}^\chi(t_2) \rangle - \langle \xi_{k_1}^\chi(t_1) \xi_{k_2}^\chi(t_2) \rangle_{\text{in}} \quad (5.43)$$

where $\langle \xi_{k_1}^\chi(t_1) \xi_{k_2}^\chi(t_2) \rangle_{\text{in}}$ is the contribution in the absence of particle production, computed by simply taking the solution (5.34) with $\alpha_k = 1$, $\beta_k = 0$. More explicitly, for the case at hand, we have

$$\begin{aligned} \langle \chi^2(t, \mathbf{x}) \rangle_{\text{ren}} &= \int \frac{d^3k}{(2\pi)^3} \left[|\chi_k^2(t)| - \frac{1}{2\omega_k(t)} \right] \\ &\equiv \langle \chi^2(t, \mathbf{x}) \rangle - \delta_M \end{aligned} \quad (5.44)$$

where δ_M is the contribution from the Coleman-Weinberg potential. This proves that our prescription reproduces the one used in [234].

Having established a scheme for renormalizing the two-point function of the Gaussian field χ it is straightforward to consider higher order correlation functions. We simply rewrite the four point function as a product of two-point functions using Wick's theorem. Then each Wick contraction is renormalized as above. Applying this prescription to (5.41) amounts to

$$\begin{aligned} \langle \xi_{k_1}^\phi(t) \xi_{k_2}^\phi(t) \rangle_{\text{ren}} &= \frac{2g^4 \dot{\phi}^2}{(2\pi)^3} \frac{1}{\Omega_{k_1}^2} \delta^{(3)}(\mathbf{k}_1 + \mathbf{k}_2) \\ &\times \int dt' dt'' t' t'' \sin[\Omega_{k_1}(t-t')] \sin[\Omega_{k_1}(t-t'')] \\ &\times \int d^3k' [\chi_{k_1-k'}(t') \chi_{k_1-k'}^*(t'') - f_{k_1-k'}(t') f_{k_1-k'}^*(t'')] \\ &\times [\chi_{k'}(t') \chi_{k'}^*(t'') - f_{k'}(t') f_{k'}^*(t'')], \end{aligned} \quad (5.45)$$

where $f_k(t)$ are the adiabatic modes defined in (5.33).

5.12.4 Spectrum of Re-scattered Modes

Let us now proceed to compute analytically the renormalized spectrum P_ϕ of re-scattered inflaton modes by inserting the solutions (5.37) and (5.33) into (5.45) and carrying out the integrations. The computation is tedious but straightforward since the time and phase space integrals factorize. We have relegated the technical details to appendix B and here we simply state the final result:

$$\begin{aligned}
P_\phi = & \frac{g^2}{16\pi^5} \frac{k^3 k_\star}{k^2 + m^2} \left\{ \frac{e^{-\pi k^2/(2k_\star^2)}}{2\sqrt{2}} \left(\frac{\pi}{4} |F|^2 + \frac{k_\star^2}{\Omega_k^2} [1 - \cos(\Omega_k t)]^2 \right) \right. \\
& + \left(e^{-\pi k^2/(4k_\star^2)} + \frac{1}{2\sqrt{2}} e^{-3\pi k^2/(8k_\star^2)} \right) \left[-\frac{\pi}{4} \text{Re} \left(e^{2i\Omega_k t - i\Omega_k^2/(2k_\star^2) - i\pi/2} F \right) + \frac{k_\star^2}{\Omega_k^2} [1 - \cos(\Omega_k t)]^2 \right] \\
& \left. + \left[\frac{4\sqrt{2}}{3\sqrt{3}} e^{-\frac{\pi k^2}{3k_\star^2}} + \frac{2\sqrt{2}}{5\sqrt{5}} e^{-\frac{3\pi k^2}{5k_\star^2}} \right] \frac{\sqrt{\pi} k_\star}{\Omega_k} [1 - \cos(\Omega_k t)] \text{Im} \left[e^{i\Omega_k t - i\Omega_k^2/(4k_\star^2) - i\pi/4} F \right] \right\} \quad (5.46)
\end{aligned}$$

Equation (5.46) is the main result of this appendix. The ‘‘form factor’’ $F(k, t)$ is given explicitly in appendix B.

5.13 APPENDIX B: Detailed Computation of P_ϕ

In this appendix we discuss in some detail the technical details associated with the computation of P_ϕ . Inserting the solutions (5.37) and (5.33) into (5.45) we find the result

$$\begin{aligned}
P_\phi = & \frac{g^2}{8\pi^5} \frac{k^3}{k^2 + m^2} \left\{ \int d^3 k' n_{k-k'} n_{k'} \int dt' dt'' \sin [\Omega_k(t-t')] \sin [\Omega_k(t-t'')] \cos^2 \left[\frac{(k_\star t')^2}{2} - \frac{(k_\star t'')^2}{2} \right] \right. \\
& + \int d^3 k' \sqrt{n_{k-k'} n_{k'}} \sqrt{1+n_{k-k'}} \sqrt{1+n_{k'}} \\
& \times \int dt' dt'' \sin [\Omega_k(t-t')] \sin [\Omega_k(t-t'')] \sin^2 \left[\frac{(k_\star t')^2}{2} + \frac{(k_\star t'')^2}{2} \right] \\
& + \int d^3 k' \left[n_{k-k'} \sqrt{n_{k'}} \sqrt{1+n_{k'}} + n_{k'} \sqrt{n_{k-k'}} \sqrt{1+n_{k-k'}} \right] \\
& \left. \times \int dt' dt'' \sin [\Omega_k(t-t')] \sin [\Omega_k(t-t'')] \sin \left[\frac{(k_\star t')^2}{2} + \frac{(k_\star t'')^2}{2} \right] \cos \left[\frac{(k_\star t')^2}{2} - \frac{(k_\star t'')^2}{2} \right] \right\} \quad (5.47)
\end{aligned}$$

We consider the time and phase space integrations separately.

5.13.1 Time Integrals

All the time integrals appearing in (5.47) can be written in terms of two functions which we call I_1 , I_2 . These involves are defined as

$$I_1(k, t) = \int_0^t dt' \sin [\Omega_k(t - t')] e^{i(k_\star t')^2} \quad (5.48)$$

$$I_2(k, t) = \int_0^t dt' \sin [\Omega_k(t - t')] \quad (5.49)$$

First consider I_1 . It is useful to factorize the answer into the product of the stationary phase result (valid for $k_\star t \gg \Omega_k/(2k_\star) \gg 1$) and a “form factor” $F(k, t)$ as follows:

$$I_1(k, t) = \frac{\sqrt{\pi}}{2k_\star} e^{i\Omega_k t - i\Omega_k^2/(4k_\star^2) - i\pi/4} F(k, t) \quad (5.50)$$

$$F(k, t) = \frac{1}{2} \left[(1 + e^{-2i\Omega_k t}) \operatorname{erf} \left(\frac{e^{-i\pi/4} \Omega_k}{2 k_\star} \right) - \operatorname{erf} \left(\frac{e^{-i\pi/4}}{2} \left(\frac{\Omega_k}{k_\star} - 2k_\star t \right) \right) - e^{-2i\Omega_k t} \operatorname{erf} \left(\frac{e^{-i\pi/4}}{2} \left(\frac{\Omega_k}{k_\star} + 2k_\star t \right) \right) \right] \quad (5.51)$$

The form factor $F(k, t)$ has a complicated structure. We have illustrated the qualitative behaviour of this function in Fig. 5.13 taking $\Omega_k/k_\star = 5$ for illustration.

Next, consider the characteristic integral I_2 , eqn. (5.52). This integration is trivial:

$$I_2(k, t) = \frac{1}{\Omega_k} [1 - \cos(\Omega_k t)] \quad (5.52)$$

Now we will show that all the time integrals appearing in (5.47) can be reduced to combinations of the characteristic functions I_1 and I_2 . First, consider the first line of

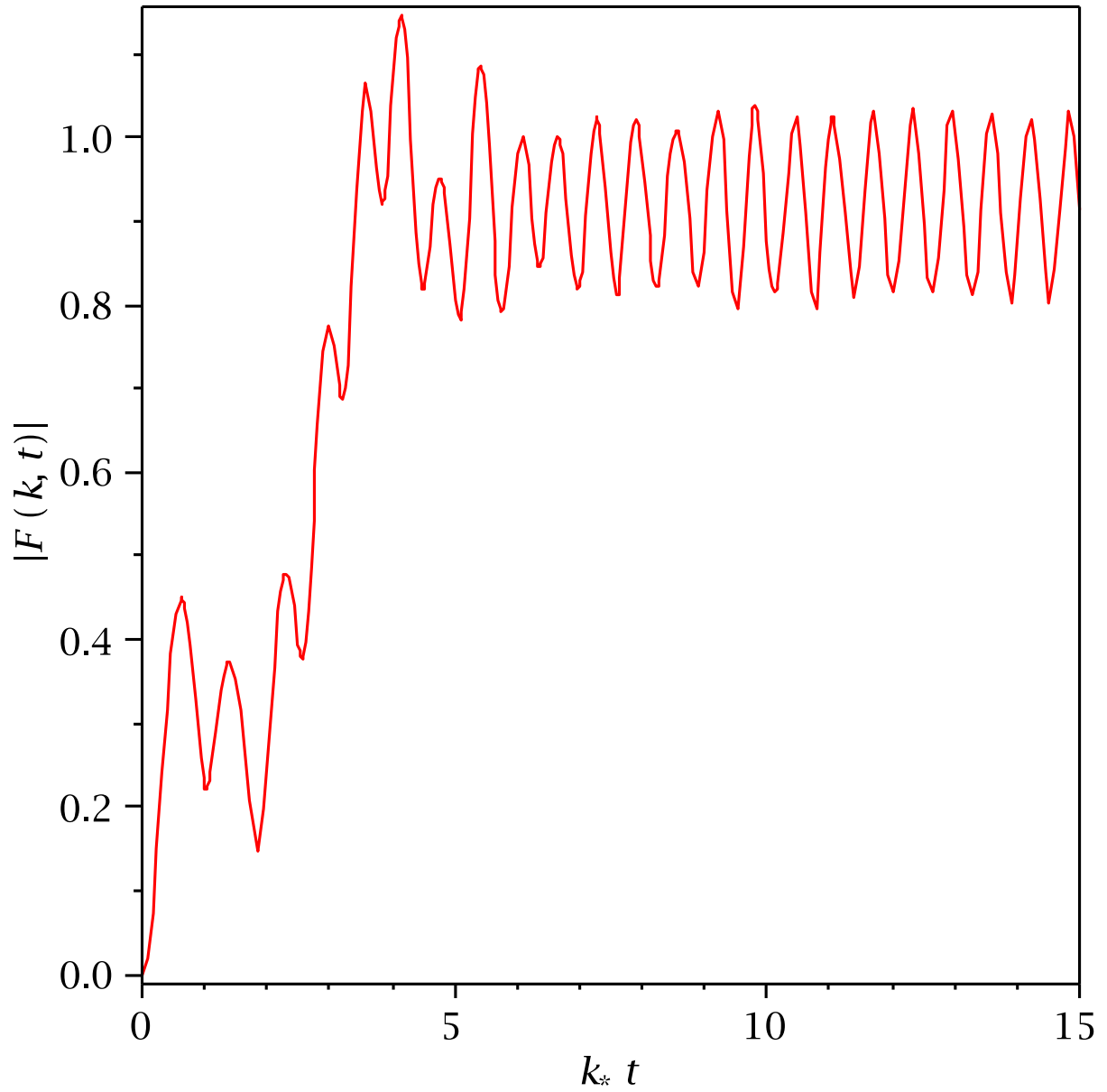


Figure 5.13: The behaviour of the function $F(k, t)$ as a function of t . For illustration we have set $\Omega_k = 5k_*$.

(5.47) where the following integral appears:

$$\begin{aligned}
& \int dt' dt'' \sin [\Omega_k(t-t')] \sin [\Omega_k(t-t'')] \\
& \quad \times \cos^2 \left[\frac{(k_\star t')^2}{2} - \frac{(k_\star t'')^2}{2} \right] \\
& = \frac{|I_1(k, t)|^2}{2} + \frac{I_2(k, t)^2}{2} \\
& = \frac{\pi}{8k_\star^2} |F(k, t)|^2 + \frac{1}{2\Omega_k^2} [1 - \cos(\Omega_k t)]^2
\end{aligned} \tag{5.53}$$

Next, consider the time integration on the second line of (5.47):

$$\begin{aligned}
& \int dt' dt'' \sin [\Omega_k(t-t')] \sin [\Omega_k(t-t'')] \\
& \quad \times \sin^2 \left[\frac{(k_\star t')^2}{2} + \frac{(k_\star t'')^2}{2} \right] \\
& = -\frac{\text{Re} [I_1(k, t)^2]}{2} + \frac{I_2(k, t)^2}{2} \\
& = -\frac{\pi}{8k_\star^2} \text{Re} \left[e^{2i\Omega_k t - i\Omega_k^2/(2k_\star^2) - i\pi/2} F(k, t)^2 \right] \\
& \quad + \frac{1}{2\Omega_k^2} [1 - \cos(\Omega_k t)]^2
\end{aligned} \tag{5.54}$$

Finally, we consider the time integration on the third line of (5.47):

$$\begin{aligned}
& \int dt' dt'' \sin [\Omega_k(t-t')] \sin [\Omega_k(t-t'')] \\
& \quad \times \sin \left[\frac{(k_\star t')^2}{2} + \frac{(k_\star t'')^2}{2} \right] \cos \left[\frac{(k_\star t')^2}{2} - \frac{(k_\star t'')^2}{2} \right] \\
& = \text{Im} [I_1(k, t) I_2(k, t)] \\
& = \frac{\sqrt{\pi}}{2k_\star \Omega_k} [1 - \cos(\Omega_k t)] \text{Im} \left[e^{i\Omega_k t - i\Omega_k^2/(4k_\star^2) - i\pi/4} F(k, t) \right]
\end{aligned} \tag{5.55}$$

5.13.2 Phase Space Integrals

Throughout the calculation integrals of the following form appears frequently:

$$\begin{aligned}
& \int d^3 k' n_{k-k'}^a n_{k'}^b \\
& = \int d^3 k' \exp [-a\pi |\mathbf{k} - \mathbf{k}'|^2/k_\star^2] \exp [-b\pi |\mathbf{k}'|^2/k_\star^2] \\
& = \frac{k_\star^3}{(a+b)^{3/2}} \exp \left[-\frac{ab}{a+b} \frac{\pi k^2}{k_\star^2} \right]
\end{aligned} \tag{5.56}$$

This formula is valid when a, b are positive real numbers. Notice that this expression is symmetric under interchange of a and b .

The phase space integral in the first line of (5.47) is computed by a trivial application of the identity (5.56):

$$\int d^3k' n_{k-k'} n_{k'} = \frac{k_\star^3}{2\sqrt{2}} e^{-\pi k^2/(2k_\star^2)} \quad (5.57)$$

The remaining integrals cannot be obtained exactly in closed form because they contain terms like $\sqrt{1+n_{k'}}$ where the Gaussian factors appear under the square root. However, because $n_k \leq 1$ it turns out to be a very good approximation to replace $\sqrt{1+n_{k'}} \cong 1 + n_{k'}/2$. (We have checked numerically that the error induced is less than a few percent.) Let us now proceed in this manner. The phase space integral on the second line of (5.47) is:

$$\begin{aligned} & \int d^3k' \sqrt{n_{k-k'} n_{k'}} \sqrt{1+n_{k-k'}} \sqrt{1+n_{k'}} \\ & \cong \int d^3k' \left[n_{k-k'}^{1/2} n_{k'}^{1/2} + \frac{1}{2} n_{k-k'}^{3/2} n_{k'}^{1/2} + \frac{1}{2} n_{k-k'}^{1/2} n_{k'}^{3/2} \right] \\ & = k_\star^3 \left[\exp\left(-\frac{\pi k^2}{4k_\star^2}\right) + \frac{1}{2\sqrt{2}} \exp\left(-\frac{3\pi k^2}{8k_\star^2}\right) \right] \end{aligned} \quad (5.58)$$

Finally, consider the phase space integral on the third line of (5.47):

$$\begin{aligned} & \int d^3k' \left[n_{k-k'} \sqrt{n_{k'}} \sqrt{1+n_{k'}} + n_{k'} \sqrt{n_{k-k'}} \sqrt{1+n_{k-k'}} \right] \\ & \cong \int d^3k' \left[n_{k-k'}^{1/2} n_{k'}^{1/2} \right. \\ & \quad \left. + \frac{1}{2} n_{k-k'}^{3/2} n_{k'}^{1/2} + \frac{1}{2} n_{k'}^{3/2} n_{k-k'}^{1/2} \right] \\ & = k_\star^3 \left[\frac{4\sqrt{2}}{3\sqrt{3}} \exp\left(-\frac{\pi k^2}{3k_\star^2}\right) + \frac{2\sqrt{2}}{5\sqrt{5}} \exp\left(-\frac{3\pi k^2}{5k_\star^2}\right) \right] \end{aligned} \quad (5.59)$$

Assembling the various results presented in this appendix one arrives straightforwardly at the result (5.46).

Chapter 6

Preheating after Modular Inflation

6.1 Introduction

This chapter presents another topic in preheating. We study the preheating in a specific early-universe scenario – the Roulette inflation model [44]. This work was done in collaboration with my advisors and Dr. Neil Barnaby. My main contribution is that I calculated the Floquet exponent for this preheating model, and modified my “HLattice” code so that it can run lattice simulations for non-canonical scalar fields. The algorithms used in the publicly available codes DEFROST and LATTICEEASY are not stable for non-canonical scalar fields. In fact, most popular numerical algorithms are not stable for a non-canonical system. My code uses a symplectic-Runge-Kutta blended algorithm, i.e., it uses a 4-th order Runge-Kutta algorithm for the non-canonical operator in the Hamiltonian, and uses a symplectic algorithm for the global evolution. Unlike a pure high-order Runge-Kutta method that costs tremendous memory, which could slow down the simulation by orders of magnitude, my algorithm performs the Runge-Kutta integration locally (with no spatial gradient operator involved), hence does not cost additional memory.

Reheating at the endpoint of inflation is a crucial requirement for any successful

model. Depending on how inflation ends and how the inflaton interacts, the process of reheating – the creation of particles from the decaying inflaton and subsequent thermalization – can proceed differently. Examples are known of perturbative inflaton reheating [297], non-perturbative preheating [237, 238] (leading to excitations of both bosons and fermions [298, 299, 300]), and also reheating via string theory mechanisms such as intermediate Kaluza-Klein (KK) modes [301, 302], etc.

In the last several years there has been significant progress in string theory related to the realization of realistic compactifications with stabilized moduli [303, 304, 305, 306]. This progress has stimulated the development of a new generation of inflationary models based on such stabilized string theory constructions; see Refs. [46, 307, 308] for reviews. Among the various possible string theory models of inflation, one can distinguish different classes depending on the origin of the inflaton. Modular inflation deals with the inflaton living in the closed string sector. On the other hand, brane inflation [41, 309] deals with that in the open string sector. In the first case it is sufficient to identify one or more moduli fields which are already present in the stabilized compactification scheme and which are displaced from the minimum of the potential. In the second case, on the top of the setting required by the stabilized compactification, the inflaton field must be engineered by including also probe D -branes. The multitude of possible inflationary scenarios in string theory may, at first glance, seem confused and far from unique. However, this multitude may all in fact be realized if the paradigm of the string theory landscape is adopted [310], leading to a picture where different types of inflation may proceed in different regions of the landscape. Indeed, even simple field theory models may admit a similar landscape of inflationary possibilities.

String theory inflation models offer a unique opportunity to study (p)reheating in an ultra-violet (UV) complete setting where it is conceivable to determine all couplings between the inflaton and the standard model (SM) sector from first principles, rather than simply assuming some *ad hoc* couplings on a phenomenological basis. Moreover, because

post-inflationary dynamics are extremely sensitive to the details of these couplings, it follows that any observables generated during preheating (such as non-Gaussianities [231, 56] or gravitational waves [311, 312]) have the potential to provide a rare observational window into stringy physics.

Reheating in brane inflation was studied in detail in a number of papers [301, 302, 313, 314, 315, 316]. One of the most interesting realizations of brane inflation is the “warped” KKLMMT model [288], constructed in the context of the KKLT stabilized vacuum [303]. The endpoint of inflation in this scenario is the annihilation of a brane-antibrane pair. (The inhomogeneous dynamics of this annihilation have been discussed in Refs. [317, 318].) The details of reheating in this model are very complicated and involve several stages of energy cascading, first from the $D - \bar{D}$ pair annihilation into closed string modes, next the closed string loops decay to excitations of Kaluza-Klein (KK) modes which finally decay to excitations of open string modes on the standard model (SM) brane(s). An adequate description of this process requires input from string theory.

Reheating after closed string inflation, on the other hand, is usually assumed to occur in the regime where ordinary quantum field theory (QFT) is applicable. Here we investigate in detail the theory of reheating after closed string modular inflation [52, 44] models. We will focus our attention in particular on the scenario of Kähler moduli [52] or Roulette [44] inflation models based on the Large Volume Compactification scheme of [304, 305, 306]. In this model the role of the inflaton is played by a Kähler modulus, τ , (corresponding to the volume of a 4-cycle of the internal Calabi Yau manifold) and also by its axionic partner, θ . However, some of our results may be applicable also in other modular inflation models, such as racetrack inflation [282, 319] based on the KKLT compactification [303].

We find that reheating after modular inflation can be quite multifarious and may proceed through a variety of different channels (including both perturbative and nonper-

turbative effects and also intrinsically stringy physics). The precise identification of these decay channels may depend on model building details, such as the location of the SM in the Calabi Yau (CY) compactification manifold. In all cases, however, the initial stages of the decay of the inflaton in modular inflation proceed via very strong nonperturbative preheating decay channels. This is due to the specific shape of the effective inflaton potential $V(\tau)$, which is very nonlinear and which has a sharp minimum. Preheating proceeds through a combination of both tachyonic (spinodal) instability and broad-band parametric resonance and leads to the copious production of $\delta\tau$ inhomogeneities (particles). Within 2-3 oscillations of the background field, nonlinear backreaction effects become important and the homogeneous condensate is completely destroyed. In fact, this is perhaps the most violent known example of preheating after inflation!

In order to understand the full dynamics of reheating in modular inflation we must also identify the decay channels of the inflaton into the visible SM sector. In the case where the SM is incorporated on a D7 brane wrapped on the inflationary 4-cycle, the Kähler modulus τ decays via a direct coupling to brane-bound SM gauge bosons. The initial stages of this decay are nonperturbative and involve parametric resonance of the gauge fields while the later stages involve perturbative decays. We also consider interactions between the inflaton τ and brane-bound MSSM fermions such as the Higgsino and gaugino.

On the other hand, the D7 brane construction described above may result in dangerous g_s -corrections to the inflaton potential which violate the smallness of the slow roll parameters and spoil inflation [320]. Therefore, it may be desirable to exclude such a wrapping. In this case the SM can still be localized on a D7 wrapping some non-inflationary 4-cycle of the CY compactification. Such a configuration forbids any direct coupling between the inflationary sector and the SM sector, thus complicating the process of reheating. In this case the inflaton may still decay to SM states via a nontrivial mixing between the inflaton fluctuations and the fluctuations of the moduli associated

with the 4-cycle that the SM D7 wraps. The latter may couple directly to brane-bound SM states. Since the intermediate stages of the inflaton decay involve bulk states, the mixing proceeds via Planck suppressed operators.

Finally, we have identified another reheating mechanism which involves distinctly stringy physics and which does not require a D7 brane to wrap the inflationary 4-cycle. An important model parameter is the value of the inflationary 4-cycles volume, τ , at the stable minimum of the effective potential, τ_m . If $\tau_m > l_s$ then the supergravity description remains valid during both inflation and reheating [52]. In this case, reheating treatment is purely field-theoretical and involves calculating the couplings between the inflaton and standard model degrees of freedom, as described above. However, as was noted in [44], although the choice of τ_m does not alter the field-theoretical treatment of inflation, it *does* crucially impact the dynamics of reheating.¹ If $\tau_{min} \leq l_s$ then the supergravity approximation is valid *only* during the slow roll (large τ) regime. At the small values of τ relevant for (p)reheating stringy degrees of freedom, in addition to the supergravity ones, will be excited. In this case the physics of reheating will change drastically from the naive picture. One expects, along the lines of [301, 302], that when τ becomes of order the string scale, light winding modes are created, and these subsequently decay into free closed strings which cascade into KK excitations. These intermediate KK modes can, finally, decay into SM states on the brane as in [301, 302]. One can also think about the shrinking 4-cycle as an enhanced symmetry point, associated with the quantum production of light degrees of freedom [234].

This chapter is organized as follows. In section 6.2 we review the large volume compactification of type IIB string theory and also discuss Kähler Moduli/Roulette inflation models embedded within that setting. In section 6.3 we discuss the decay of the inflaton

¹A simple field theoretic analogue of this scenario is a toy model where the inflaton potential is extremely flat (to provide sufficient inflation) with an extremely steep minimum. For this toy example ordinary QFT is valid during the inflationary stage. However, in the limit that the mass at the minimum approaches m_s the field theoretical treatment of reheating breaks down and one must instead turn to a stringy description.

in modular inflation via self interactions, showing that fluctuations of the Kähler modulus τ are produced copiously at the end of inflation via strong preheating effects. We study this explosive particle production first by solving the linearized equations of motion for the τ , θ fluctuations and next by performing fully nonlinear lattice field theory simulations. In section 6.4 we discuss the decay of the inflaton into SM particles (both perturbative and nonperturbative) for the scenario where the SM lives on a D7 wrapping the inflationary 4-cycle. In section 6.5 we discuss the decay of the inflaton in SM particles for the case where the SM D7 instead wraps some non-inflationary 4-cycle of the CY. In section 6.6 we propose another mechanism for reheating in modular inflation which involves distinctly stringy excitations. Finally, in section 6.7, we summarize our results and conclude. For completeness we will include here most of the contents that has already been published in [57]. Please cite our original paper for the use of these contents.

6.2 Kähler Moduli/Roulette Inflation in the Large Volume Compactification

In this section we briefly review recent progress in constructing stabilized “large volume” compactifications in type IIB string theory [304, 305, 306] and also describe recent efforts to embed inflation into such constructions [52, 44] with the role of the inflaton played by the Kähler modulus of the internal CY manifold and its axionic partner.

6.2.1 Large Volume Compactification

Let us first discuss the “large-volume” moduli stabilization mechanism of [304, 305, 306]. In this scenario the Kähler moduli of the CY manifold are stabilized by both perturbative and non-perturbative effects. As argued in [304, 305, 306], a minimum of the moduli

potential in the corresponding effective 4d theory exists for a large class of models.ⁱⁱ An effective 4d $\mathcal{N} = 1$ supergravity is completely specified by a Kähler potential, superpotential and gauge kinetic function. In the scalar field sector of the theory the action is

$$S_{\mathcal{N}=1} = \int d^4x \sqrt{-g} \left[\frac{M_P^2}{2} \mathcal{R} - \mathcal{K}_{,i\bar{j}} D_\mu \phi^i D^\mu \bar{\phi}^{\bar{j}} - V(\phi, \bar{\phi}) \right], \quad (6.1)$$

where

$$V(\phi, \bar{\phi}) = e^{\mathcal{K}/M_P^2} \left(\mathcal{K}^{i\bar{j}} D_i \hat{W} D_{\bar{j}} \bar{\hat{W}} - \frac{3}{M_P^2} \hat{W} \bar{\hat{W}} \right) + \text{D-terms}. \quad (6.2)$$

Here \mathcal{K} and \hat{W} are the Kähler potential and the superpotential respectively, \mathcal{R} is the Ricci scalar and ϕ^i represent all scalar moduli.

The α'^3 -corrected Kähler potential [321], after stabilization of the complex structure and dilaton, is

$$\frac{\mathcal{K}}{M_P^2} = -2 \ln \left(\mathcal{V} + \frac{\xi}{2} \right) + \ln(g_s) + \mathcal{K}_{cs}, \quad (6.3)$$

Here \mathcal{K}_{cs} is some constant, \mathcal{V} is the volume of the CY manifold M in units of the string length $l_s = 2\pi\sqrt{\alpha'}$ and g_s is the string coupling. The second term ξ in the logarithm represents the α' -corrections with $\xi = -\frac{\zeta(3)\chi(M)}{2(2\pi)^3}$ proportional to the Euler characteristic $\chi(M)$ of the manifold M . The Kähler metric appearing in (6.1) was computed explicitly in [44].

The superpotential depends explicitly upon the Kähler moduli T_i when non-perturbative corrections are included

$$\hat{W} = \frac{g_s^{\frac{3}{2}} M_P^3}{\sqrt{4\pi}} \left(W_0 + \sum_{i=1}^{h^{1,1}} A_i e^{-a_i T_i} \right). \quad (6.4)$$

Here W_0 is the tree level flux-induced superpotential. The exponential terms $A_i e^{-a_i T_i}$ arise due to non-perturbative (instanton) effects such as a gaugino condensate on the world-volume of a $D7$ brane, or Euclidean $D3$ brane instanton (see *e.g.* [303, 304, 305,

ⁱⁱThe only restrictions being the existence of at least one blow-up mode resolving a point-like singularity and also the requirement that $h^{1,2} > h^{1,1} > 1$, where $h^{1,2}, h^{1,1}$ are the Hodge numbers of the CY.

306]). The Kähler moduli are complex,

$$T_i = \tau_i + i\theta_i, \quad (6.5)$$

with τ_i the volume of the i -th 4-cycle and θ_i is associated axionic partner, arising from the Ramond-Ramond 4-form C_4 . In (6.4) the constants A_i , a_i depend upon the specific nature of the dominant non-perturbative mechanism. For example, $a_i = \frac{2\pi}{g_s}$ for Euclidean D3-brane instantons.

In the simplest cases (such as $\mathbb{P}^4_{[1,1,1,6,9]}$) the volume \mathcal{V} can be written in terms of the τ_i as follows:

$$\mathcal{V} = \alpha \left(\tau_1^{3/2} - \sum_{i=2}^n \lambda_i \tau_i^{3/2} \right). \quad (6.6)$$

Here α and λ_i are positive constants depending on the particular model. For example, the two-Kähler model with the orientifold of $\mathbb{P}^4_{[1,1,1,6,9]}$ studied in [305, 306, 322] has $n = 2$, $\alpha = 1/9\sqrt{2}$ and $\lambda_2 = 1$.

The formula (6.6) suggests a “Swiss-cheese” picture of a CY, in which τ_1 describes the 4-cycle of maximal size and controls the overall size of the CY. This modulus may be arbitrarily large. On the other hand, τ_2, \dots, τ_n , are the blow-up cycles which control the size of the holes in the CY. These moduli cannot be larger than the overall size of the compactification manifold. This CY manifold is schematically illustrated in Fig. 6.1.

Including both leading perturbative and non-perturbative corrections one obtains a potential for the Kähler moduli which, in general, has two types of minima. The first type is the KKLT minima [303]. Relevant for the present study are the “large-volume” AdS minima studied in [304, 305, 306]. These minima exist in a broad class of models and at arbitrary values of parameters. An important characteristic feature of these models is that the stabilized volume of the internal manifold is exponentially large, $\mathcal{V}_m \sim \exp(a\tau_m)$ (here \mathcal{V}_m , τ_m denote the values of \mathcal{V} and τ_2 at the minimum of the potential), and can be $\mathcal{O}(10^5 - 10^{20})$ in string units. The relation between the Planck scale and string scale is

$$M_P^2 = \frac{4\pi\mathcal{V}_m}{g_s^2} m_s^2 \quad (6.7)$$

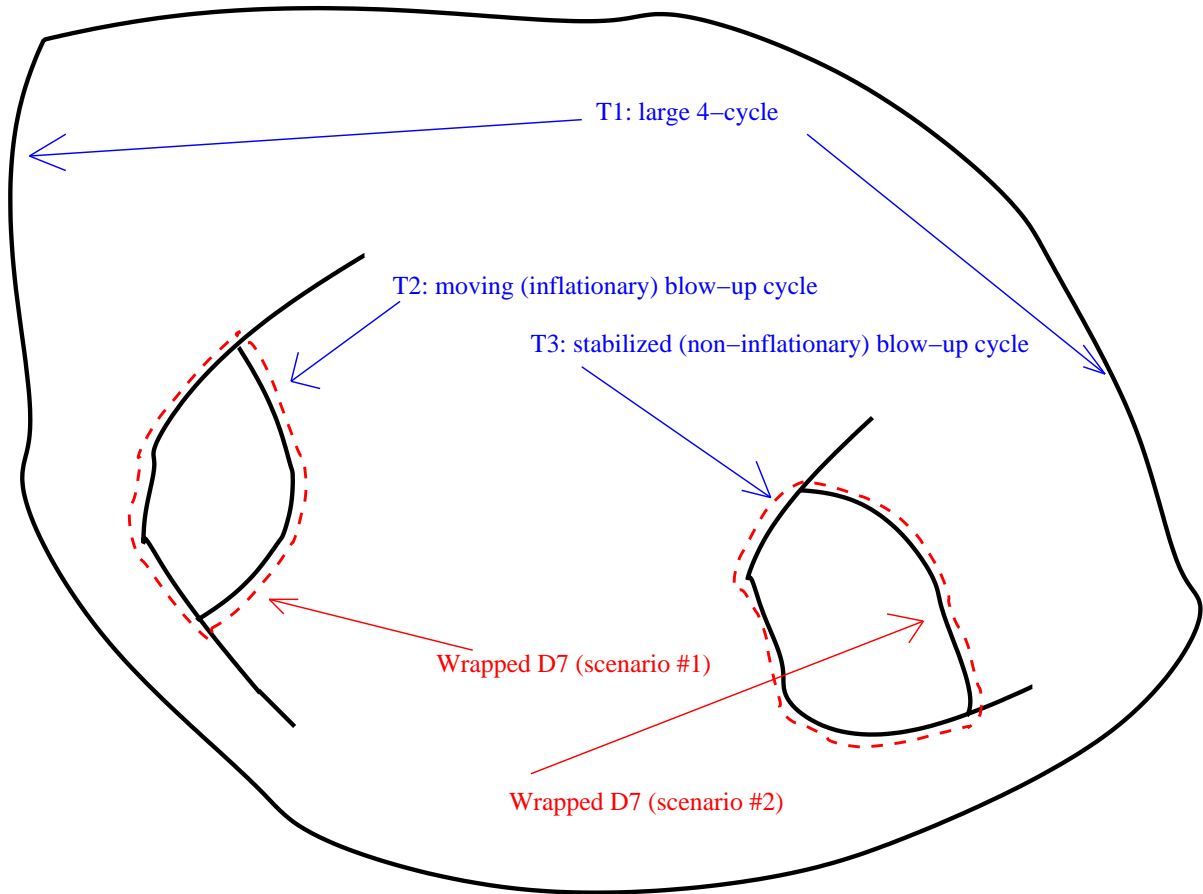


Figure 6.1: A cartoon of the large volume compactification manifold illustrating the ingredients relevant for Kähler moduli inflation and (p)reheating. The modulus $\tau_1 = \text{Re}(T_1)$ controls the overall size of the compactification while the moduli $\tau_i = \text{Re}(T_i)$ ($i \geq 2$) control the size of the blow-up 4-cycles (hole sizes). We have labelled τ_2 as the last 4-cycle to stabilize, and hence this modulus is associated with the final observable phase of inflation. The total volume τ_1 and other cycles (for example τ_3) are assumed to already be stabilized. In the text we consider two possible scenarios for the location of the SM: (i) a D7-brane wrapping the inflationary 4-cycle, τ_2 , and, (ii) a D7-brane wrapping the non-inflationary 4-cycle, τ_3 . We have illustrated these wrappings schematically.

Thus, these models can have m_s in the range between the GUT and TeV scale.

As argued in [305, 306], for generic values of the parameters W_0 , A_i , a_i one finds that $\tau_1 \gg \tau_i$ ($i \geq 2$) and $\mathcal{V} \gg 1$ at the minimum of the effective potential. In other words, the sizes of the holes are generically much smaller than the overall size of the CY.

An important consistency condition for the supergravity approximation to be valid is that the value of each τ_i at the minimum of the potential should be larger than a few. This criterion ensures that the geometrical sizes of the 4-cycles of the CY are all larger than the string scale. One expects any violation of this condition to be associated with the production of stringy (as opposed to field theoretic) degrees of freedom, such as winding modes. More on this later.

6.2.2 Roulette Inflation

Let us now consider inflation in the context of the large volume compactification described above [52, 44]. The scenario we have in mind is the following. Suppose all the moduli T_i are initially displaced from their minima. The dynamics will then drive the various fields T_i to roll towards their respective minima. For inflation, we focus on the last modulus $T_2 \equiv \tau + i\theta$ to reach its minimum so that τ, θ are still dynamical while all other moduli (in particular the total volume \mathcal{V}) are stabilized.ⁱⁱⁱ See Fig. 6.1 for a cartoon of this scenario. Note that in the Roulette inflation model *both* fields τ and θ play an important role in driving inflation. After having fixed all moduli T_i ($i \neq 2$) we find an effective potential for the inflaton fields τ, θ of the form

$$V(\tau, \theta) = \frac{g_s^4}{8\pi} \left[\frac{8(a_2 A_2)^2 \sqrt{\tau} e^{-2a_2 \tau}}{3\alpha \lambda_2 \mathcal{V}_m} + \frac{4W_0 a_2 A_2 \tau e^{-a_2 \tau} \cos(a_2 \theta)}{\mathcal{V}_m^2} + \Delta V \right], \quad (6.8)$$

where we have expanded to order $1/\mathcal{V}_m^3$ in the (exponentially) small parameter $1/\mathcal{V}_m$. In (6.8) the uplifting ΔV is some model-dependent constant which should be tuned so that $V = 0$ at the minimum.

ⁱⁱⁱThe consistency of this approach was discussed in [44], see [323] for more general types of inflationary trajectories.

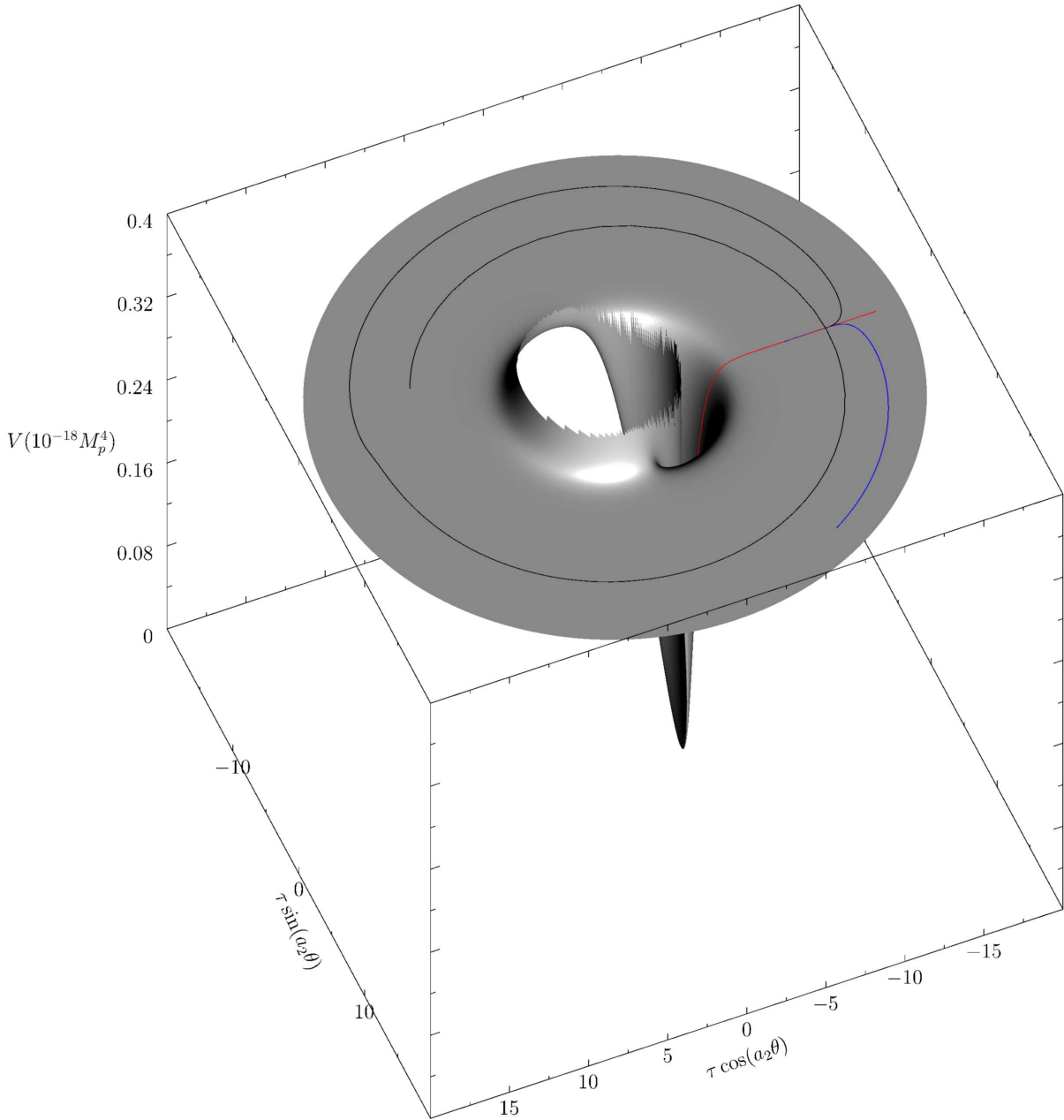


Figure 6.2: The T_2 potential $V(\tau, \theta)$ surface for a representative choice of parameters, using polar coordinates to illustrate the periodic structure of the potential in the axion direction, θ . Superimposed on the potential surface are three different inflationary trajectories, showing the rich set of possibilities in Roulette inflation. Inflation proceeds in the large τ region where the potential is exponentially flat. On the other hand, preheating after inflation takes place during the phase of oscillations the extremely steep minimum near $\tau = \mathcal{O}(1)$ and $\cos(a_2 \theta) = -1$.

The potential surface $V(\tau, \theta)$ has a rich structure, illustrated in Fig. 6.2. The potential is periodic in the axion direction and is exponentially flat (but slightly rippled) at large values of the radial coordinate τ in field space. The minimum (near $\tau = \mathcal{O}(1)$ and $\cos(a_2\theta) = -1$) is extremely steep. At $\tau \rightarrow 0$ there is a sharp potential barrier, which we have cut-off in Fig. 6.2 in order to make the salient features of the potential more transparent. The shape of the potential near the edge of the minimum is locally reminiscent of the the racetrack inflation potential [282, 319], as well as the “natural inflation” potential involving a pseudo-Goldstone boson [39, 40] (except that in our case both θ and τ must be simultaneously considered).

The potential (6.8) allows for a rich ensemble of inflationary trajectories in the Kähler moduli space [44], depending on the choice of initial conditions and model parameters. We have superposed several of these trajectories on the potential surface in Fig. 6.2 for illustration. Inflationary trajectories may undergo many revolutions at roughly constant τ , spiralling along the angular direction, θ , like a ball on a roulette wheel. At some point, the inflaton eventually gets caught in the trough along $\theta = \frac{\pi(2l+1)}{a_2}$ (where l is an integer) and rolls down to small τ . Generically the last few e-foldings of inflation occur along this trough, which is stable against $\delta\theta$ perturbations and along which $V(\tau, \theta)$ takes the form considered in [52]. Inflation ends when the inflaton rolls into the sharp minimum, like the ball on a roulette wheel falling into the pocket.

Models of this type necessarily introduce a statistical (“gambling”) aspect to the constraints that observational data imposes on inflationary model building. In [44] it was advocated to view this theory prior as a probability distribution on an energy landscape with a huge number of potential minima. In [324] the spectrum and non-Gaussianity of the curvature fluctuations for the variety of Roulette inflation trajectories was discussed. In [325] cosmological fluctuations were studied more generally in multi-field models with non-standard kinetic terms and the Roulette model was considered as a special case.

As discussed previously, consistency of the supergravity approximation requires ad-

justing the parameters so that $\tau_m \gtrsim$ a few. We note, however, that even if the SUGRA description in terms of the scalar potential is not valid at the *minimum*, it still can be valid at large τ , exactly where we wish to realize inflation. Hence a small value of τ_m does *not* constrain the Kähler Moduli/Roulette inflation. Rather, the only consequence of small τ_m is that the endpoint of inflation, reheating, would have to be described by string theory degrees of freedom (rather than simple field theoretic objects). In this work, we will propose one of the possible scenarios of this type.

Finally, we note that there are several types of perturbative corrections that could modify the classical potential (6.8) on Kähler moduli space: those related to higher string modes, or α' -corrections (coming from the higher derivative terms in both bulk and brane effective actions) and also string loop, or g_s -corrections (coming from closed and open string loop diagrams). The most dangerous corrections that could spoil exponential flatness of the potential at large τ , are the latter category: those coming from open string diagrams. This type of corrections are relevant for the models where the SM lives on a D7 brane wrapped on the 4-cycle associated with the inflationary modulus,^{iv} τ_2 , and are expected to spoil the flatness of the inflaton potential; see [320] for an estimate of this effect. One can evade this problem simply by excluding such a wrapping and assuming that the SM lives on a D7 wrapping some *other* (non-inflationary) hole in the compactification.^v This scenario has the disadvantage of complicating the reheating process, since it forbids a direct coupling between the inflaton and the visible sector. In this work, we proceed phenomenologically and consider models both with and without a D7 brane wrapped on the inflationary cycle. In both cases we identify the dominant decay channels of the inflaton into SM particles.

It will be handy for the discussion below to have estimates of the masses of the fields playing a role in inflation and reheating. Recall that from equation (6.7) the string scale

^{iv}This possibility is illustrated schematically as “scenario 1” in Fig. 6.1.

^vThis possibility is illustrated schematically as “scenario 2” in Fig. 6.1.

and Planck scale are related as $m_s/M_p \sim \mathcal{V}^{-1/2}$. The gravitino mass is $m_{3/2}/M_p \sim \mathcal{V}^{-1}$ and the masses associated with the deformations of the total volume and hole size(s) are, respectively, given by $m_{\tau_1}/M_p \sim \mathcal{V}^{-3/2}(\ln \mathcal{V})^{-1/2}$, $m_{\tau_i}/M_p \sim \ln \mathcal{V}/\mathcal{V}$ (for $i \geq 2$). See [326] for more detailed discussion.

6.3 Preheating via Self-interactions in the Inflaton Sector

In this section we study the energy transfer from the homogeneous inflaton condensate into fluctuations. We proceed by first considering the dynamics of linear perturbations about the homogeneous inflaton background and next by studying the fully nonlinear dynamics of the system using lattice field theory simulations. In the next section we study the subsequent transfer of energy from these fluctuations into excitations of the SM particles.

6.3.1 Equations for Linear Fluctuations

We consider the endpoint of inflation in the Roulette inflation model reviewed in the last section. To this end we study the action

$$S = \int d^4x \sqrt{-g} \left[\frac{1}{2} \mathcal{R} - \frac{1}{2} \mathcal{K}_{2\bar{2}} (\partial_\mu \tau \partial^\mu \tau + \partial_\mu \theta \partial^\mu \theta) - V(\tau, \theta) \right] \quad (6.9)$$

where the $(2, \bar{2})$ component of the Kähler metric depends only on the 4-cycle volume

$$\mathcal{K}_{2\bar{2}} = \frac{3\alpha\lambda_2 [2\mathcal{V}_m + \xi + 6\alpha\lambda_2\tau^{3/2}]}{2(2\mathcal{V}_m + \xi)^2 \sqrt{\tau}} \simeq \frac{3\alpha\lambda_2}{4\mathcal{V}_m} \frac{1}{\sqrt{\tau}} + \dots \quad (6.10)$$

The potential $V(\tau, \theta)$ is given explicitly by (6.8) and in the second equality of (6.10) we have expanded to leading order in \mathcal{V}_m^{-1} . Throughout the rest of this chapter we use Planck units, $M_P \equiv 1$, although we occasionally write out the factors of M_p explicitly. For simplicity we restrict ourselves to “parameter set 1” (as defined in [44]) corresponding

to the choice $W_0 = 300$, $a_2 = 2\pi/3$, $A_2 = 0.1$, $\lambda_2 = 1$, $\alpha = 1/(9\sqrt{2})$, $\xi = 0.5$, $g_s = 0.1$ and $\mathcal{V} = 10^6$. We have considered also different parameter choices and found the results to be qualitatively similar in all cases.

To understand preheating in the model (6.9), let us first consider the linearized equations for the fluctuations. In order to make the analysis tractable we introduce the canonical inflaton field ϕ defined by $d\phi = \pm\sqrt{\mathcal{K}_{2\bar{2}}} d\tau$ so that $\phi \cong \sqrt{\frac{4}{3} \frac{\alpha\lambda_2}{\mathcal{V}_m}} \tau^{3/4}$ in the large volume limit and with some arbitrary convention for the origin of field space. Now the action (6.9) takes the form

$$S = - \int d^4x \sqrt{-g} \left[\frac{1}{2} (\partial\phi)^2 + \frac{1}{2} e^{2b(\phi)} (\partial\theta)^2 + U(\phi, \theta) \right] \quad (6.11)$$

where

$$b(\phi) = \frac{1}{2} \ln [\mathcal{K}_{2\bar{2}}(\tau(\phi))] \quad (6.12)$$

$$U(\phi, \theta) = V[\tau(\phi), \theta] \quad (6.13)$$

Our choice of notation follows [325].

For generic inflationary trajectories, the final few e -foldings of inflation take place along the trough $\theta = \pi(2l+1)/a_2$ (with l integer) [44]. Thus, to study the linear regime of particle production during preheating after inflation we expand the fields as

$$\phi(t, \mathbf{x}) = \phi_0(t) + \delta\phi(t, \mathbf{x}) \quad (6.14)$$

$$\theta(t, \mathbf{x}) = \frac{(2l+1)\pi}{a_2} + \delta\theta(t, \mathbf{x}) \quad (6.15)$$

In the left panel of Fig. 6.3 we plot the effective potential for the homogeneous motion of the canonical inflaton ϕ along the $\theta = (2l+1)\pi/a_2$ trough, that is $U[\phi, (2l+1)\pi/a_2]$. This potential displays a long flat region at large ϕ which is relevant for inflation and a very steep minimum at $\phi = \phi_m$. Preheating during inflation takes place during the phase of oscillations about this minimum. In the right panel of Fig. 6.3 we plot the time dependence of the inflaton condensate $\phi_0(t)$ during this oscillatory phase. Due to the

extreme sharpness of the potential minimum the inflaton passes very quickly through the region close to ϕ_m while the extreme flatness at larger ϕ means that the inflaton spends a long time near the right-hand side of the valley. We denote the period of oscillations about the minimum by T and note that for typical parameters $T \sim 10^{-3}H^{-1}$.

Let us now consider the linear fluctuations $\delta\phi$, $\delta\theta$ in the inflaton and axion fields. The equations of motion for the Fourier modes $\delta\phi_k$ and $\delta\theta_k$ take the form

$$\delta\ddot{\phi}_k + 3H\delta\dot{\phi}_k + \left[\frac{k^2}{a^2} + U_{,\phi\phi} \right] \delta\phi_k = 0 \quad (6.16)$$

$$\delta\ddot{\theta}_k + [3H + 2b_{,\phi}] \delta\dot{\theta}_k + \left[\frac{k^2}{a^2} + e^{-2b}U_{,\theta\theta} \right] \delta\theta_k = 0 \quad (6.17)$$

where the quantities $U(\phi, \theta)$ and $b(\phi)$ (and their derivatives) are understood to be evaluated on the unperturbed values $\phi = \phi_0(t)$ and $\theta = \theta_0(t) \equiv (2l+1)\pi/a_2$. Neglecting the expansion of the universe^{vi} and defining the canonical axion fluctuation $\delta\psi$ as

$$\delta\psi_k \equiv e^b \delta\theta_k \quad (6.18)$$

we obtain oscillator-like equations for the mode functions

$$\delta\ddot{\phi}_k + \omega_{\phi,k}^2 \delta\phi_k = 0 \quad (6.19)$$

$$\delta\ddot{\psi}_k + \omega_{\psi,k}^2 \delta\psi_k = 0 \quad (6.20)$$

In (6.19,6.20) the effective frequencies are

$$\begin{aligned} \omega_{\phi,k}^2 &= k^2 + U_{,\phi\phi} \\ &\equiv k^2 + M_{\phi,\text{eff}}^2(t) \end{aligned} \quad (6.21)$$

$$\begin{aligned} \omega_{\psi,k}^2 &= k^2 - b_{,\phi}\ddot{\phi}_0 - (b_{,\phi}^2 + b_{,\phi\phi})\dot{\phi}_0^2 + e^{-2b}U_{,\theta\theta} \\ &\equiv k^2 + M_{\psi,\text{eff}}^2(t) \end{aligned} \quad (6.22)$$

and we have introduced the notation $M_{\text{eff}}^2(t)$ for the time-dependent effective masses of the fields. We solve equations (6.19,6.20) numerically. As usual [238] we initialize the modes

^{vi}This neglect is justified since typically the total time for preheating to complete is of order $10^{-3}H^{-1}$.

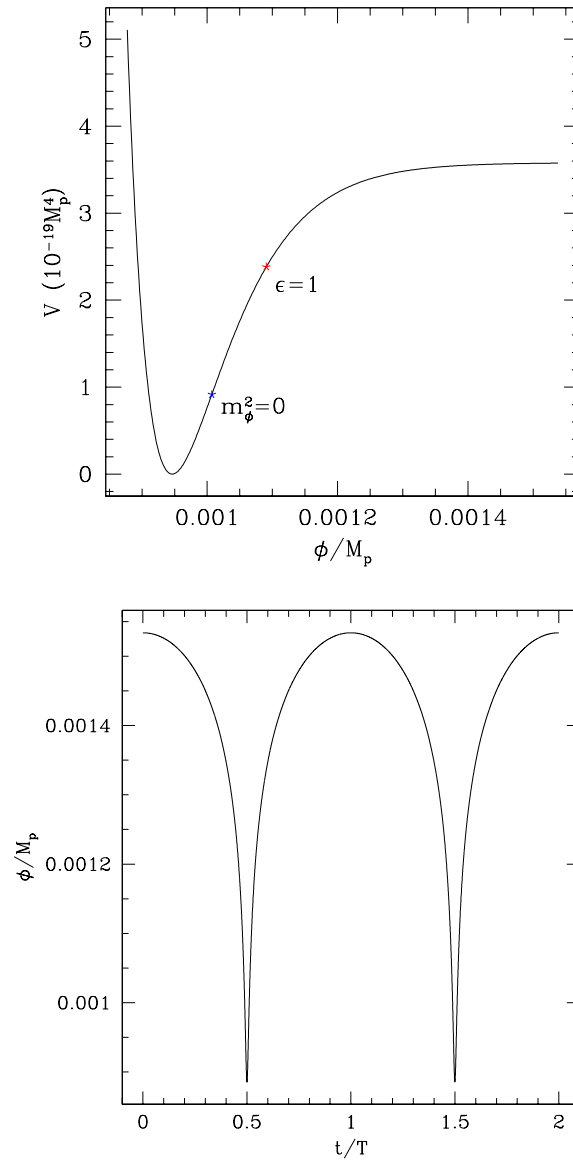


Figure 6.3: The left panel shows the effective potential for the canonical Kähler modulus ϕ along the axion trough, $U(\phi, (2l+1)\pi/a_2)$ showing the long exponentially flat region relevant for inflation and also the steep minimum relevant for the preheating phase of post-inflationary oscillations. We have labelled the point where inflation ends (where the ϵ slow roll parameter is unity) and also the point where the effective mass-squared $V''(\phi)$ flips sign, corresponding to the cross-over between the tachyonic and non-tachyonic regions. The right panel shows the oscillatory time evolution of the homogeneous inflaton $\phi_0(t)$ at the end of inflation.

as $\delta\phi_k = 1/\sqrt{2\omega_{\phi,k}}$, $\delta\dot{\phi}_k = -i\sqrt{\omega_{\phi,k}/2}$ at $t = 0$ (and similarly for $\delta\psi_k$) which, physically, corresponds to starting with pure quantum vacuum fluctuations with occupation number $n_k = 0$. Violations of the adiabaticity condition $|\dot{\omega}_k|/\omega_k^2 \ll 1$ are associated with particle production and lead to the generation of nonzero occupation number, $n_k \neq 0$. As is typical in the theory of preheating [238] we define the occupation number for the inflaton fluctuations as

$$n_k^\phi = \frac{\omega_{\phi,k}}{2} \left[\frac{|\delta\dot{\phi}_k|^2}{\omega_{\phi,k}^2} + |\delta\phi_k|^2 \right] - \frac{1}{2} \quad (6.23)$$

and similarly for the occupation number n_k^ψ associated with the axion.

6.3.2 Instability of Kähler Modulus Fluctuations

Let us first consider the equation (6.19) for the fluctuations $\delta\phi_k$ of the (canonical) inflaton. This equation can be viewed as an effective Schrodinger-like oscillator equation with “potential” determined by the effective mass term, $M_{\phi,\text{eff}}^2(t)$. In Fig. 6.4 we plot the behaviour of this effective mass (the dashed blue curve) as a function of time. We see that $M_{\phi,\text{eff}}^2$ has a very particular time dependence: the fluctuations $\delta\phi$ are nearly massless during the inflaton oscillations except for periodic “spiky” features uniformly spaced at intervals $\Delta t = T$. As long as the adiabatic invariant $|\dot{\omega}_k|/\omega_k^2$ remains small, $|\dot{\omega}_k|/\omega_k^2 \ll 1$, particles are not produced and the occupation number n_k will be close to a constant. For modes with wave-number k^2 sufficiently small, the spike structure in $M_{\phi,\text{eff}}^2$ leads to extreme violations of adiabaticity: $|\dot{\omega}_k|/\omega_k^2 \gg 1$. In Fig. 6.5 we plot the adiabaticity parameter taking $k = 0$ for illustration (the dashed blue curve). Notice that each spike in $M_{\phi,\text{eff}}^2$ is also accompanied by a tachyonic phase where $M_{\phi,\text{eff}}^2 < 0$.

The periodic time-dependent behaviour of the effective mass $M_{\phi,\text{eff}}^2$ leads to unstable momentum bands where the modes $\delta\phi_k$ grow exponentially as

$$\delta\phi_k(t) \sim e^{\mu_k t/T} f_k(t/T) \quad (6.24)$$

with $f_k(t/T)$ some periodic oscillatory function. We computed the Floquet exponent

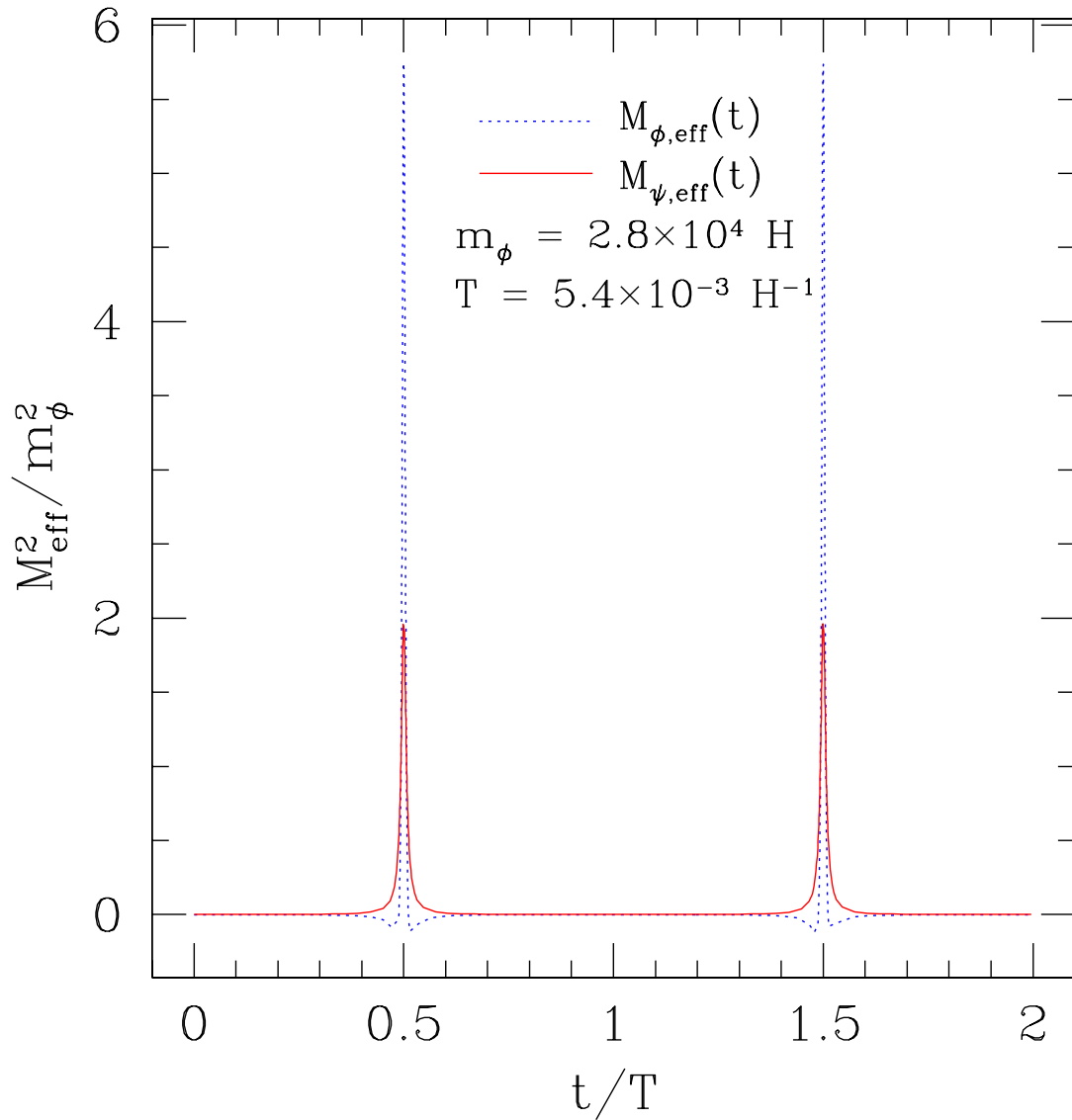


Figure 6.4: The effective mass-squared of both the Kähler modulus ϕ (the dashed blue curve) and axion ψ (the solid red curve) as a function of time. We plot the effective mass in units of m_ϕ , the mass at the minimum of the potential. Note that $M_{\text{eff}}(t)$ actually exceeds m_ϕ during the inflaton oscillations. This corresponds to the steep curvature on the left-hand-side of the potential minimum in Fig. 6.3.

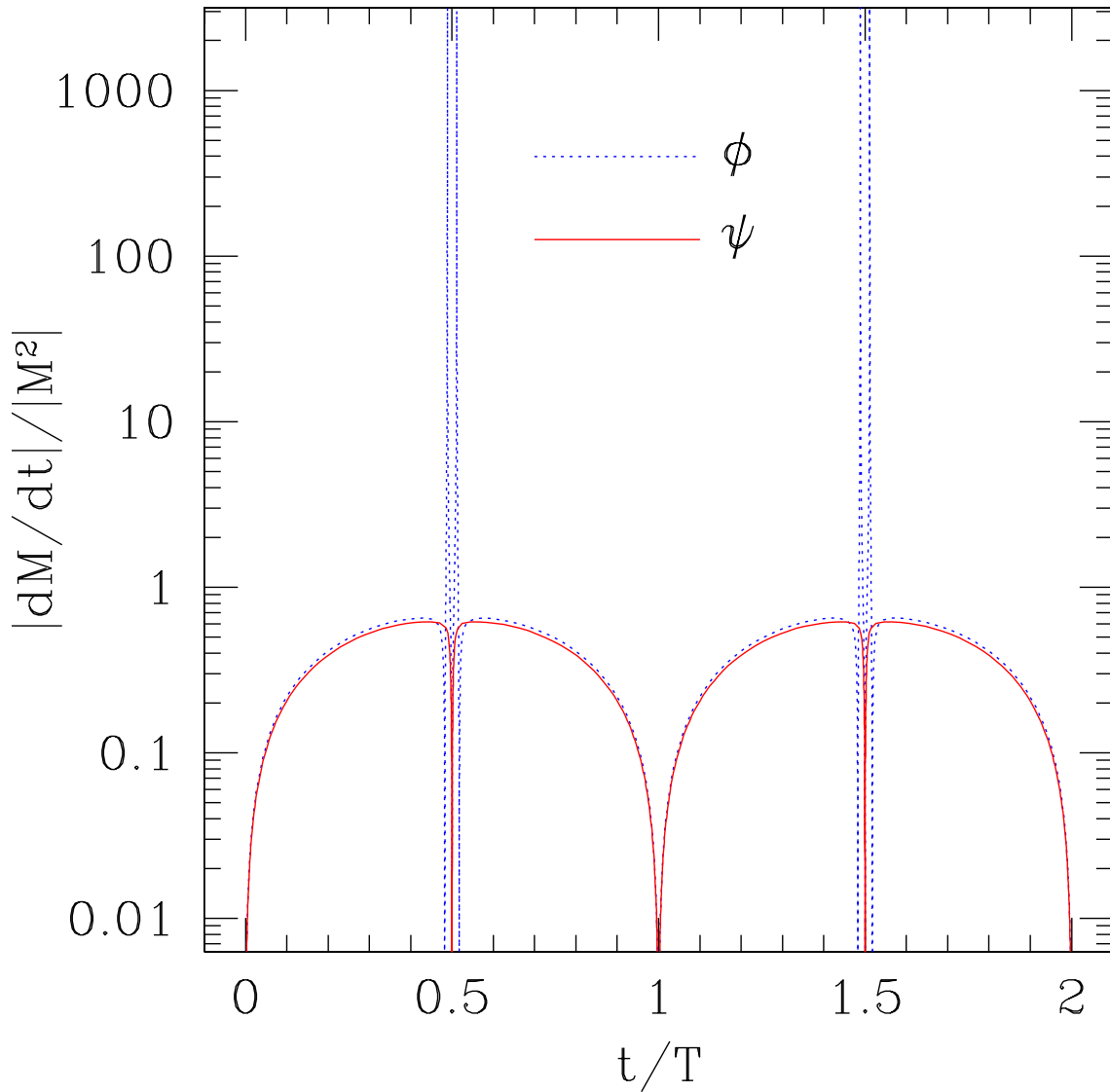


Figure 6.5: The quantity $|dM_{\text{eff}}/dt|/|M_{\text{eff}}^2|$ for both the Kähler modulus ϕ (the dashed blue curve) and axion ψ (the solid red curve) as a function of time. This quantity provides a measure of the violation of adiabaticity and coincides with the adiabatic invariant $\dot{\omega}_k/\omega_k^2$ in the IR. The Spike structure of the Kähler modulus effective mass leads to extremely strong violations of adiabaticity and particle production. On the other hand, the axion effective frequency varies slowly during the inflaton oscillations and axion particles are not produced.

μ_k appearing in (6.24) numerically and the result is displayed in Fig. 6.6. The broad unstable region at low k corresponds to tachyonic growth of IR modes coming from the $M_{\phi,\text{eff}}^2 < 0$ regions in Fig. 6.4. On the other hand, the UV region of Fig. 6.6 featuring a band structure is a result of broad-band parametric resonance. The modes $\delta\phi_k$ belonging to these two regions of phase space display very different behaviour and both tachyonic and resonance effects play a crucial role in the dynamics of preheating. In Fig. 6.7 we plot the time evolution of the Kähler modulus mode functions for $k = 0.01 m_\phi$ (corresponding to the IR tachyonic regime), $k = 0.5 m_\phi$ (corresponding to the UV regime of broad-band parametric resonance) and $k = 0.08 m_\phi$ (corresponding to the intermediate regime where these two effects cannot be disentangled). Here m_ϕ denotes the mass of the canonical inflaton at the minimum of the potential. Note that these different kinds of preheating can *only* be separated in the linear theory; at the nonperturbative level such a distinction is impossible.

To illustrate how violent the process of preheating in modular inflation is, we consider the energy density ρ_k in a given wave-number k , which coincides with $\sim k^4 n_k$ if we evaluate ρ_k at the point in the inflation oscillations where $M_{\phi,\text{eff}} = 0$ (this point is illustrated on the potential in the left panel of Fig. 6.3). This quantity is plotted as a function of k in Fig. 6.8 for three different time steps in the (linear) evolution. We see that within only three oscillations of the background field (that is, at $t = 3T$) the fluctuations contain many orders of magnitude more energy than the condensate. At this point backreaction becomes critical and the linearized treatment breaks down. Therefore, in order to study the dynamics after the first 2-3 oscillations one must turn to nonlinear lattice simulations, which we consider in the next subsection.

We have also studied the dynamics of the linear fluctuations of the axion, equation (6.20). The effective mass $M_{\psi,\text{eff}}^2(t)$ for the fluctuations $\delta\psi_k$ of the (canonical) axion. is plotted in Fig. 6.4 (the solid red curve). The behaviour is qualitatively similar to the inflaton effective mass, however, the spikes are less sharp and the tachyonic regions

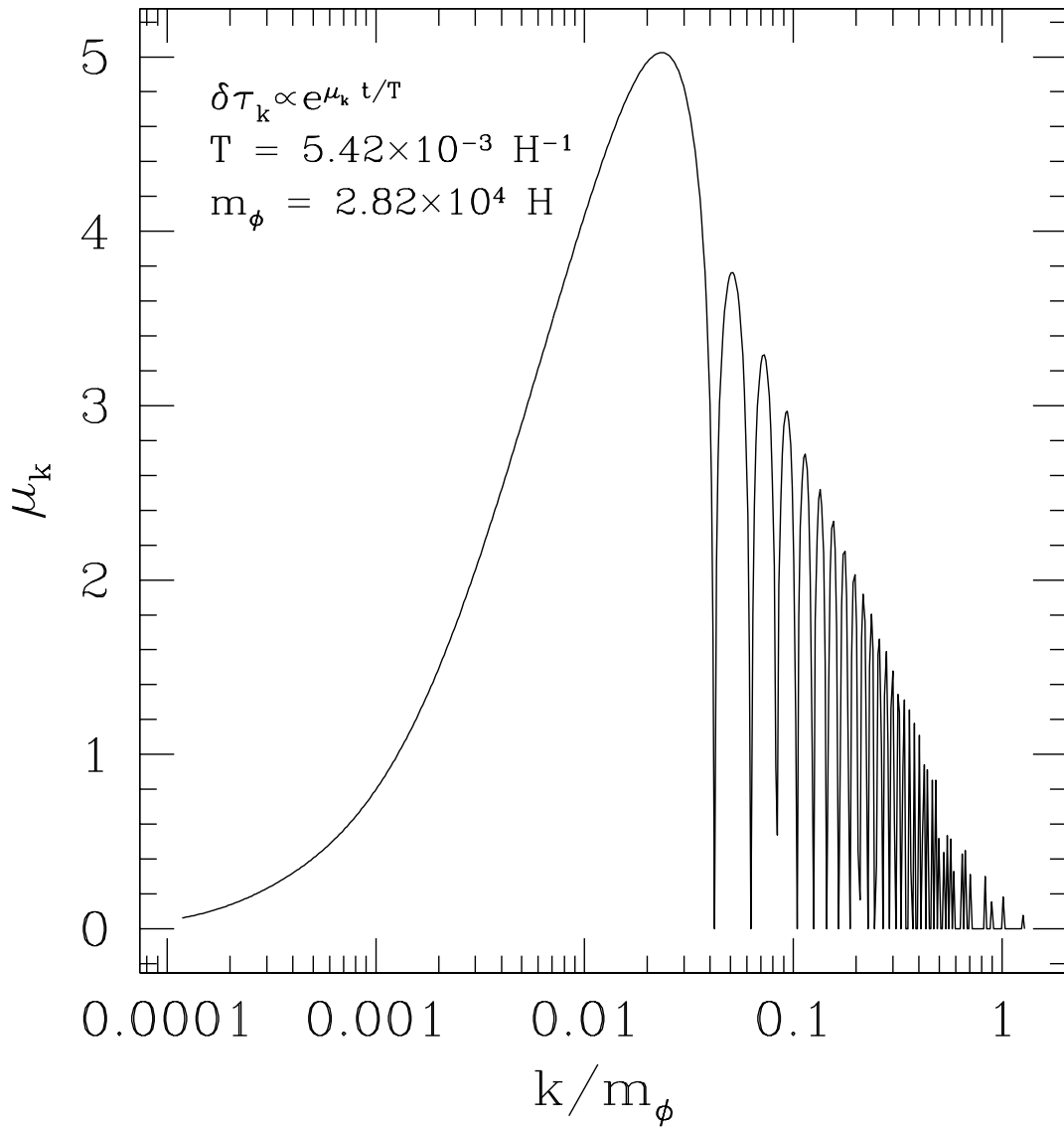


Figure 6.6: The dimensionless characteristic exponent μ_k (Floquet exponent) for the exponential instability of the (canonical) Kähler modulus fluctuations $\delta\phi_k$, defined in (6.24). The broad unstable region in the IR comes from the tachyonic regions where $M_{\phi,\text{eff}}^2 < 0$ whereas the UV region displays the band structure that is characteristic of parametric resonance. The behaviour of the modes $\delta\phi_k$ in these two regions is qualitatively different.

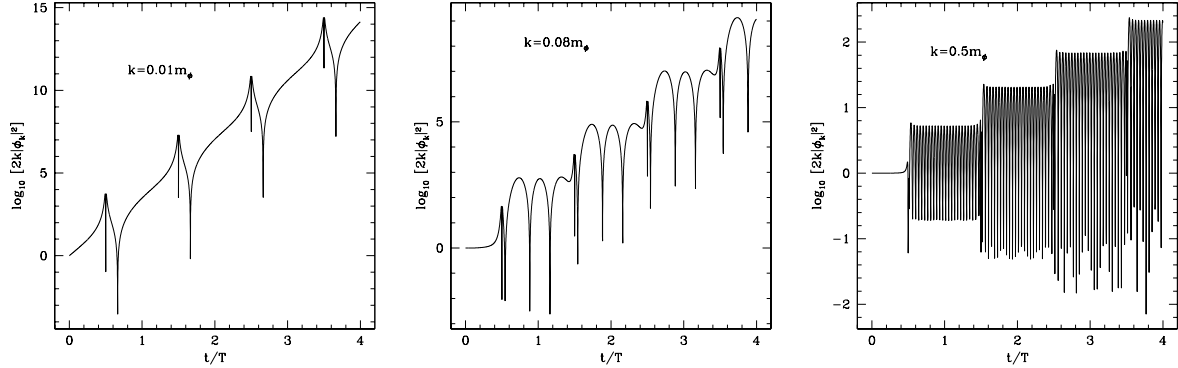


Figure 6.7: The behaviour of linear Kähler fluctuations during preheating after modular inflation illustrating the combination of tachyonic instability and parametric resonance. The left panel shows the mode behaviour for $k = 0.01m_\phi$ (corresponding to the IR tachyonic regime) while the right panel shows the mode behaviour for $k = 0.5m_\phi$ (corresponding to the UV regime of parametric resonance). The middle panel is $k = 0.08m_\phi$, corresponding to the intermediate regime where both effects are active.

are absent. Thus, we expect the production of axion fluctuations to be less efficient. This intuition is confirmed in Fig. 6.5 where we show that adiabaticity is never violated for these modes (see the solid red curve). Therefore the endpoint of modular inflation is dominated by the extremely nonperturbative production of Kähler modulus fluctuations, rather than their axionic partner. During later stages of reheating, however, axions may be produced by rescattering effects.

6.3.3 Lattice Simulations of Preheating in Roulette Inflation

In the last subsection we studied the dynamics of the linear fluctuations $\delta\tau$, $\delta\theta$ at the endpoint of inflation. We found that the particular shape of the inflaton potential (which is highly nonlinear and has a very steep minimum) imparts an extremely non-adiabatic time dependence to the 4-cycle modulus τ and leads to explosive production of $\delta\tau$ particles. Hence the linearized analysis of this dynamics breaks down very rapidly, within just

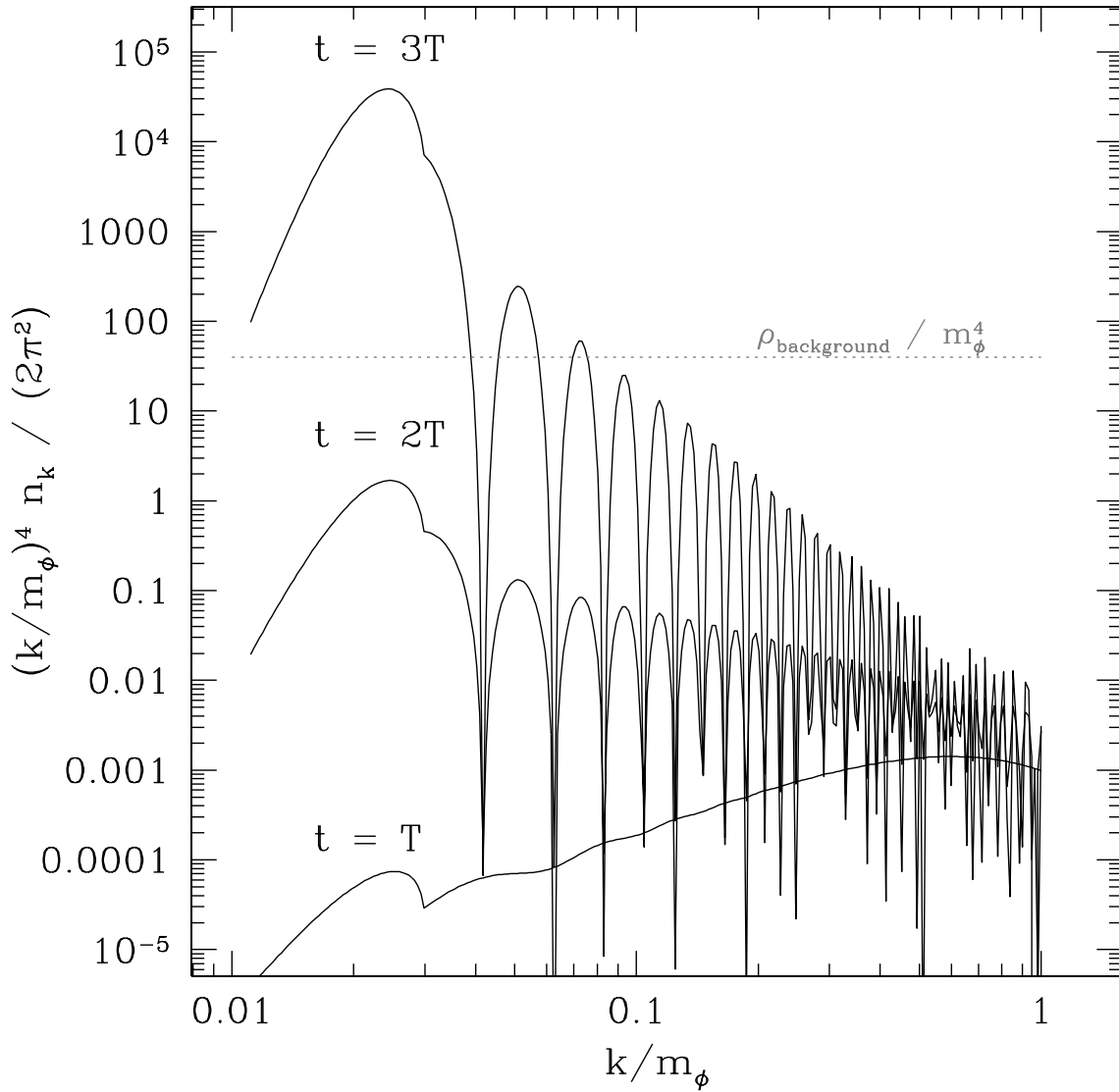


Figure 6.8: The energy spectrum $\sim k^4 n_k$ for $\delta\tau$, calculated with linear theory, showing the rapid and violent production of particles after modular inflation. Within three oscillations of the background field (by $t = 3T$) the energy density is significantly larger than the energy in the homogeneous condensate and at this point nonlinear feedback must be taken into account.

2-3 oscillations of the background field, and a full treatment requires fully nonlinear lattice field theory simulations. Hence we now study the evolution of the fields τ, θ in a fully nonlinear way, taking into account also the expansion of the universe self-consistently.

Our numerical simulations are done using a new lattice code which contains (modified) elements of both LatticeEasy [218] and DEFROST [219]. The first version of this code was employed in the paper [6, 7] to study infra-red cascading during inflation. Here we have further generalized the code to allow for scalar fields with non-canonical kinetic terms. With the MPI-parallelized code we have used 64 processors on the CITA cluster to evolve the fields τ and θ in a cubic box with 512^3 grids. Vacuum mode functions are put in as initial conditions. The very first stage of the evolution, when inhomogeneity can be treated linearly^{vii}, is performed in momentum space. From this initial stage of momentum-space evolution we can determine which Fourier modes τ_k, θ_k experience unstable growth during preheating and ensure that the relevant dynamical scales are captured by our simulations (that is, the k -modes which dominate the unstable growth are well between the IR cut-off $k_{IR} = L^{-1}$ defined by the box size L and the UV cut-off $k_{UV} = \Delta x^{-1}$ defined by the lattice spacing Δx). Once the particle occupation numbers become large we switch over to configuration-space evolution (at the switching time the gradient energy is roughly 10^{-4} as compared to the energy in the homogeneous condensate). We subsequently run our configuration-space evolution for a total time $\Delta t = \mathcal{O}(3 - 4)T$ (where T is the period of oscillations of the homogeneous background). This time scale is more than sufficient to see the homogeneous inflaton condensate completely decohered into inhomogeneous fluctuations.

To illustrate the rapid and violent development of inhomogeneities during modular preheating we study the energy density in gradients of the Kähler modulus τ , given by

$$\rho_{\text{grad}} = \mathcal{K}_{,\tau\tau} \frac{1}{a^2} \partial_i \tau \partial^i \tau = \int \frac{d \ln k}{2\pi^2} \frac{k^5}{a^2} \mathcal{K}_{,\tau\tau} |\delta\tau_k|^2 \quad (6.25)$$

^{vii}In the case of Roulette inflation this occurs only during inflation and the first oscillation of preheating.

In Fig. 6.9 we plot the power in gradient energy, given by $k^5 \mathcal{K}_{,\tau\tau} |\delta\tau_k|^2 / (2\pi^2 a^2)$, for three time steps in the evolution.

After the first oscillation, at $t \sim T$, we see the band structure of growing modes in the UV is characteristic of parametric resonance. However, by the time $t \sim 2T$ the evolution has become completely nonlinear leading to the destruction of the band structure and the cascading of power into both the IR and UV. By the time $t \sim 3T$ the energy density in gradients is comparable to the homogeneous background energy density, illustrating the decay of the condensate. By this time, however, our numerical evolution has become unreliable since the power in inhomogeneous fluctuations has cascaded down to the UV cut-off, $k_{UV} = \Delta x^{-1}$; beyond this point we are bleeding energy into the grid. In any case, at later times decays into fields which were not included, such as brane-bound gauge fields and fermions, start to become important. We consider these decays for a variety of scenarios in the remainder of this chapter.

We have also considered the dynamics of the expansion of the universe during preheating. The effective equation of state during preheating is $\omega = P/\rho \cong 0.1$, which is very close to a matter dominated expansion. This is consistent with Fig. 6.8 where we see that, in the linear theory, the $\delta\tau$ particles which dominate the energy density of the universe have momentum in the band $k/m_\phi \sim \mathcal{O}(0.01 - 0.1)$ and hence we expect these to be non-relativistic near the minimum: $\omega_k = \sqrt{k^2 + m_\phi^2} \cong m_\phi + \frac{k^2}{2m_\phi} + \dots$. (Note also that the Floquet exponent μ_k in Fig. 6.6 peaks over roughly the same range of scales.)

The violent production of inhomogeneities leads to significant backreaction effects which alter the form of the effective potential, in particular the location of the minimum and the effective mass at that minimum, m_τ . The late-time perturbative decays of the produced inflaton fluctuations $\delta\tau$ into SM fields (which we study in detail in the remainder of this chapter) depend sensitively on the value of m_τ at the minimum, hence it is important to determine whether this differs significantly from the value one obtains neglecting backreaction effects.

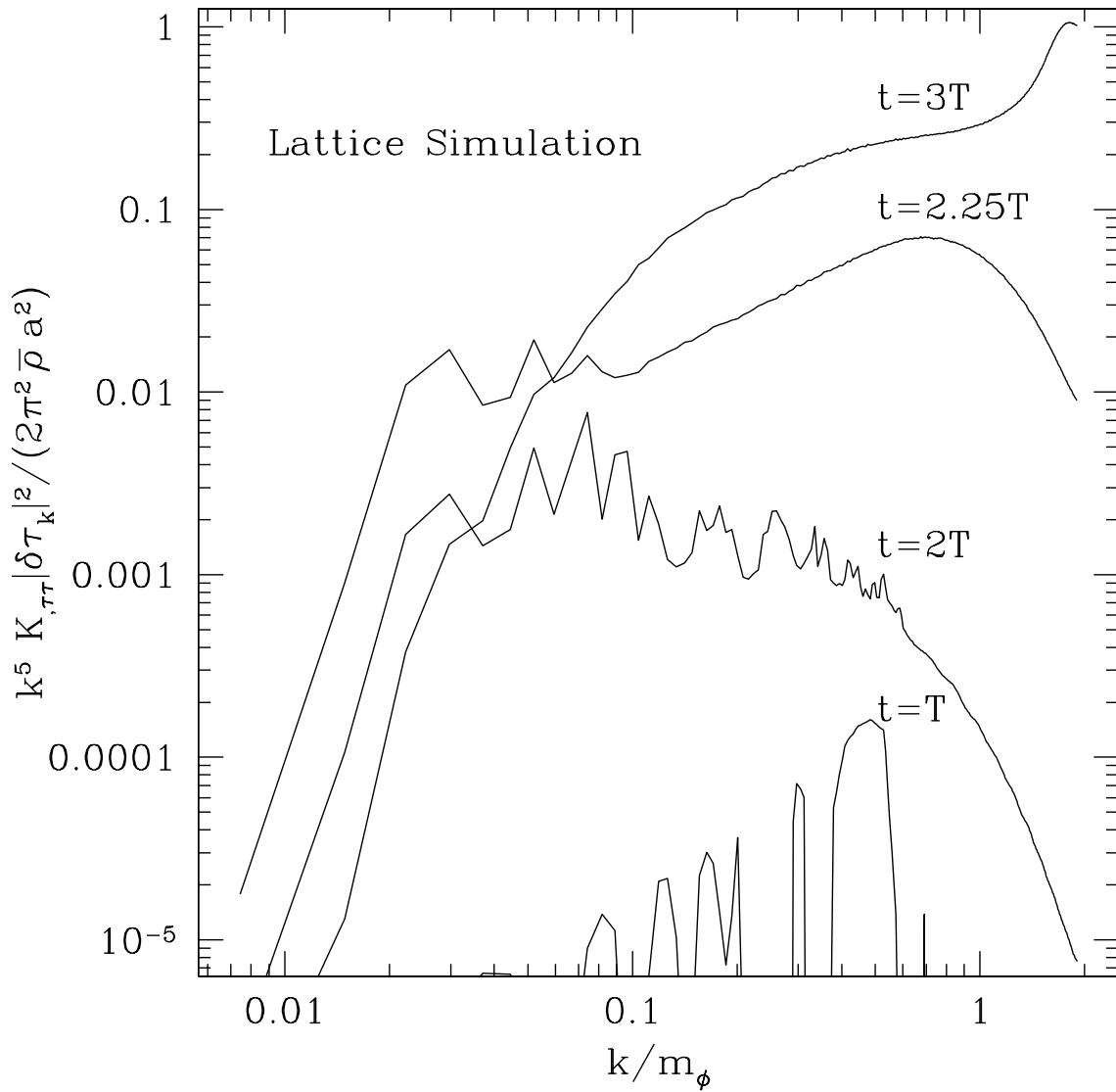


Figure 6.9: The power in Kähler modulus gradient energy, which is given by $k^5 \mathcal{K}_{,\tau\tau} |\delta\tau_k|^2 / (2\pi^2 a^2)$, from our lattice simulations, normalized this to the total background energy density, $\bar{\rho}$. The spectrum is shown for four time steps in the evolution: $t = T$, $t = 2T$, $t = 2.25T$ and $t = 3T$, illustrating the rapid decay of the homogeneous inflaton condensate into inhomogeneous fluctuations. See the text for further discussion.

To illustrate how backreaction effects modify the effective potential, consider a simple scalar field with equation of motion $\square\phi = V'(\phi)$. Writing $\phi = \langle\phi\rangle + \delta\phi$ and taking the average of the Klein-Gordon equation we find an equation for the mean field

$$\begin{aligned}\square\langle\phi\rangle &= \langle V'[\langle\phi\rangle + \delta\phi]\rangle \\ &\equiv V'_{\text{eff}}[\langle\phi\rangle]\end{aligned}\tag{6.26}$$

In general the effective potential V_{eff} will differ from $V(\phi)$. This can be illustrated explicitly by defining the averaging procedure as $\langle V'(\phi)\rangle \equiv \frac{1}{\sqrt{2\pi}\sigma_\phi} \int d[\delta\phi] e^{-\frac{\delta\phi^2}{2\sigma_\phi^2}} V'(\phi)$ with σ_ϕ the variance of ϕ . In general this averaged force differs from $V'(\phi)$. Note that in our case both inhomogeneous fluctuations and nonlinear effects are large, thus a Gaussian distribution for $\delta\tau = \tau - \langle\tau\rangle$ may not be appropriate. However, this does not alter the qualitative argument that we are making.

We have estimated the effective mass for the τ fluctuations at the minimum, m_τ , including backreaction effects, by extracting the rate of oscillation of the (spatially) averaged field $\langle\tau\rangle$ from our lattice simulations. We find that

$$m_\tau^{\text{new}} = \beta m_\tau^{\text{old}}\tag{6.27}$$

with $\beta \sim 2.5$ for our choice of parameters. Hence, the true mass including backreaction effects differs from the mass without backreaction by a factor order unity. However, since the decay of $\delta\tau$ into brane-bound gauge fields depends on the effective mass as $\Gamma \propto m_\tau^3$ the value of the factor β may be important.

We have also investigated the production of gravitational waves from the rapid development of inhomogeneities associated with the violent decay of the inflaton after modular inflation. We have quantified the production of gravitational waves numerically, following the approach adopted in [311, 312]. We did not find any significant production of gravitational waves for the model parameters considered.

6.4 Transfer of Energy into the SM Sector: D7 Wrapping the Inflationary 4-Cycle

We have seen that the initial stages of preheating in Roulette inflation proceed non-perturbatively by a very strong instability and lead to explosive production of $\delta\tau$ fluctuations (particles) which destroy the homogeneous inflaton within just a few oscillations. However, this violent particle production is not sufficient to make contact with the usual hot big bang picture. We must also ensure that the energy in $\delta\tau$ fluctuations can be efficiently transferred into excitations of the visible (SM) sector. Determining the details of this energy transfer requires a complete understanding of how the inflaton fields τ , θ couple to SM degrees of freedom and hence this is necessarily a model dependent issue. Below we will proceed phenomenologically and consider a variety of possible scenarios, identifying the dominant decay channel of the inflaton in each case. Throughout this section (and the next) we assume that the value of τ at the minimum, τ_m , is sufficiently large to validate the effective supergravity treatment and hence the details of reheating can be studied using only QFT methods. In a subsequent section we will relax this assumption.

First let us consider the case where the SM lives on a D7 brane wrapping the inflationary 4-cycle, $T_2 = \tau + i\theta$. This wrapping is illustrated schematically in Fig. 6.1 as “scenario 1”. From the computational point of view this is the simplest imaginable scenario since it allows for a direct coupling between the inflationary τ and the fields of the SM. However, as discussed previously, such couplings lead to loop corrections to the inflaton potential which are expected to spoil slow roll [320]. Until a robust calculation of such loop effects is available we will proceed phenomenologically and suppose that the offending contributions to the slow roll parameters can be cancelled by some fine tuning (or otherwise).

6.4.1 Inflaton Coupling to Photons

Since the inflaton, τ , is the volume of the 4-cycle wrapped by the SM D7 we expect that τ couples to visible states as an overall prefactor to the SM Lagrangian. Thus, an effective Lagrangian for the inflaton-photon interaction takes the form [326]

$$\mathcal{L}_\gamma = -\frac{\lambda}{4}\tau F^{\mu\nu}F_{\mu\nu} \quad (6.28)$$

where $F_{\mu\nu} = \partial_\mu A_\nu - \partial_\nu A_\mu$ is the field strength associated with the gauge field A_μ and $\lambda = \tau_m^{-1}$ once we have normalized A_μ so that it has canonical kinetic term when τ is stabilized at the minimum.

6.4.2 Photon Preheating

The strong nonperturbative production of $\delta\tau$ fluctuations observed in section 6.3 provides a motivation to look for preheating also in other bosonic fields, such as the photon, A^μ . Therefore we study the stability of the quantum fluctuations of A^μ in the background of the oscillating homogeneous inflaton $\tau_0(t)$. To this end we choose the transverse gauge: $A^0 = 0$, $\partial_i A^i = 0$. The equation of motion for the Fourier transform of the spatial components of the gauge field $A^i(t, \mathbf{x})$ in the homogeneous inflaton background takes the form

$$\ddot{A}_k + \left[H + \frac{\dot{\tau}_0}{\tau_0} \right] \dot{A}_k + \frac{k^2}{a^2} A_k = 0 \quad (6.29)$$

where we suppress the vector index i on the modes $A_k^i(t)$ for ease of presentation. Equation (6.29) can be put into oscillator-like form by introducing the field $\tilde{A}_k \equiv (a\tau_0)^{1/2} A_k$. We find

$$\left[\frac{d^2}{dt^2} + \omega_{\gamma,k}^2 \right] \tilde{A}_k = 0 \quad (6.30)$$

where the time-varying frequency is

$$\begin{aligned} \omega_{\gamma,k}^2 &= \frac{k^2}{a^2} + \frac{1}{4} \left(\frac{\dot{\tau}_0}{\tau_0} \right)^2 - \frac{1}{2} \frac{\ddot{\tau}_0}{\tau_0} - \frac{1}{2} H \frac{\dot{\tau}_0}{\tau_0} - \frac{1}{4} H^2 - \frac{1}{2} \dot{H} \\ &\equiv \frac{k^2}{a^2} + M_{\gamma,\text{eff}}^2(t) \end{aligned} \quad (6.31)$$

The time dependence of the effective photon mass $M_{\gamma,\text{eff}}^2(t)$ (neglecting the expansion of the universe) is plotted in the left panel of Fig. 6.10. The behaviour is qualitatively similar to the effective mass for the $\delta\tau$ fluctuations (up to an overall sign flip). The oscillatory behaviour of the photon effective mass leads to parametric resonance of the photon modes \tilde{A}_k with stability/instability bands in which the photon fluctuations grow exponentially as $\tilde{A}_k(t) \sim e^{\mu_k t/T}$. We have computed the Floquet exponent, μ_k , numerically and this result is plotted in the right panel of Fig. 6.10 where we see the characteristic features of narrow band parametric resonance.

We have seen that very early stages of oscillations of the inflaton condensate $\tau_0(t)$ leads to copious production of photons living on the SM D7-brane via parametric resonance preheating. This phase of violent, nonperturbative photon production is very short-lived since the production of $\delta\tau$ inhomogeneities completely destroys the condensate within 2-3 oscillations. The later stages of the production of SM photons will instead involving perturbative decays $\tau \rightarrow \gamma\gamma$, to which we now turn our attention.

6.4.3 Perturbative Decays to Photons

After the phase of violent nonperturbative particle production discussed above the homogeneous inflaton τ will settle down to the minimum of the potential and reheating will be dominated by the perturbative decays of produced inflaton fluctuations into SM photons. To study such processes let us consider the Lagrangian for the total volume modulus $\tau_1 \equiv \tau_b$ (where the subscript b stands for “big”) and the hole-size $\tau_2 \equiv \tau \equiv \tau_s$ (where the subscript s stands for “small”). Writing $\tau_i = \langle \tau_i \rangle + \delta\tau_i$ (with $i = b, s$) we have, near the vicinity of the minimum

$$\mathcal{L} = -\mathcal{K}_{ij} \partial_\mu(\delta\tau_i) \partial^\mu(\delta\tau_j) - V_0 - (M^2)_{ij}(\delta\tau_i)(\delta\tau_j) - \frac{\lambda}{4} \tau_s F^{\mu\nu} F_{\mu\nu} + \dots \quad (6.32)$$

The mass matrix $(\mathcal{K}^{-1}M^2)_{ij}$ is not diagonal, nor are the fields $\delta\tau_i$ canonically normalized. Following [326] we can put this action into a more conventional form by introducing the

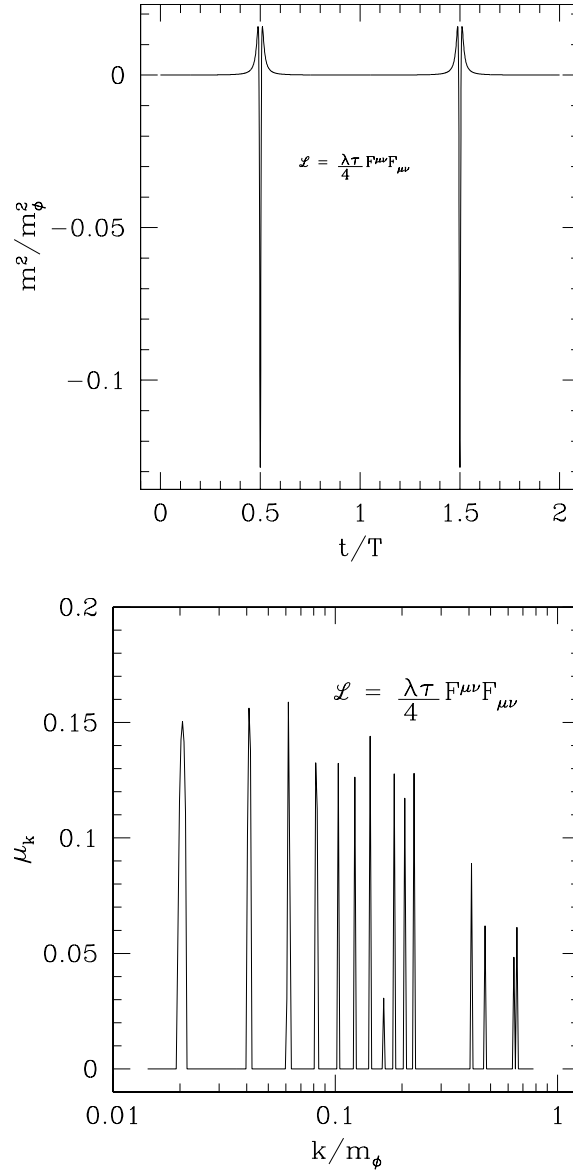


Figure 6.10: The left panel shows the time dependence of the effective photon mass, $M_{\gamma,\text{eff}}^2(t)$. The right panel shows the Floquet exponent μ_k for the mode functions $A_k(t) \sim e^{\mu_k t/T}$.

physical modulus fields Φ , χ defined by

$$\begin{pmatrix} \delta\tau_b \\ \delta\tau_s \end{pmatrix} = \begin{pmatrix} R_{b\Phi} & R_{b\chi} \\ R_{s\Phi} & R_{s\chi} \end{pmatrix} \begin{pmatrix} \Phi \\ \chi \end{pmatrix} \quad (6.33)$$

The elements of the rotation matrix R_{ij} are computed explicitly in [326], however, parametrically we have $R_{b\Phi} \sim \mathcal{V}^{1/6}$, $R_{b\chi} \sim \mathcal{V}^{2/3}$, $R_{s\Phi} \sim \mathcal{V}^{1/2}$ and $R_{s\chi} \sim \mathcal{V}^0$. Thus the canonical field Φ is mostly the small 4-cycle $\delta\tau_s$, while the field χ is mostly the big 4-cycle $\delta\tau_b$. In terms of the canonical basis χ, Φ the Lagrangian (6.32) takes the form

$$\begin{aligned} \mathcal{L} &= -\frac{1}{2}(\partial\Phi)^2 - \frac{1}{2}(\partial\chi)^2 - V_0 - \frac{m_\Phi^2}{2}\Phi^2 - \frac{m_\chi^2}{2}\chi^2 - \frac{1}{4}F^{\mu\nu}F_{\mu\nu} \\ &+ \frac{\lambda_{\chi\gamma\gamma}}{4}\chi F^{\mu\nu}F_{\mu\nu} + \frac{\lambda_{\Phi\gamma\gamma}}{4}\Phi F^{\mu\nu}F_{\mu\nu} \\ &+ \lambda_{\chi\Phi\Phi}\chi\Phi^2 + \lambda_{\Phi\chi\chi}\Phi\chi^2 + \lambda_{\chi\chi\chi}\chi^3 + \lambda_{\Phi\Phi\Phi}\Phi^3 + \dots \end{aligned} \quad (6.34)$$

The masses of the canonical moduli are

$$m_\chi \sim \frac{1}{\mathcal{V}^{3/2}(\ln \mathcal{V})^{1/2}} M_p \quad (6.35)$$

$$m_\Phi \sim \frac{\ln \mathcal{V}}{\mathcal{V}} M_p \quad (6.36)$$

so that Φ is significantly more massive than χ , consistent with the intuition that since $\tau_b \gg \tau_s$ the volume modulus should be lighter than the modulus associated with the hole size (at the minimum). The light χ particles have Planck suppressed couplings to brane-bound gauge fields

$$\lambda_{\chi\gamma\gamma} \sim \frac{1}{M_p \ln \mathcal{V}} \quad (6.37)$$

since the fluctuations of the total volume are bulk modes. On the other hand, the coupling of massive Φ particles to gauge fields are only string suppressed

$$\lambda_{\Phi\gamma\gamma} \sim \frac{1}{m_s} \sim \frac{\sqrt{\mathcal{V}}}{M_p} \quad (6.38)$$

The violent production of $\delta\tau_s$ fluctuations at the end of inflation leads to a huge number of canonical Φ particles near the minimum, in addition to a small admixture

of χ which arise due to the nontrivial mixing of $\delta\tau_s$ and $\delta\tau_b$, see equation (6.33). The massive Φ particles subsequently decay to photons via perturbative processes such as $\Phi \rightarrow \gamma\gamma$ mediated by the couplings in (6.34). The decay width was computed in [326]

$$\Gamma_{\Phi \rightarrow \gamma\gamma} = \frac{\lambda_{\Phi\gamma\gamma}^2 m_\Phi^3}{64\pi} \quad (6.39)$$

Using the estimates (6.36) and (6.38) we find

$$\Gamma_{\Phi \rightarrow \gamma\gamma} \sim \frac{(\ln \mathcal{V})^3}{\mathcal{V}^2} M_p \quad (6.40)$$

Also notice that, due to the $\delta\tau_b - \delta\tau_s$ mixing, a certain amount of χ particles will be produced from the oscillating inflaton field. This does not lead to a cosmological moduli problem because the χ particles are extremely massive for the value of \mathcal{V} which we consider. For example, taking $\mathcal{V} \sim 10^6 - 10^9$ we have $m_\chi \sim 10^4 - 10^8$ GeV which is sufficiently massive that the residual χ moduli will decay well before Big Bang Nucleosynthesis (BBN) [327].^{viii}

6.4.4 Inflaton Coupling to Fermions

The inflaton τ_s will couple not only to photons but also to fermion fields living on the world-volume of the D7 brane wrapping the inflationary 4-cycle. The effective action describing these interactions generically takes the form [328]:

$$\mathcal{L}_{\text{int}} = h_{\Phi\Psi\Psi} \Phi \bar{\Psi} \Psi \quad (6.41)$$

where $h_{\Phi\Psi\Psi}$ is the dimensionless coupling and Ψ schematically denotes any MSSM fermion. The decay rate for this type of interaction is

$$\Gamma_{\Phi \rightarrow \Psi\Psi} \cong \frac{h^2}{8\pi} m_\Phi \quad (6.42)$$

^{viii}For very large values of the compactification volume, $\mathcal{V} \sim 10^9$, the χ modulus may decay very close to the onset on BBN. For such parameters a more careful treatment of the decay of χ , taking into account factors of order unity, may be necessary.

(in the limit $m_\Phi \gg m_\Psi$).

Prior to electro-weak symmetry breaking a direct coupling to SM fields (such as the electron) is absent and the decay of Φ into fermions is dominated by the production of Higgsinos $\Phi \rightarrow \tilde{H}\tilde{H}$ and gauginos $\Phi \rightarrow \lambda\lambda$. The relevant couplings were computed in [328]

$$h_{\Phi\tilde{H}\tilde{H}} \sim \frac{1}{\mathcal{V}^{1/2} \ln \mathcal{V}} \quad (6.43)$$

$$h_{\Phi\lambda\lambda} \sim \frac{1}{\mathcal{V}^{3/2} \ln \mathcal{V}} \quad (6.44)$$

We therefore have the following estimates for the decay rates

$$\Gamma_{\Phi \rightarrow \tilde{H}\tilde{H}} \sim \frac{1}{\mathcal{V}^2 \ln \mathcal{V}} M_p \quad (6.45)$$

$$\Gamma_{\Phi \rightarrow \lambda\lambda} \sim \frac{1}{\mathcal{V}^4 \ln \mathcal{V}} M_p \quad (6.46)$$

We see that the decays of Φ into Higgsinos dominate over the decays into gauginos.

6.4.5 Reheating Temperature

Let us now estimate the reheating temperature for the scenario where the SM lives on a D7 wrapping the inflationary cycle T_2 . Note that $\Gamma_{\Phi \rightarrow \gamma\gamma} / \Gamma_{\Phi \rightarrow \tilde{H}\tilde{H}} \sim (\ln \mathcal{V})^4 \sim 10^4$ for a compactification volume of order $\mathcal{V} \sim 10^6 - 10^9$, which is of interest for Roulette inflation. Thus, comparing equations (6.40) and (6.45) we see that the lifetime of the inflaton is dominated by its decay into photons. Using the standard result from the theory of reheating [238] the reheat temperature is given by

$$T_r \sim 0.1 \sqrt{\Gamma M_p} \sim 0.1 \frac{(\ln \mathcal{V})^{3/2}}{\mathcal{V}} M_p \quad (6.47)$$

Using $\mathcal{V} \sim 10^6$ we obtain $T_r \sim 10^{13}$ GeV and using $\mathcal{V} \sim 10^9$ we have $T_r \sim 10^{10}$ GeV. Normally such a high reheat temperature would lead to a gravitino problem (specifically the late decays of the gravitino interfere with the successful predictions of Big Bang Nucleosynthesis). However, in our case the gravitino mass is extremely high [326]:

$$m_{3/2} \sim \frac{M_p}{\mathcal{V}} \quad (6.48)$$

For $\mathcal{V} \sim 10^6 - 10^9$ we have $m_{3/2} \sim 10^9 - 10^{12}$ GeV, hence the gravitino is so massive that it decays well before nucleosynthesis [327]. The disadvantage of such a high gravitino mass temperature is that SUSY is broken at too high a scale to explain the electro-weak hierarchy of the SM. An alternative scenario to explain the fine-tuning of the Higgs mass is through vacuum selection effects on the string landscape [329, 330]. On the other hand, see [331] for a scenario where this gravitino mass is compatible with TeV scale soft terms.

There is, however, another cause for concern. At sufficiently high temperatures thermal corrections to the effective potential tend to destabilize the moduli and drive them to infinity, leading to decompactification [328]. The decompactification temperature, T_{\max} , can be accurately approximated by $T_{\max} \cong V_b^{1/4}$ where $V_b \cong m_{3/2}^3 M_p$ is the height of the potential barrier separating the large volume AdS minimum from the supersymmetric minimum at infinity in moduli space. The maximum allowed reheat temperature (above which the internal space decompactifies) is therefore

$$T_{\max} \cong \frac{M_p}{\mathcal{V}^{3/4}} \tag{6.49}$$

Comparing (6.47) to (6.49) one sees that, keeping track only of factors of the total volume \mathcal{V} , we have T_r is marginally below the decompactification temperature. However, this conclusion could easily be altered by factors of order unity which we have not taken into account. Such factors depend sensitively on the details of the compactification and we leave a careful determination to future studies. Indeed, the requirement $T_r < T_{\max}$ may significantly constraint the parameter space of the model [328].

6.5 Transfer of Energy into the SM Sector: D7 Wrapping a Non-Inflationary 4-Cycle

As discussed previously, the wrapped D7 scenario of the previous section may lead to dangerous g_s -corrections to the inflaton potential. Thus, it may be desirable to exclude such a wrapping. Doing so, of course, also forbids a direct coupling between the inflaton and the SM fields. In this case the inflaton may still decay to SM particles via some intermediate bulk states. Such decays which involve bulk modes must necessarily be suppressed by the compactification volume, which is exponentially large. Here we discuss one possible scenario of this type.

We could imagine the SM living on a D7 which wraps the big cycle T_1 , however, this leads to unnaturally small gauge couplings [326] and hence is phenomenologically disfavoured. Instead, let us suppose the SM lives on a D7 wrapping some stabilized non-inflationary cycle, T_3 , which is stabilized to a value $\langle \tau_3 \rangle = \mathcal{O}(1)$. This wrapping is illustrated schematically in Fig. 6.1 as “scenario 2”.

At this point we must extend the discussion from section 6.4.3 to the case with more than two moduli fields, namely, instead of 2 fields τ_b ($= \tau_1$) and τ_s ($= \tau_2$) (corresponding to canonical moduli χ and Φ) we consider 3 fields τ_1 , τ_2 and τ_3 (corresponding to canonical moduli χ , Φ_2 and Φ_3).

As we have seen, the endpoint of inflation is marked by the violent production of fluctuations $\delta\tau_2$ of the inflationary 4-cycle, T_2 . Near the minimum of the potential these τ_2 fluctuations mix with the total volume τ_1 and the non-inflationary hole τ_3 through an off-diagonal mass matrix similar to (6.33), except now there are three relevant moduli rather than two. Diagonalizing the mass matrix one finds three canonical fields χ and Φ_i

($i = 2, 3$) which are schematically related to the 4-cycle volumes as

$$\delta\tau_1 \sim \mathcal{O}(\mathcal{V}^{2/3})\chi + \sum_i \mathcal{O}(\mathcal{V}^{1/6})\Phi_i \quad (6.50)$$

$$\delta\tau_i \sim \mathcal{O}(\mathcal{V}^{1/2})\Phi_i + \mathcal{O}(1)\chi + \sum_{j \neq i} \mathcal{O}(\mathcal{V}^{-1/2})\Phi_j \quad \text{where } i = 2, 3 \quad (6.51)$$

so that χ is mostly the total volume $\delta\tau_1$ while Φ_2, Φ_3 are mostly the blow-up modes $\delta\tau_2$ and $\delta\tau_3$ respectively. The modulus χ is light, having mass

$$m_\chi \sim \frac{1}{\mathcal{V}^{3/2}(\ln \mathcal{V})^{1/2}} M_p \quad (6.52)$$

while the moduli Φ_2, Φ_3 are heavier

$$m_{\Phi_2} \sim m_{\Phi_3} \sim \frac{\ln \mathcal{V}}{\mathcal{V}} M_p \quad (6.53)$$

These moduli couple to gauge fields living on the D7 wrapping T_3 via the interaction $\tau_3 F_{\mu\nu} F^{\mu\nu}$, which gives us

$$\mathcal{L}_{\text{int}} = \frac{\lambda_{\chi\gamma\gamma}}{4} \chi F^{\mu\nu} F_{\mu\nu} + \sum_{i=2,3} \frac{\lambda_{\Phi_i\gamma\gamma}}{4} \Phi_i F^{\mu\nu} F_{\mu\nu} \quad (6.54)$$

using equations (6.32) and (6.51). Physically, these couplings originate from the mixing between τ_2 and τ_1, τ_3 . From equation (6.51) we can estimate the magnitude of the moduli couplings. The largest coupling is, obviously, the one involving Φ_3 since the SM D7 wraps the cycle T_3 . This coupling is set by the string scale

$$\lambda_{\Phi_3\gamma\gamma} \sim \frac{1}{m_s} \sim \frac{\mathcal{V}^{1/2}}{M_p} \quad (6.55)$$

On the other hand, the coupling to the large cycle is

$$\lambda_{\chi\gamma\gamma} \sim \frac{1}{M_p \ln \mathcal{V}} \quad (6.56)$$

where the factor M_p^{-1} comes from that fact that χ is a bulk mode and the factor of $(\ln \mathcal{V})^{-1}$ is nontrivial [326]. The coupling between the inflationary 4-cycle T_2 and brane-bound SM gauge fields is

$$\lambda_{\Phi_2\gamma\gamma} \sim \frac{1}{M_p} \frac{1}{\mathcal{V}^{1/2}} \quad (6.57)$$

This is even more than Planck suppressed.

Thus, the picture of reheating in this scenario is the following. Preheating produces copious amounts of $\delta\tau_2$ fluctuations which lead to a large number of canonical Φ_2 moduli near the minimum, plus a small admixture of light χ and heavy Φ_3 moduli. The Φ_3 particles are the first to decay, they produce brane-bound SM photons via the process $\Phi_3 \rightarrow \gamma\gamma$ with a rate identical to (6.40):

$$\Gamma_{\Phi_3 \rightarrow \gamma\gamma} \sim \frac{(\ln \mathcal{V})^3}{\mathcal{V}^2} M_p \quad (6.58)$$

This decay, however, does not correspond to true reheating since at this point the energy density of the universe is dominated by the almost nonrelativistic^{ix} Φ_2 particles with matter dominated equation of state, rather than SM radiation. Thus, the SM radiation which is produced at by the decay of Φ_3 is rapidly diluted, $\rho_{\text{radn}} \sim a^{-4}$, relative to the nonrelativistic Φ_2 particles whose energy density dilutes as: $\rho_{\Phi_2} \sim a^{-3}$.

True reheating occurs when the Φ_2 particles subsequently decay into SM states via the suppressed coupling (6.57). This decay proceeds with rate:

$$\Gamma_{\Phi_2 \rightarrow \gamma\gamma} \sim \frac{m_{\Phi_2}^3}{M_p^2 \mathcal{V}} \sim \frac{(\ln \mathcal{V})^3}{\mathcal{V}^4} M_p \quad (6.59)$$

It is the decay rate (6.59) which determines the reheat temperature of the universe:

$$T_r \sim 0.1 \sqrt{\Gamma M_p} \sim 0.1 \frac{(\ln \mathcal{V})^{3/2}}{\mathcal{V}^2} M_p \quad (6.60)$$

This is smaller than the result of the previous section, equation (6.47), by a factor of \mathcal{V}^{-1} corresponding to the fact that the Φ_2 is a bulk mode in this set-up with suppressed coupling to brane-bound states (6.57). This suppression is actually favorable since it keeps the reheat temperature (6.60) well below the decompactification scale T_{max} , given by (6.49). Taking $\mathcal{V} \sim 10^6$ we have $T_r \sim 10^7$ GeV and taking $\mathcal{V} \sim 10^9$ we have $T_r \sim 10$ GeV. Hence, for extremely large values of the compactification volume, $\mathcal{V} \sim 10^9$, the

^{ix}See subsection 6.3.3 for a discussion of the fact that the bulk of the inflation fluctuations produced by preheating are nonrelativistic near the minimum.

reheating temperature is so low that it may be difficult to realize baryogenesis at the electroweak phase transition. We leave this issue to future investigations.

In this scenario the gravitino decays too early in the history of the universe to interfere with BBN: for $\mathcal{V} \sim 10^6 - 10^9$ we have $m_{3/2} \sim 10^9 - 10^{12}$ GeV. As previously, the residual volume modulus χ particles decay after reheating but before BBN.

The results of this section may also have some relevance for the scenario where the SM cycle is much smaller than the string scale, see [331]. We leave a detailed investigation to future studies.

6.6 Stringy Reheating via Kähler Moduli Shrinking

In this section, we propose yet another reheating mechanism in Kähler moduli inflation models. This mechanism can operate even in the absence of a D7 wrapping the inflationary 4-cycle. Hence, in the ensuing text we suppose (as in section 6.5) that the SM lives on a D7 wrapping T_3 .

The inflationary dynamics of $\tau(t)$ corresponds to the shrinking of the 4-cycle associated with T_2 . If this inflationary cycle of the internal CY shrinks to a minimal size τ_m comparable with the string scale, supergravity description breaks down and new, stringy degrees of freedom must kick in. A natural candidate for such degrees of freedom is winding modes: closed strings with a nonzero winding number with respect to the inflationary 4-cycle. Because of winding number conservation winding strings are created in pairs with winding numbers of equal absolute value but having opposite signs. Two such closed strings can merge into a one with zero winding number, *i.e.* a string that can move away from the inflationary 4-cycle and into the bulk region of the CY. In other words, the energy of the shrinking inflationary cycle (*i.e.* inflaton kinetic energy) is transferred into closed string excitations living in the bulk. This is somewhat similar to the energy transfer from annihilating branes into closed string excitations that occurs at the end of

stringy warped throat brane inflation [301, 302]. The excited closed strings decay via many cascades into closed strings with the lowest level of excitation, *i.e.*, KK gravitons. The produced KK gravitons interact with the SM brane scalar moduli Y_i (corresponding to the transverse fluctuations of the brane) and also SM particles. Consider, for example, the interaction between KK gravitons and brane moduli Y_i . This interaction is gravitational and can be described by a vertex $\frac{1}{M_P^2} h_{\mu\nu}^{KK} T^{\mu\nu}(Y)$, the corresponding decay width is

$$\Gamma_{KK \rightarrow Y} \sim \frac{m_{KK}^3}{M_P^2}. \quad (6.61)$$

As discussed in [302], this coupling is sufficiently generic to work for any low-lying degrees of freedom on the SM brane world. (In particular, world-volume fermions.) For the purposes of making a rough estimate of the reheat temperature we can safely assume that $\Gamma_{KK \rightarrow Y} \sim \Gamma_{KK \rightarrow SM}$.

Let us now estimate (6.61). The KK modes have typical mass $m_{KK} \sim 1/R_{CY}$, where the overall size of the internal CY is $R_{CY} \sim \mathcal{V}^{1/6} \sqrt{\alpha'}$. In the models under consideration we have

$$\sqrt{\alpha'} \sim \frac{1}{m_s} \sim \frac{\sqrt{\mathcal{V}}}{M_P}, \quad (6.62)$$

so that $R_{CY} \sim \frac{\mathcal{V}^{2/3}}{M_P}$, $m_{KK} \sim \frac{M_P}{\mathcal{V}^{2/3}}$, and from (6.61) we have

$$\Gamma_{KK \rightarrow SM} \sim \frac{M_P}{\mathcal{V}^2}. \quad (6.63)$$

The decay rate (6.63) is suppressed as compared to the case with the wrapped D7, equation (6.40) by a logarithm which gives a numerical factor of about 10^{-3} .

The decay rate (6.63) allows us to estimate the reheat temperature as

$$T_r \sim 0.1 \frac{1}{\mathcal{V}} M_P \quad (6.64)$$

Taking, for illustration, $\mathcal{V} \sim 10^6$ we have $T_r \sim 10^{11}$ GeV and taking $\mathcal{V} \sim 10^9$ we have $T_r \sim 10^8$ GeV. As in the scenarios discussed in sections 6.4 and 6.5, such a high reheat temperature is phenomenologically sensible because the gravitino is extremely massive.

As in the scenario discussed in section 6.5 (but unlike the scenario in section 6.4) this reheat temperature is well below the decompactification scale, $T_r/T_{\max} < \mathcal{V}^{-1/4} \ll 1$.

6.7 Summary and Discussion

Modular inflation, and other string theory inflation models, provide a natural playground for studying reheating in a context where (at least in theory) one can actually determine all decay channels of the inflaton to the visible (SM) sector from first principles. Here we investigated in detail reheating after modular/Roulette string theory inflation models in the context of large volume compactifications. Our results show that in realistic microscopic models the details of reheating can be rather complicated and may proceed through a variety of channels, including perturbative decays, nonperturbative preheating and also inherently stringy processes.

We found that modular inflation models (such as Kähler modulus or Roulette inflation) in particular display very rich post-inflationary dynamics.

- *The initial stages* of the decay of the inflaton proceed via extremely efficient non-perturbative particle production involving a combination of tachyonic instability and parametric resonance. This combination may lead to the most violent example of preheating known in the literature.

The subsequent stages of reheating involve the transfer of energy from the inflaton into excitations of the visible sector. This phase is more model dependent since we must identify the location of the standard model of particle physics in the compactification volume. We have considered three separate scenarios for transferring the energy from the inflaton fluctuations $\delta\tau$ into SM degrees of freedom. These are as follows:

- *D7 wrapping T_2* (assuming a SUGRA description of reheating is valid, i.e., the minimum hole size is larger than the string length): In this case the SM fields live

on a D7 wrapping the inflationary 4-cycle, T_2 , so that there is a direct coupling between the SM fields and the inflaton τ . Photon production (both perturbative and non-perturbative) dominates the decay of the inflaton. The resulting reheat temperature is given by (6.47). Using $\mathcal{V} \sim 10^6$ we obtain $T_r \sim 10^{13}$ GeV and using $\mathcal{V} \sim 10^9$ we have $T_r \sim 10^{10}$ GeV. Although such reheat temperatures are extremely high, there is no problem with BBN because $m_{3/2} \sim 10^9 - 10^{12}$ GeV is so large that the gravitinos decay before the onset of nucleosynthesis. However, such a high reheat temperature may lead to decompactification. This scenario also has the disadvantage that g_s -corrections may spoil the flatness of the inflaton potential.

- *D7 wrapping T_3* (assuming a SUGRA description of reheating is valid, i.e., the minimum hole size is larger than the string length): In this case the SM fields live on at D7 wrapping some non-inflationary 4-cycle, T_3 (we exclude the big cycle T_1 since this would give unacceptably small gauge couplings). Near the minimum of the potential the produced inflaton fluctuations $\delta\tau_2$ mix with the fluctuations of the big 4-cycle $\delta\tau_1$ and also of the small non-inflationary 4-cycle $\delta\tau_3$ through a non-diagonal mass matrix. The decay of the $\delta\tau_2$ fluctuations into brane-bound SM states via Planck suppressed operators leads to reheating. This scenario evades any dangerous g_s -corrections to the inflaton potential and the fact that reheating proceeds through Planck suppressed operators suppresses the reheat temperature to well below the decompactification scale. Taking $\mathcal{V} \sim 10^6$ we have $T_r \sim 10^7$ GeV and taking $\mathcal{V} \sim 10^9$ we have $T_r \sim 10$ GeV. As above, there is no gravitino problem because $m_{3/2} \sim 10^9 - 10^{12}$ GeV.
- *Stringy reheating*: In this case closed strings are produced when the inflationary 4-cycle size becomes of order the string length. These closed strings cascade into KK gravitons which can subsequently interact with brane-bound SM fields (wrapping some non-inflationary 4-cycle) via Planck-suppressed operators. Taking, for illus-

tration, $\mathcal{V} \sim 10^6$ we have $T_r \sim 10^{11}$ GeV and taking $\mathcal{V} \sim 10^9$ we have $T_r \sim 10^8$ GeV. There is, again, no gravitino problem because $m_{3/2}$ is so large. Decompactification is evaded due to the Planck suppression of the interactions between bulk and brane modes. This scenario also evades potentially dangerous g_s -corrections to the inflaton potential.

For convenience we summarize the rates for the dominant decay channel of the inflaton in the various scenarios in the following table:

Summary of Dominant Decay Rates	
Γ/M_p	Scenario
$\sim \frac{(\ln \mathcal{V})^3}{\mathcal{V}^2}$	D7 wrapping T_2
$\sim \frac{(\ln \mathcal{V})^3}{\mathcal{V}^4}$	D7 wrapping T_3
$\sim \frac{1}{\mathcal{V}^2}$	stringy reheating from shrinking hole

In all cases considered there is the disadvantage that SUSY is broken at too high a scale to explain the small value of the Higgs mass. This happens because the typical compactification volumes which are favorable for inflation $\mathcal{V} \sim 10^6 - 10^9$ are much smaller than the value $\mathcal{V} \sim 10^{15}$ that is favored for particle phenomenology [326].^x See, however, [331] for a scenario where $\mathcal{V} \sim 10^6 - 10^7$ may be compatible with TeV soft terms.

Our first scenario, the SM D7 wrapping T_2 , is afflicted by two potential complications: g_s -corrections may destroy the flatness of the inflaton potential and the reheat tempera-

^xThis tension is similar to what happens in KKLMNT brane inflation where the value of the warping that would be required to solve the hierarchy problem *à la* Randall and Sundrum is much larger than the warping that is favorable for inflation. In the case of KKLMNT this can be evaded by adding additional throats to the compactification [301] at the expense of complicating the reheating process.

ture is so high that it may lead to decompactification. Both of these issues will require further study, however, at first glance this scenario seems disfavoured. On the other hand, the scenario with the SM D7 wrapping T_3 evades both of these potential difficulties and therefore seem most promising. For such models there are again a number of directions open for further study. Also, it would be interesting to perform a more detailed study the topology-changing transition in the case where the inflationary hole size shrinks to the string length at the end of inflation. We leave these, and other, interesting issues to future investigations.

Chapter 7

Cosmological Constraints on Decaying Dark Matter

7.1 Introduction

The last chapter of the thesis is about decaying dark matter, based on my published work [58]. The observational signatures of dark matter decay or dark matter annihilation can be put into two categories – the astrophysical signals and the cosmological signals. The advantage of considering cosmological signals, which will be discussed here, is that it is independent of the dark matter halo models and other astrophysical sources that may mimic the dark matter decay or annihilation. My main contribution in this project was to modify the publicly available package CAMB to include the dynamic equations for the decaying dark matter cosmology. Using this modified code I calculated the cosmological constraints on the lifetime of decaying dark matter with MCMC method. For completeness we will include here most of the content that has already been published in [58]. Please cite our original paper for the use of these contents.

The identity of dark matter is hypothesized to be one of the new particles in theories that extend the Standard Model of particle physics. This confluence and cross-

fertilization of ideas from two major fields of scientific endeavor promises to herald an exciting new era in understanding of the universe. With the resumption of operation of the Large Hadron Collider at CERN, we are possibly months away from collider detection, albeit indirectly through missing energy signatures, of dark matter particles.

Yet this avenue too is plagued with troubling questions that need to be addressed if we are to take the idea seriously that some particle from an extension of the Standard Model is indeed the elusive yet ubiquitous dark matter of the universe. Most worryingly, to ensure the presence of a dark matter candidate in a number of beyond the Standard Model theories of particle physics, it is often necessary to impose global symmetries. For instance, we have the T-parity in Little Higgs [332] and R-parity in supersymmetry [333]. In the limit where the global symmetries are exact, the lightest particle carrying such a global charge would be stable from decay to lighter particles that do not possess such a charge. It is this point that could potentially destroy this promising marriage of ideas from cosmology and particle physics, for it is well known that global symmetries are never exact.

The presence of anomalies, as in the case of T-parity [334], or R-parity violating terms in supersymmetry [335] would often mean that the dark matter candidates arising from these theories are neither stable nor long-lived in the cosmological sense. Even if this had not been the case, the presence of gravity might induce the violation of global symmetries as was first revealed in studies of black holes [336, 337, 338, 339]. So the lightest particle charged under a particular global symmetry would have, at best, a very long lifetime. Indeed, it has even been conjectured that discrete global symmetries are violated maximally by gravity [340, 341].

Additional motivation can be found in numerical simulations of the universe (based on the conventional Λ CDM cosmology) which predict an overabundance of substructures as compared to actual observations. Models with decaying dark matter [342, 343] provide an extremely compelling and natural mechanism for suppressing the power spectrum at

small scales thus resolving the discrepancy.

Continuing on the line of thought leading from particle physics to cosmology, the question that then naturally springs to mind is “What can cosmology say about decaying dark matter and the particle physics theories that contain them?” It is this intriguing prospect that we explore in this work.

There have been a few papers [9, 344, 345] in recent years analyzing DM decay into electromagnetically non-interacting particles using just the cosmic microwave background data (Ref. [344] also includes supernova data). In this work, we revisit this scenario using a Markov Chain Monte Carlo (MCMC) analysis employing all available data sets from the cosmic microwave background (CMB), Type Ia supernova (SN), Lyman- α forest ($\text{Ly}\alpha$), large scale structure (LSS) and weak lensing (WL) observations. We find that the lifetime of decaying DM is constrained predominantly by the late time Integrated Sachs Wolfe (ISW) effect to be $\Gamma^{-1} \gtrsim 100$ Gyr. In the main body of this chapter, we will comment on the discrepancies between the results of Refs.[9, 344, 345].

The studies in the preceding paragraph considered only the case where there was negligible reionization of the universe due to DM decay. In an attempt to address this, Ref. [346] analyzed the scenario of DM decaying into only electromagnetically interacting products, that get partially absorbed by the baryonic gas, using a subset of the available CMB data sets. Our work extends their analysis by using all the available CMB data sets, and also the SN, $\text{Ly}\alpha$, LSS and WL data sets. Besides the smaller selection of data sets, their analysis also ignores the impact of DM decay on cosmological perturbations which renders it ineffectual in the parameter space where there is negligible reionization. Our treatment allows the decay products to not only reionize the universe but also takes into account the effect of DM decay on cosmological perturbation. This allows us to generate many other observables, particularly, the late time ISW effect that is crucial to constrain the lifetimes at low reionization. Another key difference between the analyses is that we use a combined reionization parameter for both DM reionization and phe-

nomenological star formation reionization, rather than just treating them separately as was done in Ref. [346], because current observations cannot distinguish which contribution to reionization is the dominant one. Doing the MCMC analysis, we find that the lifetime of decaying DM in this scenario constrained to be $(f\Gamma)^{-1} \gtrsim 5.3 \times 10^8$ Gyr, where f is a phenomenological parameter introduced by Ref. [346] and related to the degree of reionization.

Astrophysical constraints together with additional assumptions have also been used [347, 348] to give even tighter bounds than ours on the lifetime of the decaying DM. While interesting and complementary, these lie outside the scope of this work.

Having obtained the bounds on the lifetime of decaying dark matter, we will then explore the implications of our cosmological analysis on particle physics models beyond the Standard Model. We will present a complete list of cross-sections for spin-0, spin-1/2 and spin-1 dark matter to decay into Standard Model degrees of freedom via effective operators. Obviously, this can be easily extended to other models with additional light degrees of freedom (for instance, hidden valley models [349]) by appropriate substitution of the parameters. Applying the bound on the lifetime of the decaying DM, we can then place limits on the size of the parameters of theories. For generic theories with a decaying dark matter of ~ 100 GeV mass, the coupling constant in the effective dimension-4 operators responsible for dark matter decay will be shown to be $\lesssim 10^{-22}$. We will also look at specific representative cases of theories beyond the Standard Model physics and investigate the possibility of viable dark matter candidates: the spin-0 messenger DM in the context of gauge mediation messenger number violation, the spin-1/2 bino DM in the scenario with R-parity violation and the spin-1 “massive photon partner” DM in the framework of T-parity violation.

The rest of this chapter is organized as follows. In Section 2, we discuss the physics of decaying dark matter cosmology as well as introduce the data sets that we will be using. Section 3 contains our Markov Chain Monte Carlo results and discussions of the

cosmological implications. In Section 4, we explore the consequences of these results for particle physics theories by enumerating the decay channels and partial widths. Representative models from theories of gauge-mediated supersymmetry breaking, minimal supergravity and little Higgs were also investigated using the results of our analysis. We conclude and briefly comment on future prospects in Section 5.

7.2 Decaying Cold Dark Matter Cosmology

We will assume the standard picture of Λ CDM cosmology, i.e. a Friedman-Robertson-Walker universe that is principally composed of dark energy and cold dark matter, with one crucial modification; that is, we have a cold dark matter that is very long-lived but ultimately decays. As we are considering lifetimes of gigayears (Gyr), the fraction of DM decays happening during or soon after big bang nucleosynthesis (BBN) is negligible and hence would not alter the predictions of BBN. To perform a model-independent analysis, we allowed decays to all possible SM particles. However, we will assume that the long term decay products are relativistic. While we include branching ratios to intermediate non-relativistic states, they are assumed to be short-lived and will rapidly decay into light relativistic degrees of freedom.

The evolution of background and first order perturbation in decaying cold dark matter model was first formulated in longitudinal gauge [9], which means the decay rate has to be treated with care as the CDM is not at rest in the longitudinal gauge. We, on the other hand, will work in CDM rest frame using synchronous gauge with the line element written as

$$ds^2 = a^2(\tau) [-d\tau^2 + (\delta_{ij} + h_{ij})dx^i dx^j]. \quad (7.1)$$

where τ is conformal time, and t the cosmological time ($dt = a(\tau)d\tau$). In this chapter we follow the convention $a_0 = 1$ today.

The decay equation

$$\frac{d\rho_{\text{cdm}}}{dt} = -\Gamma\rho_{\text{cdm}}, \quad (7.2)$$

can be reformulated in a covariant form

$$T^\mu_{\nu;\mu}(\text{CDM}) = G_\nu, \quad (7.3)$$

where the force density vector G_ν can be calculated from its value in CDM rest frame

$$G_\nu|_{\text{CDM rest}} = (-\Gamma\rho_{\text{cdm}}, 0, 0, 0). \quad (7.4)$$

The conservation of total energy momentum tensor requires

$$T^\mu_{\nu;\mu}(\text{dr}) = -G_\nu, \quad (7.5)$$

where the daughter radiation (dr) is composed of the CDM decay productsⁱ.

The equations describing the evolution of background are

$$\dot{\rho}_{\text{cdm}} = -3\mathcal{H}\rho_{\text{cdm}} - a\Gamma\rho_{\text{cdm}}, \quad (7.6)$$

$$\dot{\rho}_{\text{dr}} = -4\mathcal{H}\rho_{\text{dr}} + a\Gamma\rho_{\text{cdm}}, \quad (7.7)$$

where dot denotes the derivative with respect to conformal time τ . We have defined the conformal expansion rate to be $\mathcal{H} \equiv \frac{\dot{a}}{a}$.

We will only consider scalar metric perturbations, which in Fourier space can be expanded as following [350].

$$h_{ij}(\mathbf{x}, \tau) = \int d^3\mathbf{k} e^{i\mathbf{k}\cdot\mathbf{x}} \left[\mathbf{n}_i \mathbf{n}_j h(\mathbf{k}, \tau) + 6(\mathbf{n}_i \mathbf{n}_j - \frac{1}{3}\delta_{ij})\eta(\mathbf{k}, \tau) \right], \quad (7.8)$$

where $\mathbf{n} \equiv \mathbf{k}/|\mathbf{k}|$.

Our choice of gauge and coordinates lead to the following simple density perturbation equation for CDM,

$$\dot{\delta}_{\text{cdm}} = -\frac{1}{2}\dot{h}. \quad (7.9)$$

ⁱHere “daughter radiation” stands for any relativistic decay products, not just literally for radiation (photons).

The terms containing Γ all cancel out, because the background density and overdensity are decaying with the same rate.

Instead of using simple hydrodynamic approximation for the decay product [351], which might give correct order of magnitude but less accurate results, we use the full Boltzmann equations to describe the decay product, which were first given by Ref. [11], and recently updated by [345] for decaying DM cosmology,

$$\dot{\delta}_{\text{dr}} = -\frac{2}{3}\dot{h} - \frac{4}{3}k v_{\text{dr}} + a\Gamma \frac{\rho_{\text{cdm}}}{\rho_{\text{dr}}} (\delta_{\text{cdm}} - \delta_{\text{dr}}), \quad (7.10)$$

$$\dot{v}_{\text{dr}} = k\left(\frac{1}{4}\delta_{\text{dr}} - \frac{1}{2}\Pi_{\text{dr}}\right) - a\Gamma \frac{\rho_{\text{cdm}}}{\rho_{\text{dr}}} v_{\text{dr}}, \quad (7.11)$$

$$\dot{\Pi}_{\text{dr}} = k\left(\frac{8}{15}v_{\text{dr}} - \frac{3}{5}F_3\right) + \frac{4}{15}\dot{h} + \frac{8}{5}\dot{\eta} - a\Gamma \frac{\rho_{\text{cdm}}}{\rho_{\text{dr}}} \Pi_{\text{dr}}, \quad (7.12)$$

$$\dot{F}_l = \frac{k}{2l+1} [lF_{l-1} - (l+1)F_{l+1}] - a\Gamma \frac{\rho_{\text{cdm}}}{\rho_{\text{dr}}} F_l, \quad (7.13)$$

where $l = 3, 4, 5, \dots$, $F_2 = \Pi$ and for the rest, we have used the conventions of Ref. [350]. Because CDM particles are heavy and non-relativistic, we have treated the CDM as a perfect fluid.

For the case where the DM candidate also decays into electromagnetically interacting particles (e.g. photons or electron/positrons), we have to be more careful. This is because the decays may deposit significant energy into baryonic gas and contribute to the reionization of universe. Following [352, 346, 353], we introduced a phenomenological factor f as the fraction of the decay energy deposited in the baryonic gas. For long-lifetime dark matter models, the reionization due to dark matter decay only depends on the combination $\zeta = f\Gamma/H_0$. We use ζ as an additional parameter in our MCMC analysis. Without a prior on f , the constraint on ζ does not directly give any information on Γ . However, for given dark matter models, one should in principle be able to calculate the decay branches, and therefore give a rough estimate for f under certain additional assumptions. Following Ref. [346, 353], we modify RECFAST [354, 355] to calculate the reionization due to DM decay. In this scenario, the reionization is dominated by DM decay at redshift $z > 20$, and is competing with the contribution from star formation (or

other sources) at some redshift between $z = 6$ and $z = 20$. Without knowing the details of star formation or other reionization sources, we use the following phenomenological model, which can be regarded as a combination of CosmoMC phenomenological formula and DM decay reionization formula,

$$x_e = \max \left\{ x_e^{\text{RECFAST}}, \frac{1 + f_{\text{He}}}{2} \left[1 + \tanh \left(\frac{(1+z)^{1.5} - (1+z_{\text{re}})^{1.5}}{1.5\sqrt{\Delta z}} \right) \right] \right\}, \quad (7.14)$$

where x_e , the ionized fraction, is defined as the ratio of free electron number density to hydrogen number density; f_{He} is the ratio of helium number density to hydrogen number density; x_e^{RECFAST} is the modified RECFAST output ionized fraction (i.e., the ionized fraction assuming DM decay is the only source of reionization); Δz is the redshift width of reionization (due to other sources), for which we have taken the CosmoMC [113] default value 0.5; the last free parameter, reionization redshift z_{re} , is determined by the total optical depth τ_{re} .

With all the above equations, we modified CosmoMC to analyze the decaying CDM model. In addition, we also incorporated weak lensing data into the Markov Chain Monte Carlo (MCMC) analysis. The data sets used in this chapter are listed below. For each dataset, we either wrote a new module to calculate the likelihood or modified the default CosmoMC likelihood codes to include the features of the decaying CDM model.

Cosmic Microwave Background (CMB)

We employ the CMB data sets from WMAP-5yr [271, 226], BOOMERANG [3, 4, 5], ACBAR [120, 121, 122, 123], CBI [127, 125, 126, 124], VSA [128], DASI [272, 273], and MAXIMA [129]. Also included are the Sunyaev-Zeldovich (SZ) effect for WMAP-5yr, ACBAR and CBI data sets. The SZ template is obtained from hydrodynamical simulation [133]. When calculating the theoretical CMB power spectrum, we have also turned on CMB lensing in CosmoMC.

Type Ia Supernova (SN)

The Union Supernova Ia data (307 SN Ia samples) from The Supernova Cosmology Project [274] was utilized. For parameter estimation, systematic errors were always included.

Large Scale Structure (LSS)

For large scale structure we will use the combination of 2dFGRS dataset [275] and SDSS Luminous Red Galaxy Samples from SDSS data release 4 [276]. It should be noted that the power spectrum likelihood already contains the information about BAO (Baryon Acoustic Oscillation [356, 357]).

Weak Lensing (WL)

Five weak lensing data sets were employed. See Section 2.4

The weak lensing data only measure matter power spectrum at angular scales less than a few degrees, which corresponds to scales less than a few hundred Mpc. This is much less than the Jean's length of the daughter radiation and therefore we can ignore the daughter radiation when calculating the power spectrum of projected density field.

$$\begin{aligned}
 P_l(\kappa) &= \left(\frac{4\pi G}{c^4}\right)^2 \int_0^{\chi_H} \rho_m^2 a^4 P_{3D}\left(\frac{l}{d_{cA}(\chi)}; \chi\right) \\
 &\quad \times \left[\int_{\chi}^{\chi_H} d\chi' n(\chi') \frac{d_{cA}(\chi' - \chi)}{d_{cA}(\chi')} \right]^2. \tag{7.15}
 \end{aligned}$$

We should stress that this is specific to the decaying CDM model and differs from the conventional CDM model [358, 359].

Lyman- α Forest

The following Ly α forest data sets were applied.

1. The dataset from Viel *et. al.* [152] consist of LUQAS sample [153] and the Croft *et. al.* data [154].

2. The SDSS Ly α data presented in McDonald *et. al.* [155, 156]. To calculate the likelihood, we interpolated the χ^2 table in the three-dimensional amplitude-index-running space.

We explore the likelihood in nine-dimensional parameter space, i.e., the Hubble parameter h , the baryon density $\Omega_{b0}h^2$, the amplitude and index of primordial power spectrum (A_s and n_s), the DM decay reionization parameter ζ , the total reionization optical depth τ_{re} , the SZ amplitude A_{SZ} , the decay rate normalized by Hubble parameter $\frac{\Gamma}{H_0}$, and the CDM density in early universe $\Omega_{\text{cdm,e}}h^2$. The parameter $\Omega_{\text{cdm,e}}$ is defined to be

$$\Omega_{\text{cdm,e}} \equiv \frac{(\rho_{\text{cdm}}a^3)|_{a \ll 1}}{\rho_{\text{crit0}}}, \quad (7.16)$$

where $\rho_{\text{crit0}} \equiv \frac{3H_0^2}{8\pi G}$ is today's critical density. As the CDM in our case decays, we made a distinction between $\Omega_{\text{cdm,e}}$ and $\Omega_{\text{cdm,0}}$ where the latter is defined to be the usual fractional CDM density today ($\rho_{\text{cdm0}}/\rho_{\text{crit0}}$).

7.3 Markov Chain Monte Carlo Results and Discussion

For the case with negligible reionization, we generated 8 MCMC chains, each of which contains about 3000 samples. The posterior probability density function of CDM decay rate can be directly calculated from the Markov Chains, as shown in Fig. 7.1. The corresponding 68.3% and 95.4% confidence level lower bounds on lifetime are $\Gamma^{-1} \gtrsim 230\text{Gyr}$ and $\Gamma^{-1} \gtrsim 100\text{Gyr}$, respectively. If we take the lifetime of universe to be 14Gyr, the 95.4% confidence level limit (i.e. lifetime 100Gyr) corresponds to a scenario that roughly 15% of CDM has decayed into relativistic particles by today.

In our analysis, all the early universe physics before recombination remains unchanged. The CMB power spectrum is however significantly modified due to two effects.

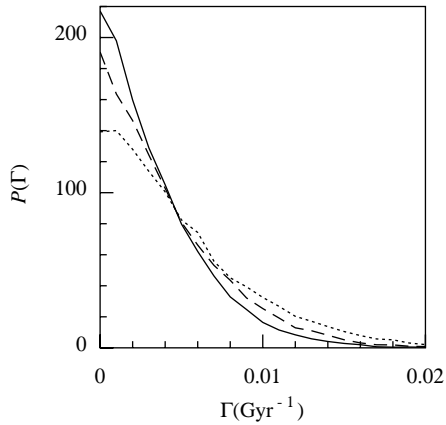


Figure 7.1: Posterior probability density function of the decay rate Γ . Solid line: using all the data sets. Dashed line: CMB + SN + LSS + $\text{Ly}\alpha$. Dotted line: CMB only. The probability density function is normalized as $\int P(\Gamma)d\Gamma = 1$.

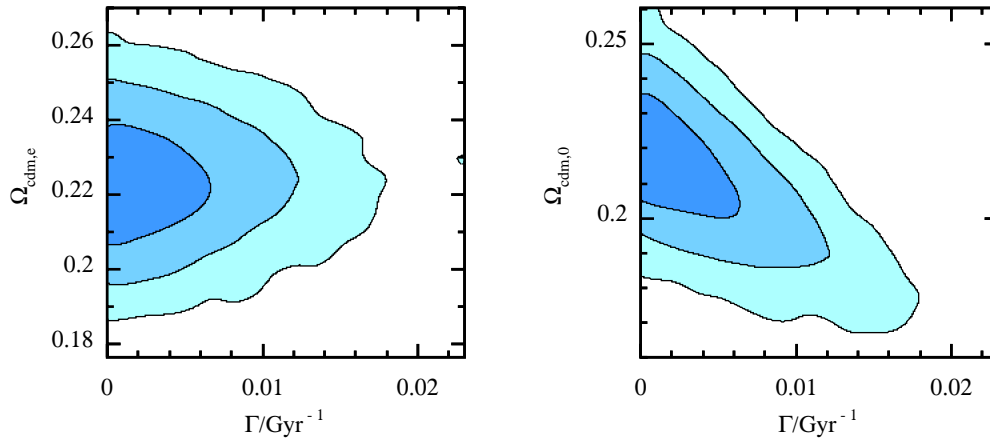


Figure 7.2: Constraints on the early universe CDM density parameter $\Omega_{\text{cdm},e}$ (defined in Eq. 7.16) and decay rate Γ , using all the data sets, is plotted on the left panel. For comparison, the present day CDM density parameter Ω_{c0} and decay rate Γ is plotted on the right panel. The inner and outer contours correspond to 68.3% and 95.4% confidence levels, respectively.

One is that the decay of CDM modifies the evolution of background, which results in a different distance to last scattering surface compared to the conventional case. The second one is that the decay of CDM affects the cosmological perturbations in late universe, resulting in an enhancement of the integrated Sachs-Wolfe (ISW) effect beyond that due to the cosmological constant. And it is this effect, anticipated by Kofman *et. al.* [351], that gives us the most restrictive bound on the lifetime of decaying dark matter for the scenario with negligible reionization.

Let us review the inconsistency between past papers on this issue. We start with Ref. [344]. Now, CMB and SN observations today can measure the fractional CDM density to a roughly 15% level [226] (within 95% confidence level). We will expect the constraints on CDM decay ratio to be the same order of magnitude. This simple estimation does not take into account the fact that the decayed product still forms part of the matter component (the equation of state is changed to $\frac{1}{3}$), and that the DM decay happens mostly at low redshift. Therefore if we do not take the cosmological perturbation into account, the data should allow about 15% dark matter to have decayed by today, i.e., we should not get a bound better than 100 Gyr. This simple analysis implies that the recent lower bound of lifetime ($\Gamma^{-1} > 700\text{Gyr}$ at 95.4% confidence level) obtained by Ref. [344], which does not take into consideration the impact of DM decay on cosmological perturbation (the location of first CMB peak is affected only through the change of background evolution), may not be credible. If indeed the CDM lifetime is 700Gyr, only about 2% of CDM has decayed into relativistic particles by today, and by the time of recombination, less than 10^{-6} of CDM has decayed. The change in background evolution is so tiny that it should not be detectable by current cosmological data.

To compare with Ichiki *et. al.* [9], we re-did the analysis using just the CMB data sets, and found the CDM lifetime $\Gamma^{-1} \gtrsim 70$ Gyr at 95.4% CL, which is consistent with their results. The reason we obtained a more constrained value than their $\Gamma^{-1} \gtrsim 52$ Gyr at 95.4% C.L. is probably because we used WMAP-5yr compared with their WMAP-1yr

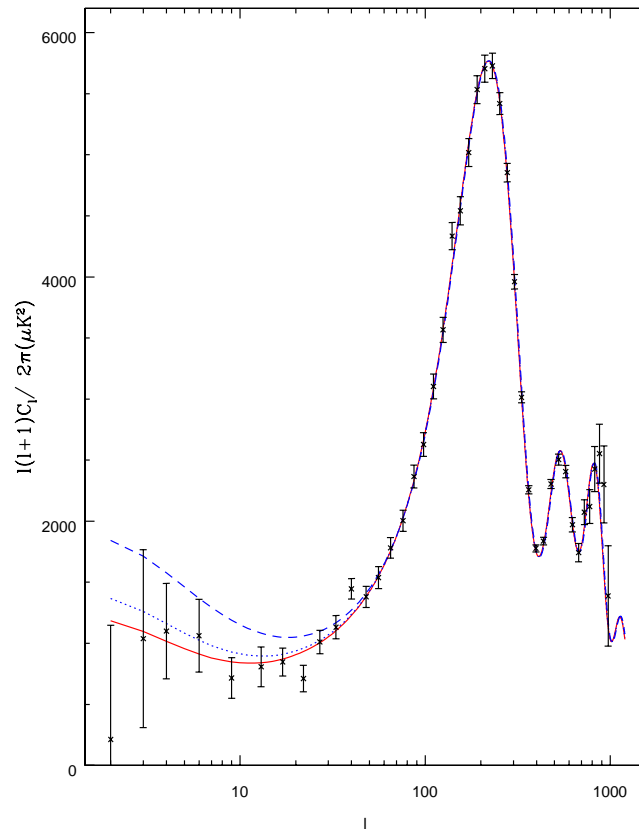


Figure 7.3: CMB power spectrum for different dark matter decay rate, assuming the decayed particles are relativistic and weakly interacting. For the CDM density parameter, we choose $\Omega_{\text{cdm},e}h^2$ to be the same as WMAP-5yr median $\Omega_{\text{c}0}h^2$. For the other cosmological parameters we use WMAP-5yr median values. By doing this, we have fixed the CDM to baryon ratio at recombination. In a similar plot in Ichiki *et. al.* [9] $\Omega_{\text{c}0}h^2$ is instead fixed. Therefore the height of first peak, which has dependence on CDM to baryon ratio at recombination, will significantly change as one varies the decay rate. In this plot the red line corresponds to a stable dark matter. The blue dotted line corresponds to dark matter with a lifetime 100 Gyr, and the blue dashed line 27 Gyr. The data points are WMAP-5yr temperature auto-correlation measurements.).

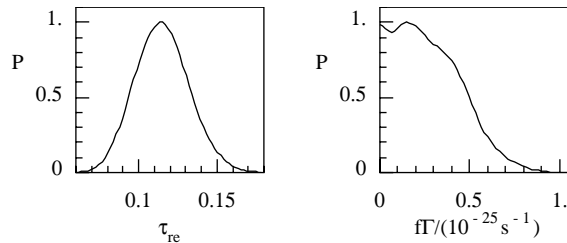


Figure 7.4: The marginalized posterior likelihood of the total optical depth and that of the DM decay reionization parameter.

dataset. We expect the WMAP-9yr dataset, when published and analyzed, to exhibit only a modest improvement because the information from the late time ISW effect is limited by cosmic variance. Recently, Lattanzi *et. al.* [345] obtained a bound of $\Gamma^{-1} \gtrsim 250$ Gyr at 95.4% C.L. with just the WMAP-3yr data, which is not consistent with both Ichiki *et. al.* and our results. We notice that in the Fig. 3 of their paper, the proximity between 68.3% and 95.4% confidence level bounds on Γ indicates a sudden drop of marginalized likelihood $\mathcal{L}(\Gamma)$. In our result, as shown in Fig. 7.1, this sudden drop feature is not seen.

Let us move on to the scenario where there is significant reionization due to the decaying dark matter. We generated another 8 MCMC chains, each of which contains about 6000 samples. The results of our analysis can be seen in Fig. 7.4 and 7.5, where we show the constraints on DM decay reionization parameter. A few things should be noted. Firstly, the sharp boundary (reflected in the closeness of the three contours) on the rising edge in Fig. 7.5 is due to the fact that for a given τ_{re} , DM decay has an upper limit because the optical depth due to DM decay should not extend beyond τ_{re} . Secondly, the plateau of likelihood around $f\Gamma = 0$ in Fig. 7.4 indicates that current CMB polarization data can only constrain the total optical depth, but cannot distinguish between DM decay reionization and star formation reionization. In other words, the data does not favor or disfavor DM decay reionization, as long as its contribution to total optical depth is not larger than the preferred τ_{re} .

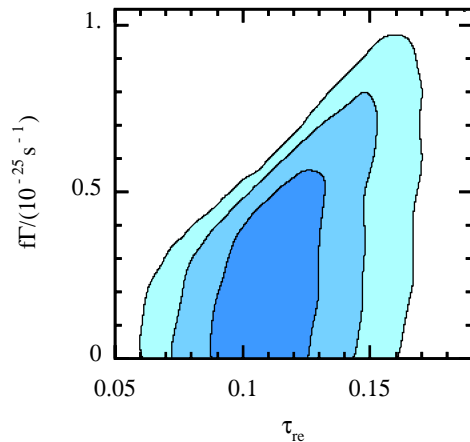


Figure 7.5: The marginalized 2D likelihood contours. The contours correspond to 68.3% , 95.4% and 99.7% confidence levels, respectively.

The constraint we have obtained is $f \Gamma \lesssim 0.59 \times 10^{-25} \text{s}^{-1}$ at 95.4% confidence level. This result is about a factor of 3 better than Ref. [346]. In the limit where reionization is negligible, Ref. [346] cannot give a strong bound on Γ because they have ignored the impact of DM decay on cosmological perturbations. Hence, their constraint on DM decay is essentially only from CMB polarization data. Our analysis, which combines many different cosmological data sets and includes the calculation of the impact of DM decay on all the observables, gives a stringent constraint on Γ even in the $f = 0$ limit. As for the limit of significant reionization, our bounds are, as mentioned earlier, a significant improvement over Ref. [346]. The difference may be due to the fact that we have used more data sets. However, the priors of the parameters may also alter the result. A notable difference between the models is due to the fact that one of the parameters they have adopted, the optical depth without DM decay, is ill-defined in our model. Also in their model, the cutoff of DM decay reionization at $z = 7$ was explicitly chosen. These differences might have led to Fig. 1 in their paper which shows a preference for a zero dark matter decay rate, which is absent in our analysis.

7.4 Implications for Particle Physics Models with Decaying Cold Dark Matter

Our results most certainly impose constraints on extensions of the Standard Model of particle physics (SM) with DM candidates. Making the assumption that DM decays into SM fields, we will investigate all the probable decay channels unless forbidden by either symmetry or kinematics, or highly suppressed by phase space considerations. We then sum up their partial decay widths to obtain the functional form for the lifetime of each of the decaying DM candidates. One might be worried about including even the decays to non-relativistic particles as that might invalidate our earlier assumption that cosmologically, the dark matter decay products are relativistic. While it is true that the DM particle can and will decay (provided it is not kinematically forbidden) into non-relativistic massive gauge bosons or heavy quarks, these heavy particles themselves will be assumed to subsequently decay very rapidly into much lighter particles of the SM that will be relativistic. Obviously in specific models, certain channels could be expressly forbidden by symmetries and this can also be handled by our analysis.

To obtain the functional form for the lifetime of the decaying DM, we will approach it from the point of view of effective field theory. We will do a model independent analysis by considering generic Lagrangian terms for these decays with the corresponding coupling constants acting as Wilson coefficients. Since the DM is electrically neutral, the total charge of decay products should also be zero. Moreover, the decay rates for different channels are dependent on the intrinsic spin of the DM because of possible spin-dependent couplings. Below we discuss the decays of DM with spin 0, 1/2 and 1. We will only consider decay processes of the lowest order, as higher-order processes involve more vertex insertions and so are assumed to be suppressed. Additionally in our approach, we will work in the framework where all the gauge symmetries (including those of Grand Unified Theories if present) except for $SU(3)_c \times U(1)_{em}$ are broken and the

effects encoded in the coupling constants of the effective operators. This can potentially give rise to naturally very small coupling constants as they could contain loop factors or powers of very small dimensionless ratios. This is a more cost-effective and model-independent way of taking into account the myriad possibilities of UV-completing the Standard Model of particle physics.

Having obtained the functional form of the lifetime in terms of the fundamental parameters of the underlying particle physics models, we can then compare it with the numerical value obtained from the cosmological analysis of the previous section. This would allow us to place definitive bounds on the fundamental parameters of candidate models for the particle physics theory beyond the Standard Model. It should be noted that we will be using the most conservative 95.4% confidence level bound on the lifetime of the decaying dark matter, i.e. without significant reionization. To assume otherwise would require a more complete knowledge of the ionization history of the universe than is currently understood.

Let us now proceed to the case of a generic scalar DM candidate and see how the above ideas are implemented.

7.4.1 Spin-0 Dark Matter

We first consider a spin-zero DM candidate, S . Decays into right-handed neutrinos and left-handed anti-neutrinos are not considered as the former may be more massive than S . Even if they are light enough for S to decay into, we expect the decay into SM (anti-) neutrinos to be dominant. For this decay channel, we can proceed in the same way as in the case of neutral pion decay. In the SM, (anti-) neutrinos couple to other matter in the form of the chiral current $\bar{\nu}_L \gamma^\mu \nu_L$ since S carries no Lorentz index. The lowest dimension operator responsible for this decay will be of the form $g_0 \bar{f} \gamma^\mu (1 + r_a \gamma_5) f \partial_\mu S / \Lambda$, where we parameterize g_0 as the coupling constant of dimension zero, and Λ is some cutoff scale. The presence or absence of γ_5 in the operator depends on whether S couples to the SM

neutrinos in a vectorial or axial-vectorial way. The corresponding decay rate is given by

$$\Gamma = \frac{g_0^2 r_a^2 m_f^2 m_S}{2\pi \Lambda^2} \sqrt{1 - 4 \frac{m_f^2}{m_S^2}}, \quad (7.17)$$

where m_f is the mass of the decay product. Here we have assumed that (anti-) neutrinos have Dirac mass.

We focus our attention on DM with mass $m_S \gg m_f$. Then for decay products such as (anti-) neutrinos (or other light SM particles), it is safe to make the approximation $1 - 4m_f^2/m_S^2 \simeq 1$. Since the neutrino is left handed, we take $r_a = -1$. If S decays dominantly into $\nu_e \bar{\nu}_e$, our lower bound on Γ then constrains the following parameter,

$$\frac{g_0^2 m_f^2 m_S}{\Lambda^2} \lesssim 1.3 \times 10^{-42} \text{GeV} \quad (95.4\% \text{ confidence level}), \quad (7.18)$$

where we have used $1 \text{Gyr}^{-1} = 2.087 \times 10^{-41} \text{GeV}$.

Here we can see that helicity suppression is at work. When the mass of the decaying particles is very small, the decay of the spin-zero DM candidate will be suppressed as expected. The presence of helicity suppression gives us a value of g_0 that is larger than in most other cases, as we will see. For example, if the mass of the DM candidate is $m_S \sim 100 \text{GeV}$, the neutrino mass around $m_f \sim 2 \text{eV}$, and the cutoff is $\Lambda \sim 10 \text{TeV}$, then the coupling constant g_0 has to be $\sim 10^{-11}$. If on the other hand the coupling constant g_0 is $\mathcal{O}(1)$ and we take the same values of the neutrino masses and of the DM candidate, then we have that $\Lambda \sim 10^{13} \text{GeV}$.

Table 7.1 in the Appendix lists out possible Lagrangian terms for the decay of S into SM particles, and the corresponding decay rates, summing over final state spins. Apart from focusing solely on the $S \rightarrow \nu \bar{\nu}$ channel, we can consider scenarios in which all the interaction terms in Table 7.1 are present to contribute to the decay rate of S , with all coupling constants of the same order of magnitude, g_0 . For simplicity, we will also assume $m_{\text{decay product}}/m_S$ is negligible compared to 1. This would immediately imply that the helicity-suppressed term, $g_0 \bar{f} \gamma^\mu (1 + r_a \gamma_5) f \partial_\mu S / \Lambda$, gives rise to insignificant decay rate

when compared to other terms. So the most relevant terms are the ones that come from the operator $g_0 S \bar{f}(1 + ir_p \gamma_5) f$. Then we have

$$\begin{aligned} \sum_{f \in \text{SM}} \Gamma(S \rightarrow f \bar{f}) &\approx \frac{g_0^2 m_S}{8\pi} (1 + r_p^2) \sum_{f \in \text{SM}} N_f \\ &= \frac{21 g_0^2 m_S}{8\pi} (1 + r_p^2). \end{aligned} \quad (7.19)$$

Here the decay to $t\bar{t}$ is not included as this channel may not be kinematically feasible for a DM particle of $\sim 100\text{GeV}$. The parameter r_p is also assumed to be the same for all f . In a similar way, rates for the other decays into SM gauge bosons can be worked out:

$$\begin{aligned} &\Gamma(S \rightarrow \gamma\gamma) + \Gamma(S \rightarrow gg) + \Gamma(S \rightarrow ZZ) + \Gamma(S \rightarrow W^+W^-) + \Gamma(S \rightarrow Z\gamma) \\ &\approx \frac{g_0^2 m_S}{64\pi} (80 + 640 + 82 + 81 + 10). \end{aligned} \quad (7.20)$$

Our result imposes an upper bound on the sum of decay rates via all the channels. Taking $r_p = 0$ as an example, our result would give us the constraint

$$g_0^2 m_S \lesssim 3.9 \times 10^{-44} \text{GeV} \quad (95.4\% \text{ confidence level}). \quad (7.21)$$

Messenger number violation in gauge-mediated supersymmetry breaking theories

Let us now investigate the messenger parity in gauge-mediated supersymmetry breaking theories. In these models, there could potentially be a dark matter candidate coming from the electromagnetically-neutral scalar field that is formed from the $SU(2)$ doublets of the $\mathbf{5}$ and $\bar{\mathbf{5}}$ of the messenger sector [360]. However, it is usually not easy to realize this because the lightest odd-messenger parity particle (LOMPP) often turns out not to be the electromagnetically-neutral field that we require. It has been claimed in the same paper that certain F-terms would lift the degeneracy. If we further assume that it does not significantly modify the effective low energy theory, the analysis becomes very much model-independent as there are only certain couplings that lead to decay of the LOMPP.

Following [360], the Kahler potential is given by

$$K = \int d^4\theta \left(\bar{5}_M^\dagger \bar{5}_M + 5_M^\dagger 5_M + \bar{5}_F^\dagger \bar{5}_F + 10_F^\dagger 10_F \right) + \frac{g_0}{M_p} \left(\bar{5}_M^\dagger 10_F^2 + 5_M^\dagger \bar{5}_F 10_F + h.c. \right), \quad (7.22)$$

where $\bar{5}_M$ and 5_M are the messengers and $\bar{5}_F$ and 10_F are the ordinary superfields. The terms that are Planck suppressed are the ones that violate messenger number by one unit.

As for the superpotential, we have

$$W = \int d^2\theta \rho \bar{5}_M 5_M + \frac{g'_0}{M_p} \bar{5}_M 10_F^3, \quad (7.23)$$

where ρ is the supersymmetry breaking spurion field and once again the terms that are Planck suppressed are dimension-5 messenger number violating terms. Without full knowledge of the UV-sensitive physics (F-terms that lift the other fields while retaining a viable LOMPP), we can still give an estimate of the order of magnitude of the decay rate of the LOMPP,

$$\Gamma \sim N \frac{g_0^2 m_{\text{mess}}^3}{M_p^2 \pi} F_k, \quad (7.24)$$

where N are the different degrees of freedom that the LOMPP can decay into. F_k is a function that contains the kinematic information and we will assume that is close to one. We can then put a constraint on the coupling constant and on the messenger mass. Since the lifetime is 100Gyr, then for $F_k \sim 1$ and $N \sim 100$, we have

$$g_0^2 \left(\frac{m_{\text{mess}}^3}{M_p^2} \right) \lesssim 6 \times 10^{-45} \text{GeV}, \quad (7.25)$$

where we have assumed one universal coupling constant g_0 . For the sake of discussion, if we consider a coupling constant of order one, we get a small messenger mass $m_{\text{mess}} \sim 0.02 \text{GeV}$. This can be improved if we go to dimension six operators which gives a generic decay rate of the form

$$\Gamma \sim \frac{N g_0^2 m_{\text{mess}}^5}{M_p^4 \pi} F, \quad (7.26)$$

Note that instead of a m_{mess}^3/M_p^2 suppression, we now have m_{mess}^5/M_p^4 . This gives a viable scenario since the messenger mass now needed is $m_{\text{mess}} \sim 4000$ TeV, for a coupling constant of order one.

7.4.2 Spin-1/2 Dark Matter

We now consider a massive DM of spin-1/2 (let us call it ψ) that decays into SM particles. Without a specific model, we assume ψ decays dominantly via two-body decays and focus our attention to this phenomenon. This means ψ must decay into one SM fermion f and one SM gauge boson G . Since the DM candidate must be neutral, the possibilities for a two body decay of spin 1/2 DM into SM particles are $(f, G) = (\nu, Z), (l^\pm, W^\mp)$. For the case that ψ is a Dirac fermion, the two-body decays are mediated by the effective operator $g_D G_\mu \bar{f} \gamma^\mu (1 + r \gamma_5) \psi + g_D^* G_\mu^* \bar{\psi} \gamma^\mu (1 + r \gamma_5) f$. The first term gives rise to ψ decay while the second one is responsible for the decay of $\bar{\psi}$. Again summing over the final state spins and averaging over the spin of the decaying ψ , we find the decay rate to be

$$\Gamma(\psi \rightarrow fG) = \Gamma(\bar{\psi} \rightarrow \bar{f}\bar{G}) = \frac{|g_D|^2 m_\psi^3}{16\pi m_G^2} \sqrt{\lambda\left(\frac{m_G}{m_\psi}, \frac{m_f}{m_\psi}\right)} \left[\omega\left(\frac{m_G}{m_\psi}, \frac{m_f}{m_\psi}\right) + r^2 \omega\left(\frac{m_G}{m_\psi}, -\frac{m_f}{m_\psi}\right) \right], \quad (7.27)$$

where $\lambda(a, b) = (1 + a - b)(1 - a - b)(1 - a + b)(1 + a + b)$ and $\omega(a, b) = (1 + a - b)(1 - a - b)[2a^2 + (1 + b)^2]$, and m_A denotes respectively the mass of particle A .

Now consider the case where the decay of the fermionic DM candidate comes from an operator $g_D \bar{\psi} H (1 + i r_p \gamma_5) f + g_D^* \bar{f} H (1 + i r_p \gamma_5) \psi$, where H is the Higgs bosonⁱⁱ of the SM. In this case the decay rate of $\psi \rightarrow H + \nu$ is given by

$$\Gamma(\psi \rightarrow H\nu) = \Gamma(\bar{\psi} \rightarrow H\bar{\nu}) = \frac{|g_D|^2 m_\psi}{16\pi} \sqrt{\lambda\left(\frac{m_H}{m_\psi}, \frac{m_f}{m_\psi}\right)} \left[z\left(\frac{m_f}{m_\psi}, \frac{m_H}{m_\psi}\right) + r_p^2 z\left(-\frac{m_f}{m_\psi}, \frac{m_H}{m_\psi}\right) \right], \quad (7.28)$$

ⁱⁱWe consider the Higgs in this particular case because this interaction would arise at the same or lower order than the other one we considered. With decaying DM of other spins, there would be an additional suppression from the ratio of electroweak scale over the cut-off scale.

where $z(a, b) = 1 + a^2 - b^2 + 2a$.

We can now consider a simple scenario in which $r = r_p = 0$ for all the decay channels and they all have the same coupling constant g_D . Then the total decay rate of ψ is given by summing over all the possible channels:

$$\begin{aligned} \Gamma(\psi \rightarrow 2 \text{ body}) &= 3 \Gamma(\psi \rightarrow Z\nu) + \Gamma(\psi \rightarrow W^+e^-) + \Gamma(\psi \rightarrow W^+\mu^-) \\ &\quad + \Gamma(\psi \rightarrow W^+\tau^-) + 3 \Gamma(\psi \rightarrow H\nu) \\ &= 126.5 |g_D|^2 \end{aligned} \quad (7.29)$$

where we have picked $m_\psi \sim 200\text{GeV}$, $H \sim 100\text{GeV}$ and assumed all three generations of neutrinos have masses $\sim 1\text{eV}$. The factor 3 in Equation (7.29) is for three generations of neutrinos. Our cosmological bound then gives us the constraint

$$\text{Dirac fermion : } |g_D| \lesssim 4.0 \times 10^{-23} \text{ (95.4\% confidence level)}. \quad (7.30)$$

For the case that ψ is a Majorana fermion, the above analysis follows through. Given the same interaction terms as those shown above, the partial decay rates of a Majorana ψ are exactly the same as Equations (7.27) and (7.28). There are, however, no distinction between ψ and $\bar{\psi}$ in this case any more. In a four-component spinor notation, ψ and $\bar{\psi}$ relate to each other via the charge conjugation matrix. This means the total decay rate of a Majorana ψ has contributions from decays into ‘particles’ and decays into ‘anti-particles’.

In the same simple scenario we considered above, the total decay rate of a Majorana ψ will be increased by a factor of 2 compared to Equation (7.29). The constraint on the coupling constant will correspondingly be tightened by a factor of $\sqrt{2}$:

$$\text{Majorana fermion : } |g_M| \lesssim 2.8 \times 10^{-23} \text{ (95.4\% confidence level)}. \quad (7.31)$$

R-parity violation in minimal supergravity models

Undoubtedly, the most thoroughly investigated models in the supersymmetric menagerie are the minimal supergravity (mSUGRA) models [361, 362, 363, 364, 365]. While the

theoretical motivation for universality of scalar masses, gaugino masses and trilinear terms is questionable (since these values depend on the mechanism by which supersymmetry breaking is transmitted to our sector), it has nevertheless remained a useful benchmark. For our purposes, it is sufficient for us to use the fact that in a variety of these mSUGRA models, the lightest supersymmetric particle (LSP) is a neutral particle that is overwhelmingly composed of the spin-1/2 supersymmetric partner of the B-gauge boson called the bino, \tilde{B} . There are of course technically natural classes of models [366, 367, 368] very similar to mSUGRA theories that will give bino as the LSP, and the analysis below would similarly apply to them.

In the presence of R-parity violation, the bino LSP would of course decay. Traditionally, theories with R-parity violation were often assumed to be unable to provide a dark matter candidate. Here, we can turn this around and ask what the couplings of the theory have to be so that the theory can still furnish us with viable dark matter candidate. To do that, we need to first explore the possible decays.

While the two-body decay might seem to have a more favorable phase space, these decays however would arise from Feynman diagrams [369] only if we have the R-parity violating terms together with the introduction of an additional loop and further suppression by dimensionless ratios of electroweak scale over the cut-off scale. We will therefore assume that the bino will dominantly decay into three SM particles via the trilinear R-parity violating terms. If for some particular models, one needs to add in some of the two-body decay terms, one can look up the Appendix or the previous subsection for the relevant cross-sections and include them in the overall analysis.

Neglecting all final state masses, the decay rate for a three-body bino decay is given by

$$\Gamma = \frac{1}{64\pi^3 m_{\tilde{B}}} \int_0^{\frac{1}{2}m_{\tilde{B}}} dE_1 \int_{\frac{1}{2}m_{\tilde{B}}-E_1}^{\frac{1}{2}m_{\tilde{B}}} dE_2 \sum_{\text{spins}} |\mathcal{M}|^2 \quad (7.32)$$

where E_i is the energy of the final particle i^{iii} , and the summation symbol means averaging

ⁱⁱⁱOf course the identification of a final particle as particle i is arbitrary. This arbitrariness does not

over initial spins and summing over final spins. The amplitudes squared for three-body decays of neutralino due to trilinear R-parity violating terms have been evaluated and shown in [370, 371, 335], with the appropriate spin summing/averaging. Strictly speaking a neutralino is a superposition of the bino and three other fermionic supersymmetric particles but for our purposes, it is sufficient to consider the bino to the lightest neutralino and the LSP. The results in [371] can be easily applied to LSP decay by demanding the neutralino has a 100% bino component, i.e. by setting $N_{\chi_1} = 1$ and $N_{\chi_n} = 0, n = 2, 3, 4$ in the notation of [371]. For simplicity, all final state masses are neglected in the analysis below. We have also ignored the mixings and the widths of the sfermions, which mediate the decay as internal lines in the Feynman diagrams.

Given the R-parity violating superpotential term

$$W_{\text{LLE}} = \epsilon^{\sigma\rho} \lambda_{ijk} L_{i\sigma} L_{j\rho} E_k^c \quad (7.33)$$

(where i, j and k , each of which runs from 1 to 3, are generation indices, σ and ρ are $SU(2)_L$ indices, and the superscript c indicates charge conjugation), the decay channel $\tilde{B} \rightarrow e_i^+ \bar{\nu}_j e_k^-$ is possible. Using the generic expression for amplitude squared in [371] and putting in our simplifications, we get the decay rate

$$\begin{aligned} \Gamma(\tilde{B} \rightarrow e_i^+ \bar{\nu}_j e_k^-) &= \frac{8}{128\pi^3} |\lambda_{ijk}|^2 g'^2 m_{\tilde{B}} \left[2Y_L^2 K\left(\frac{m_{\tilde{e}_i}}{m_{\tilde{B}}}\right) + 2Y_L^2 K\left(\frac{m_{\tilde{\nu}_j}}{m_{\tilde{B}}}\right) \right. \\ &\quad + 2Y_E^2 K\left(\frac{m_{\tilde{e}_k}}{m_{\tilde{B}}}\right) - 2Y_L^2 P\left(\frac{m_{\tilde{\nu}_j}}{m_{\tilde{B}}}, \frac{m_{\tilde{e}_i}}{m_{\tilde{B}}}\right) + 2Y_L Y_E P\left(\frac{m_{\tilde{e}_k}}{m_{\tilde{B}}}, \frac{m_{\tilde{e}_i}}{m_{\tilde{B}}}\right) \\ &\quad \left. + 2Y_L Y_E P\left(\frac{m_{\tilde{e}_k}}{m_{\tilde{B}}}, \frac{m_{\tilde{\nu}_j}}{m_{\tilde{B}}}\right) \right] \quad (7.34) \end{aligned}$$

where g' is the gauge coupling of $U(1)_Y$, $m_{\tilde{f}_n}$ is the mass of the scalar superpartner of particle \tilde{f}_n and Y_S denotes the hypercharge of a superfield S (for example, $Y_E = -1$). $K(x)$ and $P(x, y)$ are functions defined in the Appendix.

Another trilinear R-parity violating superpotential term is

$$W_{\text{LQD}} = \epsilon^{\sigma\rho} \lambda'_{ijk} L_{i\sigma} Q_{j\rho\alpha} D_{k\alpha}^c \quad (7.35)$$

change the final expression for Γ .

with the $SU(3)_c$ index α . This term gives rise to the decays $\tilde{B} \rightarrow e_i^+ \bar{u}_j d_k$ and $\tilde{B} \rightarrow \bar{\nu}_i \bar{d}_j d_k$. The decay rates for these channels are similar to the one above, with the appropriate substitution of superpartner masses and prefactors:

$$\begin{aligned} \Gamma(\tilde{B} \rightarrow e_i^+ \bar{u}_j d_k) &= \frac{6}{128\pi^3} |\lambda'_{ijk}|^2 g'^2 m_{\tilde{B}} \left[2Y_L^2 K \left(\frac{m_{\tilde{e}_i}}{m_{\tilde{B}}} \right) + 2Y_Q^2 K \left(\frac{m_{\tilde{u}_j}}{m_{\tilde{B}}} \right) \right. \\ &\quad + 2Y_D^2 K \left(\frac{m_{\tilde{d}_k}}{m_{\tilde{B}}} \right) - 2Y_L Y_Q P \left(\frac{m_{\tilde{u}_j}, m_{\tilde{e}_i}}{m_{\tilde{B}}, m_{\tilde{B}}} \right) + 2Y_L Y_D P \left(\frac{m_{\tilde{d}_k}, m_{\tilde{e}_i}}{m_{\tilde{B}}, m_{\tilde{B}}} \right) \\ &\quad \left. + 2Y_Q Y_D P \left(\frac{m_{\tilde{d}_k}, m_{\tilde{u}_j}}{m_{\tilde{B}}, m_{\tilde{B}}} \right) \right] \end{aligned} \quad (7.36)$$

and

$$\begin{aligned} \Gamma(\tilde{B} \rightarrow \bar{\nu}_i \bar{d}_j d_k) &= \frac{6}{128\pi^3} |\lambda'_{ijk}|^2 g'^2 m_{\tilde{B}} \left[2Y_L^2 K \left(\frac{m_{\tilde{\nu}_i}}{m_{\tilde{B}}} \right) + 2Y_Q^2 K \left(\frac{m_{\tilde{d}_j}}{m_{\tilde{B}}} \right) \right. \\ &\quad + 2Y_D^2 K \left(\frac{m_{\tilde{d}_k}}{m_{\tilde{B}}} \right) - 2Y_L Y_Q P \left(\frac{m_{\tilde{d}_j}, m_{\tilde{\nu}_i}}{m_{\tilde{B}}, m_{\tilde{B}}} \right) + 2Y_L Y_D P \left(\frac{m_{\tilde{d}_k}, m_{\tilde{\nu}_i}}{m_{\tilde{B}}, m_{\tilde{B}}} \right) \\ &\quad \left. + 2Y_Q Y_D P \left(\frac{m_{\tilde{d}_k}, m_{\tilde{d}_j}}{m_{\tilde{B}}, m_{\tilde{B}}} \right) \right]. \end{aligned} \quad (7.37)$$

Note that the numerical value of an $SU(3)_c$ colour factor has been included in the prefactors of Equations (7.36) and (7.37).

In a similar way, the decay channel $\tilde{B} \rightarrow \bar{u}_i \bar{d}_j \bar{d}_k$ is allowed by the superpotential term

$$W_{UDD} = \epsilon^{\alpha\beta\gamma} \lambda''_{ijk} U_{i\alpha}^c D_{j\beta}^c D_{k\gamma}^c, \quad (7.38)$$

where α , β and γ are all $SU(3)_c$ indices. The corresponding decay rate is

$$\begin{aligned} \Gamma(\tilde{B} \rightarrow \bar{u}_i \bar{d}_j \bar{d}_k) &= \frac{48}{128\pi^3} |\lambda''_{ijk}|^2 g'^2 m_{\tilde{B}} \left[2Y_U^2 K \left(\frac{m_{\tilde{u}_i}}{m_{\tilde{B}}} \right) + 2Y_D^2 K \left(\frac{m_{\tilde{d}_j}}{m_{\tilde{B}}} \right) \right. \\ &\quad + 2Y_D^2 K \left(\frac{m_{\tilde{d}_k}}{m_{\tilde{B}}} \right) - 2Y_U Y_D P \left(\frac{m_{\tilde{d}_j}, m_{\tilde{u}_i}}{m_{\tilde{B}}, m_{\tilde{B}}} \right) - 2Y_U Y_D P \left(\frac{m_{\tilde{d}_k}, m_{\tilde{u}_i}}{m_{\tilde{B}}, m_{\tilde{B}}} \right) \\ &\quad \left. - 2Y_D^2 P \left(\frac{m_{\tilde{d}_k}, m_{\tilde{d}_j}}{m_{\tilde{B}}, m_{\tilde{B}}} \right) \right]. \end{aligned} \quad (7.39)$$

Here a different $SU(3)_c$ colour factor has been included in the prefactor.

It should be pointed out that the bino is a Majorana fermion. This means what we shown above is only half of its possible decay channels: the other decay channels are

obtained by applying charge conjugation to all the final particles in any of the above channels. The decay rates, however, are invariant under charge conjugation.

Because the LLE term contains two copies of L 's and they contract with the Levi-Civita tensor, λ_{ijk} is anti-symmetric in i and j . Thus it only represents nine couplings. Similarly, λ''_{ijk} is anti-symmetric in j and k . This argument is not applicable to λ'_{ijk} , so it does indeed contain 27 couplings (see, for example, [370, 371, 335]).

As a simple application of our cosmological constraint on the DM decay rate, we assume $m_{\tilde{B}} \sim 100\text{GeV}$ and all the sfermions have masses $\sim 300\text{GeV}$. We also assume all the non-zero R-parity violating couplings attain the same value λ , i.e.

$$\lambda_{i_1 j_1 k_1} = \lambda'_{i_2 j_2 k_2} = \lambda''_{i_3 j_3 k_3} = \lambda, \quad i_1 \neq j_1, j_3 \neq k_3. \quad (7.40)$$

Summing over all the possible 3-body decay channels of bino, the total decay rate is given by

$$\begin{aligned} \Gamma(\tilde{B} \rightarrow 3 \text{ body}) &= 2 [9 \Gamma(\tilde{B} \rightarrow e_i^+ \bar{\nu}_j e_k^-) + 27 \Gamma(\tilde{B} \rightarrow e_i^+ \bar{u}_j d_k) \\ &\quad + 27 \Gamma(\tilde{B} \rightarrow \bar{\nu}_i \bar{d}_j d_k) + 9 \Gamma(\tilde{B} \rightarrow \bar{u}_i \bar{d}_j \bar{d}_k)] \\ &= 0.00144 |\lambda|^2 \end{aligned} \quad (7.41)$$

where we have used $g' = 0.36$. Our cosmological bound then constrain the coupling constant to be

$$|\lambda| \lesssim 1.2 \times 10^{-20} \text{ (95.4\% confidence level)}. \quad (7.42)$$

In comparison, one of the strongest constraint on R-parity violation comes from the consequent baryon number violation that arises due to the former. Ref. [372] gives a value of $\lambda'' \lesssim 10^{-9}$ for the most constrained of all the λ 's. So if indeed the assumption that we have bino-like DM holds true, then the most stringent limits on R-parity violation would come from our analysis.

7.4.3 Spin-1 Dark Matter

We now consider a massive DM of spin-1 (let us call it χ) that decays into SM particles. Since the χ^μ field carries one Lorentz index, it contracts with other SM fields differently from the spin-0 DM, thus giving rise to different interaction terms and decay rates.

In contrast to the decay of spin-0 DM, helicity suppression is not observed in the decay of $\chi \rightarrow \nu\bar{\nu}$. χ^μ can directly coupled to the neutrino current $\bar{\nu}_L\gamma_\mu\nu_L$, without any insertion of ∂^μ . On the other hand, every spin-1 particle has to obey the Landau-Yang theorem [373, 374] which states that because of rotational invariance, it cannot decay into two massless spin-1 particles. Hence, the decays $\chi \rightarrow \gamma\gamma$ and $\chi \rightarrow gg$ are not allowed. The possible partial decay widths (with summing over final state spins and averaging over the initial state spin) for a spin-1 DM are rather numerous and not that illuminating to list them all here. So we have relegated them to Table 7.4 in the Appendix. In the case where the DM is indeed an additional U(1) gauge field that is massive, the possibility of kinetic mixing with the photon [375] must be considered. Such a term could be radiatively generated via exchange of a field that is charged under both U(1)'s. Following Refs.[376, 377], we can manipulate the Lagrangian into a form where the mixing manifests itself in the coefficients of the following terms, $g_1\chi_\mu\bar{f}\gamma^\mu(1+r\gamma_5)f$. But this is a term that has already been considered in Table 7.4.

To get a feel for the numbers involved, let us now consider a simple model where all the interaction terms in Table 7.4 exist, with all the coupling constants real and of the same order of magnitude. Again, we will also assume $m_{\text{decay product}}/m_\chi \ll 1$. Then

$$\Gamma(\chi \rightarrow Z\gamma) + \Gamma(\chi \rightarrow ZZ) + \Gamma(\chi \rightarrow W^+W^-) \approx \frac{g_1^2 m_\chi^3}{96\pi} \left(\frac{5}{m_Z^2} + \frac{2}{m_Z^2} + \frac{4}{m_W^2} \right). \quad (7.43)$$

Because m_f/m_χ is small for the value of m_χ we are considering,

$$\begin{aligned} \sum_{f \in \text{SM}} \Gamma(\chi \rightarrow f\bar{f}) &\approx \frac{g_1^2 m_\chi}{12\pi} (1+r^2) \sum_{f \in \text{SM}} N_f \\ &= \frac{7g_1^2 m_\chi}{4\pi} (1+r^2). \end{aligned} \quad (7.44)$$

Similar to the case of spin-0 DM, the decay to $t\bar{t}$ is not included here, and the parameter r is also assumed to be the same for all f . Note also that we have different m_χ dependence for the decays into fermion-antifermion and massive gauge bosons, unlike in the spin-0 case.

Our result then gives an upper bound on the sum of all the decay rates into SM particles. For illustration, we consider $m_\chi \sim 100\text{GeV}$ and $r = 0$. Our bound on Γ can then be translated into a constraint on the coupling constant:

$$g_1 \lesssim 5.8 \times 10^{-23} \text{ (95.4\% confidence level)}, \quad (7.45)$$

where we have substituted $m_W = 80\text{GeV}$ and $m_Z = 91\text{GeV}$.

T-Parity violation in little Higgs models

Little Higgs models with T-parity violation is another possible scenario in which the dark matter candidate decays. Analogous to R-parity in SUSY models, all non-SM particles in Little Higgs model are assigned to be T-odd, while all SM ones T-even. The T-parity then requires all coupling terms to have an even number of non-SM fields. This forbids the contribution of the non-SM particles to the oblique electroweak parameters, and consequently, the symmetry breaking scale f can be lowered to about 1TeV [378]. The Lightest T-odd Particle (LTOP), moreover, is stable and has often been nominated as a dark matter candidate.

However, Ref. [334] has pointed out that anomalies in general give rise to a Wess-Zumino-Witten (WZW) term, which breaks the T-parity (Refs.[379, 380] have constructed Little Higgs models free of the usual WZW term). This means the LTOP is not exactly stable. Indeed, phenomenological consequences of the WZW term in the Littlest Higgs model have been studied in Ref. [381, 382]. In their model, the LTOP is the massive partner of photons (denoted by A_H) and the WZW term contains direct couplings of A_H to the Standard Model W bosons, Z bosons and photons. Ref. [382],

moreover, pointed out that such couplings can generate two-body decay of A_H to SM fermions, $A_H \rightarrow f\bar{f}$, via triangular loop diagrams.

In an attempt to be as model-independent as possible, we parameterize the couplings of A_H to the SM gauge bosons as

$$L \supset -\frac{g'}{f^2}\epsilon_{\mu\nu\rho\sigma}A_H^\mu[N_Z m_Z^2 Z^\nu \partial^\rho Z^\sigma + N_W m_W^2 (W^{+\nu} \partial^\rho W^{-\sigma} + W^{-\nu} \partial^\rho W^{+\sigma}) + N_{AZ} m_Z^2 Z^\nu F^{\rho\sigma}], \quad (7.46)$$

where f is the symmetry breaking scale, g' the $U(1)$ gauge coupling, N_Z , N_W and N_{AZ} are numbers whose values depend on the exact realization and the UV completion.

Generically, the mass of A_H is proportional to f . If we take f to be the natural symmetry breaking scale (i.e. $\sim 1\text{TeV}$) in Little Higgs models, then $m_{A_H} \gtrsim 2m_Z$. As an example, in [381, 382], we have

$$m_{A_H} = \frac{g'f}{\sqrt{5}} \left[1 - \frac{5v^2}{8f^2} + \mathcal{O}\left(\frac{v^4}{f^4}\right) \right], \quad (7.47)$$

where $v = 246\text{GeV}$ is the Higgs vev. The condition for $m_{A_H} \gtrsim 2m_Z$ is satisfied when $g' \sim 0.36$ and $f \gtrsim 1165\text{GeV}$.

In the case of $m_{A_H} \gtrsim 2m_Z$, the decay channels of $A_H \rightarrow ZZ$ and $A_H \rightarrow W^+W^-$ are kinematically allowed, and, for simplicity, we assume these processes (together with $A_H \rightarrow Z\gamma$) to be the dominant ones. With the interaction terms in equation (7.46), the decay rates for these channels at the lowest order are given by

$$\Gamma(A_H \rightarrow ZZ) = \frac{g'^2 N_Z^2 m_{A_H}^3 m_Z^2}{96\pi f^4} \left(1 - 4\frac{m_Z^2}{m_{A_H}^2} \right)^{\frac{5}{2}}, \quad (7.48)$$

$$\Gamma(A_H \rightarrow W^+W^-) = \frac{g'^2 N_W^2 m_{A_H}^3 m_W^2}{48\pi f^4} \left(1 - \frac{m_W^2}{m_{A_H}^2} \right)^{\frac{5}{2}}, \quad (7.49)$$

$$\Gamma(A_H \rightarrow Z\gamma) = \frac{g'^2 N_{AZ}^2 m_{A_H}^3 m_Z^2}{24\pi f^4} \left(1 + \frac{m_Z^2}{m_{A_H}^2} \right) \left(1 - \frac{m_Z^2}{m_{A_H}^2} \right)^3. \quad (7.50)$$

The sum of these decay rates is then constrained by our bound on the dark matter lifetime. For the Littlest Higgs model, $N_{AZ} = 0$ and $N_W = N_Z$. The sum of the above decay rates is then reduced to

$$\Gamma = \frac{g'^5 N_Z^2 m_Z^2}{160\sqrt{5}\pi f}, \quad (7.51)$$

where we have used the approximations $m_W \simeq m_Z$, $m_{A_H} \simeq g'f/\sqrt{5}$ and have neglected all the mass ratios. Our bound on Γ then gives us the constraint

$$\frac{N_Z^2}{f} < 4.7 \times 10^{-42} \text{GeV} \text{ (95.4\% confidence level)}, \quad (7.52)$$

which of course is not reasonable as we typically expect $N_Z \sim 1$ and $f \sim 1$ TeV. But it vividly illustrates the utility of our approach when it comes to ruling out particle physics models that claim to have dark matter candidates.

7.4.4 General Dimensional Considerations

We can draw some generalizations from the above cases if we do a simple dimensional analysis. The coupling of a spin-0, spin-1/2 or spin-1 dark matter candidate S to an operator O can be parameterized, with suppression of indices and $\mathcal{O}(1)$ factors, as

$$L \supset g \frac{S}{\Lambda^{n-4}} O, \quad (7.53)$$

where g is a dimensionless coupling constant, Λ is the scale where unknown new physics is integrated out to give the operator O , and n is the sum of the dimensions of S and O . The decay rate for such dark matter candidate is given in general by

$$\Gamma = \frac{g^2}{\Lambda^{2n-8}} m_S^{2n-7} F_k, \quad (7.54)$$

where F_k is a function that contains the kinematics of the decay, assumed to be of order one for simplicity. For $n = 5$, $m_S = 100 \text{ GeV}$ and $g \sim \mathcal{O}(1)$, the cutoff scale should be of the order of $\Lambda \gtrsim 10^{24} \text{ GeV}$, suggesting that we must go to operators of higher dimensions and thus more Λ suppression. For $n = 6$, $m_S = 100 \text{ GeV}$ and $g \sim \mathcal{O}(1)$, the cutoff scale can be as low as $\Lambda \sim 10^{13} \text{ GeV}$. On the other hand, for $n = 5$, if the cutoff is taken at the Planck scale ($\Lambda \sim 10^{19} \text{ GeV}$) and we keep the same value of m_S , the coupling constant can only be as large as $g \sim 10^{-5}$. Finally to recover the cases discussed above for spin-0, spin-1/2 and spin-1 particles, we can take $n = 4$ and $m_S \sim 100 \text{ GeV}$ to give us a coupling constant as large as $g \sim 10^{-22}$.

A few words should be reiterated about the smallness of the coupling constant. We had taken an extremely conservative value for our cutoffs, usually ~ 10 TeV. In an effective theory with a low cutoff arising from a high scale fundamental theory, say at Planck scale, there will be a multitude of effective operators containing mass insertions (leading to small dimensionless ratios such as m/M_P) or loops (giving factors of $1/16\pi^2$), making these tiny coupling constants natural. The small dimensionless ratios could arise from, say, the decay being mediated by some massive field much like what we have in proton decay via exchange of heavy X bosons in the context of Grand Unified Theories. The onus is then on the model builders to refine their models in a technically natural way to satisfy the constraints we have derived above without having to compromise other phenomenological constraints on their models.

7.5 Conclusions and Outlook

We have performed a full cosmological analysis using the available data sets from cosmic microwave background, Type Ia supernova, Lyman- α forest, galaxy clustering and weak lensing observations to determine the extent by which we can constrain decaying dark matter models which are very typical in most extensions of the Standard Model of particle physics.

In the scenario where there is negligible reionization of the baryonic gas by the decaying dark matter, we have found that the late-time Integrated Sachs-Wolfe effect gives the strongest constraint. The lifetime of a decaying dark matter has the bound $\Gamma^{-1} \gtrsim 100\text{Gyr}$ (at 95.4% confidence level). Because of cosmic variance, the results are not likely to improve significantly with the WMAP-9yr data.

When there is significant reionization of the baryonic gas due to the decaying dark matter, the bounds become more restrictive as the CMB polarization is well measured. In this scenario, the lifetime of a decaying dark matter is $(f\Gamma)^{-1} \gtrsim 5.3 \times 10^8 \text{ Gyr}$ (at

95.4% confidence level) where f is a phenomenological factor related to the degree of reionization. With even more CMB polarization data, one could conceivably distinguish the reionization due to decaying dark matter from reionization due to star formation, thereby giving us even better bounds on the lifetime of the dark matter. We expect that the the 21cm cosmological observation in the future would give us even greater precision as it is expected to probe the reionization history at redshifts $6 < z < 30$.

Having obtained the cosmological constraints, we turned our attentions to the particle physics aspects of it. For completeness and motivated by the utility of such an exercise, we systematically tabulated the decay cross-sections for a spin-0, spin-1/2 and spin-1 dark matter candidate into the Standard Model degrees of freedom. This enabled us to simply sum up all the relevant contributions for a particular model of particle physics and arrive at the functional form of the lifetime of the decaying dark matter. We repeated this process for a variety of representative models from the following classes of theories: generic supersymmetric scenario, gauge-mediated supersymmetry breaking models and the little Higgs theories. Imposing the limits from our cosmological analysis, we find that generically for most models we have looked at, the dimensionless coupling for a decaying dark matter to Standard Model fields should be smaller than 10^{-22} .

This restriction can be slightly relaxed if the dark matter decays solely into light particles via helicity suppressed interaction terms, in which case, the small mass of the decay products suppresses the decay rate. If, for instance, the dark matter decays purely via helicity suppressed terms into $\nu\bar{\nu}$ with Dirac mass of $\sim 2\text{eV}$, then the dimensionless coupling can be as large as 10^{-11} . In addition to constraining the coupling, one can assume it to be of $\mathcal{O}(1)$ and estimate the scale of new physics which suppresses the decay rate. In all cases, either the coupling attains a small value or the new physics come from a huge scale, both of which would need interesting and exotic physics to realize if indeed the dark matter does decay via dimension-4 or dimension-5 terms. In the case of exclusive helicity suppressed decays, moreover, one has to explain why other interaction

terms are absent in the model. A more promising avenue, which we briefly mentioned in the previous section, is to look at models where the dark matter decays via dimension-6 operators. The Large Hadron Collider might provide us with the identity for dark matter in the very near future, but on the basis of our analysis, there will still be much to understand about physics of the dark matter sector and how it interacts with the Standard Model.

In a future work, we hope to address some of the astrophysical issues of decaying dark matter. The recent spate of results from astrophysical experiments [383, 384, 385, 386] has given us much to ponder. The immediate goal would of course be to combine all the astrophysical data sets with the cosmological ones that we have considered in the present work and arrive at a set of characteristics that a phenomenologically viable decaying dark matter must possess. However, we expect considerable tension between the two classes of constraints. The astrophysical ones require that the decays to be significant enough to account for the as-yet-unexplained phenomena, while the cosmological ones need decays to be small enough because of the late time ISW effect and the CMB polarization observations. To reconcile and resolve these two seemingly conflicting classes of observations could be the defining challenge of dark matter physics in the next decade.

7.6 Appendix: Compendium of Decay Rates

This appendix summarizes the lowest order decay rates due to various generic interaction terms in the Lagrangian, averaging over the spin of the DM and summing over the spins of the decay products. Tables 7.1, 7.2 and 7.4 respectively tabulate the decay of a spin-0 DM particle S , a spin-1/2 DM particle ψ and a spin-1 DM particle χ , into SM particles. In a model-independent way, we write down generic Lagrangian terms which describe possible decay channels of DM particles to SM particles. The exact mechanisms which mediate these decays are captured by the dimensionless coupling constants, g_0 , g_D and

g_1 . The reality of the interaction terms requires the coupling constants to be real, except in the case of $\chi \rightarrow W^+W^-$ and the decay of ψ , in which a complex coupling constant is possible.

We follow standard conventions in denoting our fields. Y^μ represents a gauge field while $Y^{\mu\nu}$ is the corresponding field strength tensor. For various decay channels, N_f and N_g respectively denote the number of colours of a fermion species f and a gluon g . r , r_p and r_a are parameters that describe the relative size of two interaction terms.

Table 7.1: Decay Rate of Spin-0 DM via Different Interaction Terms

Interaction Term	Decay Rate
$g_0 S \bar{f}(1 + ir_p \gamma_5) f$	$\Gamma(S \rightarrow f \bar{f}) = \frac{g_0^2 m_S N_f}{4\pi} \sqrt{1 - 4 \frac{m_f^2}{m_S^2}} \times \left(\frac{1+r_p^2}{2} - 2 \frac{m_f^2}{m_S^2} \right)$
$\frac{g_0}{\Lambda} \bar{f} \gamma^\mu (1 + r_a \gamma_5) f \partial_\mu S$	$\Gamma(S \rightarrow f \bar{f}) = \frac{g_0^2 r_a^2 N_f}{2\pi} m_f \frac{m_f m_S}{\Lambda^2} \sqrt{1 - 4 \frac{m_f^2}{m_S^2}}$
$\frac{g_{0s}}{\Lambda} S F_{\mu\nu} F^{\mu\nu}$	$\Gamma(S \rightarrow \gamma\gamma) = \frac{g_{0s}^2 m_S^3}{4\pi \Lambda^2}$
$\frac{g_{0p}}{\Lambda} S \epsilon_{\mu\nu\sigma\lambda} F^{\mu\nu} F^{\sigma\lambda}$	$\Gamma(S \rightarrow \gamma\gamma) = \frac{g_{0p}^2}{\pi \Lambda^2} m_S^3$
$\frac{g_{0s}}{\Lambda} S G_{\mu\nu}^a G^{a,\mu\nu}$	$\Gamma(S \rightarrow gg) = \frac{g_{0s}^2 m_S^3 N_g}{4\pi \Lambda^2}$
$\frac{g_{0p}}{\Lambda} S \epsilon_{\mu\nu\sigma\lambda} G^{a,\mu\nu} G^{a,\sigma\lambda}$	$\Gamma(S \rightarrow gg) = \frac{g_{0p}^2}{\pi \Lambda^2} N_g m_S^3$
$\frac{g_0 m_Z^2}{\Lambda} S Z_\mu Z^\mu$	$\Gamma(S \rightarrow ZZ) = \frac{g_0^2 m_S^3}{32\pi \Lambda^2} \sqrt{1 - 4 \frac{m_Z^2}{m_S^2}} \times \left(1 - 4 \frac{m_Z^2}{m_S^2} + 12 \frac{m_Z^4}{m_S^4} \right)$
$\frac{g_{0s}}{\Lambda} S Z_{\mu\nu} Z^{\mu\nu}$	$\Gamma(S \rightarrow ZZ) = \frac{g_{0s}^2 m_S^3}{4\pi \Lambda^2} \sqrt{1 - 4 \frac{m_Z^2}{m_S^2}} \times \left(1 - 4 \frac{m_Z^2}{m_S^2} + 6 \frac{m_Z^4}{m_S^4} \right)$
$\frac{g_{0p}}{\Lambda} S \epsilon_{\mu\nu\sigma\lambda} Z^{\mu\nu} Z^{\sigma\lambda}$	$\Gamma(S \rightarrow ZZ) = \frac{g_{0p}^2 m_S^3}{\pi \Lambda^2} \left(1 - 4 \frac{m_Z^2}{m_S^2} \right)^{\frac{3}{2}}$
$\frac{g_0 m_W^2}{\Lambda} S W_\mu^+ W^{-\mu}$	$\Gamma(S \rightarrow W^+W^-) = \frac{g_0^2 m_S}{64\pi \Lambda^2} \sqrt{1 - 4 \frac{m_W^2}{m_S^2}} \times \left(1 - 4 \frac{m_W^2}{m_S^2} + 12 \frac{m_W^4}{m_S^4} \right)$
$\frac{g_{0s}}{\Lambda} S W_{\mu\nu}^+ W^{-\mu\nu}$	$\Gamma(S \rightarrow W^+W^-) = \frac{g_{0s}^2 m_S^3}{4\pi \Lambda^2} \sqrt{1 - 4 \frac{m_W^2}{m_S^2}} \times \left(1 - 4 \frac{m_W^2}{m_S^2} + 6 \frac{m_W^4}{m_S^4} \right)$
$\frac{g_{0p}}{\Lambda} S \epsilon_{\mu\nu\sigma\lambda} W^{+\mu\nu} W^{-\sigma\lambda}$	$\Gamma(S \rightarrow W^+W^-) = \frac{g_{0p}^2 m_S^3}{\pi \Lambda^2} \left(1 - 4 \frac{m_W^2}{m_S^2} \right)^{\frac{3}{2}}$
$\frac{g_{0s}}{\Lambda} F^{\mu\nu} Z_\mu \partial_\nu S$	$\Gamma(S \rightarrow Z\gamma) = \frac{g_{0s}^2 m_S^3}{32\pi \Lambda^2} \left(1 - \frac{m_Z^2}{m_S^2} \right)^3$
$\frac{g_{0p}}{\Lambda} \epsilon_{\mu\nu\sigma\lambda} F^{\mu\nu} Z^\sigma \partial^\lambda S$	$\Gamma(S \rightarrow Z\gamma) = \frac{g_{0p}^2 m_S^3}{8\pi \Lambda^2} \left(1 - \frac{m_Z^2}{m_S^2} \right)^3$

Table 7.2: Two-Body Decay Rate of Spin-1/2 DM via Generic Interaction Terms

Interaction Term	Decay Rate
$g_D G_\mu \bar{f} \gamma^\mu (1 + r \gamma_5) \psi$ $+ g_D^* G_\mu^* \bar{\psi} \gamma^\mu (1 + r \gamma_5) f$	$\Gamma(\psi \rightarrow f G) = \Gamma(\bar{\psi} \rightarrow \bar{f} \bar{G})$ $= \frac{ g_D ^2 m_\psi^3}{16\pi m_G^2} \sqrt{\lambda\left(\frac{m_G}{m_\psi}, \frac{m_f}{m_\psi}\right)} \left[\omega\left(\frac{m_G}{m_\psi}, \frac{m_f}{m_\psi}\right) + r^2 \omega\left(\frac{m_G}{m_\psi}, -\frac{m_f}{m_\psi}\right) \right]$
$g_D \bar{\psi} H (1 + i r_p \gamma_5) f$ $+ g_D \bar{f} H (1 + i r_p \gamma_5) \psi$	$\Gamma(\psi \rightarrow H f) = \Gamma(\bar{\psi} \rightarrow H \bar{f})$ $= \frac{g_D^2 m_\psi}{16\pi} \sqrt{\lambda\left(\frac{m_H}{m_\psi}, \frac{m_f}{m_\psi}\right)} \left[z\left(\frac{m_f}{m_\psi}, \frac{m_H}{m_\psi}\right) + r_p^2 z\left(-\frac{m_f}{m_\psi}, \frac{m_H}{m_\psi}\right) \right]$

Table 7.3: Functions used for the Analysis of Bino Decay

$K(x)$	$\frac{1}{16} \left[-5 + 6x^2 + 2(1 - 4x^2 + 3x^4) \ln\left(1 - \frac{1}{x^2}\right) \right]$
$P(x, y)$	$\frac{1}{24} \left[\frac{3}{2} + \left(\frac{\pi^2 y^2}{2} - 6 \right) x^2 \right] + \frac{x^2 y^2}{4} \ln(x^2 + y^2 - 1) \left[-\frac{1}{2} \ln(x^2 + y^2 - 1) + \ln(x^2 - 1) \right]$ $+ \frac{x^2}{4} (x^2 - 1) \ln\left(\frac{x^2}{x^2 - 1}\right) + \frac{x^2 y^2}{4} \ln(y^2) \ln\left(\frac{x}{x^2 - 1}\right) - \frac{x^2 y^2}{4} \text{Li}_2\left(\frac{x^2 - 1}{x^2 + y^2 - 1}\right) + x \leftrightarrow y$

Table 7.4: Decay Rate of Spin-1 DM via Different Interaction Terms

Interaction Term	Decay Rate
$g_1 \chi_\mu \bar{f} \gamma^\mu (1 + r \gamma_5) f$	$\Gamma(\chi \rightarrow f \bar{f}) = \frac{g_1^2 N_f}{12\pi} m_\chi \sqrt{1 - 4 \frac{m_f^2}{m_\chi^2}} \times \left[1 + 2 \frac{m_f^2}{m_\chi^2} + r^2 \left(1 - 4 \frac{m_f^2}{m_\chi^2} \right) \right]$
$\frac{g_1}{\Lambda} \chi^\mu \bar{f} \partial_\mu f$	$\Gamma(\chi \rightarrow f \bar{f}) = \frac{g_1^2 m_\chi^3}{64\pi \Lambda^2} \left(1 - 4 \frac{m_f^2}{m_\chi^2} \right)^{\frac{3}{2}}$
	$\Gamma(\chi \rightarrow \gamma\gamma \text{ or } gg) = 0$ forbidden by the Landau-Yang theorem
$g_1 Z_\mu Z^\nu \partial_\nu \chi^\mu$	$\Gamma(\chi \rightarrow ZZ) = \frac{g_1^2 m_\chi^3}{96\pi m_Z^2} \left(1 - 4 \frac{m_Z^2}{m_\chi^2} \right)^{\frac{3}{2}}$
$g_1 \epsilon_{\mu\nu\rho\sigma} \chi^\mu Z^\nu \partial^\sigma Z^\rho$	$\Gamma(\chi \rightarrow ZZ) = \frac{g_1^2 m_\chi^3}{96\pi m_Z^2} \left(1 - 4 \frac{m_Z^2}{m_\chi^2} \right)^{\frac{3}{2}}$
$g_1 W_\mu^+ W^{-\nu} \partial_\nu \chi^\mu$ $+ g_1^* W_\mu^- W^{+\nu} \partial_\nu \chi^\mu$	$\Gamma(\chi \rightarrow W^+ W^-) = \frac{m_\chi^5}{192\pi m_W^4} \left(1 - 4 \frac{m_W^2}{m_\chi^2} \right)^{\frac{3}{2}}$ $\times \left\{ 4 [Re(g_1)]^2 \frac{m_W^2}{m_\chi^2} + [Im(g_1)]^2 \left(1 + 4 \frac{m_W^2}{m_\chi^2} \right) \right\}$
$g_1 \epsilon_{\mu\nu\rho\sigma} \chi^\mu W^{+\nu} \partial^\sigma W^{-\rho}$ $+ g_1^* \epsilon_{\mu\nu\rho\sigma} \chi^\mu W^{-\nu} \partial^\sigma W^{+\rho}$	$\Gamma(\chi \rightarrow W^+ W^-) = \frac{m_\chi^3}{48\pi m_W^2} \sqrt{1 - 4 \frac{m_W^2}{m_\chi^2}}$ $\times \left\{ [Re(g_1)]^2 \left(1 - 4 \frac{m_W^2}{m_\chi^2} \right)^2 + [Im(g_1)]^2 \left(1 + 2 \frac{m_W^2}{m_\chi^2} \right) \right\}$
$g_1 \chi_\mu Z_\nu F^{\mu\nu}$	$\Gamma(\chi \rightarrow Z\gamma) = \frac{g_1^2 m_\chi^3}{96\pi m_Z^2} \left(1 + \frac{m_Z^2}{m_\chi^2} \right) \left(1 - \frac{m_Z^2}{m_\chi^2} \right)^3$
$g_1 \epsilon_{\mu\nu\rho\sigma} \chi^\mu Z^\nu F^{\sigma\rho}$	$\Gamma(\chi \rightarrow Z\gamma) = \frac{g_1^2 m_\chi^3}{24\pi m_Z^2} \left(1 + \frac{m_Z^2}{m_\chi^2} \right) \left(1 - \frac{m_Z^2}{m_\chi^2} \right)^3$

Chapter 8

Conclusions and Outlook

In the first part of this thesis (Chapters 2-3), we extended the minimal parametrizations for cosmic inflations.

For the late-universe acceleration we considered a popular alternative interpretation of dark energy – the quintessence model. We explicitly answered which physical parameters (related to the quintessence potential and the field velocity) can – and which cannot – be measured with current and future cosmological observations. For the simplest slow-roll thawing model, we showed how to break the degeneracy between phenomenological dark energy parameters, e.g. w_0 and w_a . In the future we will extend this project to more dynamic dark energy models: the $f(R)$ gravity; the k-essence; the Tachyon field; and more. Open or closed universe with dynamic dark energy will also be considered.

For early-universe inflation we studied generic primordial power spectra of metric perturbations from inflation, going beyond the slow-roll assumption. Two complementary reconstruction strategies were offered. We examined the bottom-up reconstruction method by testing a variety of interpolation methods and number of knots, and concluded that this is a robust statistical tool to study primordial power spectra. Using the top-down approach, we showed that the slow-roll assumption, which at present is usually taken as a prior, can be tested with the upcoming cosmological observational data. One

future aspect of this project will be applying it to the real Planck data that is expected in 2012. Another future aspect will be to explore whether the single-field inflation model can be *robustly* tested with the power spectra only.

In the second part of this thesis (Chapters 4-6), we studied a series of models related to particle production after or during inflation. New predictions on the primordial power spectra and non-Gaussianity were made. A new lattice simulation code was developed to simulate dynamics of scalar fields, which can be canonical (Chapters 4-5) or non-canonical (Chapter 6). A future improvement for this code will be including feedback of metric perturbations on the scalar field dynamics. We will study the curvature fluctuations from preheating beyond the specific model discussed in Chapter 4.

In the last chapter we studied the cosmological constraint on the lifetime of decaying dark matter. We showed that CMB ISW effect will be the strongest probe, assuming DM decays into relativistic particles or radiation. Further constraints were obtained by assuming that the decayed product contributes part of its energy to reionization of the universe. However, we have assumed instant energy injection for reionization, which is likely to be over-simplifying the physics in question. This will be improved in the future work.

Bibliography

- [1] E. Komatsu *et al.*, (2010), 1001.4538.
- [2] N. Jarosik *et al.*, (2010), 1001.4744.
- [3] W. C. Jones *et al.*, *New Astronomy Review* **50**, 945 (2006).
- [4] F. Piacentini *et al.*, *Astrophys. J.* **647**, 833 (2006), arXiv:astro-ph/0507507.
- [5] T. E. Montroy *et al.*, *Astrophys. J.* **647**, 813 (2006), astro-ph/0507514.
- [6] N. Barnaby, Z. Huang, L. Kofman, and D. Pogosyan, *Phys. Rev. D* **80**, 043501 (2009), 0902.0615.
- [7] N. Barnaby and Z. Huang, *Phys. Rev. D* **80**, 126018 (2009).
- [8] A. E. Romano and M. Sasaki, *Phys. Rev. D* **78**, 103522 (2008), 0809.5142.
- [9] K. Ichiki, M. Oguri, and K. Takahashi, *Phys. Rev. Lett.* **93**, 071302 (2004), astro-ph/0403164.
- [10] J. R. Bond, *Theory and Observations of the Cosmic Background Radiation* (in Les Houches Session LX, ed. R. Schaeffer, Elsevier Science Press, 1996).
- [11] J. R. Bond and G. Efstathiou, *Astrophys. J., Lett.* **285**, L45 (1984).
- [12] J. A. Peacock, *Cosmological Physics* (Cambridge University Press, 1999).

- [13] V. F. Mukhanov, *Physical Foundations of Cosmology* (Cambridge University Press, 2005).
- [14] S. Weinberg, *Cosmology* (Cambridge University Press, 2008).
- [15] V. C. Rubin and W. K. Ford, Jr., *Astrophys. J.***159**, 379 (1970).
- [16] T. Treu, ArXiv e-prints (2010), 1003.5567.
- [17] M. J. Henriksen, *The physical characteristics of the X-ray emitting gas in clusters of galaxies and constraints on dark matter*, PhD thesis, Maryland Univ., College Park., 1985.
- [18] E. Hayashi and S. D. M. White, *Mon. Not. R. Astron. Soc.***370**, L38 (2006), arXiv:astro-ph/0604443.
- [19] V. A. Ryabov, V. A. Tsarev, and A. M. Tskhovrebov, *Physics Uspekhi* **51**, 1091 (2008).
- [20] A. G. Riess *et al.*, *Astrophys. J.* **699**, 539 (2009), 0905.0695.
- [21] D. J. Fixsen, *Astrophys. J.***707**, 916 (2009), 0911.1955.
- [22] V. M. Lobashev, *Nucl. Phys.* **A719**, 153 (2003).
- [23] A. G. Riess *et al.*, *Astron. J.***116**, 1009 (1998), astro-ph/9805201.
- [24] S. Perlmutter *et al.*, *Astrophys. J.***517**, 565 (1999), arXiv:astro-ph/9812133.
- [25] J. R. Bond and A. H. Jaffe, *Royal Society of London Philosophical Transactions Series A* **357**, 57 (1999), arXiv:astro-ph/9809043.
- [26] P. Astier *et al.*, *Astron. Astrophys.***447**, 31 (2006), arXiv:astro-ph/0510447.
- [27] R. Kessler *et al.*, *Astrophys. J. Suppl.* **185**, 32 (2009), 0908.4274.

- [28] E. J. Copeland, M. Sami, and S. Tsujikawa, *International Journal of Modern Physics D* **15**, 1753 (2006).
- [29] A. A. Starobinsky, *Physics Letters B* **91**, 99 (1980).
- [30] A. H. Guth, *Phys. Rev. D* **23**, 347 (1981).
- [31] K. Sato, *Mon. Not. R. Astron. Soc.* **195**, 467 (1981).
- [32] A. D. Linde, *Physics Letters B* **108**, 389 (1982).
- [33] A. Albrecht and P. J. Steinhardt, *Physical Review Letters* **48**, 1220 (1982).
- [34] A. D. Linde, *Physics Letters B* **175**, 395 (1986).
- [35] D. J. Fixsen *et al.*, *Astrophys. J.* **473**, 576 (1996), arXiv:astro-ph/9605054.
- [36] H. V. Peiris *et al.*, *Astrophys. J., Suppl.* **148**, 213 (2003), arXiv:astro-ph/0302225.
- [37] D. N. Spergel *et al.*, *Astrophys. J., Suppl.* **148**, 175 (2003), arXiv:astro-ph/0302209.
- [38] D. N. Spergel *et al.*, *Astrophys. J., Suppl.* **170**, 377 (2007), arXiv:astro-ph/0603449.
- [39] K. Freese, J. A. Frieman, and A. V. Olinto, *Physical Review Letters* **65**, 3233 (1990).
- [40] F. C. Adams, J. R. Bond, K. Freese, J. A. Frieman, and A. V. Olinto, *Phys. Rev. D* **47**, 426 (1993), arXiv:hep-ph/9207245.
- [41] G. Dvali and S. Tye, *Physics Letters B* **450**, 72 (1999), arXiv:hep-ph/9812483.
- [42] P. Binétruy and M. K. Gaillard, *Phys. Rev. D* **34**, 3069 (1986).
- [43] T. Banks, M. Berkooz, S. H. Shenker, G. Moore, and P. J. Steinhardt, *Phys. Rev. D* **52**, 3548 (1995), arXiv:hep-th/9503114.

- [44] J. R. Bond, L. Kofman, S. Prokushkin, and P. M. Vaudrevange, *Phys. Rev. D* **75**, 123511 (2007), arXiv:hep-th/0612197.
- [45] S. Tsujikawa, *ArXiv High Energy Physics - Phenomenology e-prints* (2003), arXiv:hep-ph/0304257.
- [46] L. McAllister and E. Silverstein, *General Relativity and Gravitation* **40**, 565 (2008), 0710.2951.
- [47] D. Langlois, *Inflation and Cosmological Perturbations*, in *Lecture Notes in Physics, Berlin Springer Verlag*, edited by G. Wolschin, , *Lecture Notes in Physics*, Berlin Springer Verlag Vol. 800, pp. 1–57, 2010, 1001.5259.
- [48] E. D. Stewart and D. H. Lyth, *Physics Letters B* **302**, 171 (1993), arXiv:gr-qc/9302019.
- [49] S. Dodelson, W. H. Kinney, and E. W. Kolb, *Phys. Rev. D* **56**, 3207 (1997), arXiv:astro-ph/9702166.
- [50] E. W. Kolb, *NASA STI/Recon Technical Report N* **2**, 14556 (1999), arXiv:hep-ph/9910311.
- [51] Planck Science Team, *Planck: The Scientific Programme (Blue Book). ESA-SCI (2005)-1. Version 2.* (European Space Agency., 2009).
- [52] J. P. Conlon and F. Quevedo, *Journal of High Energy Physics* **1**, 146 (2006), arXiv:hep-th/0509012.
- [53] K. Jedamzik, M. Lemoine, and J. Martin, *ArXiv e-prints* (2010), 1002.3039.
- [54] J. E. Strömberg, *ArXiv Mathematical Physics e-prints* (2005), arXiv:math-ph/0510076.

- [55] B. A. Berg, *Markov Chain Monte Carlo Simulations and Their Statistical Analysis With Web-Based Fortran Code* (World Scientific Publishing Co.Pte.Ltd., 2004).
- [56] J. R. Bond, A. V. Frolov, Z. Huang, and L. Kofman, *Physical Review Letters* **103**, 071301 (2009), 0903.3407.
- [57] N. Barnaby, J. R. Bond, Z. Huang, and L. Kofman, *Journal of Cosmology and Astro-Particle Physics* **12**, 21 (2009), 0909.0503.
- [58] S. DeLope Amigo, W. Man-Yin Cheung, Z. Huang, and S.-P. Ng, *Journal of Cosmology and Astro-Particle Physics* **6**, 5 (2009), 0812.4016.
- [59] Z. Huang, J. R. Bond, and L. Kofman, *ArXiv e-prints* (2010), 1007.5297.
- [60] M. Kamionkowski, *ArXiv e-prints* (2007), 0706.2986.
- [61] E. V. Linder, *Reports of Progress in Physics* **71**, 056901 (2008), arXiv:0801.2968.
- [62] E. V. Linder, *American Journal of Physics* **76**, 197 (2008), arXiv:0705.4102.
- [63] A. Silvestri and M. Trodden, *ArXiv e-prints* (2009), 0904.0024.
- [64] M. Chevallier and D. Polarski, *International Journal of Modern Physics D* **10**, 213 (2001).
- [65] E. V. Linder, *Physical Review Letters* **90**, 091301 (2003).
- [66] Y. Wang and M. Tegmark, *Physical Review Letters* **92**, 241302 (2004), arXiv:astro-ph/0403292.
- [67] A. Upadhye, M. Ishak, and P. J. Steinhardt, *Phys. Rev. D* **72**, 063501 (2005).
- [68] A. R. Liddle, P. Mukherjee, D. Parkinson, and Y. Wang, *Phys. Rev. D* **74**, 123506 (2006), arXiv:astro-ph/0610126.
- [69] M. J. Francis, G. F. Lewis, and E. V. Linder, *ArXiv e-prints* **704** (2007), 0704.0312.

- [70] F. Y. Wang, Z. G. Dai, and Z.-H. Zhu, ArXiv e-prints: astro-ph 0706.0938 **706** (2007), 0706.0938.
- [71] A. Albrecht *et al.*, ArXiv Astrophysics e-prints (2006), arXiv:astro-ph/0609591.
- [72] E. V. Linder and D. Huterer, Phys. Rev. D**72**, 043509 (2005), arXiv:astro-ph/0505330.
- [73] D. Huterer and G. Starkman, Physical Review Letters **90**, 031301 (2003), arXiv:astro-ph/0207517.
- [74] R. G. Crittenden and L. Pogosian, arXiv: astro-ph/0510293 (2005), astro-ph/0510293.
- [75] D. Rapetti, S. W. Allen, M. A. Amin, and R. D. Blandford, Mon. Not. R. Astron. Soc.**375**, 1510 (2007), arXiv:astro-ph/0605683.
- [76] J. R. Bond, C. Contaldi, Z. Huang, L. Kofman, and P. M. Vaudrevange, in preparation (2010).
- [77] B. Ratra and P. J. E. Peebles, Phys. Rev. D**37**, 3406 (1988).
- [78] C. Wetterich, Nuclear Physics B **302**, 668 (1988).
- [79] J. A. Frieman, C. T. Hill, A. Stebbins, and I. Waga, Physical Review Letters **75**, 2077 (1995), arXiv:astro-ph/9505060.
- [80] P. Binétruy, Phys. Rev. D**60**, 063502 (1999), arXiv:hep-ph/9810553.
- [81] T. Barreiro, E. J. Copeland, and N. J. Nunes, Phys. Rev. D**61**, 127301 (2000), astro-ph/9910214.
- [82] P. H. Brax and J. Martin, Physics Letters B **468**, 40 (1999), arXiv:astro-ph/9905040.

- [83] E. J. Copeland, N. J. Nunes, and F. Rosati, *Phys. Rev. D* **62**, 123503 (2000), arXiv:hep-ph/0005222.
- [84] A. de La Macorra and C. Stephan-Otto, *Physical Review Letters* **87**, A261301+ (2001), arXiv:astro-ph/0106316.
- [85] E. V. Linder, *Phys. Rev. D* **73**, 063010 (2006), arXiv:astro-ph/0601052.
- [86] D. Huterer and H. V. Peiris, *Phys. Rev. D* **75**, 083503 (2007), arXiv:astro-ph/0610427.
- [87] E. V. Linder, *Gen. Rel. Grav.* **40**, 329 (2008), 0704.2064.
- [88] C. Armendariz-Picon, V. Mukhanov, and P. J. Steinhardt, *Phys. Rev. D* **63**, 103510 (2001), astro-ph/0006373.
- [89] M. Malquarti, E. J. Copeland, and A. R. Liddle, *Phys. Rev. D* **68**, 023512 (2003), astro-ph/0304277.
- [90] M. Malquarti, E. J. Copeland, A. R. Liddle, and M. Trodden, *Phys. Rev. D* **67**, 123503 (2003), astro-ph/0302279.
- [91] R. de Putter and E. V. Linder, *Astroparticle Physics* **28**, 263 (2007), arXiv:0705.0400.
- [92] S. Capozziello and L. Z. Fang, *International Journal of Modern Physics D* **11**, 483 (2002), arXiv:gr-qc/0201033.
- [93] S. M. Carroll, V. Duvvuri, M. Trodden, and M. S. Turner, *Phys. Rev. D* **70**, 043528 (2004), arXiv:astro-ph/0306438.
- [94] Á. de La Cruz-Dombriz and A. Dobado, *Phys. Rev. D* **74**, 087501 (2006), arXiv:gr-qc/0607118.

- [95] S. Nojiri and S. D. Odintsov, ArXiv High Energy Physics - Theory e-prints (2006), arXiv:hep-th/0601213.
- [96] A. de Felice and S. Tsujikawa, Living Reviews in Relativity **13**, 3 (2010), 1002.4928.
- [97] T. P. Sotiriou and V. Faraoni, Reviews of Modern Physics **82**, 451 (2010), 0805.1726.
- [98] S. M. Carroll, M. Hoffman, and M. Trodden, Phys. Rev. D**68**, 023509 (2003), arXiv:astro-ph/0301273.
- [99] R. R. Caldwell, Physics Letters B **545**, 23 (2002), arXiv:astro-ph/9908168.
- [100] R. R. Caldwell, M. Kamionkowski, and N. N. Weinberg, Phys. Rev. Lett. **91**, 071301 (2003), astro-ph/0302506.
- [101] N. Kaloper and L. Sorbo, Journal of Cosmology and Astro-Particle Physics **4**, 7 (2006), arXiv:astro-ph/0511543.
- [102] S. Dutta and R. J. Scherrer, Phys. Rev. D**78**, 083512 (2008), 0805.0763.
- [103] J. M. Cline, S. Jeon, and G. D. Moore, Phys. Rev. D**70**, 043543 (2004), hep-ph/0311312.
- [104] S. Sergienko and V. Rubakov, ArXiv e-prints (2008), 0803.3163.
- [105] P. J. Steinhardt, L. Wang, and I. Zlatev, Phys. Rev. D**59**, 123504 (1999), arXiv:astro-ph/9812313.
- [106] A. A. Sen and S. Sethi, Phys. Lett. **B532**, 159 (2002), gr-qc/0111082.
- [107] I. P. Neupane, Class. Quant. Grav. **21**, 4383 (2004), hep-th/0311071.
- [108] I. P. Neupane, Mod. Phys. Lett. **A19**, 1093 (2004), hep-th/0402021.
- [109] L. Jarv, T. Mohaupt, and F. Saueressig, JCAP **0408**, 016 (2004), hep-th/0403063.

- [110] R. R. Caldwell and E. V. Linder, *Physical Review Letters* **95**, 141301 (2005).
- [111] S. Sullivan, A. Cooray, and D. E. Holz, *ArXiv: 0706.3730* **706** (2007), 0706.3730.
- [112] R. J. Scherrer and A. A. Sen, *Phys. Rev. D* **77**, 083515 (2008), arXiv:0712.3450.
- [113] A. Lewis and S. Bridle, *Phys. Rev. D* **66**, 103511 (2002), arXiv:astro-ph/0205436.
- [114] D. S. Salopek and J. R. Bond, *Phys. Rev. D* **42**, 3936 (1990).
- [115] E. J. Copeland, A. R. Liddle, and D. Wands, *Phys. Rev. D* **57**, 4686 (1998), gr-qc/9711068.
- [116] A. R. Liddle and R. J. Scherrer, *Phys. Rev. D* **59**, 023509 (1999), astro-ph/9809272.
- [117] The ACT Collaboration *et al.*, *ArXiv e-prints* (2010), 1001.2934.
- [118] H. C. Chiang *et al.*, *Astrophys. J.* **711**, 1123 (2010), 0906.1181.
- [119] QUaD, . P. G. Castro *et al.*, *Astrophys. J.* **701**, 857 (2009), 0901.0810.
- [120] C. L. Reichardt *et al.*, *Astrophys. J.* **694**, 1200 (2009), 0801.1491.
- [121] C.-L. Kuo *et al.*, *Astrophys. J.* **664**, 687 (2007), astro-ph/0611198.
- [122] M. C. Runyan *et al.*, *Astrophys. J., Suppl.* **149**, 265 (2003), arXiv:astro-ph/0303515.
- [123] J. H. Goldstein *et al.*, *Astrophys. J.* **599**, 773 (2003), arXiv:astro-ph/0212517.
- [124] J. L. Sievers *et al.*, *Astrophys. J.* **660**, 976 (2007).
- [125] A. C. S. Readhead *et al.*, *Astrophys. J.* **609**, 498 (2004), arXiv:astro-ph/0402359.
- [126] A. C. S. Readhead *et al.*, *Science* **306**, 836 (2004), arXiv:astro-ph/0409569.
- [127] T. J. Pearson *et al.*, *Astrophys. J.* **591**, 556 (2003), arXiv:astro-ph/0205388.
- [128] C. Dickinson *et al.*, *Mon. Not. Roy. Astron. Soc.* **353**, 732 (2004), astro-ph/0402498.

- [129] S. Hanany *et al.*, *Astrophys. J.* **545**, L5 (2000), astro-ph/0005123.
- [130] R. A. Sunyaev and Y. B. Zeldovich, *Comments on Astrophysics and Space Physics* **4**, 173 (1972).
- [131] R. A. Sunyaev and I. B. Zeldovich, *Annual Review of Astronomy and Astrophysics***18**, 537 (1980).
- [132] J. R. Bond, M. I. Ruetalo, J. W. Wadsley, and M. D. Gladders, Probing SZ Source Detection with Gasdynamical Simulations, in *AMiBA 2001: High-Z Clusters, Missing Baryons, and CMB Polarization*, edited by L.-W. Chen, C.-P. Ma, K.-W. Ng, & U.-L. Pen, , Astronomical Society of the Pacific Conference Series Vol. 257, pp. 15–+, 2002, arXiv:astro-ph/0112499.
- [133] J. R. Bond *et al.*, *Astrophys. J.* **626**, 12 (2005), astro-ph/0205386.
- [134] N. Battaglia, J. R. Bond, C. Pfrommer, J. L. Sievers, and D. Sijacki, ArXiv e-prints (2010), 1003.4256.
- [135] E. Komatsu and U. Seljak, *Mon. Not. Roy. Astron. Soc.* **336**, 1256 (2002), astro-ph/0205468.
- [136] N. Sehgal *et al.*, *Astrophys. J.* **709**, 920 (2010), 0908.0540.
- [137] G. Miknaitis *et al.*, *Astrophys. J.* **666**, 674 (2007), astro-ph/0701043.
- [138] ESSENCE, W. M. Wood-Vasey *et al.*, *Astrophys. J.* **666**, 694 (2007), astro-ph/0701041.
- [139] P. M. Garnavich *et al.*, *Astrophys. J., Lett.***493**, L53+ (1998), arXiv:astro-ph/9710123.
- [140] Supernova Cosmology Project, R. A. Knop *et al.*, *Astrophys. J.* **598**, 102 (2003), astro-ph/0309368.

- [141] A. G. Riess *et al.*, *Astrophys. J.***607**, 665 (2004).
- [142] A. G. Riess *et al.*, *Astrophys. J.***659**, 98 (2007), arXiv:astro-ph/0611572.
- [143] B. A. Reid *et al.*, (2009), 0907.1659.
- [144] R. Massey *et al.*, *Astrophys. J., Suppl.***172**, 239 (2007), arXiv:astro-ph/0701480.
- [145] J. Lesgourgues, M. Viel, M. G. Haehnelt, and R. Massey, *Journal of Cosmology and Astro-Particle Physics* **11**, 8 (2007), arXiv:0705.0533.
- [146] H. Hoekstra *et al.*, *Astrophys. J.***647**, 116 (2006), arXiv:astro-ph/0511089.
- [147] C. Schimd *et al.*, *Astron. Astrophys.***463**, 405 (2007), arXiv:astro-ph/0603158.
- [148] H. Hoekstra *et al.*, *Astrophys. J.***572**, 55 (2002), arXiv:astro-ph/0202285.
- [149] H. Hoekstra, H. K. C. Yee, and M. D. Gladders, *Astrophys. J.* **577**, 595 (2002), astro-ph/0204295.
- [150] L. Van Waerbeke, Y. Mellier, and H. Hoekstra, *Astron. Astrophys.***429**, 75 (2005), arXiv:astro-ph/0406468.
- [151] J. Benjamin *et al.*, *Mon. Not. R. Astron. Soc.***381**, 702 (2007), arXiv:astro-ph/0703570.
- [152] M. Viel, M. G. Haehnelt, and V. Springel, *Mon. Not. R. Astron. Soc.***354**, 684 (2004), arXiv:astro-ph/0404600.
- [153] T.-S. Kim, M. Viel, M. G. Haehnelt, R. F. Carswell, and S. Cristiani, *Mon. Not. R. Astron. Soc.***347**, 355 (2004), arXiv:astro-ph/0308103.
- [154] R. A. C. Croft *et al.*, *Astrophys. J.***581**, 20 (2002), arXiv:astro-ph/0012324.
- [155] P. McDonald *et al.*, *Astrophys. J.***635**, 761 (2005), arXiv:astro-ph/0407377.

- [156] P. McDonald *et al.*, *Astrophys. J., Suppl.***163**, 80 (2006), arXiv:astro-ph/0405013.
- [157] G. Steigman, *International Journal of Modern Physics E* **15**, 1 (2006), arXiv:astro-ph/0511534.
- [158] J. M. O’Meara *et al.*, *Astrophys. J., Lett.***649**, L61 (2006), arXiv:astro-ph/0608302.
- [159] P. G. Ferreira and M. Joyce, *Physical Review Letters* **79**, 4740 (1997), arXiv:astro-ph/9707286.
- [160] R. Bean, S. H. Hansen, and A. Melchiorri, *Phys. Rev. D***64**, 103508 (2001), astro-ph/0104162.
- [161] N. Dauphas, *Nature* **435**, 1203 (2005).
- [162] J. A. Tauber, The Planck Mission, in *New Cosmological Data and the Values of the Fundamental Parameters*, edited by A. N. Lasenby and A. Wilkinson, , IAU Symposium Vol. 201, pp. 86–+, 2005.
- [163] J. Clavel and J. A. Tauber, The Planck Mission, in *EAS Publications Series*, edited by L. I. Gurvits, S. Frey, and S. Rawlings, , EAS Publications Series Vol. 15, pp. 395–403, 2005.
- [164] Euclid Study Team, *Euclid Assessment study report (SRE-2009-2)* (European Space Agency., 2009).
- [165] D. J. Schlegel *et al.*, SDSS-III: The Baryon Oscillation Spectroscopic Survey (BOSS), in *Bulletin of the American Astronomical Society*, , Bulletin of the American Astronomical Society Vol. 38, pp. 966–+, 2007.
- [166] T.-C. Chang, U.-L. Pen, J. B. Peterson, and P. McDonald, *Phys. Rev. Lett.* **100**, 091303 (2008), 0709.3672.
- [167] J. B. Peterson *et al.*, (2009), 0902.3091.

- [168] M. F. Morales and J. S. B. Wyithe, ArXiv e-prints (2009), 0910.3010.
- [169] CMBPol Study Team, D. Baumann *et al.*, AIP Conf. Proc. **1141**, 10 (2009), 0811.3919.
- [170] J. Dunkley *et al.*, (2008), 0811.3915.
- [171] H.-J. Seo *et al.*, (2009), 0910.5007.
- [172] H.-J. Seo and D. J. Eisenstein, *Astrophys. J.* **665**, 14 (2007), astro-ph/0701079.
- [173] O. Dore, T. Lu, and U.-L. Pen, (2009), 0905.0501.
- [174] Z. Ma, W. Hu, and D. Huterer, *Astrophys. J.* **636**, 21 (2006), arXiv:astro-ph/0506614.
- [175] U. Seljak *et al.*, *Phys. Rev. D* **71**, 103515 (2005), arXiv:astro-ph/0407372.
- [176] S. Hannestad and E. Mörtzell, *Journal of Cosmology and Astro-Particle Physics* **9**, 1 (2004), arXiv:astro-ph/0407259.
- [177] P. S. Corasaniti and E. J. Copeland, ArXiv: astro-ph/020554 (2002), astro-ph/0205544.
- [178] T. Chiba, *Phys. Rev. D* **81**, 023515 (2010), 0909.4365.
- [179] R. Crittenden, E. Majerotto, and F. Piazza, *Physical Review Letters* **98**, 251301 (2007), arXiv:astro-ph/0702003.
- [180] T. Chiba, *Phys. Rev. D* **79**, 083517 (2009), 0902.4037.
- [181] U. Alam, V. Sahni, and A. A. Starobinsky, *Journal of Cosmology and Astro-Particle Physics* **6**, 8 (2004), arXiv:astro-ph/0403687.
- [182] V. Sahni, T. D. Saini, A. A. Starobinsky, and U. Alam, *Soviet Journal of Experimental and Theoretical Physics Letters* **77**, 201 (2003), arXiv:astro-ph/0201498.

- [183] U. Alam, V. Sahni, and A. A. Starobinsky, *Journal of Cosmology and Astro-Particle Physics* **2**, 11 (2007), arXiv:astro-ph/0612381.
- [184] M. Sahlén, A. R. Liddle, and D. Parkinson, *Phys. Rev. D* **72**, 083511 (2005), astro-ph/0506696.
- [185] E. Fernandez-Martinez and L. Verde, *ArXiv e-prints* **806** (2008), 0806.1871.
- [186] R. K. Sachs and A. M. Wolfe, *Astrophys. J.* **147**, 73 (1967).
- [187] A. D. Linde and V. F. Mukhanov, *Phys. Rev. D* **56**, 535 (1997), astro-ph/9610219.
- [188] D. H. Lyth and D. Wands, *Phys. Rev. D* **68**, 103516 (2003), astro-ph/0306500.
- [189] A. A. Starobinsky, *Gravitation and Cosmology* **4**, 88 (1998), arXiv:astro-ph/9811360.
- [190] R. E. Smith *et al.*, *Mon. Not. R. Astron. Soc.* **341**, 1311 (2003), arXiv:astro-ph/0207664.
- [191] B. P. Crill *et al.*, SPIDER: a balloon-borne large-scale CMB polarimeter, in *Society of Photo-Optical Instrumentation Engineers (SPIE) Conference Series*, , Presented at the Society of Photo-Optical Instrumentation Engineers (SPIE) Conference Vol. 7010, 2008, 0807.1548.
- [192] J. P. Boyd, *Chebyshev and Fourier Spectral Methods* (DOVER Publications, Inc., 2000).
- [193] H. V. Peiris and R. Easther, *Journal of Cosmology and Astro-Particle Physics* **10**, 17 (2006), arXiv:astro-ph/0609003.
- [194] R. Easther and H. V. Peiris, *Journal of Cosmology and Astro-Particle Physics* **9**, 10 (2006), arXiv:astro-ph/0604214.

- [195] P. Adshead and R. Easther, *Journal of Cosmology and Astro-Particle Physics* **10**, 47 (2008), 0802.3898.
- [196] J. Lesgourgues and W. Valkenburg, *Phys. Rev. D* **75**, 123519 (2007), arXiv:astro-ph/0703625.
- [197] J. Hamann, J. Lesgourgues, and W. Valkenburg, *Journal of Cosmology and Astro-Particle Physics* **4**, 16 (2008), 0802.0505.
- [198] P. Mukherjee and Y. Wang, *Astrophys. J.* **599**, 1 (2003), arXiv:astro-ph/0303211.
- [199] P. Mukherjee and Y. Wang, *Journal of Cosmology and Astro-Particle Physics* **12**, 7 (2005), arXiv:astro-ph/0502136.
- [200] S. Leach, *Mon. Not. R. Astron. Soc.* **372**, 646 (2006), arXiv:astro-ph/0506390.
- [201] R. Nagata and J. Yokoyama, *Phys. Rev. D* **78**, 123002 (2008), 0809.4537.
- [202] R. Nagata and J. Yokoyama, *Phys. Rev. D* **79**, 043010 (2009), 0812.4585.
- [203] G. Nicholson and C. R. Contaldi, *Journal of Cosmology and Astro-Particle Physics* **7**, 11 (2009), 0903.1106.
- [204] A. Shafieloo and T. Souradeep, *Phys. Rev. D* **70**, 043523 (2004), arXiv:astro-ph/0312174.
- [205] A. Shafieloo, T. Souradeep, P. Manimaran, P. K. Panigrahi, and R. Rangarajan, *Phys. Rev. D* **75**, 123502 (2007), arXiv:astro-ph/0611352.
- [206] A. Shafieloo and T. Souradeep, *Phys. Rev. D* **78**, 023511 (2008), 0709.1944.
- [207] N. Kogo, M. Matsumiya, M. Sasaki, and J. Yokoyama, *Astrophys. J.* **607**, 32 (2004), arXiv:astro-ph/0309662.

- [208] D. Tocchini-Valentini, M. Douspis, and J. Silk, *Mon. Not. R. Astron. Soc.* **359**, 31 (2005), arXiv:astro-ph/0402583.
- [209] S. L. Bridle, A. M. Lewis, J. Weller, and G. P. Efstathiou, *New Astronomy Review* **47**, 787 (2003).
- [210] S. Hannestad, *Journal of Cosmology and Astro-Particle Physics* **4**, 2 (2004), arXiv:astro-ph/0311491.
- [211] M. Bridges, A. N. Lasenby, and M. P. Hobson, *Mon. Not. R. Astron. Soc.* **369**, 1123 (2006), arXiv:astro-ph/0511573.
- [212] M. Bridges, A. N. Lasenby, and M. P. Hobson, *Mon. Not. R. Astron. Soc.* **381**, 68 (2007), arXiv:astro-ph/0607404.
- [213] M. Bridges, F. Feroz, M. P. Hobson, and A. N. Lasenby, *Mon. Not. R. Astron. Soc.* **400**, 1075 (2009), 0812.3541.
- [214] C. Sealfon, L. Verde, and R. Jimenez, *Phys. Rev. D* **72**, 103520 (2005), arXiv:astro-ph/0506707.
- [215] L. Verde and H. Peiris, *Journal of Cosmology and Astro-Particle Physics* **7**, 9 (2008), 0802.1219.
- [216] H. V. Peiris and L. Verde, *Phys. Rev. D* **81**, 021302 (2010), 0912.0268.
- [217] C. Dvorkin and W. Hu, *Phys. Rev. D* **82**, 043513 (2010), 1007.0215.
- [218] G. Felder and I. Tkachev, *Computer Physics Communications* **178**, 929 (2008), arXiv:hep-ph/0011159.
- [219] A. V. Frolov, *Journal of Cosmology and Astro-Particle Physics* **11**, 9 (2008), 0809.4904.

- [220] K. A. Malik and D. Wands, *Phys. Rept.* **475**, 1 (2009), 0809.4944.
- [221] L. Kofman, *ArXiv Astrophysics e-prints* (2003), arXiv:astro-ph/0303614.
- [222] A. Chambers and A. Rajantie, *Physical Review Letters* **100**, 041302 (2008), 0710.4133.
- [223] P. B. Greene, L. Kofman, A. Linde, and A. A. Starobinsky, *Phys. Rev. D* **56**, 6175 (1997), arXiv:hep-ph/9705347.
- [224] A. A. Starobinsky, *Physics Letters B* **117**, 175 (1982).
- [225] M. Sasaki and E. D. Stewart, *Progress of Theoretical Physics* **95**, 71 (1996), arXiv:astro-ph/9507001.
- [226] E. Komatsu *et al.*, *ArXiv e-prints* **803** (2008), 0803.0547.
- [227] M. Cruz, E. Martínez-González, and P. Vielva, *The WMAP Cold Spot*, in *Highlights of Spanish Astrophysics V*, edited by J. M. Diego, L. J. Goicoechea, J. I. González-Serrano, & J. Gorgas, pp. 275–+, 2010, 0901.1986.
- [228] L. A. Kofman and A. D. Linde, *Nuclear Physics B* **282**, 555 (1987).
- [229] L. A. Kofman and D. Y. Pogosyan, *Physics Letters B* **214**, 508 (1988).
- [230] D. S. Salopek, J. R. Bond, and J. M. Bardeen, *Phys. Rev. D* **40**, 1753 (1989).
- [231] N. Barnaby and J. M. Cline, *Phys. Rev. D* **73**, 106012 (2006), arXiv:astro-ph/0601481.
- [232] N. Barnaby and J. M. Cline, *Phys. Rev. D* **75**, 086004 (2007), arXiv:astro-ph/0611750.
- [233] D. J. H. Chung, E. W. Kolb, A. Riotto, and I. I. Tkachev, *Phys. Rev. D* **62**, 043508 (2000), arXiv:hep-ph/9910437.

- [234] L. Kofman *et al.*, *Journal of High Energy Physics* **5**, 30 (2004), arXiv:hep-th/0403001.
- [235] D. Green, B. Horn, L. Senatore, and E. Silverstein, *Phys. Rev. D***80**, 063533 (2009), 0902.1006.
- [236] E. Silverstein and A. Westphal, *Phys. Rev. D***78**, 106003 (2008), 0803.3085.
- [237] L. Kofman, A. Linde, and A. A. Starobinsky, *Physical Review Letters* **73**, 3195 (1994), arXiv:hep-th/9405187.
- [238] L. Kofman, A. Linde, and A. A. Starobinsky, *Phys. Rev. D***56**, 3258 (1997), arXiv:hep-ph/9704452.
- [239] S. Y. Khlebnikov and I. I. Tkachev, *Physical Review Letters* **77**, 219 (1996), arXiv:hep-ph/9603378.
- [240] S. Y. Khlebnikov and I. I. Tkachev, *Physics Letters B* **390**, 80 (1997), arXiv:hep-ph/9608458.
- [241] S. Khlebnikov and I. Tkachev, *Phys. Rev. D***56**, 653 (1997), arXiv:hep-ph/9701423.
- [242] S. Khlebnikov and I. Tkachev, *Physical Review Letters* **79**, 1607 (1997), arXiv:hep-ph/9610477.
- [243] G. Felder and L. Kofman, *Phys. Rev. D***63**, 103503 (2001), arXiv:hep-ph/0011160.
- [244] R. Micha and I. I. Tkachev, *Physical Review Letters* **90**, 121301 (2003), arXiv:hep-ph/0210202.
- [245] R. Micha and I. I. Tkachev, *Phys. Rev. D***70**, 043538 (2004), arXiv:hep-ph/0403101.
- [246] J. Berges, A. Rothkopf, and J. Schmidt, *Physical Review Letters* **101**, 041603 (2008), 0803.0131.

- [247] J. Berges and G. Hoffmeister, Nuclear Physics B **813**, 383 (2009), 0809.5208.
- [248] G. J. Mathews, D. J. Chung, K. Ichiki, T. Kajino, and M. Orito, Phys. Rev. **D70**, 083505 (2004), arXiv:astro-ph/0406046.
- [249] Ø. Elgarøy, S. Hannestad, and T. Haugbølle, Journal of Cosmology and Astro-Particle Physics **9**, 8 (2003), arXiv:astro-ph/0306229.
- [250] D. Langlois and L. Sorbo, Journal of Cosmology and Astro-Particle Physics **8**, 14 (2009), 0906.1813.
- [251] J. Adams, B. Cresswell, and R. Easther, Phys. Rev. **D64**, 123514 (2001), arXiv:astro-ph/0102236.
- [252] P. Hunt and S. Sarkar, Phys. Rev. **D70**, 103518 (2004), arXiv:astro-ph/0408138.
- [253] P. Hunt and S. Sarkar, Phys. Rev. **D76**, 123504 (2007), 0706.2443.
- [254] M. J. Mortonson, C. Dvorkin, H. V. Peiris, and W. Hu, Phys. Rev. **D79**, 103519 (2009), 0903.4920.
- [255] M. M. Anber and L. Sorbo, Phys. Rev. **D81**, 043534 (2010), 0908.4089.
- [256] A. Berera, Physical Review Letters **75**, 3218 (1995), arXiv:astro-ph/9509049.
- [257] L. McAllister, E. Silverstein, and A. Westphal, ArXiv e-prints (2008), 0808.0706.
- [258] R. Flauger, L. McAllister, E. Pajer, A. Westphal, and G. Xu, Journal of Cosmology and Astro-Particle Physics **6**, 9 (2010), 0907.2916.
- [259] A. Berera and T. W. Kephart, Physical Review Letters **83**, 1084 (1999), arXiv:hep-ph/9904410.
- [260] L. Covi, J. Hamann, A. Melchiorri, A. Slosar, and I. Sorbera, Phys. Rev. **D74**, 083509 (2006), arXiv:astro-ph/0606452.

- [261] J. Hamann, L. Covi, A. Melchiorri, and A. Slosar, *Phys. Rev. D* **76**, 023503 (2007), arXiv:astro-ph/0701380.
- [262] J. M. Cline and L. Hoi, *Journal of Cosmology and Astro-Particle Physics* **6**, 7 (2006), arXiv:astro-ph/0603403.
- [263] L. Hoi and J. M. Cline, *International Journal of Modern Physics D* **18**, 1863 (2009), 0706.3887.
- [264] C. Burgess, Are inflationary predictions sensitive to very high energy physics?, in *The Davis Meeting On Cosmic Inflation*, 2003, arXiv:astro-ph/0306236.
- [265] G. Felder, L. Kofman, and A. Linde, *Phys. Rev. D* **64**, 123517 (2001), arXiv:hep-th/0106179.
- [266] G. Felder *et al.*, *Physical Review Letters* **87**, 011601 (2001), arXiv:hep-ph/0012142.
- [267] R. N. Lerner and J. McDonald, *Phys. Rev. D* **79**, 023511 (2009), 0811.1933.
- [268] M. Joy, V. Sahni, and A. A. Starobinsky, *Phys. Rev. D* **77**, 023514 (2008), 0711.1585.
- [269] X. Chen, R. Easther, and E. A. Lim, *Journal of Cosmology and Astro-Particle Physics* **6**, 23 (2007), arXiv:astro-ph/0611645.
- [270] X. Chen, R. Easther, and E. A. Lim, *Journal of Cosmology and Astro-Particle Physics* **4**, 10 (2008), 0801.3295.
- [271] WMAP, G. Hinshaw *et al.*, *Astrophys. J. Suppl.* **180**, 225 (2009), 0803.0732.
- [272] N. W. Halverson *et al.*, *Astrophys. J.* **568**, 38 (2002), arXiv:astro-ph/0104489.
- [273] E. M. Leitch *et al.*, *Astrophys. J.* **624**, 10 (2005), arXiv:astro-ph/0409357.
- [274] M. Kowalski *et al.*, *Astrophys. J.* **686**, 749 (2008), 0804.4142.

- [275] The 2dFGRS, S. Cole *et al.*, Mon. Not. Roy. Astron. Soc. **362**, 505 (2005), astro-ph/0501174.
- [276] M. Tegmark *et al.*, Phys. Rev. D**74**, 123507 (2006), arXiv:astro-ph/0608632.
- [277] V. Springel *et al.*, Nature**435**, 629 (2005), arXiv:astro-ph/0504097.
- [278] N. Dalal, O. Doré, D. Huterer, and A. Shirokov, Phys. Rev. D**77**, 123514 (2008), 0710.4560.
- [279] M. Lo Verde, A. Miller, S. Shandera, and L. Verde, Journal of Cosmology and Astro-Particle Physics **4**, 14 (2008), 0711.4126.
- [280] P. McDonald, Phys. Rev. D**78**, 123519 (2008), 0806.1061.
- [281] N. Afshordi and A. J. Tolley, Phys. Rev. D**78**, 123507 (2008), 0806.1046.
- [282] J. J. Blanco-Pillado *et al.*, Journal of High Energy Physics **11**, 63 (2004), arXiv:hep-th/0406230.
- [283] N. Barnaby, T. Biswas, and J. M. Cline, Journal of High Energy Physics **4**, 56 (2007), arXiv:hep-th/0612230.
- [284] N. Barnaby and J. M. Cline, Journal of Cosmology and Astro-Particle Physics **7**, 17 (2007), 0704.3426.
- [285] N. Barnaby and J. M. Cline, Journal of Cosmology and Astro-Particle Physics **6**, 30 (2008), 0802.3218.
- [286] N. Barnaby, D. J. Mulryne, N. J. Nunes, and P. Robinson, Journal of High Energy Physics **3**, 18 (2009), 0811.0608.
- [287] N. Barnaby, Canadian Journal of Physics **87**, 189 (2009), 0811.0814.

- [288] S. Kachru *et al.*, Journal of Cosmology and Astro-Particle Physics **10**, 13 (2003), arXiv:hep-th/0308055.
- [289] K. Dasgupta, C. Herdeiro, S. Hirano, and R. Kallosh, Phys. Rev. D**65**, 126002 (2002), arXiv:hep-th/0203019.
- [290] M. Alishahiha, E. Silverstein, and D. Tong, Phys. Rev. D**70**, 123505 (2004), arXiv:hep-th/0404084.
- [291] R. H. Brandenberger, A. Knauf, and L. C. Lorenz, Journal of High Energy Physics **10**, 110 (2008), 0808.3936.
- [292] R. Saito, J. Yokoyama, and R. Nagata, Journal of Cosmology and Astro-Particle Physics **6**, 24 (2008), 0804.3470.
- [293] R. Saito and J. Yokoyama, Physical Review Letters **102**, 161101 (2009), 0812.4339.
- [294] S. Weinberg, Phys. Rev. D**72**, 043514 (2005), arXiv:hep-th/0506236.
- [295] D. Seery, K. A. Malik, and D. H. Lyth, Journal of Cosmology and Astro-Particle Physics **3**, 14 (2008), 0802.0588.
- [296] S. Weinberg, Phys. Rev. D**78**, 063534 (2008), 0805.3781.
- [297] L. Kofman, Preheating After Inflation, in *Inflationary Cosmology*, edited by M. Lemoine, J. Martin, & P. Peter, , Lecture Notes in Physics, Berlin Springer Verlag Vol. 738, pp. 55–+, 2008.
- [298] P. B. Greene and L. Kofman, Physics Letters B **448**, 6 (1998).
- [299] P. B. Greene and L. Kofman, Phys. Rev. D**62**, 123516 (2000), arXiv:hep-ph/0003018.
- [300] M. Peloso and L. Sorbo, Journal of High Energy Physics **5**, 16 (2000), arXiv:hep-ph/0003045.

- [301] N. Barnaby, A. Berndsen, J. M. Cline, and H. Stoica, *Journal of High Energy Physics* **6**, 75 (2005), arXiv:hep-th/0412095.
- [302] L. Kofman and P. Yi, *Phys. Rev. D* **72**, 106001 (2005), arXiv:hep-th/0507257.
- [303] S. Kachru, R. Kallosh, A. Linde, and S. P. Trivedi, *Phys. Rev. D* **68**, 046005 (2003), arXiv:hep-th/0301240.
- [304] V. Balasubramanian and P. Berglund, *Journal of High Energy Physics* **11**, 85 (2004), arXiv:hep-th/0408054.
- [305] V. Balasubramanian, P. Berglund, J. P. Conlon, and F. Quevedo, *Journal of High Energy Physics* **3**, 7 (2005), arXiv:hep-th/0502058.
- [306] J. P. Conlon, F. Quevedo, and K. Suruliz, *Journal of High Energy Physics* **8**, 7 (2005), arXiv:hep-th/0505076.
- [307] R. Kallosh, *Inflation in String Theory*, in *Inflationary Cosmology*, edited by M. Lemoine, J. Martin, & P. Peter, , Lecture Notes in Physics, Berlin Springer Verlag Vol. 738, pp. 119–+, 2008, arXiv:hep-th/0702059.
- [308] J. M. Cline, *ArXiv High Energy Physics - Theory e-prints* (2006), arXiv:hep-th/0612129.
- [309] C. P. Burgess *et al.*, *Journal of High Energy Physics* **7**, 47 (2001), arXiv:hep-th/0105204.
- [310] L. Susskind, *The Anthropic Landscape of String Theory*, in *The Davis Meeting On Cosmic Inflation*, 2003, arXiv:hep-th/0302219.
- [311] J. Dufaux, A. Bergman, G. Felder, L. Kofman, and J. Uzan, *Phys. Rev. D* **76**, 123517 (2007), 0707.0875.

- [312] J. Dufaux, G. Felder, L. Kofman, and O. Navros, *Journal of Cosmology and Astro-Particle Physics* **3**, 1 (2009), 0812.2917.
- [313] N. Barnaby and J. M. Cline, *Phys. Rev. D* **70**, 023506 (2004), arXiv:hep-th/0403223.
- [314] J. F. Dufaux, L. Kofman, and M. Peloso, *Phys. Rev. D* **78**, 023520 (2008), 0802.2958.
- [315] A. Buchel and L. Kofman, *Phys. Rev. D* **78**, 086002 (2008), 0804.0584.
- [316] A. R. Frey, A. Mazumdar, and R. C. Myers, *Phys. Rev. D* **73**, 026003 (2006), arXiv:hep-th/0508139.
- [317] G. Felder, L. Kofman, and A. Starobinsky, *Journal of High Energy Physics* **9**, 26 (2002), arXiv:hep-th/0208019.
- [318] N. Barnaby, C. P. Burgess, and J. M. Cline, *Journal of Cosmology and Astro-Particle Physics* **4**, 7 (2005), arXiv:hep-th/0412040.
- [319] J. j. Blanco-Pillado *et al.*, *Journal of High Energy Physics* **9**, 2 (2006), arXiv:hep-th/0603129.
- [320] M. Cicoli, C. P. Burgess, and F. Quevedo, *Journal of Cosmology and Astro-Particle Physics* **3**, 13 (2009), 0808.0691.
- [321] K. Becker, M. Becker, M. Haack, and J. Louis, *Journal of High Energy Physics* **6**, 60 (2002), arXiv:hep-th/0204254.
- [322] F. Denef, M. R. Douglas, and B. Florea, *Journal of High Energy Physics* **6**, 34 (2004), arXiv:hep-th/0404257.
- [323] J. J. Blanco-Pillado, D. Buck, E. J. Copeland, M. Gomez-Reino, and N. J. Nunes, *ArXiv e-prints* (2009), 0906.3711.

- [324] A. C. Vincent and J. M. Cline, *Journal of High Energy Physics* **10**, 93 (2008), 0809.2982.
- [325] Z. Lalak, D. Langlois, S. Pokorski, and K. Turzyński, *Journal of Cosmology and Astro-Particle Physics* **7**, 14 (2007), 0704.0212.
- [326] J. P. Conlon and F. Quevedo, *Journal of Cosmology and Astro-Particle Physics* **8**, 19 (2007), 0705.3460.
- [327] M. Kawasaki, K. Kohri, and T. Moroi, *ArXiv High Energy Physics - Phenomenology e-prints* (2004), arXiv:hep-ph/0410287.
- [328] L. Anguelova, V. Calò, and M. Cicoli, *Journal of Cosmology and Astro-Particle Physics* **10**, 25 (2009), 0904.0051.
- [329] N. Arkani-Hamed and S. Dimopoulos, *Journal of High Energy Physics* **6**, 73 (2005), arXiv:hep-th/0405159.
- [330] G. F. Giudice and A. Romanino, *Nuclear Physics B* **699**, 65 (2004), arXiv:hep-ph/0406088.
- [331] R. Blumenhagen, J. P. Conlon, S. Krippendorff, S. Moster, and F. Quevedo, *Journal of High Energy Physics* **9**, 7 (2009), 0906.3297.
- [332] M. Schmaltz and D. Tucker-Smith, *Ann. Rev. Nucl. Part. Sci.* **55**, 229 (2005), hep-ph/0502182.
- [333] S. P. Martin, (1997), hep-ph/9709356.
- [334] C. T. Hill and R. J. Hill, *Phys. Rev.* **D76**, 115014 (2007), 0705.0697.
- [335] R. Barbier *et al.*, *Phys. Rept.* **420**, 1 (2005), hep-ph/0406039.
- [336] W. Israel, *Phys. Rev.* **164**, 1776 (1967).

- [337] W. Israel, *Commun. Math. Phys.* **8**, 245 (1968).
- [338] B. Carter, *Phys. Rev. Lett.* **26**, 331 (1971).
- [339] R. M. Wald, *Phys. Rev. Lett.* **26**, 1653 (1971).
- [340] T. Banks, *Nucl. Phys.* **B323**, 90 (1989).
- [341] L. M. Krauss and F. Wilczek, *Phys. Rev. Lett.* **62**, 1221 (1989).
- [342] R. Cen, (2000), [astro-ph/0005206](#).
- [343] F. Borzumati, T. Bringmann, and P. Ullio, *Phys. Rev.* **D77**, 063514 (2008), [hep-ph/0701007](#).
- [344] Y. Gong and X. Chen, (2008), [0802.2296](#).
- [345] M. Lattanzi, *AIP Conf. Proc.* **966**, 163 (2008).
- [346] L. Zhang, X. Chen, M. Kamionkowski, Z.-g. Si, and Z. Zheng, *Phys. Rev.* **D76**, 061301 (2007), [0704.2444](#).
- [347] S. Palomares-Ruiz, *Phys. Lett.* **B665**, 50 (2008), [0712.1937](#).
- [348] H. Yuksel and M. D. Kistler, *Phys. Rev.* **D78**, 023502 (2008), [0711.2906](#).
- [349] M. J. Strassler and K. M. Zurek, *Phys. Lett.* **B651**, 374 (2007), [hep-ph/0604261](#).
- [350] C.-P. Ma and E. Bertschinger, *Astrophys. J.* **455**, 7 (1995), [astro-ph/9506072](#).
- [351] L. Kofman, D. Pogosyan, and A. A. Starobinsky, *Sov. Astron. Lett.* **12**, 175 (1986).
- [352] X.-L. Chen and M. Kamionkowski, *Phys. Rev.* **D70**, 043502 (2004), [astro-ph/0310473](#).
- [353] D. R. G. Schleicher, R. Banerjee, and R. S. Klessner, *Phys. Rev.* **D78**, 083005 (2008), [0807.3802](#).

- [354] S. Seager, D. D. Sasselov, and D. Scott, *Astrophys. J., Lett.* **523**, L1 (1999), arXiv:astro-ph/9909275.
- [355] S. Seager, D. D. Sasselov, and D. Scott, *Astrophys. J., Suppl.* **128**, 407 (2000), arXiv:astro-ph/9912182.
- [356] SDSS, D. J. Eisenstein *et al.*, *Astrophys. J.* **633**, 560 (2005), astro-ph/0501171.
- [357] W. J. Percival *et al.*, *Astrophys. J.* **657**, 645 (2007), arXiv:astro-ph/0608636.
- [358] N. Kaiser, *Astrophys. J.* **388**, 272 (1992).
- [359] N. Kaiser, *Astrophys. J.* **498**, 26 (1998), arXiv:astro-ph/9610120.
- [360] S. Dimopoulos, G. F. Giudice, and A. Pomarol, *Phys. Lett.* **B389**, 37 (1996), hep-ph/9607225.
- [361] A. H. Chamseddine, R. L. Arnowitt, and P. Nath, *Phys. Rev. Lett.* **49**, 970 (1982).
- [362] R. Barbieri, S. Ferrara, and C. A. Savoy, *Phys. Lett.* **B119**, 343 (1982).
- [363] L. J. Hall, J. D. Lykken, and S. Weinberg, *Phys. Rev.* **D27**, 2359 (1983).
- [364] E. Cremmer, P. Fayet, and L. Girardello, *Phys. Lett.* **B122**, 41 (1983).
- [365] N. Ohta, *Prog. Theor. Phys.* **70**, 542 (1983).
- [366] H.-S. Goh, M. A. Luty, and S.-P. Ng, *JHEP* **01**, 040 (2005), hep-th/0309103.
- [367] H.-S. Goh, S.-P. Ng, and N. Okada, *JHEP* **01**, 147 (2006), hep-ph/0511301.
- [368] S.-P. Ng and N. Okada, *JHEP* **09**, 040 (2007), 0705.2258.
- [369] S. Dawson, *Nucl. Phys.* **B261**, 297 (1985).
- [370] H. K. Dreiner and P. Morawitz, *Nucl. Phys.* **B428**, 31 (1994), hep-ph/9405253.

- [371] E. A. Baltz and P. Gondolo, *Phys. Rev.* **D57**, 2969 (1998), hep-ph/9709445.
- [372] M. Chemtob, *Prog. Part. Nucl. Phys.* **54**, 71 (2005), hep-ph/0406029.
- [373] L. D. Landau, *Dokl. Akad. Nauk Ser. Fiz.* **60**, 207 (1948).
- [374] C.-N. Yang, *Phys. Rev.* **77**, 242 (1950).
- [375] B. Holdom, *Phys. Lett.* **B166**, 196 (1986).
- [376] K. S. Babu, C. F. Kolda, and J. March-Russell, *Phys. Rev.* **D54**, 4635 (1996), hep-ph/9603212.
- [377] K. S. Babu, C. F. Kolda, and J. March-Russell, *Phys. Rev.* **D57**, 6788 (1998), hep-ph/9710441.
- [378] H.-C. Cheng and I. Low, *JHEP* **08**, 061 (2004), hep-ph/0405243.
- [379] C. Csaki, J. Heinonen, M. Perelstein, and C. Spethmann, (2008), 0804.0622.
- [380] D. Krohn and I. Yavin, *JHEP* **06**, 092 (2008), 0803.4202.
- [381] V. Barger, W.-Y. Keung, and Y. Gao, *Phys. Lett.* **B655**, 228 (2007), 0707.3648.
- [382] A. Freitas, P. Schwaller, and D. Wyler, (2008), 0806.3674.
- [383] A. W. Strong *et al.*, *Astron. Astrophys.* **444**, 495 (2005), astro-ph/0509290.
- [384] AMS-01, M. Aguilar *et al.*, *Phys. Lett.* **B646**, 145 (2007), astro-ph/0703154.
- [385] DAMA, R. Bernabei *et al.*, *Eur. Phys. J.* **C56**, 333 (2008), 0804.2741.
- [386] O. Adriani *et al.*, (2008), 0810.4995.